UNIVERSITY OF SOUTHAMPTON

EXPERIMENTAL STUDIES OF DIRECTOR DYNAMICS AND DISTRIBUTIONS IN LIQUID CRYSTALS

by

Christopher John Dunn

A dissertation submitted in partial
fulfilment of the requirements for
the degree of Doctor of Philosophy
at the University of Southampton

Department of Chemistry

November 1998

UNIVERSITY OF SOUTHAMPTON

ABSTRACT

FACULTY OF SCIENCE

CHEMISTRY

Doctor of Philosophy

EXPERIMENTAL STUDIES OF DIRECTOR DYNAMICS AND DISTRIBUTIONS IN LIQUID CRYSTALS

by Christopher John Dunn

This Thesis reports the results of investigations into the director dynamics and the director distributions in several thermotropic, calamitic liquid crystal systems, made using EPR spectroscopy. Chapter 1 gives an introduction to liquid crystals, including a description of the principal phase types and a review of basic structure-property relationships. The fundamental properties of liquid crystals are described, and a link is made with the techniques that are used to study them and how they are used. In Chapter 2, the EPR experiment and its applicability to the study of liquid crystal systems is described. In Chapter 3, the experiment that is used to measure the rate of magnetic field-induced director realignment in the nematic phase of a typical low molar mass liquid crystal is described. The EPR experiment shows very clearly that the macroscopic alignment of the director is maintained during relaxation through 45° but is lost upon relaxation through ~80°. In Chapter 4, the technique developed in Chapter 3 is used to study the different director reorientation responses in the nematic phases formed by an odd and even dimer from a homologous series and in a monomer that may be considered to be the basic building block of these two dimers: the most striking result is that the monomer shows a much faster director reorientation than either of the dimers and that there is very little to differentiate between the rates of the response of the odd and the even dimer. The director distribution in a rapidly spinning nematic sample situated in a magnetic field is studied in Chapter 5 using field gradient EPR spectroscopy which gives added information about the spatial distribution of the director that is not available in conventional EPR studies. A simple model distribution function can be parameterised to give a good fit to all of the experimental spectra. In Chapter 6, the director distribution in an unusual smectic phase formed by several odd dimers is studied using EPR. Simultaneous fitting of several of the angular-dependent EPR spectra suggest that the experimental spectra are well fitted using a simple analytical function for the director distribution.

CONTENTS

CHAPTER 4 **Viscoelastic properties of the nematic phase of an odd and an even Liquid Crystal dimer measured using an EPR technique**

CHAPTER 5 **The use of field gradient EPR in the study of rotating Nematic Liquid Crystals**

CHAPTER 6 **The director distribution in the Sm phase of liquid crystal dimers. A study using EPR spectroscopy.**

APPENDICES

ACKNOWLEDGEMENTS

First of all, I would like to thank my supervisor, Geoffrey Luckhurst, for his continued support and guidance which have been essential in seeing me through to completion of this Thesis.

I would also like to thank Professor Gian Franco Pedulli and Dr Marco Lucarini at the University of Bologna for their help in carrying out the field gradient experiments presented in Chapter 5. Thanks also go to Pete Barnes and to Mark Wilson for the synthesis of CB7CB and CBO6CT which were studied in Chapter 6. I am also grateful to all of the past and present members of the Liquid Crystal group who have always been a pleasure to work with, if sometimes a wanted or unwanted distraction: thank you Jason, Shaun, Andrew, Lizzy, Flavio, Ian, Mark, Pete (Le M.), Dinali and to everyone else who has contributed less directly. Thanks also go to everyone else in Southampton and elsewhere who have been more supportive than they realise in pushing and pulling me towards handing in this Thesis: Jane, Martin, Stuart, Twig, Helen, Kiron, Alison and to Gareth and Sue. Thank you to Mum, Dad, Ste and Loz who have been supportive and encouraging throughout and to Johanna who has had great belief in me.

Finally, I would like to express my gratitude to the University of Southampton and to Courtaulds for the award of a research studentship.

Chapter 1

Introduction to Liquid Crystals

1.1 Introduction

It is well-known that the molecules in a crystalline solid have both long range positional and orientational order whilst those in a liquid possess neither positional nor orientational order extending over large distances [1]. It is not difficult to imagine an intermediate state in which a system composed of anisometric (geometrically anisotropic) units retains some long range orientational order but little or no positional order, except over short distances. The discovery of a phase with this distinctive property can be traced back to the work of the Austrian botanist Reinitzer over a century ago when he noted that a sample of cholesteryl benzoate apparently showed two melting points upon heating, the first at 145.5°C from a crystal to a mobile, cloudy liquid and the second at 178.5°C from the cloudy liquid to a clear liquid [2]. Later studies by Lehmann showed that the turbid fluid was birefringent, a property normally associated with crystalline solids, but was mobile, like a liquid: this apparently contradictory combination of properties prompted Lehmann to describe the curious fluid as a 'liquid crystal'. These anisotropic liquids are referred to as liquid crystals or mesophases and a compound that forms a mesophase is referred to as a mesogen. Today, a large number of mesophases are known, in which the characteristic orientational order of the constituent anisometric units is complemented by varying degrees of positional order and literally thousands of mesogens have been synthesized or isolated with an extensive variety of molecular architectures which exhibit one or more of these mesophases [3, 4, 5, 6].

Liquid crystals fall into two main categories, lyotropic and thermotropic, which differ in the nature of the anisometric units. Both categories have huge industrial and commercial importance and a diverse range of applications ranging from the everyday to the highly specialized [7, 8, 9, 10]. In lyotropic systems, the anisotropic building blocks that form the mesophase are molecular aggregates of different types (micelles, cylinders, layers) that self-assemble in mixtures of two or more components depending upon the composition of the mixture. One of the components in these mixtures frequently acts as a solute (and is typically an amphiphile) and another as a solvent, as is the case, for example, when soap and water form a lyotropic system [11]. The phospholipid bilayers that make up cell membranes are a hugely important example of a lyotropic mesophase in living systems. Thermotropic liquid crystals can consist of a single component or a mixture of several components, but their principal characteristics are that the anisotropic units are the individual molecules themselves and that the appearance of a mesophase is brought about by changes in temperature. They may be described as enantiotropic or monotropic, according to whether or not the mesophase is the thermodynamically most stable phase at any temperature, and this dictates whether the mesophase is seen on both heating and cooling, or just upon cooling when supercooling occurs. Thermotropic systems may be broadly subdivided into calamitic liquid crystals, in which the molecular shape can be approximated by an elongated rod, ellipsoid or lath, and discotics, in which the molecules may be approximated by a disc shape.

In a mesophase, molecular motion is rapid but not random, on average the long axes of calamitic molecules, which for now, we approximate as ellipsoids, line up parallel to a preferred direction in space called the director which is denoted by a unit vector **n** and defines a local symmetry axis of the mesophase [12]. This partial orientational order leads to the anisotropic properties that characterise a mesophase: measurements of a property of a mesophase measured along the director will be different from those measured at some angle to it [13]. The orientation of the director is often sensitive to an external field and the control or manipulation of the director orientation using the effects of external fields [14, 15] is usually the basis for the use of thermotropic liquid crystals in, for example, a range of electro-optic displays, as high tensile fibres and as templates in the control of the nanostructure of materials in industrial syntheses.

This Thesis is concerned solely with thermotropic calamitic systems and, in particular, with the dynamic and static behaviour of the director in the mesophases of several compounds. This Chapter begins with a description of the principal phase types, then goes on to review relevant properties, consider some of the relationships between molecular structure and mesophase behaviour and then to a more detailed description of the order that characterises a mesophase.

1.2 Principal phase types [16]

1.2.1 The Nematic phase (N)

The simplest and most disordered liquid crystal phase is the nematic phase, N, pictured in figure 1a in which the anisometric mesogenic molecules are represented as ellipsoids. The molecules in the nematic have no positional order (except at very short range, reflected in the liquid-like mobility of the phase) but retain some average long range orientational order about some preferred direction which defines the local director. The nematic phase has uniaxial symmetry about the director, which is identified with the single optical axis of the phase, and is apolar (even though it may comprise polar molecules, this does not lead to a macroscopic effect). In an unperturbed nematic sample the orientation of the director naturally varies slowly over distances very much larger than the molecular dimensions although in some regions there are discontinuities in the director pattern. Application of a small magnetic or electric field or the influences of surface forces in a thin cell can be used to align the director in different parts of the sample and produce true macroscopic orientational order [17].

It is convenient to use the nematic phase to introduce an order parameter which is used to describe, at the molecular level, the partial orientational order that exists in all mesophases. In the study of phase transitions, a convenient choice of an order parameter equals 0 in the disordered phase and 1 in the case of complete order in the more ordered phase. The parameter most commonly used to describe the orientational order in a liquid crystal is the quantity $\overline{P}_2$ given by

$$\overline{P}_2 = \frac{(3\ \overline{\cos^2\beta}\ -1)}{2} \qquad (1.1)$$

in which β is the angle between the director and the molecular symmetry axis (the molecular long axis and the molecular short axis in calamitic and discotic systems, respectively). The bar indicates a time or ensemble average. $\overline{P}_2$ equals 1 in the case of complete orientational order of the molecular long axes along the director in the nematic phase, 0 in an isotropic liquid, and -½ in the event that all of the molecular long axes lie perpendicular to the symmetry axis of the mesophase. The degree of orientational order in a mesophase and, in particular, the onset of, or changes in, the orientational order at a phase transition are important in the development of theoretical models of liquid crystals.

1.2.2 The Cholesteric phase (N*)

The cholesteric or chiral nematic phase, N*, is closely related to the nematic phase: on a microscopic scale they are virtually indistinguishable but, macroscopically, the two phases are very different. The chiral nematic phase is formed by chiral systems which contain a preponderance of one enantiomer, or by adding a chiral dopant to a nematic phase. In an unperturbed nematic phase the director is randomly oriented in space, but in a chiral nematic, the chiral molecules impart a continuous and systematic spatial variation to the director, so that it naturally describes a helix on passing through the phase as shown in figure 1b. The distance over which the director is rotated through 360° defines the pitch length p of the phase. When this is of the order of the wavelength of visible light, this phase is highly coloured with a colour that depends upon the pitch length. Thermochromic materials make use of the fact that the pitch length and therefore the colour of the material is sensitive to temperature [18]. A nematic may be thought of as a chiral nematic phase with an infinite pitch length.

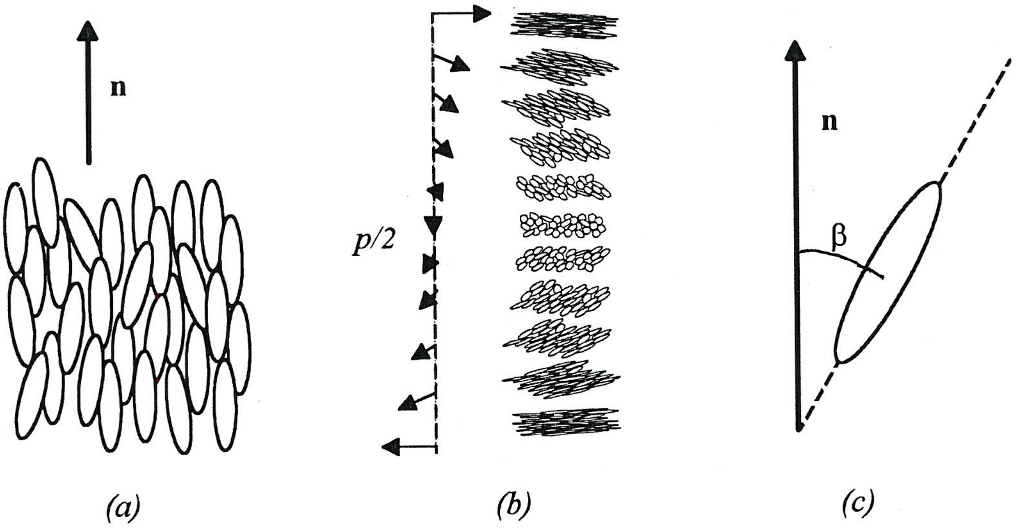

(a) (b) (c)

Figure 1 A schematic diagram of the orientational order of ellipsoidal particles in (a) a nematic phase and (b) a chiral nematic phase showing the director **n** *and the (c) the angle* β *between the molecular long axis and the director that is used to define the orientational order parameter* $\overline{P}_2$.

1.2.3 Smectic Phases

A large number of smectic phases have been identified in which partial orientational order is complemented by some long range positional order as the molecules are more or less confined to layers. They are indicated by a letter prefixed by the label Sm. They may be classified into orthogonal phases, for example, the SmA and SmB, and tilted phases, for example, SmC, depending upon whether the director is parallel to or is tilted with respect to the layer normal. The classification of smectic phases also includes at least seven other recognized modifications (designated SmE-K) which are associated with differing degrees of positional order within and between the layers. In another modification; the SmD (or D) phase, the layered structure is not as distinct as in the other modifications, and this phase bears more structural similarity to micellar systems. In this brief review of phase types, we summarize only the main types and some of their variants which relate to the systems we have studied, the interested reader is referred to some of the many reviews in the literature for a more complete account [16, 19, 20].

1.2.4 The Smectic A Phase (SmA)

In the SmA phase the centres of mass of the molecules are confined to layers but there is no correlation of their positions within or between layers. Molecules can rotate freely about their long axes and pass from one layer to another relatively easily. The SmA phase may be thought of as an analogue of the nematic phase with the addition of some (usually weak) positional order. The SmA phase is uniaxial and the director lies along the layer normal. The ratio d/l of the interlayer repeat distance, d (obtained from X-ray diffraction experiments) to the molecular length, l, is conventionally ~1 and this monolayer structure is sometimes indicated by the label SmA_1 and it is this version that is shown in figure 2a. A number of variants have been found in which d/l is significantly different from 1, this is normally attributed to strong associations between polar groups on neighbouring molecules. Thus, in the SmA_2, $d \sim 2l$, and a bilayer structure results from antiferroelectric ordering of the molecules, that is, the molecules arrange themselves antiparallel to each other in adjacent layers. In the interdigitated smectic A phase, denoted SmA_d, a partial bilayer structure is formed with $d \sim 1.4\text{-}1.6l$. In the intercalated smectic A phase, SmA_c, formed by certain dimer mesogens, $d \sim 0.5l$

(this is discussed later). The smectic A antiphase, SmÃ, contains a stable mixture of mono- and bilayer regions.

1.2.5 The Smectic C Phase (SmC)

The SmC phase shows the same characteristics of positional order as the SmA phase, however, the director lies at an angle to the layer normal, referred to as the tilt angle α, which reflects the fact that the molecular long axis is tilted on average with respect to the layer normal. Another angle around the layer normal, the tilt direction, is needed as well as the tilt angle, to locate the director with respect to the layer normal. Consequently the SmC phase is biaxial. Depending upon the system and how the phase forms, the tilt direction may vary from layer to layer (for example, in the SmC* formed by chiral systems, the tilt direction describes a helix on passing through the layers). As for the SmA phase, strongly polar molecules form a number of variants on the basic SmC structure.

1.2.6 Added positional order

In the uniaxial smectic B phase the molecules are arranged locally in a hexagonally close-packed array with their long axes oriented perpendicular to the layer planes. Although there is no long range positional order of the molecules on a single hexagonal lattice, the orientation of the local hexagonal lattices is maintained within a single layer and across adjacent layers, and consequently the smectic B phase is said to possess bond orientational order. Tilted versions of the smectic B exist: in the smectic F and smectic I phases the tilt is directed towards a side and an apex of the hexagonal lattice, respectively. In other modifications, rotation about the molecular long axes becomes hindered. A series of crystal modifications bear the same letter as many of the smectic phases, these are really soft crystals in which the local positional order of the smectic counterpart is extended into true long range positional order both within and across layers.

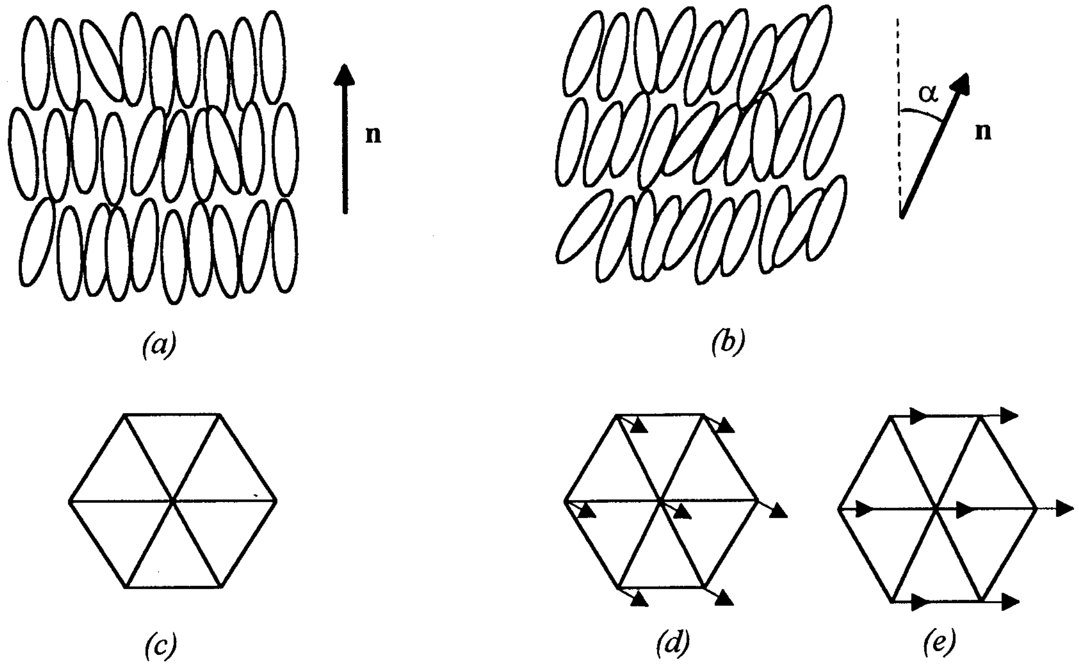

Figure 2 A schematic representation of the positional and orientational order in the (a) SmA and (b) SmC phases. The additional hexagonal ordering of the centres of mass within the smectic layers of the SmB phase is shown in (c) and the differing tilt directions with respect to the hexagonal net is shown for the (d) SmF and the (e) SmI phases.

1.3 Properties of Liquid Crystals

The applications of liquid crystals and the techniques that are used to study and characterise them follow from their interesting properties, some of which are now outlined.

1.3.1 Thermodynamic Properties

In thermotropic systems mesophase behaviour is seen as a function of temperature. Changes in temperature produce a number of phase transitions, from an isotropic liquid to a mesophase, from one mesophase to another, and from a mesophase to a crystal or glass. Heating or cooling a mesophase also produces changes in the degree of orientational and/or positional order and therefore in the anisotropic and other properties of the mesophase. The thermal behaviour of a sample is studied using Differential Scanning Calorimetry (DSC) which measures the input of energy that is required to maintain the temperature of a test sample equal to that of a reference sample as its temperature is increased or decreased. This information is used to draw inferences about the changes in the degree of order and the phase behaviour of a sample although it can not be used to identify particular phases directly.

An important part of the science of liquid crystals is concerned with the study of phase transitions [21, 22]. The Helmholtz free energy A of a system is given by,

$$A = U - TS \tag{1.2}$$

in which U is the internal energy of the system, T the absolute temperature and S the entropy. According to the Ehrenfest classification, a transition of order n is characterised by the first $(n-1)$ derivatives of the Helmholtz free energy being continuous and the n^{th} being discontinuous. A first order transition is characterised by a jump in the first derivative of the free energy (that is, in the entropy S) and a latent heat given by $T\Delta S$. Thus, the melting transitions of cholesteryl benzoate have associated with them a latent heat; as such they are termed first order phase transitions, and a peak is seen on the DSC trace upon heating with the area of the peak equal to the latent heat of the transition. The nematic-isotropic transition is associated with a small latent heat and is often referred to as being a weak first order transition. A second order transition is characterised by a continuous change in the entropy and a discontinuity in the second derivative, reflecting a change in the heat capacity C_V of the sample. This is seen as a change in the baseline of the DSC trace at the transition. The classification of phase transitions is important in the development of the theory of liquid crystals.

1.3.2 Interaction with electromagnetic fields

The interaction of light with liquid crystals underpins their applications in display devices. The refractive indices for light travelling parallel and perpendicular to the director are different, consequently, liquid crystals are birefringent and therefore have the ability to rotate the plane of polarized light [23, 24]. Normally no light emerges from crossed polarizers because the light transmitted by the first polarizer can not pass through the second polarizer. A liquid crystal placed between crossed polarizers can rotate the plane of polarization if the director is not uniformly aligned parallel to either of the polarizers or the direction of travel of the light, and therefore some light emerges from the second polarizer. Figures 1 and 2 showed idealized sketches of the molecular organisation within several mesophases. In real samples these structures are often not perfectly reproduced and are punctuated by defects (at points, along lines or along planes) and distortions where the director orientation can not be defined or changes rapidly. The type and number of these defects and distortions varies from phase to phase and from one material to another but, essentially, different phases and patterns of the director produce different and characteristic textures when viewed on the polarizing microscope which are discussed in greater detail elsewhere [19, 25, 26]. Mesophases are usually studied as thin sections of sample placed on a microscope slide, which is sometimes pretreated to control the orientations of the director at the boundaries of the sample [27], and placed between crossed polarizers. The polarizing microscope equipped with a hot stage is an essential tool in the characterisation of liquid crystals as it allows mesophases to be identified and the temperatures of phase transitions to be determined. The latter gives a good indication of sample purity: sharp transitions indicate a pure material, while the presence of non-mesogenic impurities leads to a depression of the transition temperatures and transitions which occur over a wider temperature range.

The interaction of electromagnetic radiation of other frequencies occurs for liquid crystals as for comparable isotropic samples of molecules with similar structures and gives information about both the static and dynamic properties of the liquid crystal [28]. But, in general, the absorption spectrum of an isotropic sample represents a particularly simple case as rapid isotropic molecular motion leads to an averaging of the molecular interactions and the spectra take on their most simple form. In a liquid crystal, the strong anisotropy of molecular interactions means that such averaging does not occur and it is common to observe a large number or bandwidth of absorptions in the spectrum. As a consequence the interpretation of the spectra of liquid crystal samples is, in general, not a trivial task and may necessitate simplifying assumptions. At higher frequencies, X-ray and neutron diffraction studies of liquid crystals are an invaluable tool in the study and characterisation of liquid crystals where they are used to determine average intermolecular distances and molecular distribution functions and to confirm phase identifications [29].

1.3.3 Liquid Crystals in external fields

When a magnetic field is applied to a liquid crystal sample, the director experiences a magnetic torque

$$T_{\mathrm{B}}(\xi) = -\frac{1}{2\mu_0}\Delta\tilde{\chi}\, B^2 \sin(2\xi) \tag{1.3}$$

in which ξ is the angle between the magnetic field and the director, $\Delta\tilde{\chi}$ is the anisotropy of diamagnetic susceptibility (the difference between the magnetic susceptibilities measured parallel and perpendicular to the director, that is, $\Delta\tilde{\chi} = \tilde{\chi}_{\parallel} - \tilde{\chi}_{\perp}$) and B the magnetic flux density. This creates an anisotropic magnetic contribution to the free energy given by

$$F_{\mathrm{B}}(\xi) = -\frac{1}{3\mu_0}\Delta\tilde{\chi}\, B^2 P_2(\cos\xi) \tag{1.4}$$

Analogous expressions, in which $\Delta\tilde{\varepsilon}$ and E replace $\Delta\tilde{\chi}$ and B respectively, describe the torque on the director and the electric contribution to the free energy in an external electric field. In what follows we consider only the case of a magnetic field. Most calamitic molecules have a positive $\Delta\tilde{\chi}$ and therefore the director lies parallel to the magnetic field (ξ=0°) in the state with the lowest orientational magnetic energy, see figure 3. Note from figure 3 that the magnetic torque on the director is zero when the magnetic field and the director are parallel or perpendicular to each other but that the magnetic energies of these two states are very different, taking their minimum and maximum values respectively.

As we have mentioned, in the absence of an external field the director usually varies slowly through space over many molecular lengths although the orientational order of molecules with respect to the local director S_l (equivalent to $\overline{P}_2$ introduced earlier) is constant as this is a property of the liquid crystal itself. The spatial variation of the director on a macroscopic scale means that the orientational order over a whole sample with respect to any space fixed direction equals zero, $S_G = 0$. This is an unaligned or multidomain liquid crystal sample. In this state the mesophase may be thought of as an elastic medium, in which any distortions of the director away from macroscopic alignment store elastic energy. The director field can undergo distortion in several ways, but these can be resolved into components of three basic types of distortion, splay, twist and bend, each of which has associated with it an elastic constant [30].

The length scales over which the director varies and the distortions which the director undergoes depend upon the relative values of these three elastic constants but are always much larger than the molecular dimensions. This has lead to the formulation of a continuum theory in which the behaviour of the sample on a macroscopic scale is described in a way which disregards the details of the structure on the molecular scale [31, 32]. In this Thesis we shall use this same general idea as we treat the orientational order of the molecules (or mesogenic groups) with respect to the local director separately from the orientation of the director with respect to a laboratory reference frame (In fact, the EPR experiments which are described in Chapter 2 naturally make this same distinction).

In the presence of a magnetic field, the director experiences a magnetic torque tending to align the director with the magnetic field and to minimize the contribution of the magnetic energy to the free energy of the system. If the magnetic field is above a certain threshold value, then the local directors will reorient so as to all align parallel to the magnetic field and form a monodomain or macroscopically aligned liquid crystal sample in which S_G=S_l (sometimes called a single liquid crystal). In such a sample, the bulk properties of the monodomain such as $\Delta\tilde{\chi}$ and $\Delta\tilde{\varepsilon}$ are proportional to (and therefore can be used as a measure of) the orientational order parameter $\overline{P}_2$ ($\equiv S_l$) of the mesophase [33]. In theory, these field-induced reorientations of the director can occur without any movement of the centres of mass of the particles of the mesophase, but in practice rotations of the director are often accompanied by flow of the particles of the mesophase (the reverse is often also true) and the interpretation of these processes is complex [34]. The director variation over a multidomain nematic sample and over a monodomain nematic is shown schematically in two dimensions in figure 4.

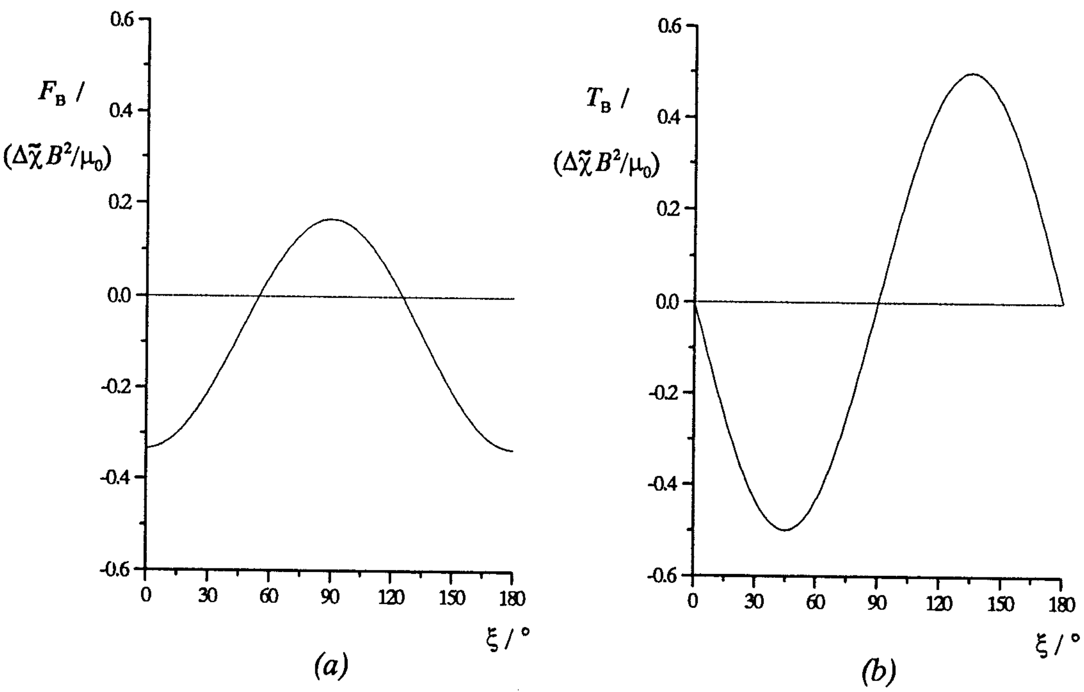

Figure 3 The anisotropy in (a) the magnetic energy and (b) the magnetic torque on the director as a function of the angle ξ between the director and a magnetic field (in reduced units).

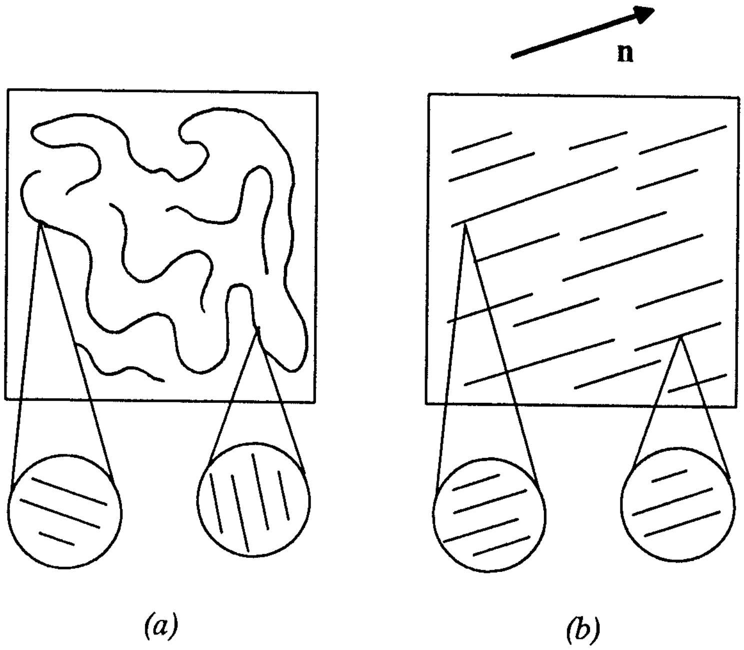

Figure 4 The director variation in (a) a multidomain and (b) a monodomain sample in a magnetic field.

In a nematic phase formed by most low molar mass liquid crystals, the barrier to rotation of the director is low and so the magnetic field that is needed to create a monodomain is also low, typically several hundred Gauss (n.b. 10,000G ≡ 1T). In the case of other phases the degree of director alignment depends on the history of the sample. If a smectic sample has already formed as a multidomain, then the application of moderate fields will not produce a torque large enough to reorient the layers to form a monodomain as the degree of disruption to the local structure provides an insurmountable barrier to director reorientation. A much higher field strength must be employed to reorient the layers and create a monodomain. A multidomain smectic will often form at low fields because the relatively large entropy change of transition to a smectic phase means that the major contribution to the free energy comes from the change in positional order at the transition. This dominates the magnetic contribution of the orientational free energy and as a result many small domains are produced at the transition with a largely random orientation and the smectic sample grows into a multidomain. Formation of a monodomain smectic sample in a small magnetic field (<10,000G) frequently requires that the compound possesses a nematic phase above the smectic phase or exhibits pretransitional smectic ordering. In this case, the director can be uniformly aligned in the nematic phase and a monodomain smectic phase grown from this by annealing, that is, by cycling the temperature through the phase transition for most of the sample and seeding the thermodynamically most stable monodomain smectic from the aligned nematic phase. It should be noted that this description applies to orthogonal smectic phases, the behaviour of the director in biaxial smectic phases is more complicated, depending more critically on the orientation of the magnetic field with respect to the smectic layers. Thus in tilted phases, there is often only a small barrier to the rotation of the director about the layer normal, that is, changing the tilt direction without changing the tilt angle α, as this can occur without disruption of the layers [35]. In Chapter 2, Electron Paramagnetic Resonance (EPR) as a tool in the study of liquid crystals is introduced, as we see in more detail then, a static magnetic field is an integral part of this spectroscopic technique. Here it is sufficient to note that the strength of the magnetic field used, typically 3300 to 6000G, is strong enough to align most nematic samples. This allows production of monodomain smectic samples if carefully prepared, but will not change the orientation of smectic layers after they have formed although care must be taken when dealing with tilted smectic phases in which the director may rotate within the existing layer structure.

1.4 Structure-property relationships

Over the years a huge research effort has been invested in the investigation and development of materials with appropriate properties for the existing and projected range of applications for liquid crystals. In the course of these studies correlations have been recognized between the structure of the mesogenic molecule and the properties and structure of the mesophase that it forms. Some of these structure-property relationships are discussed in this section.

1.4.1 Liquid Crystal molecules

Thus far we have represented and described mesogenic molecules as rigid, elongated, rods or ellipsoids. This is a reasonable first approximation of a low molar mass calamitic liquid crystal molecule and at least serves to communicate the central point that an anisometric structural unit or mesogenic group is incorporated in, and is an essential component of, any liquid crystal. In this section we shall discuss some of the structure-property relationships of calamitic liquid crystals and we shall see that this approximation is less appropriate for representing the range of molecular architectures of real systems and understanding their mesophase behaviour. In particular, some degree of molecular flexibility is tolerated and is often essential if a material is to exhibit a stable mesophase [3, 4, 5]. In addition to the mesogenic groups which are an essential feature of any mesogenic system, figure 5 represents and shows some examples of the other structural moieties that comprise a typical liquid crystal molecule and exert a range of influences on its behaviour. Also shown is a prototype liquid crystal structure, showing how these units typically fit together in a real system.

(a)

mesogenic group

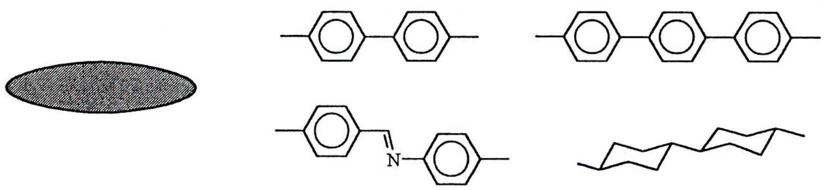

terminal chain	T	C_nH_{2n+1} , OC_nH_{2n+1} , $(CH_2CH_2O)_nH$, $(OSi(OH)_2O)_nH$
spacer group	S	$(CH_2)_n$, $O(CH_2)_nO$, $(CH_2CH_2O)_n$, $(OSi(CH_3)_2O)_n$.
lateral group	L	CH_2CH_3 , Cl , F .
polar substituent	P	CN, NO_2 , OH .

(b)

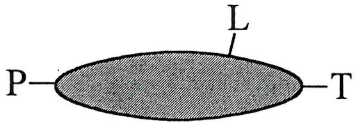

Figure 5 (a) the components of a typical calamitic liquid crystal and (b) a prototype liquid crystal molecule

These moieties may be combined to produce a number of different classes of liquid crystal. A monomer consists of a single mesogenic core to which are usually attached one or more terminal substituents. For example, in the historically important series of 4-alkyl-4'-cyanobiphenyls, abbreviated to *n*CB and known as the K series, a flexible alkyl terminal chain containing *n* C atoms is attached to one end of the rigid, elongated, biphenyl core and a polar cyano group to the other [36]. The general monomer structure of the *n*CB series is shown in figure 6a. Liquid crystal dimers are formed by linking two mesogenic cores by a flexible or semi-flexible chain, referred to as a spacer. For example, the series of α,ω-bis(4-cyanobiphenylyl)alkanes, the CB*n*CB series, is formed by linking two mesogenic cyanobiphenyl cores by a spacer containing *n* methylene units [37]. The general structures of two examples of liquid crystal dimers are shown in figure 6b. A trimer may be formed by addition of another mesogenic core through a second spacer. This process may be repeated to form a polymer, referred to as a main-chain liquid crystal polymer, when the mesogenic groups and spacers form the backbone of the polymer chain [38]. Alternatively, a side-group liquid crystal polymer may be formed by attachment of mesogenic groups to a flexible polymer backbone by spacer groups. These two types are shown in figure 6c and d respectively. In the examples shown, symmetric dimers and trimers and polymers have been formed by linking together identical mesogenic groups, it is also possible to link different mesogenic cores to form non-symmetric dimers and trimers or mixed oligomers and polymers.

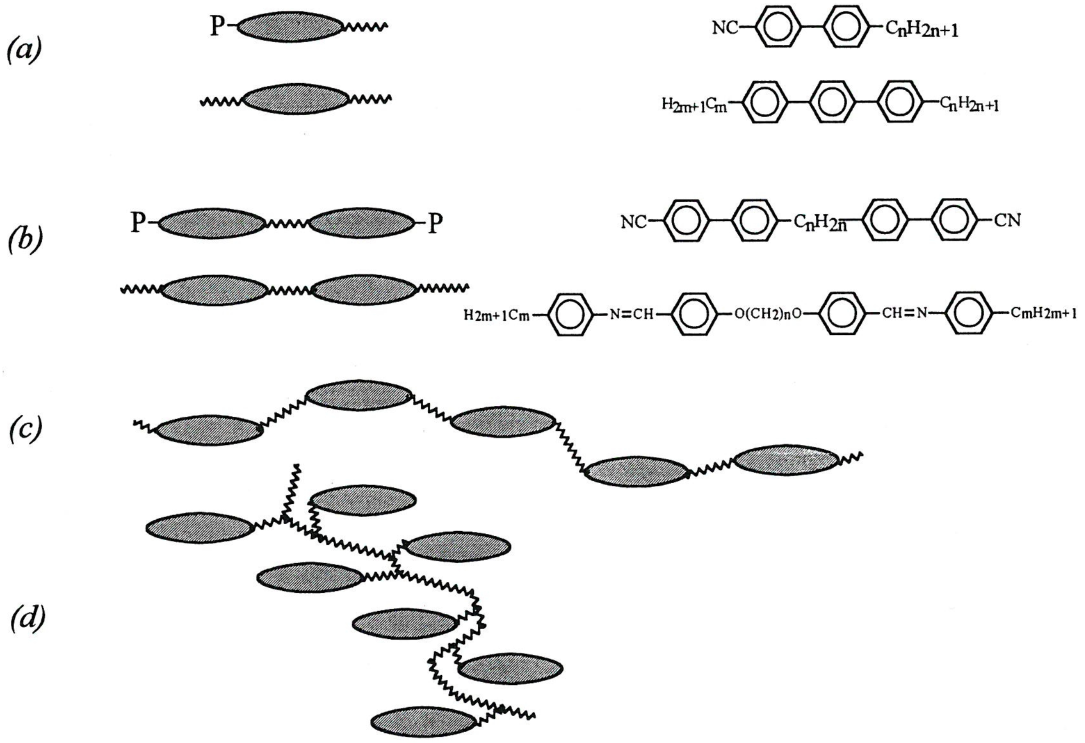

Figure 6 Types of calamitic liquid crystal molecules, (a) monomers, (b) dimers and (c) main-chain and (d) side-chain liquid crystal polymers.

In this section, some of the main features of the effect of the structure of the different parts of the liquid crystal molecule on the properties and the type of mesophase formed are reviewed, paying particular attention to mesophase stability as indicated by the temperature of the liquid crystal-isotropic transition. This review is necessarily brief and is limited to achiral monomers and dimers with a relatively simple molecular architecture, although the guiding principles that are outlined apply equally to other calamitic systems. We consider first some structure-property relationships for monomeric liquid crystals.

1.4.2 Liquid Crystal Monomers

Systematic studies across a large range of compounds have lead to an understanding of the molecular features in the basic monomer structure pictured in figure 5 which increase mesophase stability [39, 40]. A rigid, elongated core gives rise to anisotropic intermolecular forces between neighbouring molecules which stabilizes a mesophase with respect to an isotropic phase and therefore tends to elevate the liquid crystal-isotropic transition temperature. Frequently such a material will also have a high melting point. The presence of terminal chains which dilute the strength of the interactions between mesogenic cores tends to depress the melting point and, to a lesser extent the clearing temperature, making it more likely that a mesophase will be formed, and if a mesophase is formed, they can also exert some more subtle effects. It is not surprising to find that structural features which promote the rigidity of the elongated core, such as aromatic and alicyclic rings, and multiple bonds about which rotation is restricted, are common in mesogenic groups, and that monomers containing highly elongated mesogenic groups form mesophases with greater thermal stability. In an aromatic mesogenic core, a large π-system is created. This contains mobile electron density which increases the polarizability anisotropy, $\Delta\alpha$, and therefore increases the dispersion forces between neighbouring molecules in a mesophase although the relative importance of this against the simple consequences of the anisometric shape of the mesogenic core is a matter of some debate [40, 41, 42]. Some polar terminal substituents can also conjugate with an aromatic core, further extending the π-system. More importantly, most polar groups introduce a dipole to the molecule which gives rise to strong dipole-dipole interactions between neighbouring molecules and this leads to elevated clearing temperatures and generally increased smectic tendencies. Such compounds may also form mesophases with the additional feature of antiparallel correlations of the molecular dipoles in adjacent molecules which leads to some variations of the basic phase types, for example, the $\mathrm{SmA_d}$ phase with $d \sim 1.4l$ seen for some members of the *n*CB series [19].

The effect of different terminal chain lengths is revealed in the behaviour along a homologous series. The *n*CB series, **1** demonstrate typical influences of chain length. The transition temperatures for this series are shown in figure 7a. For *n*=1-4, the melting point is too high and these compounds exhibit a nematic phase on cooling only, that is, a monotropic nematic phase. At longer chain lengths, an enantiotropic nematic phase is seen as the melting point drops below the nematic-isotropic transition temperature. This is increasingly replaced by smectic behaviour as the chain is lengthened further; initially the smectic phase forms below the nematic phase, but beyond *n*=9, only smectic behaviour is seen. The formation of a smectic phase may be thought of as a microphase separation in which the mesogenic cores constitute one microphase and the alkyl chains the other. Such a separation may be expected on both energetic and entropic grounds as the terminal alkyl chain is lengthened. Energetically, the mean of the core-core and the chain-chain interactions may be less than the mixed core-chain interaction; the disruption of the core-core interactions by short chains will be less severe but longer chains will be more disruptive and therefore beyond a certain chain length the mixed interaction will not be tolerated and the nematic phase is extinguished. Entropically, a chain positioned between mesogenic cores will be ordered by the cores and is hence disfavoured. The entropic cost of chain ordering is not severe at short chain lengths and is outweighed by the entropy gain accruing from mixing cores and chains but becomes more significant as the chain is lengthened.

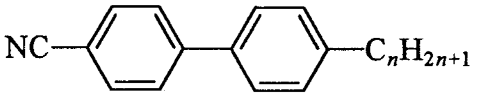

1

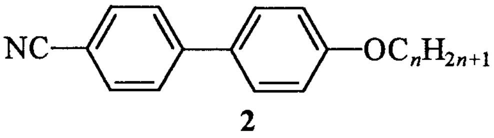

2

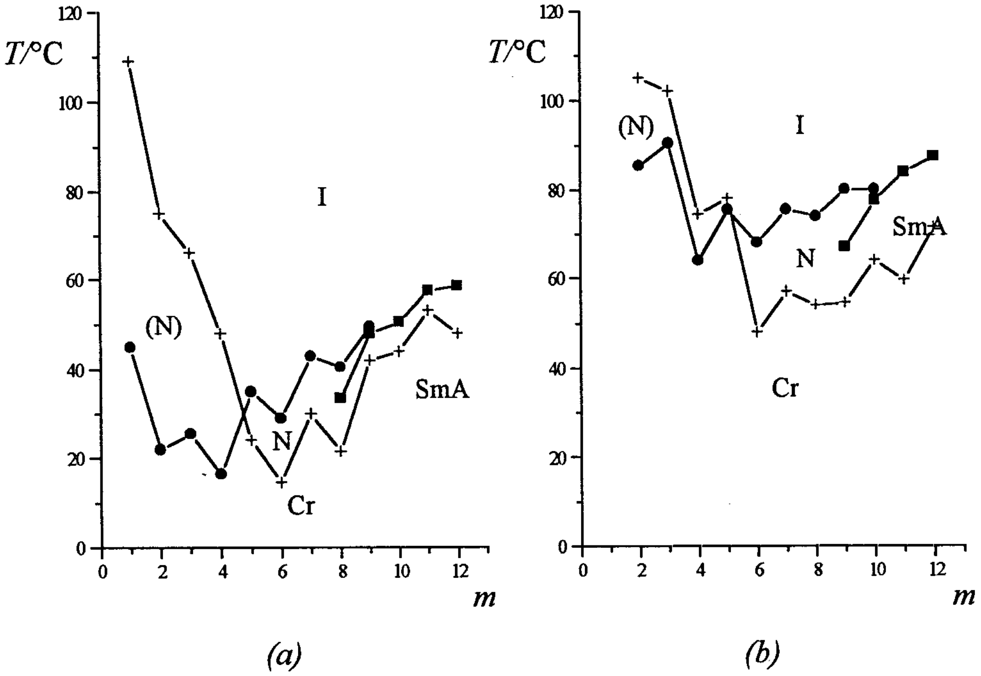

Figure 7 The transition temperatures for (a) the nCB and (b) the nOCB series as a function of m, the total number of C and O atoms in the terminal chain. m=n for the nCB series, m=n+1 for the nOCB series. + = melting point, • = N-I, ▪ = SmA-N or SmA -I.

Overlying these general trends in phase behaviour and transition temperatures is a dependence on the parity of the terminal alkyl group, the so-called odd-even effect. It is observed that odd members of the series have higher transition temperatures than the neighbouring even members of the series. This has been explained by assuming that, although the alkyl chain is flexible, the dominant conformations of the chain in the odd members elongate the molecule with no increase in breadth over that of the preceding even member. The ease of packing these more elongated units favours greater orientational order for the odd members of a homologous series [43]. This maximizes the influence of the anisotropic intermolecular forces which leads to an increase in the thermal stability of the mesophase formed by the odd members, relative to that of the even members, for the reasons that were outlined when discussing features of the mesogenic core itself. The odd-even alternation is attenuated at longer chain lengths as the chains generally disrupt the core-core interactions which stabilize the mesophase and are less able to be ordered by them whatever their parity. An odd-even alternation is also observed in other phase properties such as Δn, $\Delta\tilde{\chi}$ and $\Delta\tilde{\varepsilon}$ and transitional properties which depend upon the orientational order. In a nematic phase in particular, the degree of orientational order also influences the conformational distribution of the flexible alkyl chains: a high degree of orientational order favours the more elongated conformers which, in turn, facilitates greater orientational order. The entropy change at the nematic-isotropic transition is influenced by the degree of orientational order that is lost at the transition. In the odd monomers, there is a loss of a high degree of orientational order and some conformational order, and, therefore, a large entropy change at the nematic-isotropic transition. In the even monomers, the weaker orientational order leads to less conformational order, there is therefore a smaller entropy change at the nematic-isotropic associated with the loss of the weak orientational order and virtually no additional conformational contribution to the entropy change at the transition. As a consequence of the synergy that exists between orientational and conformational order, the odd-even alternation in the entropies at the nematic-isotropic transition is pronounced with the odd monomers having the larger values. Unlike the alternation in the clearing temperatures, this alternation is generally not attenuated with increasing chain length.

The link angle between the terminal chain and the mesogenic core also exerts an important influence on transitional properties. For example, a comparison of the transitional properties of the *n*CB series with those of the 4-alkyloxy-4'-cyanobiphenyls or *n*OCB series **2** reveals that, for the same length of the alkyl and the alkyloxy chains, the nematic-isotropic transition temperatures are higher for the *n*OCB series and show a much smaller odd-even alternation. This has been explained in terms of the different bond angles at the C and O atoms that link the terminal chains to the mesogenic cores in the *n*CB and *n*OCB series respectively. Assuming perfect tetrahedral geometry, a bond angle of 109.5° is estimated at the linking C atom in the *n*CB series. A bond angle of ~120° is estimated at the O atom in the ethylene-linked *n*OCB series on the basis that the O atom conjugates with the aromatic biphenyl core: although this also increases the polarizability and slightly increases the length of the rigid core over that of the methylene-linked *n*CB series, the differences in geometry are believed to be more important in determining transitional properties [42]. In fact, ^{2}H NMR work with several chain-deuterated *n*CB and *n*OCB homologues suggests that the bond angle at the linking C atom is approximately 113.5° in the *n*CB series and that the O-C bond makes an angle of 126.4° with the *para* axis of the cyanobiphenyl group in the *n*OCB series [44, 45]. These angles are presumably different from the 109.5° and the 120° bond angle expected at a sp^3 hybidized C atom and an sp^2 hybridized O atom, respectively, as a result of steric repulsions between the cyanobiphenyl group and the terminal chain. However, these differences do not affect our observations on the relative shapes of these two systems. Considering the all-*trans* conformations as representative of the flexible chains (the same effects are also reproduced using other likely chain conformations), the more open bond angle at the O atom means that both odd and even monomers in the *n*OCB series are more elongated than their C-linked counterparts. This is pictured in figure 8. The more open bond angle at the O linkage also leads to a less-pronounced alternation in the overall molecular shape as successive methylene groups are added to the alkyl chain which explains the smaller alternation in the transitional properties of the *n*OCB series. This too is pictured in figure 8.

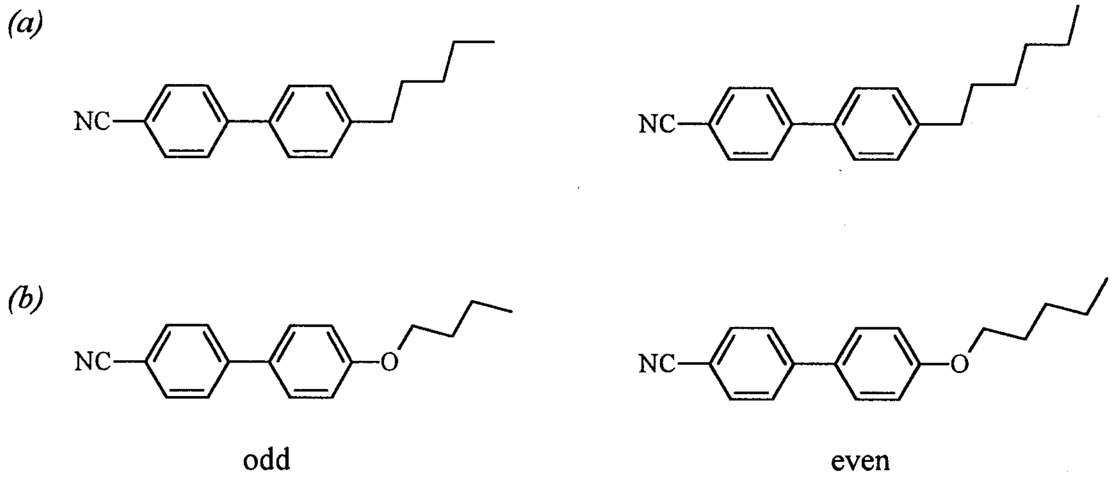

Figure 8 The shapes of odd and even members of the (a) nCB and (b) nOCB series in the all-trans conformation of the terminal chain.

1.4.3 Liquid Crystal Dimers

Structure-property relationships for dimers have also been formulated as a result of systematic studies on homologous series of dimeric liquid crystals. The transition temperatures for dimers are observed to be higher than those of their constituent monomers. The same overall molecular features influence mesophase stability in dimers as in monomers, for example, a more elongated molecular shape increases the thermal stability of a mesophase formed by either system. The behaviour of a dimer is strongly influenced by the length and parity of the spacer. The flexibility of a spacer is not total and therefore the spacer places physical constraints on the relative orientations that the two linked mesogenic groups in a dimer molecule can adopt with respect to each other. Changing the spacer parity therefore has a very large effect upon the overall molecular shape and this is reflected in the very large odd-even alternation in the transitional properties of a homologous series of dimers. This alternation is much more pronounced in dimers than in monomers, as the changes in molecular shape on changing the spacer parity in a dimer are far greater than on changing the parity of a terminal chain in a monomer, and exert a greater influence on the orientational properties of the mesogenic groups themselves.

Some of the properties of liquid crystal dimers are best illustrated by considering the trends in behaviour of members of a homologous series of dimers. As an example, we consider the CBO*n*OCB series **3** [46], which may be considered the dimeric analogues of the *n*OCB series.

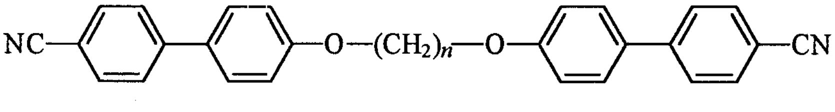

3

The transition temperatures and entropies for this series are shown in figure 9. The dependence of these transitional properties on the length and parity of the spacer is marked and follows a common trend for dimers. There is a pronounced odd-even alternation in the nematic-isotropic temperatures as the parity of the spacer is altered which is attenuated as the length of the spacer is increased. An odd-even alternation is also observed in the entropy changes at the nematic-isotropic transition which does not attenuate as the length of the spacer is increased. The underlying reason for the

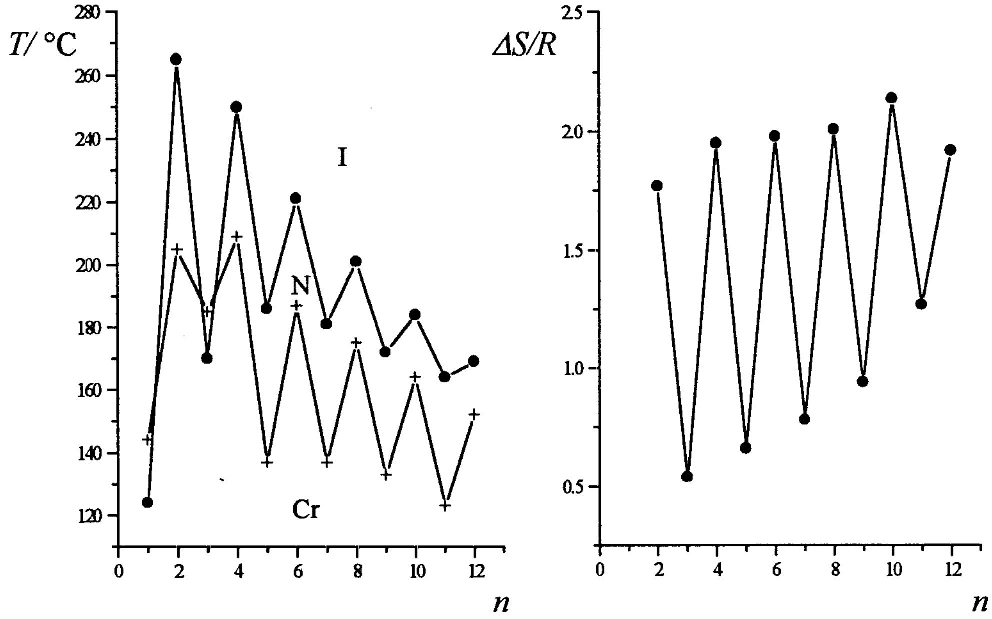

(a) *(b)*

Figure 9 (a) the transition temperatures and (b) the transition entropies for the CBOnOCB series. + = melting point, • = N-I.

higher values for the even dimers of both the entropy and the temperature of the nematic-isotropic transition can be seen in the first part of figure 10, which shows caricatures of an odd and an even dimer in the all-*trans* conformation of the spacer. The more elongated shape of the even dimer leads to a more anisotropic intermolecular potential and an ease of packing which favours greater orientational order [47]. This both increases the clearing temperature and the entropy change at the nematic-isotropic transition associated with the loss of this high degree of orientational order. It is at first surprising to note that the entropy changes at the nematic-isotropic transition for the odd dimers are comparable with those of the monomers, whilst those of the even dimers are considerably larger (It might be expected that those of the even dimers would be similar to those of the monomers, with those of the odd dimers being considerably lower due to the lower orientational order of the mesogenic groups because of the large bend in the odd dimer imposed by the spacer). To understand this observation, it is necessary to consider the overall molecular shape and the relative orientations of the two mesogenic groups in other realistic conformations of the spacer in the odd and even dimers and the distribution of spacer conformations that exists in the mesophase. Figure 10a and b shows a two-dimensional caricature of an odd and even dimer with five and six methylene units in the spacer respectively, in the all-*trans* conformation of the spacer, and then the effect of introducing a single *gauche* link into the spacer and its effect as its position is moved along the spacer. For simplicity we have assumed that there is no distortion from the tetrahedral bond angles at all atoms in the spacer. The two mesogenic groups are parallel in the all-*trans* conformation of the even spacer but lie at an angle of 109.5° to each other in the odd spacer. Some positions of the *gauche* link in the even spacer preserve the parallelism of the mesogenic groups, but no positions of the *gauche* link in the odd spacer are able to create parallelism of the mesogenic groups in the odd dimer. These trends are repeated if multiple *gauche* links are introduced into the spacer. This figure, however, does not emphasize the point made for monomers about the self-reinforcing orientational order in the nematic environment and its influence on the conformational distribution of the even spacer in particular. Thus, in addition to the fact that the even spacer is able to adopt conformations which preserve the parallelism of the mesogenic groups, the nematic environment also favours these over those that do not. There is no such reinforcement possible in the case of the odd spacer, as there are no low energy conformations of the odd spacer (especially for short spacer lengths) that are able to produce parallel orientations of the mesogenic groups which can be favoured in the nematic phase (A hairpin molecular shape in which the two mesogenic groups in a single molecule lie side by side and parallel to each other is possible, but this conformation of the spacer has a high energy). Therefore, the loss of the greater order, with both a larger orientational and a significant conformational contribution, for the even dimer at the nematic-isotropic transition explains the greater entropy change associated with this transition for the even dimer than for the odd, in which the transition is associated with the loss of weaker orientational order and virtually no change in the conformational order. In fact, the results of calculations on a different dimer system using a molecular theory developed for dimer-type systems [48], show that the conformational contribution to the entropy change at the nematic-isotropic transition is some 20% of the total for the even dimer, and almost zero for the odd dimer [49]. Therefore, although the conformational freedom of the spacer does not play a large, direct role in the determination of the odd-even alternation, the parity of the spacer plays a very important role in determining the orientational order of the mesogenic groups that is possible, and it is this which accounts for the pronounced odd-even effect in liquid crystal dimers.

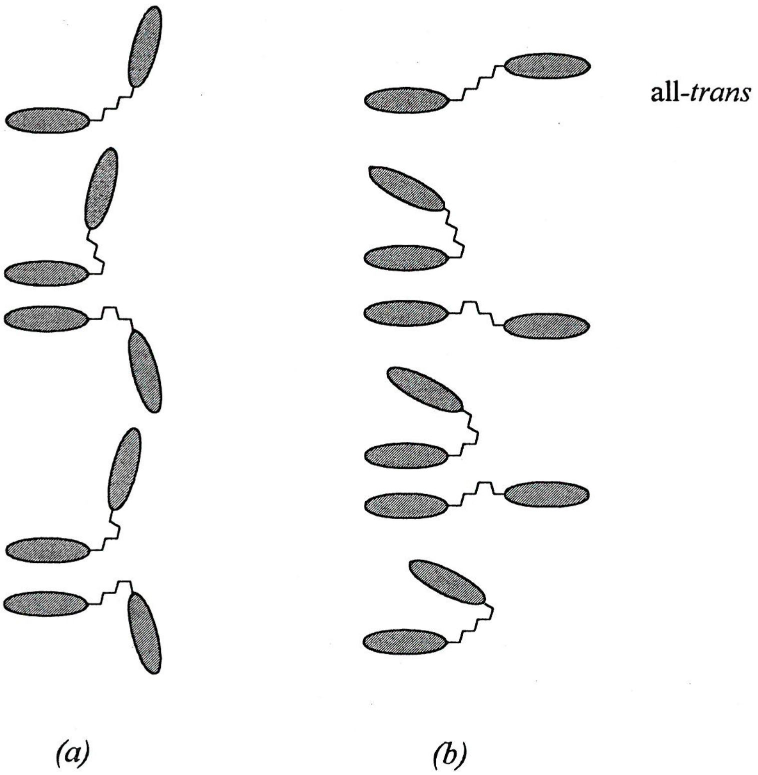

Figure 10 Two-dimensional caricatures of (a) an odd dimer with spacer length 5 and (b) an even dimer with spacer length 6 in the all-trans spacer conformation and with a single gauche link introduced into different positions along the spacer.

Thus far in the discussion of the structure-property relationships of dimers, we have considered the odd-even effect within a homologous series of nematogens as the spacer length is altered as this has particular importance for the experimental study in Chapter 4 of this Thesis. Changes in the moieties in a molecule also exert an influence on the types of mesophases that are formed as well as their stability. One of these takes on particular importance in Chapter 6. In dimers, as in monomers, strong lateral associations between mesogenic groups, mesogenic groups which are able to pack efficiently in a layered structure, and a high degree of inhomogeneity in the molecular structure are features which will tend to drive smectic phase formation. Thus, on the latter point, in dimer systems with terminal chains, increasing the length of the terminal chains for a given spacer length will lead to increased smectic behaviour (in fact, a rather specific relation holds true for the vast majority of systems: smectic phases will be formed only when the length of the terminal chains exceeds half the spacer length [49]). One of the few exceptions to this general rule occurs when an intercalated smectic phase is formed by some unsymmetric dimers with short terminal chains [50]. However, even in these systems, for slightly longer chain lengths the intercalated smectic phase is replaced by a nematic phase, and then the general trend is reestablished as smectic behaviour reappears for longer terminal chains.

We have seen in this section that molecular flexibility plays an important role in the determination of mesophase behaviour and properties. In the next section we shall develop the description of orientational ordering in a mesophase based on a description of the orientational order of rigid particles. This description applies reasonably well to the mesogenic groups that form part of mesogenic molecules incorporating varying degrees of internal flexibility in other parts of the molecule, but here we shall extend it to the conformationally-averaged structures of the flexible mesogenic molecules which we regard as fictitious rigid species for these purposes.

1.5 The Description of Ordering

The previous sections have treated the bulk properties of liquid crystals and their observed macroscopic behaviour separate from a brief view of the local, microscopic structure that is characteristic of liquid crystals and the molecular features that promote liquid crystallinity. Statistical mechanics makes the link between experimental observables and the microscopic description, based on the principle that the experimental observables simply reflect averages of molecular properties [1, 51]. Predictions of the macroscopic behaviour are based on a knowledge of the molecular energy levels of the system which are translated *via* the Boltzmann distribution into a distribution function that specifies the state of a system, and this is used to calculate the average of any macroscopic quantity. The results of these calculations can be compared with real experimental observations which allows a more refined picture of the microscopic state of the system and the energy levels of its constituent particles to be constructed.

The definition of a distribution function is based on a system characterised by a fixed number of particles (N) in a given volume (V) at a given temperature (T) known as a canonical ensemble. In the most general description, the state of an ensemble of N rigid particles of arbitrary shape (that is, biaxial particles) is specified by the position of each particle r(x,y,z) and three Euler angles Ω (= $\phi\theta\psi$) that determine the orientation of each molecule with respect to a space-fixed laboratory axis system (see figure 11a) [52]. A configurational partition function for the system can be written as

$$Q_N = \frac{1}{N!}\int \exp\left(-\frac{U(\{X^N\})}{kT}\right)\{dX^N\} = \frac{Z_N}{N!} \qquad (1.5)$$

in which U is the potential energy of the N particles and kT the Boltzmann factor. X denotes the six variables xyz and $\phi\theta\psi$ and the curly brackets the N variables. Thus $\{X^N\} = X_1, X_2,....X_N$ and $\{dX^N\} = dX_1\, dX_2.....dX_N$. The volume element dX is equivalent to $dr\,d\Omega$ with $dr=dx\,dy\,dz$ and $d\Omega=d\phi\,\sin\theta\,d\theta\,d\psi$, the spatial variables are integrated over the sample volume and the orientational variables over the usual domains, which are, $0<\phi<2\pi$, $0<\theta<\pi$ and $0<\psi<2\pi$. To simplify the notation a single integration sign indicates integration over the multiple variables.

The probability of finding n particles out of the N in the range X_1—X_1+dX_1 , X_2—X_2+dX_2 ..... X_n—X_n+dX_n , is given by the n-particle distribution function

$$p^{(n)}(\{X^n\}) = \frac{N!}{(N-n)!\,Z_N}\int \exp\left(-\frac{U(\{X^N\})}{kT}\right)\{dX^N_{n+1}\} \qquad (1.6)$$

in which $\{dX_m^N\} = dX_m\, dX_{m+1}\, ...dX_N$. $p^{(n)}$ is normalized to the number of n-particle subsets that can be chosen from the set of N particles, that is, to N!/(N-n)! . This distribution can be used to obtain the canonical ensemble average, <T> of any n-particle property depending upon the position and orientation of n particles.

$$\langle T(X_n)\rangle = \frac{(N-n)!}{N!}\int A(X_n)\, p^{(n)}(X_n)\,\{dX_n\} \qquad (1.7)$$

Of major interest for comparison with experiment are the one- and two-particle distributions; in this Thesis there is particular interest in the one-particle average

$$\langle T(X_1)\rangle = \frac{1}{N}\int A(X_1)\, p^{(1)}(X_1)\, dX_1 \qquad (1.8)$$

in which $p^{(1)}(X_1)$ is the singlet distribution function which gives the probability of finding a single particle with a particular position and orientation, this is given by

$$\mathrm{p}^{(1)}(\mathrm{X}_1) = \frac{\mathrm{N}}{\mathrm{Z_N}} \int \exp\left(-\frac{\mathrm{U}(\{\mathrm{X}^{\mathrm{N}}\})}{\mathrm{kT}}\right) \{\mathrm{dX}_2^{\mathrm{N}}\} \tag{1.9}$$

Thus, the distribution function which goes to determine the canonical ensemble average has been related to the individual molecular energies and this is of obvious importance in the interpretation of experiments. By the same processes, the configurational contributions to the thermodynamic functions can be written in terms of the partition functions, for example, we obtain

$$A = -\,kT \ln Q_{\mathrm{N}} \tag{1.10}$$

$$S = -\,(\partial A/\partial T)_{\mathrm{V}} \tag{1.11}$$

$$P = -\,(\partial A/\partial V)_{\mathrm{T}} \tag{1.12}$$

$$U = A + TS \;=\; -T^2\,(\partial(A/T)/\partial T)_{\mathrm{V}} \;=\; kT^2(\partial(\ln Q_{\mathrm{N}})/\partial T)_{\mathrm{V}} \tag{1.13}$$

$$C_{\mathrm{V}} = (\partial U/\partial T)_{\mathrm{V}} \;=\; -\mathrm{T}(\partial^2 A/\partial T^2)_{\mathrm{V}}\,. \tag{1.14}$$

Calculations of the free energy are used by theoreticians to predict the temperatures of phase transitions (for example, the nematic-isotropic transition, which is located where the free energies of the isotropic and nematic phases are identical) and the changes in other thermodynamic properties associated with a transition for a model system based on relatively simple initial assumptions for the energy variation of the particles of the fluid [48].

1.5.1 Orientational Order in Liquid Crystals

The internal flexibilities in a real mesogenic molecule mean that it is not normally possible to locate a fixed set of axes on the molecule which can be used to define a set of Euler angles for the whole molecule. In the more detailed discussion that follows, we shall instead assume that a set of axes can be located on each mesogenic group, as these approximate to rigid units (this is a natural choice, given that it is the mesogenic groups that are responsible for mesogenic behaviour, but other portions of the molecule could equally well be used), or on the conformationally averaged structure which we regard as a fictitious rigid unit, and use these to develop the description of orientational order in the mesophase. The defining property of a mesophase is the presence of long range orientational order [12]: in this Thesis this is studied using a spectroscopic technique that is directly sensitive only to the orientation of the molecules of the liquid crystal and not to their positions. Therefore, in the calculation of relevant ensemble averages, we need consider only the singlet orientational distribution function and may neglect the positional component of the full singlet distribution function. Often it is the orientational distribution with respect to the director that is of interest, and it is sensible to treat the calculation of experimental observables in two stages. The first stage contains all of the details about the orientational order of the mesogen molecules or the mesogenic groups with respect to the director. The second stage, which is considered in Chapter 2, relates the orientation of the director to a laboratory axis system. Many theoretical studies of liquid crystals aim to establish the precise origin and description of the first stage and to convert the probabilities of the previous section into an orientational distribution function $f(\Omega)$ of the molecular axis system with respect to the director, which is required for rigorous testing of theories of the orientational ordering of liquid crystals. In what follows, the angles $\alpha\beta\gamma$ are a particular set of the general Euler angles Ω $(=\phi\theta\psi)$, and specification of the Euler angles as $\alpha\beta\gamma$ presupposes that the external reference frame contains the director, see figure 11a. For the rest of this Chapter, we shall limit ourselves to the first stage and to the description of the orientational order of mesogenic groups and of molecules with respect to the director.

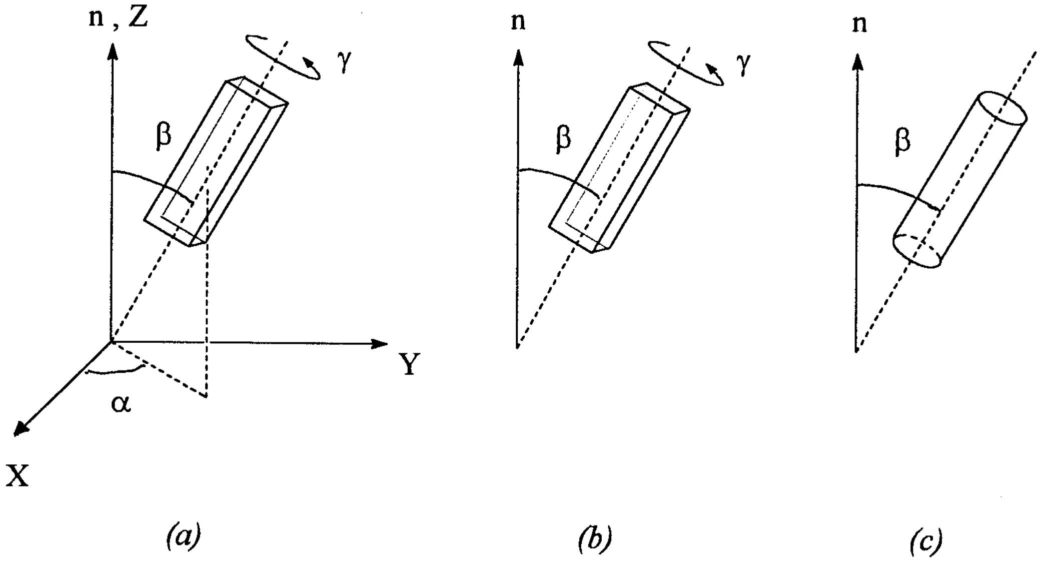

Figure 11 The set of Euler angles Ω that describe the orientational order of (a) a biaxial particle in a biaxial phase, (b) a biaxial particle in a uniaxial phase and (c) a uniaxial particle in a uniaxial phase.

The form of the singlet orientational distribution function f(Ω) is not known. To obtain an unknown function such as f(Ω) a common approach is to expand f(Ω) in terms of a set of quantities which are known and well-behaved functions of Ω, that is, of the Euler angles αβγ. In this context, well-behaved means that the functions form an orthogonal basis set spanning the whole of orientational space. Initially, we expand the singlet orientational distribution function f(Ω) in terms of the orthogonal set of Wigner rotation matrices which are easy to manipulate and simplify. Later we expand the same function f(Ω) in terms of the direction cosines of the director with respect to a molecular fixed frame and introduce the Saupe ordering matrix **S**: this approach is more appropriate in the context of a spectroscopic treatment as the direction cosines relate more obviously to the behaviour of features in the spectrum.

Expanding f(Ω) in terms of the basis set of Wigner rotation matrices, $D^L_{m,n}(\Omega)$ that are orthogonal when integrated over dα sinβdβ dγ, we obtain

$$f(\Omega) = \sum_{L\,m\,n} f_{Lmn}\, D^L_{m,n}(\Omega) \tag{1.15}$$

by multiplying both sides by $D^{L*}_{m,n}(\Omega)$ and integrating we obtain the following equation from which the coefficients f_{Lmn} which contain the orientational order parameters can be obtained using the orthogonality properties of the basis set of functions.

$$\int f(\Omega)\, D^{L*}_{m,n}(\Omega)\, d\alpha\, \sin\beta d\beta\, d\gamma = \sum_{L\,m\,n} f_{Lmn} \int f(\Omega)\, D^L_{m,n}(\Omega)\, D^{L*}_{m,n}(\Omega)\, d\alpha\, \sin\beta d\beta\, d\gamma \tag{1.16}$$

Substitution of these coefficients gives, for the case of a rigid molecule of arbitrary shape,

$$f(\alpha\beta\gamma) = \sum_{L\,m\,n} \tfrac{2L+1}{8\pi^2} \langle D^{L*}_{m,n} \rangle\, D^L_{m,n}(\Omega) \tag{1.17}$$

in which the coefficients $\langle D^{L*}_{m,n} \rangle$ represent the full set of order parameters that describe the orientational order of biaxial particles in a biaxial phase.

If the mesophase is uniaxial, then any measured property is invariant to the polar angle α around the director. Further, if we assume that the phase is apolar, then it possesses a symmetry plane perpendicular to the director, therefore only terms of even rank L contribute and f(αβγ) can be simplified to

$$f(\beta\gamma) = \sum_{L\ \mathrm{even},\, n} \tfrac{2L+1}{4\pi} \left\langle D^{L*}_{0,n} \right\rangle D^L_{0,n}(\beta\gamma) \tag{1.18}$$

This describes the singlet orientational distribution function for a biaxial molecule in a uniaxial phase and the coefficients $\langle D^{L*}_{0,n} \rangle$ are the full set of orientational order parameters in this case.

Simplifying further, if we assume that the molecule itself possesses effective cylindrical symmetry, then the angle γ is also redundant and equation 1.17 reduces to

$$f(\beta) = \sum_{L\ \mathrm{even}} \frac{2L+1}{2} \langle D^{L*}_{0,0} \rangle D^{L}_{0,0}(\beta) \tag{1.19}$$

in which the set of $D^{L}_{0,0}(\beta)$ are identical to the set of Legendre polynomials $P_L(\cos\beta)$ and each coefficient $\langle D^{L*}_{0,0} \rangle$ represents the average over the Legendre polynomial $\overline{P}_L$. The complete distribution function for rigid, cylindrically symmetric particles in a uniaxial phase depends on the single angle β between the molecular symmetry axis and the director, shown in figure 11c, and equation 1.19 can be rewritten as

$$f(\beta) = \sum_{L\ \mathrm{even}} p_L P_L(\cos\beta) \tag{1.20}$$

in which the terms $p_L = \frac{2L+1}{2} \overline{P}_L$. Writing this explicitly as an expansion

$$f(\beta) = \tfrac{1}{2} + \tfrac{5}{2} \overline{P}_2 P_2(\cos\beta) + \tfrac{9}{2} \overline{P}_4 P_4(\cos\beta) + \ldots \tag{1.21}$$

The first non-trivial term in this expansion contains the orientational order parameter $\overline{P}_2$ introduced in section 1.2. However, to fully characterise the orientational properties of a cylindrically symmetric liquid crystal in a uniaxial phase, we must determine the full singlet orientational distribution function $f(\beta)$, which implies that we know, can calculate or can measure the full set of order parameters $\overline{P}_L$. Some techniques in principle offer a route to the measurement of $f(\beta)$ [53], but in practice this is difficult to obtain experimentally. Magnetic resonance spectroscopies such as NMR and EPR (which we consider in Chapter 2) measure quantities which are formally described as partially-averaged second-rank tensorial quantities, which depend on and can be used to determine $\overline{P}_2$, while the relaxation rates of these processes are sensitive to the $\overline{P}_4$ term and so $\overline{P}_4$ can also be obtained from magnetic resonance experiments [54]. In general the approximation of the expansion to $f(\beta)$ is poor when truncated early. Thus truncation at the second term implies that $f(\beta)$ can be negative which is obviously not meaningful when we consider that $f(\beta)$ is a probability. However any property depending only upon $\overline{P}_2$, such as the magnetic couplings in EPR which we consider later, will be calculated correctly using this truncation. The poor quality of the fit for early truncation may seem to imply that it is a pointless exercise to obtain only the first few terms, however this is not so, for even then useful inferences can be drawn which place restrictions on the form of f(β). The functions $P_0(\cos\beta)$, $P_2(\cos\beta)$, $P_4(\cos\beta)$ and $P_6(\cos\beta)$ are shown in figure 12. A simple experimental finding that $\overline{P}_2$ is positive implies that on average the molecular long axis makes an angle of less than the magic angle 54.7° with the director, if $\overline{P}_4$ for the same system is measured as negative, then this alone implies that the average molecular long axis makes an angle with the director of between 30.5° and 70.1°. Taken together with the knowledge of $\overline{P}_2$, the average angle made by the molecular long axis with the director must lie between 30.5° and 54.7°. Knowledge of higher order parameters places further constraints on the distribution function.

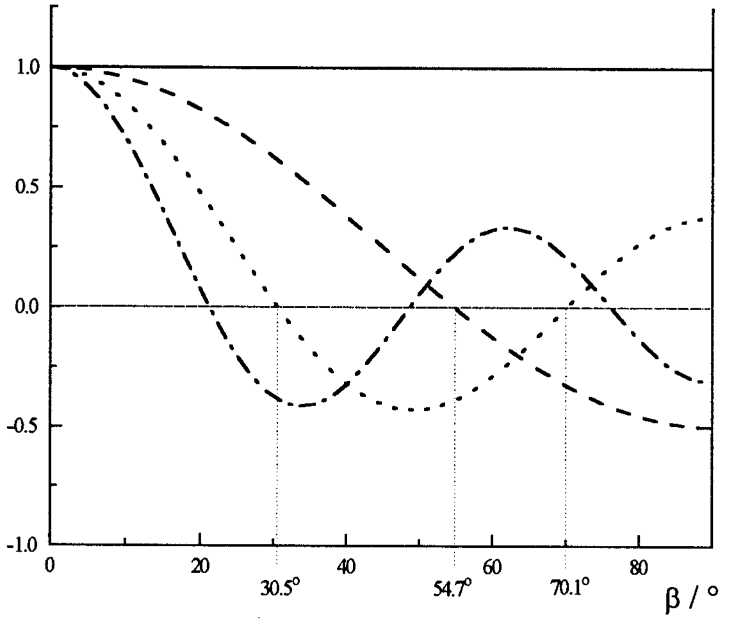

Figure 12 The Legendre polynomials $P_0(\cos\beta)$ —, $P_2(\cos\beta)$ ----, $P_4(\cos\beta)$ ····· *and (d)* $P_6(\cos\beta)$ -•-•- *as a function of* β *in the range 0 to 90°.*

The problem of finding the best approximation to the whole of f(β) starting from a knowledge of just the first few order parameters, say up to $\overline{P}_{L'}$, is solved in the maximum entropy approach using information theory [51]. A set of coefficients a_L with L taking values up to L' are sought which maximize the entropy

$$S(\{a_L\}) \propto -\int f(\beta, \{a_L\}) \ln(f(\beta, \{a_L\}) \sin\beta \, d\beta \qquad (1.22)$$

The best distribution subject to the constraints of the known values P_L and the coefficients a_L is found to be:

$$f(\beta) = \exp\{ \sum_{L=0}^{L'} a_L P_L(\cos\beta) \} \tag{1.23}$$

This process allows construction of the most probable full distribution for f(β) consistent with and using the limited amount of data available, as such it is a mathematical construction and gives no information about the molecular origin of the distribution nor of its likely evolution if experimental conditions such as temperature are changed. It should be noted that the exponential character ensures that the probability is always positive.

1.5.2 The Saupe ordering matrix

In the previous sections f(Ω) was expanded in terms of the Wigner rotation matrices; an alternative way of defining the orientational order parameters is by expanding f(Ω) in terms of a set of orthogonal ordering matrices which contain the direction cosines l_α (α =1,2,3) that relate the director and a set of axes (123) located in the molecule. The first three terms of the expansion are

$$f(\Omega) = \frac{1}{8\pi^2} (1 + 5 \sum_{\alpha\beta} S_{\alpha\beta}\, l_\alpha l_\beta + 9 \sum S_{\alpha\beta\gamma\delta}\, l_\alpha l_\beta l_\gamma l_\delta + \ldots) \tag{1.24}$$

which $S_{\alpha\beta} = \frac{(3\overline{l_\alpha l_\beta} - \delta_{\alpha\beta})}{2}$ are the nine elements of the three-by-three Saupe ordering matrix S and $S_{\alpha\beta\gamma\delta}$ are the elements of a super matrix which we do not consider further here [52].

The matrix S was originally introduced by Saupe [55] in order to describe the extent of solute ordering in liquid crystals although the same formalism also describes the orientational order of the molecules of the liquid crystal. Like the magnetic interactions that occur in magnetic resonance experiments, S is formally described as a second-rank tensor. Since the terms in the expansion of f(Ω) are orthogonal, the magnetic couplings are purely determined by S and therefore can be used to determine S and give some information about f(Ω).

Specification of a tensor presupposes a coordinate system in which the tensor is specified, thus the coordinate system we have chosen here contains the director and two axes orthogonal to it. There are certain properties associated with **S** and with any other quantity that behaves as a second-rank tensor. One of these is that the trace of a matrix representing a tensor, defined as the sum of the diagonal elements so that the trace of a matrix **T** is given by $\mathrm{Tr(T)} = \Sigma_i(T_{ii})$, is invariant to the choice of coordinate system. In any coordinate system, **S** is real and symmetric, that is, $S_{\alpha\beta}=S_{\beta\alpha}$, and traceless, that is $S_{11}+S_{22}+S_{33}=0$, which follows from the properties of the direction cosines. It also follows that there are at most five independent elements of **S** in an arbitrary coordinate system but this number can be reduced by making use of the symmetry of the phase and of the molecules themselves. A tensor can always be specified in a so-called principal axis system in which the only non-zero elements lie along the leading diagonal. The director defines the symmetry axis of the mesophase and lies along one of the principal axes of **S**. Given that we also know **S** is traceless, there remain only two independent elements in **S**, these are the two orientational order parameters of second rank (L=2) which describe the orientational ordering of a biaxial molecule in a uniaxial mesophase. If axis 1 lies along the molecular long axis, then the order parameters are usually quoted as S_{11} which describes the orientational order of the molecular long axis, and $S_{22}-S_{33}$ which describes the orientational ordering of the axes perpendicular to the molecular long axis, by convention chosen so that $S_{11} > |S_{22}-S_{33}|$ and $S_{22}>S_{33}$. The situation is simpler when we consider cylindrically symmetric molecules in a uniaxial phase, for then $(S_{22}-S_{33})= 0$. The orientational ordering at second rank and the matrix **S** is then entirely characterised by the single parameter S_{11} which describes the orientational order of the molecular long axis, and this is exactly the parameter $\overline{P}_2$ introduced in section 1.2 and derived as part of the expansion in terms of the Wigner rotation matrices. In such cases S_{11} is often abbreviated to just S. We shall make more use of **S** in Chapter 2.

1.5.3 The molecular potential for the nematic phase

Statistical mechanics relates the macroscopic behaviour of a system to the potential energies of the constituent particles. The stability of the nematic phase results from the anisotropic interactions between constituent molecules in the mesophase. The intermolecular forces are typically due to dispersion forces, dipolar, quadrupolar or electrostatic interactions between the particles of the fluid but, for now, we neglect the origin of these forces and observe that their effect is that neighbouring molecules prefer to lie parallel to each other on average. Statistical mechanics allows the calculation of the experimental observables for a system which is straightforward in the molecular field approximation when the complexity of having to consider the many intermolecular interactions is removed; instead we attempt to mimic all of the intermolecular interactions that a single particle experiences with an effective single molecule potential function. From a phenomenological point of view, the simplest form for this potential of mean torque compatible with the phase symmetry that also reflects the fact that the strength of the field is dependent on the orientational order within the system is the potential function [56],

$$U(\cos\beta) = -u_2 \overline{P}_2 P_2(\cos\beta) \tag{1.25}$$

in which $P_2(\cos\beta)$ is the second Legendre polynomial, $\overline{P}_2$ is its averaged value and u_2 is an adjustable parameter that accounts for the overall strength of the intermolecular interactions for different materials and their variation with, for example, temperature and density. $U(\cos\beta)$ clearly contains the correct orientational dependence. The factor $-P_2(\cos\beta)$ and therefore $U(\cos\beta)$ is a minimum when the molecule lies along the director and a maximum when the molecule lies perpendicular to the director. The $\overline{P}_2$ term ensures that $U(\cos\beta)$ is anisotropic in a highly ordered phase and zero in the isotropic phase.

In the Maier-Saupe theory a potential of this form is used as the starting point for the calculation of the canonical ensemble averages that were discussed in the previous sections which can then be compared with experimental observations [57, 58]. This theory predicts, amongst other things, a universal dependence of the orientational order parameter $\overline{P}_2$ on the reduced temperature T/T_{NI} which is qualitatively correct for many liquid crystals [59]. The agreement between calculation and experiment can be impressive considering the simplicity of the approach in the development of the potential of mean torque outlined here. Other forms for the potential of mean torque have been developed that extend the simple Maier-Saupe model. Thus, Humphries *et al.* added further terms in the expansion to obtain a pseudopotential that contains all of the Legendre polynomials [60],

$$U(\cos\beta) = \sum_{L\,\mathrm{even}} - u_L \bar{P}_L P_L(\cos\beta) \qquad (1.26)$$

which improves the agreement with experiment [59]. Real mesogenic molecules very rarely possess cylindrical symmetry, and frequently have varying degrees of internal flexibility, while specific interactions between near neighbours are often important. In the spirit of a more realistic model of a real liquid crystal, pseudopotentials have been developed for a rigid biaxial particle in a uniaxial phase, that is, one that depends on the angle γ as well as on β [61], while in the Marcelja-Luckhurst theory specific account is taken of flexibility in the mesogenic molecule [48, 62]. On this second point, we have already seen that molecular flexibility plays an important role in the determination of mesophase behaviour and mesophase properties in real systems.

1.5.4 Probe studies of liquid crystals

In section 1.4 we saw that real mesogenic molecules are often complicated, they are usually flexible and asymmetric, and therefore a full theoretical treatment is often difficult [63] and necessitates certain approximations, for example, the assumption of rigidity used to develop the description of $f(\Omega)$. Many spectroscopic studies use a probe dissolved in the mesophase to report on the structure and dynamics of the liquid crystal [28, 64, 65, 66]. Care must be taken to ensure that the probe reflects the properties of the mesophase being explored without causing significant disruption to its structure, and this usually means working at low probe concentration, but even then it must be remembered that it is the properties of the probe dissolved in the mesophase and not those of the pure mesophase that are determined. The choice of a suitable probe depends primarily on the experimental technique employed, but may also depend upon the chemistry of the liquid crystal host, its shape or polarity anisotropy, or the portion, mesogenic or aliphatic, and, more generally, the aspect of the behaviour of the liquid crystal host under study. In most cases it is useful if the order of the probe can be described in a simple way, in the context of liquid crystals and orientational ordering, this frequently means that the probe is of rigid structure and high effective symmetry, just the simplifications that were introduced in the previous sections. This is obvious in figure 13 which shows examples of some probe molecules used in the study of liquid crystals. The ordering potential that the probe experiences is assumed to be analogous to that experienced by the molecules of the liquid crystal, equation 1.26, that is, for the nematic phase

$$U_{\text{probe}}(\cos\beta) = \sum_{\text{L eve}} -u_{\text{L}}^{\text{p-s}}\, \bar{P}_{\text{L}}\, P_{\text{L}}(\cos\beta) \qquad (1.27)$$

in which $u_{\text{L}}^{\text{p-s}}$ is a probe-solvent interaction parameter analogous to the solvent-solvent strength parameter u_{L} considered earlier. Ideally, a probe has a simple spectrum in which some features, such as the splittings or line broadenings, have a straightforward correlation with the physical properties of the mesophase under study [67]. Probe studies greatly increase the range of experimental techniques that can be used to explore features of mesophase behaviour. For example, the experiments in this Thesis make use of paramagnetic spin probes to study the director behaviour in diamagnetic liquid crystals. Other probes allow investigation using fluorescence spectroscopy of liquid crystals which do not have a fluorophore in the correct region of the spectrum [66]. In the next Chapter the EPR experiment is introduced, first in the general case and then to the specific case of EPR spectroscopy of spin probes dissolved in liquid crystals.

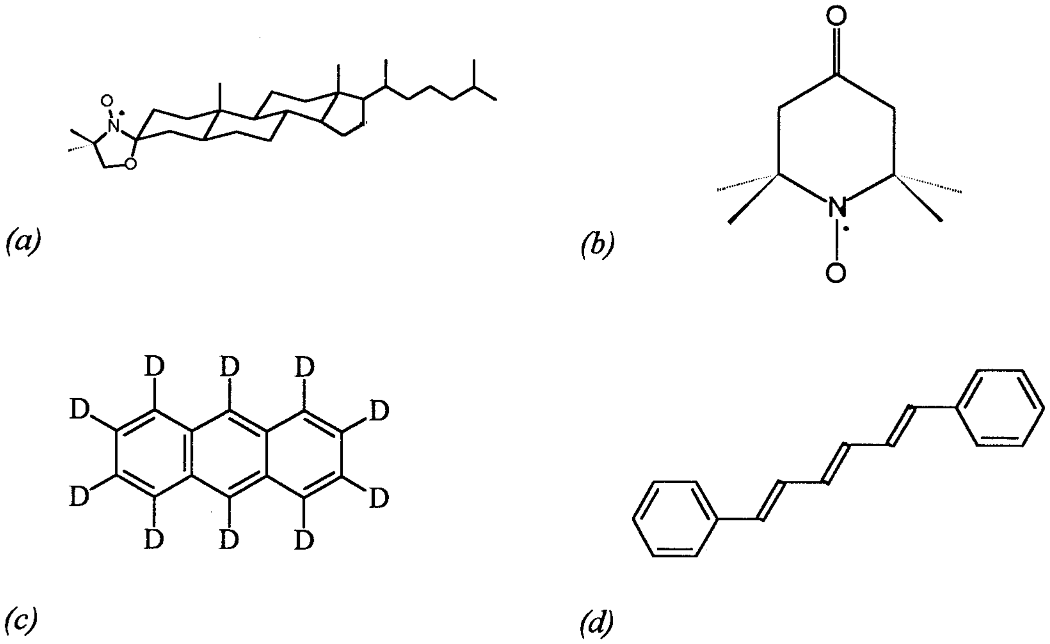

Figure 13 Some probe molecules for the study of liquid crystals: (a) cholestane and (b) tempone for EPR studies (see Chapter 2), (c) anthracene-d_{10} *for* ^{2}*H NMR studies, and (d) 1,6-diphenylhexatriene (DPH) used in fluorescence studies.*

1.6 References

[1] see, for example, ATKINS, P.W., *Physical Chemistry*, 3rd edition, Oxford University Press, 1987.

[2] REINITZER, F., *Monatsh. Chem.*, **9** 421, 1888.

[3] DEMUS, D., DEMUS, H. and ZASCHKE, H., *Flüssige Kristalle in Tabellen,* VEB Deutscher Verlag fur Grundstoffindustrie, Leipzig, 1976.

[4] DEMUS, D. and ZASCHKE, H., *Flüssige Kristalle in Tabellen 2,* VEB Deutscher Verlag fur Grundstoffindustrie, Leipzig, 1984.

[5] DEMUS, D., *Liq. Crystals,* **5** 75, 1989.

[6] various authors, Part 3, vol. 2B, *Handbook of Liquid Crystals,* eds. D. Demus, J.W. Goodby, G.W. Gray, H.-W. Spiess and V. Vill, Wiley-VCH, 1998.

[7] various authors, Chapter IX, vol. 1, *Handbook of Liquid Crystals,* eds. D. Demus, J.W. Goodby, G.W. Gray, H.-W. Spiess and V. Vill, Wiley-VCH, 1998.

[8] various authors, Chapter 7, vol.1, *Liquid Crystals and Plastic Crystals,* eds. G.W.Gray and P.A. Winsor, Ellis Horwood, 1974.

[9] see, for example: *Applications of Liquid Crystals,* Meier, G., Sackmann, E. and Grabmaier, J.G., Springer Verlag, 1975.

[10] KAHN, F.J., *Physics Today,* **35** 66, May 1982.

[11] COLLINGS, P.J., Chapter 8, *Liquid Crystals: Nature's Delicate Phase of Matter,* Adam Hilger, Bristol, 1990.

[12] DE GENNES, P.G., Chapter 1, *The Physics of Liquid Crystals,* Clarendon Press, Oxford, 1974.

[13] DUNMUR, D and TORIYAMA, K., Chapter VII, vol.1, *Handbook of Liquid Crystals,* eds. D. Demus, J.W. Goodby, G.W. Gray, H.-W. Spiess and V. Vill, Wiley-VCH, 1998.

[14] COLLINGS, P.J., Chapter 3, *Liquid Crystals: Nature's Delicate Phase of Matter,* Adam Hilger, Bristol, 1990.

[15] BLINOV, L.M. and JÉRÔME, B., Chapter VII, vol.1, *Handbook of Liquid Crystals,* eds. D. Demus, J.W. Goodby, G.W. Gray, H.-W. Spiess and V. Vill, Wiley-VCH, 1998.

[16] see, for example, LEADBETTER, A.J., Chapter 1, *Thermotropic Liquid Crystals,* ed. G.W.Gray, CRAC, John Wiley, 1987.

[17] Collings, P.J., Chapter 3, *Liquid Crystals: Nature's Delicate Phase of Matter,* Adam Hilger, Bristol, 1990.

[18] McDonnell, D.G., Chapter 5, *Thermotropic Liquid Crystals,* ed. G.W.Gray, CRAC, John Wiley, 1987.

[19] Gray, G.W. and Goodby, J.W., *Smectic Liquid Crystals: Textures and Structures,* Leonard Hill, 1984.

[20] Goodby, J.W., Chapter 1, vol. 2A, *Handbook of Liquid Crystals,* eds. D. Demus, J.W. Goodby, G.W. Gray, H.-W. Spiess and V. Vill, Wiley-VCH, 1998.

[21] Sheng, P. and Priestley, E.B., Chapters 5 and 10, *Introduction to Liquid Crystals,* E.B. Priestley, P.J. Wojtowicz, and P. Sheng, Plenum Press, 1975.

[22] Martire, D.E., Chapter 10, *The Molecular Physics of Liquid Crystals,* eds. G.R. Luckhurst and G.W. Gray, Academic Press, 1979.

[23] Collings, P.J., Chapters 4 and 5, *Liquid Crystals: Nature's Delicate Phase of Matter,* Adam Hilger, Bristol, 1990.

[24] de Jeu, W.H., Chapter 4, *Physical Properties of Liquid Crystalline Materials,* Gordon and Breach, 1980.

[25] Demus, D. and Richter, L., *Textures of Liquid Crystals,* Verlag Chemie, Weinheim, New York, 1978.

[26] Bouligand, Y., Chapter VII, vol. 1, *Handbook of Liquid Crystals,* eds. D. Demus, J.W. Goodby, G.W. Gray, H.-W. Spiess and V. Vill, Wiley-VCH, 1998.

[27] de Jeu, W.H., Chapter 2, *Physical Properties of Liquid Crystalline Materials,* Gordon and Breach, 1980.

[28] various authors, *The Molecular Dynamics of Liquid Crystals,* eds. G.R. Luckhurst and C.A.Veracini, Kluwer, 1994.

[29] Leadbetter, A.J., Chapter 13, *The Molecular Physics of Liquid Crystals,* eds. G.R. Luckhurst and G.W. Gray, Academic Press, 1979.

[30] de Jeu, W.H., Chapter 6, *Physical Properties of Liquid Crystalline Materials,* Gordon and Breach, 1980.

[31] de Gennes, P.G., Chapter 3, *The Physics of Liquid Crystals,* Clarendon Press, Oxford, 1974.

[32] Leslie, F.M., Chapter III, vol. 1, *Handbook of Liquid Crystals,* eds. D. Demus, J.W. Goodby, G.W. Gray, H.-W. Spiess and V. Vill, Wiley-VCH, 1998.

[33] DE JEU, W.H., Chapter 3, *Physical Properties of Liquid Crystalline Materials*, Gordon and Breach, 1980.

[34] DE GENNES, P.G., Chapter 5, *The Physics of Liquid Crystals*, Clarendon Press, Oxford, 1974.

[35] MEIBOOM, S. and HEWITT, R.C., *Phys. Rev. Lett.*, **34** 1146, 1975.

[36] GRAY, G.W., HARRISON, K.J. and NASH, J.A., *Electron. Lett.*, **9** 130, 1973.

[37] KIMURA, T., TORIUMI, H. and WATANABE, H., *Preprints 14th Liquid Crystal Conference Japan*, **14** 238, 1988.

[38] H. FINKELMANN, Chapter 6, *Thermotropic Liquid Crystals*, ed. G.W.Gray, CRAC, John Wiley, 1987.

[39] GRAY, G.W., *Molecular Structure and the Properties of Liquid Crystals*, Academic Press, London/New York 1962.

[40] TOYNE, K.J., Chapter 2, *Thermotropic Liquid Crystals*, ed. G.W.Gray, CRAC, John Wiley, 1987.

[41] LUCKHURST, G.R., Chapter 4, *The Molecular Physics of Liquid Crystals*, eds. G.R. Luckhurst and G.W. Gray, Academic Press, 1979.

[42] EMERSON, A.P.J. and LUCKHURST, G.R., *Liq. Crystals*, **10** 861, 1991.

[43] LUCKHURST, G.R., Chapter 3, *Nuclear Magnetic Resonance of Liquid Crystals*, ed. J.W. Emsley, Reidel, 1985.

[44] COUNSELL, C.J.R., EMSLEY, J.W., HEATON, N.J. and LUCKHURST, G.R., *Molec. Phys.*, **54** 847, 1985.

[45] COUNSELL, C.J.R., EMSLEY, J.W., LUCKHURST, G.R. and SACHDEV, H.S., *Molec. Phys.*, **63** 33, 1988.

[46] EMSLEY, J.W., LUCKHURST, G.R. SHILSTONE, G.N. and SAGE, I., *Mol. Cryst. Liq. Cryst. Lett.*, **102** 223, 1984.

[47] EMSLEY, J.W., LUCKHURST, G.R. and SHILSTONE, G.N., *Molec. Phys.*, **53** 1023,1984

[48] LUCKHURST, G.R., Chapter 7, *Recent Advances in Liquid Crystalline Polymers*, ed. L.L. Chapoy, Elsevier, 1985.

[49] DATE, R.W., IMRIE, C.T., LUCKHURST, G.R. and SEDDON, J.M., *Liq. Crystals*, **12** 203, 1992.

[50] ATTARD, G.S., DATE, R.W., IMRIE, C.T., LUCKHURST, G.R., ROSKILLY, S.J., SEDDON, J.M. and TAYLOR, L., *Liq. Crystals*, **16** 529, 1994.

[51] ZANNONI, C., Chapter 2, *The Molecular Dynamics of Liquid Crystals*, eds. G.R. Luckhurst and C.A.Veracini, Kluwer, 1994.

[52] ZANNONI, C., Chapter 3, *The Molecular Physics of Liquid Crystals*, eds. G.R. Luckhurst and G.W. Gray, Academic Press, 1979.

[53] LEADBETTER, A.J. and RICHARDSON, R.M., Chapter 20, *The Molecular Physics of Liquid Crystals*, eds. G.R. Luckhurst and G.W.Gray, Academic Press, 1979.

[54] LUCKHURST, G.R., SMITH, S.W. and SUNDHOLM, F., *Acta Chemica Scandinavica*, **A41** 218, 1987.

[55] SAUPE, A., *Z. Naturf.*, **19a** 161, 1964.

[56] this same function has been arrived at using varying degrees of rigour, but see WOJTOWICZ, P.J., Chapter 3, *Introduction to Liquid Crystals*, eds. E.B. Priestley, P.J. Wojtowicz, and P. Sheng, Plenum Press, 1975, for a simple qualitative account.

[57] MAIER, W. and SAUPE, A., *Z. Naturf.*, **14a** 882, 1959.

[58] MAIER, W. and SAUPE, A., *Z. Naturf.*, **15a** 287, 1960.

[59] LUCKHURST, G.R., Chapter 7, *Liquid Crystals and Plastic Crystals*, vol. 2, eds. G.W. Gray and P.A.Winsor, Ellis Horwood, 1974.

[60] HUMPHRIES, R.L., JAMES, P.G. and LUCKHURST, G.R., *J. Chem. Soc. Faraday Trans. II*, **68** 1031, 1970.

[61] LUCKHURST, G.R., ZANNONI, C., NORDIO, P.L. and SEGRE, U., *Molec. Phys.*, **30** 1345, 1975.

[62] MARCELJA, S., *J. Chem. Phys.*, **60** 3599, 1974.

[63] ZANNONI, C., Chapter 2, *Nuclear Magnetic Resonance of Liquid Crystals*, ed. J.W. Emsley, Reidel, 1985.

[64] various authors, *Spin Labeling: Theory and Application*. ed. L.J. Berliner, Academic Press, 1976.

[65] various authors, *Nuclear Magnetic Resonance of Liquid Crystals*, ed. J.W. Emsley, Reidel, 1985.

[66] various authors, *Polarized Spectroscopy of Ordered Systems*, eds. B. Samori, and E.W. Thulstrup, Kluwer, 1988.

[67] VERACINI, C.A. and SHILSTONE, G.N., Chapter 10, *The Molecular Dynamics of Liquid Crystals*, eds. G.R. Luckhurst and C.A. Veracini, Kluwer, 1994.

Chapter 2

Electron Paramagnetic Resonance of Liquid Crystals

2.1 Introduction

Electron Paramagnetic Resonance or EPR is a spectroscopic technique that studies the transitions between different Zeeman levels of a paramagnetic substance in a static magnetic field induced by an rf field. Gross features of the EPR spectrum such as splittings due to coupling to other electrons or magnetic nuclei give information about the magnetic environment of the electron [1, 2, 3]. The strengths of these couplings can be used to map electron densities in a molecule and to study the ordering of anisotropic systems. Linewidths contain information about the dynamic processes within the system under study. There are many good treatments in the literature of the whole subject of EPR, these include more complete quantum mechanical descriptions, not all of which is relevant or necessary for an understanding of the experiments discussed in this Thesis [4, 5]. Most liquid crystals are diamagnetic and their direct study by EPR is not possible, therefore most experiments use the spectra of paramagnetic solutes, or spin probes, dissolved in trace amount in the liquid crystal to report information about the liquid crystal [6]. The use of paramagnetic probes with just a single unpaired electron in trace quantities in the liquid crystal ensures that electron-electron spin-spin interactions may be neglected. In this Chapter, the treatment begins with the fundamentals of the EPR technique and is then geared towards the study of liquid crystals using nitroxide spin probes. We shall consider in detail the case in which resolved couplings are seen in the spectrum due to hyperfine couplings between the electron and a single ^{14}N nucleus (I=1). In later Chapters, some additional hyperfine couplings due to the ^{13}C nucleus (I=½) are included. The EPR spectrum also contains hyperfine couplings due to weaker couplings to the ^{1}H nucleus (I=½) but, as these and some fine couplings due to the presence of paramagnetic oxygen are never resolved in our experiments, we shall discuss these couplings only in the context of the deviation they cause from the underlying natural lineshape of the spectral peak.

2.2 Basic Theory

An electron or an atom containing an unpaired electron has associated with it a permanent magnetic dipole μ given by

$$\mu = -g \mu_B \mathbf{J} \tag{2.1}$$

in which g is the spectroscopic g-factor, μ_B the Bohr magneton and **J** the electronic angular momentum, which may have contributions from both the spin angular momentum **S** and the orbital angular momentum **L** (in an atom or molecule). We consider only the effect of the spin angular momentum as this is the dominant contribution for the present purposes. The electron has spin $S = ½$, and can therefore exist in one of two spin states which are equal in energy in the absence of a magnetic field. When a magnetic field is applied, the degeneracy of these two states is lifted by the Zeeman interaction between the electron and the magnetic field and the spin is quantized along the magnetic field direction. These two states have energies

$$E_Z = g \mu_B B m_S \tag{2.2}$$

in which the electron spin quantum number m_S may take the values $\pm½$.

Transitions between the two spin states can be excited by absorption of the energy of an oscillating magnetic field applied normal to the stationary magnetic field when the energy of the rf radiation matches the energy difference between the two states, this occurs at a frequency ν that satisfies the resonance condition.

$$h\nu = g \mu_B B \quad (= E(m_S = +½) - E(m_S = -½)) \tag{2.3}$$

A lorentzian lineshape is characteristic of the resonance when no other magnetic couplings occur.

It should be noted that, in principle, the resonance condition can be satisfied at any frequency ν provided the appropriate magnetic field can be attained, this becomes relevant in Chapter 6 in which we use a field gradient in an imaging experiment. In practice, resonant frequencies falling in certain bands are used, for example, 3.2GHz (S band), 9.4GHz (X band) and 35GHz (Q band), falling in the microwave region of the electromagnetic spectrum, with typical corresponding magnetic field strengths in EPR spectrometers of 1100, 3400 and 15000G (0.11, 0.34 and 1.5T) respectively [7].

When the electron is part of a molecule and in the vicinity of a magnetic nucleus with spin I (which also has a Zeeman interaction with the magnetic field that can be neglected here), then the magnetic field experienced by the electron is dependent upon the spin state of the nucleus. When the selection rules, $\Delta m_S = \pm 1$, $\Delta m_I = 0$, are taken into account, it is clear that the single resonance of the isolated electron predicted by equation 2.3 is split into $(2I+1)$ equally spaced hyperfine lines of equal intensity by the presence of the nucleus according to which of the $(2I+1)$ values the nuclear spin quantum number m_I takes. Figure 1a shows the case of an isolated electron interacting with a magnetic field and 1b the case of the electron coupling to a nucleus, such as ^{14}N ($I=1$), when the electron-nuclear interaction gives rise to three hyperfine lines in the EPR spectrum.

The resonance condition is modified to take account of this coupling,

$$(\Delta E =)\ h\nu = g\,\mu_B\,B + a\,m_I \tag{2.4}$$

in which a is the isotropic hyperfine coupling constant. In most cases the spectrum is obtained by measuring the absorption of an rf field of constant frequency ν as the magnetic field is swept, in which case resonance occurs at fields B_r given by rearranging equation 2.4,

$$B_r = \frac{h\nu}{g\,\mu_B} - \frac{a\,m_I}{g\,\mu_B} \tag{2.5}$$

The Zeeman term in equation 2.5 determines where the spectrum is centred on the frequency scale for a given magnetic field strength or *vice versa* with the g-factor playing a role similar to the more familiar chemical shift in NMR and containing information about the electronic environment of the unpaired electron in a molecule. The deviations of the g-factor from that of the free electron value are small for most organic radicals. The pattern and strength of hyperfine splittings in an EPR spectrum is useful in conjunction with the g-factor in identifying the presence of certain paramagnetic species in a sample and to map the electron density in the molecular orbital containing the unpaired electron [3].

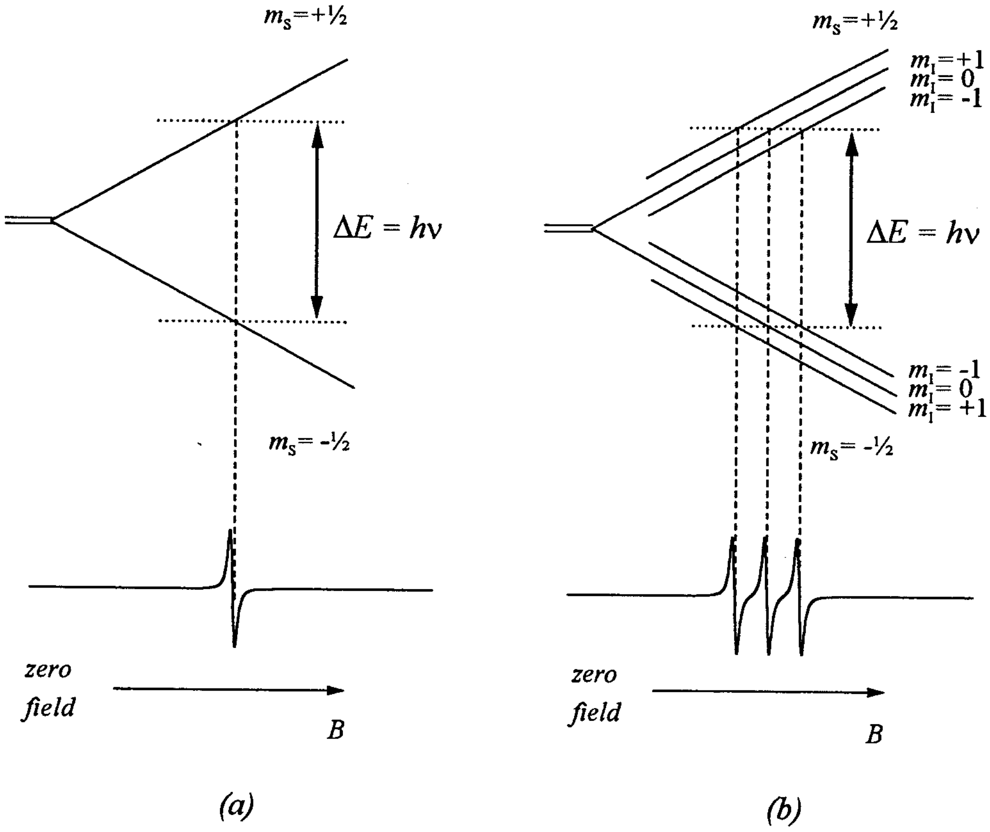

Figure 1 The energy levels and EPR spectrum of (a) an isolated electron and (b) an electron coupling to a nucleus with I=1. The spectra are shown in the first derivative mode.

Equations 2.4 and 2.5 use scalars g and a to denote the g-factor and the strength of the hyperfine interaction A, this is correct only for the case in which molecular rotation is rapid and isotropic. In fact, the g-factor and the hyperfine interaction are each made up of an isotropic and an anisotropic component. The isotropic term a in the hyperfine interaction is due to the Fermi contact interaction between the magnetic nucleus and the unpaired electron in an orbital with some s-character and is the only non-vanishing term when molecular motion is rapid and isotropic. However, the anisotropic contribution to the hyperfine interaction, which is due to the dipolar interaction between the nucleus and the unpaired electron in any orbital without spherical symmetry (p,d or f), does not average to zero if the molecular motion is slow or anisotropic. The strength of both components of the total hyperfine interaction is obtained by averaging over the spatial coordinates of the electronic wavefunction [8] (and therefore depends upon the average electron-nucleus distance). In the nitroxide spin probes, the unpaired electron essentially occupies a nitrogen $2p$ orbital which has some s-character and there are both anisotropic and isotropic contributions to the hyperfine splitting. On cooling an isotropic sample containing some nitroxide spin probe into a mesophase, the three lines remain but their positions and the separation between them changes as the anisotropic contributions to the g-factor and the hyperfine splitting are no longer averaged to zero. As we shall see, the strength of the anisotropic components are related to the anisotropy of the mesophase, specifically, to the orientational order parameter $\overline{P}_2$ ($\equiv S_{11}$ or just S) introduced in Chapter 1. Formally, the hyperfine interaction and the g-factor are described not by scalars but by second-rank tensors, as **A** and **g**. In general a tensor of rank n requires 3^n elements to describe it, although the number of independent elements is fewer than this. A second-rank tensor is normally presented as a three-by-three matrix of nine elements [9].

In the next sections the relationships between the tensor properties **A** and **g** and the appearance of the spectrum is discussed, first in relation to the spin probe molecule itself and later to the case of the probe molecule dissolved in a mesophase.

2.3 Single crystal studies of spin probes

In order to calculate the hyperfine interaction and the g-factor when the motion of the spin probe is not rapid and isotropic it is necessary to consider the behaviour of the **A** and **g** tensors in more detail. It is convenient to illustrate this behaviour by considering the (3-spiro-[2'-N-oxyl-3',3'-dimethyloxazolidine])-5α-cholestane spin probe, hereafter referred to as cholestane (shown in figure 13a, Chapter 1), because of the geometry of the nitrogen $2p$ orbital with respect to the long axis of the molecule. (The same guiding principles also apply to other spin probes in which the orientation of the $2p$ orbital is less easy to define with respect to the long axis of the molecule). Figure 2 shows the orientation of a set of cartesian axes *123* located on the N atom of a nitroxide group which forms part of a cholestane probe molecule. The *1*-axis lies along the long axis of the cholestane probe molecule, the *3*-axis lies along the axis of the $2p$ orbital in which the unpaired electron is largely confined and the *2*-axis is defined by a right-handed coordinate system (the nitrogen hyperfine tensor has cylindrical symmetry about the axis *3* and we shall use this property later). The *123* axis system defines the so-called principal axis systems for the hyperfine and **g** tensors in which only the three diagonal elements are non-zero (**A** and **g** and, in fact, any second-rank tensor, are therefore characterised by at most three independent elements and this number can often be reduced by exploiting their symmetry properties). In this coordinate system, the tensors are specified as

$$\mathbf{A} = \begin{pmatrix} A_{11} & 0 & 0 \\ 0 & A_{22} & 0 \\ 0 & 0 & A_{33} \end{pmatrix} \qquad \mathbf{g} = \begin{pmatrix} g_{11} & 0 & 0 \\ 0 & g_{22} & 0 \\ 0 & 0 & g_{33} \end{pmatrix} \qquad (2.6)$$

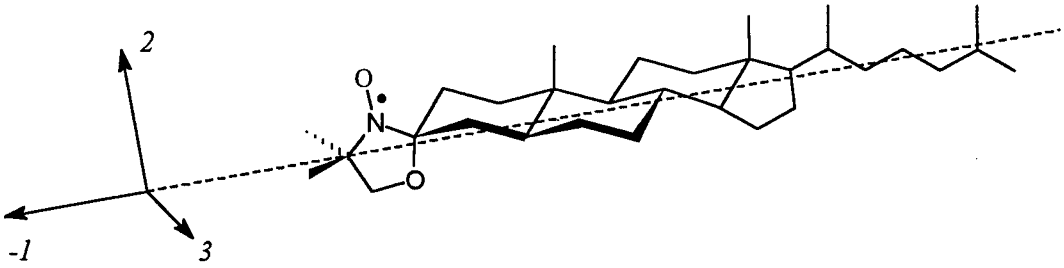

Figure 2 The principal axis system 123 for the **A** *and* **g** *tensors set in the cholestane spin probe.*

In what follows we consider the hyperfine tensor **A** only, mindful of the fact that the **g** tensor shows the same transformational properties. The manifested strength of the coupling between the electron and nuclear magnetic moments and therefore the hyperfine spacing in the EPR spectrum depends upon the angles that the principal axis system for the **A** tensor makes with the magnetic field (it also depends upon the average electron-nucleus distance but this is invariant and we do not consider this further). If a magnetic field is parallel to a principal axis of the hyperfine tensor then the measured value of the hyperfine splitting will be the principal component appropriate to that axis. If the magnetic field makes some arbitrary angle with the principal axis system of the hyperfine tensor then the measured hyperfine splitting is essentially given by the resolved component of the hyperfine tensor along the field direction [8]. This is obtained by specifying the hyperfine tensor in a coordinate system that contains the magnetic field.

We digress for a moment to describe how this coordinate transformation is effected. For a tensor **T** with elements $T_{\alpha\beta}$ specified in a particular coordinate system, the elements of the tensor expressed in another coordinate system T_{ab} are given by

$$T_{ab} = \sum_{\alpha,\beta} l_{a\alpha}\, l_{b\beta}\, T_{\alpha\beta} \qquad (2.7)$$

in which α and β take the values *1*, *2* and *3* and $l_{a\alpha}$ is the cosine of the angle between the *a* and α axes. The trace of a matrix **T**, defined as $\mathrm{Tr}(\mathbf{T}) = \sum_i T_{ii}$, is invariant to coordinate transformations and represents an isotropic component of the tensor **T**. A tensor is said to be traceless if Tr(**T**)=0 in which case **T** is purely anisotropic.

Where we are concerned with the measured hyperfine splitting, we are interested in the component of the hyperfine tensor resolved along the magnetic field direction *Z* which is given by

$$A_{ZZ} = \sum_{\alpha,\beta} l_{Z\alpha}\, l_{Z\beta}\, A_{\alpha\beta} \qquad (2.8)$$

$A_{\alpha\beta}$ on the right hand side of this expression may be split into an isotropic component $a = 1/3\mathrm{Tr}(\mathbf{A})$ and a traceless, anisotropic remainder $A'_{\alpha\beta}$

$$A_{\alpha\beta} = a\delta_{\alpha\beta} + A'_{\alpha\beta} \qquad (2.9)$$

allowing equation 2.8 to be rewritten

$$A_{ZZ} = a + \sum_{\alpha,\beta} l_{Z\alpha}\, l_{Z\beta}\, A'_{\alpha\beta} \qquad (2.10)$$

A similar treatment gives the resolved component of the **g** tensor along the magnetic field as

$$g_{ZZ} = g + \sum_{\alpha,\beta} l_{Z\alpha}\, l_{Z\beta}\, g'_{\alpha\beta} \qquad (2.11)$$

These two equations are central to the determination of the effective *A* and *g*-factors which replace *a* and *g* respectively in equation 2.5 and determine the position of lines in the EPR spectrum of a sample when the molecular motion is not rapid and/or isotropic. As we shall see shortly, the direction cosines in equations 2.10 and 2.11 reflect a number of time-dependent and time-independent factors.

2.4 The EPR timescale

Different spectroscopic techniques are characterised by different intrinsic timescales [10]. In the EPR spectrum of a nitroxide spin probe the anisotropy in the hyperfine interaction (A_{33}–A_{11}, which is equal to A_{33}–A_{22}) is typically 100MHz in frequency units. The experimental window is therefore some 10^{-8}s wide in EPR experiments using nitroxide spin probes. The EPR spectrum of the spin probe is determined by the orientation of the principal axes of the hyperfine and **g** tensors with respect to the magnetic field during this time. For the purposes of this Thesis, processes in the sample that lead to probe reorientation are reflected in two different ways in the spectrum according to the timescale on which they occur [11]. Whilst the EPR window is open, reorientational processes that occur many times lead to an average signal in the spectrum and are said to occur in the fast exchange limit. Those that occur slowly do not lead to exchange between the different orientational states on the EPR timescale and therefore contribute distinct lines to the spectrum with the positions of each given by equations 2.10 and 2.11. This is referred to as the slow exchange limit and in this case the EPR spectrum is a superposition in which the distribution of the different orientational states of the spin probe in the sample is reflected by the different intensities of the subspectrum contributed by each orientational state. The sample spectrum is a weighted sum of the subspectra contributed by each orientational state and as a function of magnetic field B is given by

$$h(B) = \sum_{r} \int L(B, B_r, T_2^{-1})\, \mathrm{f}(\Omega)\mathrm{d}\Omega \qquad (2.12)$$

in which $L(B, B_r, T_2^{-1})$ is the lineshape function for each spectral peak which is most commonly a lorentzian or a gaussian and is discussed later. The summation over r reflects the fact that three hyperfine lines result from coupling to the N nucleus. The weighting function $\mathrm{f}(\Omega)\mathrm{d}\Omega$ reflects the population distribution of all of the orientational states of the principal axes that exist in the slow exchange limit whilst the line position B_r for each state is governed by all of the other molecular motions for that state that occur in the fast exchange limit. A spectrum given by an integration of this sort is termed a powder spectrum.

If the sample of the spin probe is polycrystalline then the molecular motion is quenched. The molecular-fixed principal axes of the **A** and **g** tensors make every possible angle with the laboratory axis system and this is reflected in the distribution of the direction cosines of equations 2.10 and 2.11. Each orientation of the principal axes with respect to the magnetic field gives rise to a subspectrum with the hyperfine splitting and *g*-factor predicted by equations 2.10 and 2.11. The powder spectrum is therefore the weighted sum of these subspectra given by equation 2.12. The weighting function $f(\Omega)d\Omega$ gives the probability of finding the principal axis system of the **A** and **g** tensors between Ω and $\Omega+d\Omega$ with respect to the magnetic field; in fact, just two angles are needed to define Ω (this is analogous to the fact that two angles were needed to describe the orientation of a biaxial particle with respect to the director in a uniaxial phase in figure 11b, Chapter 1). The form of $f(\Omega)d\Omega$ that reflects the uniform orientational distribution in a polycrystalline sample is given by,

$$f(\Omega)d\Omega = \sin\theta d\theta \, d\psi \qquad (2.13)$$

in which θ and ψ are the two polar angles that relate the molecular-fixed axes to the field direction. This is substituted in equation 2.12 to obtain the spectrum for a three-dimensional powder pattern. In cases in which the molecular distribution is not uniform the spectrum is still given by equation 2.12 but the form of $f(\Omega)d\Omega$ will be different to reflect the new molecular distribution.

2.5 Spin probes dissolved in a mesophase

If the spin probe is dissolved in a mesophase then the molecular motion is not quenched. Rotation of the spin probe with respect to the local director is rapid on the EPR timescale, but director fluctuations and diffusion of the spin probe between regions that may have different director orientations is slow on the EPR timescale. This has important implications for the form of the resulting EPR spectrum. Thus, in a mesophase, the direction cosines in equations 2.10 and 2.11 are not static but fluctuate in time, and it is their fluctuations on the timescale of the EPR experiment that determine their resolved components along the magnetic field direction [11, 12]. In the study of the orientational ordering of spin probes in a mesophase, we wish to relate the hyperfine spacing and the *g*-factor of the spectrum to the orientational order parameters of the spin probe. If the molecular motion is fast we need to take the time or ensemble averages of equations 2.10 and 2.11, which are

$$\overline{A_{ZZ}} = a + \sum_{\alpha\beta} \overline{l_{Z\alpha} l_{Z\beta}}\, A'_{\alpha\beta} \tag{2.14}$$

$$\overline{g_{ZZ}} = g + \sum_{\alpha\beta} \overline{l_{Z\alpha} l_{Z\beta}}\, g'_{\alpha\beta} \tag{2.15}$$

The averages $\overline{A_{ZZ}}$ and $\overline{g_{ZZ}}$ are normally denoted by $\bar{a}$ and $\bar{g}$, these contain the averages over the direction cosines which describe the angular fluctuations of the principal axes of the hyperfine and **g** tensors with respect to the director when it is parallel to the magnetic field. These are related to the orientational order of the molecular long axes which was described in Chapter 1 using the ordering matrix **S**. Rewriting equations 2.14 and 2.15 gives $\bar{a}$ and $\bar{g}$ in terms of the ordering matrix **S** as

$$\bar{a} = a + \tfrac{2}{3} \sum_{\alpha,\beta} S_{\alpha\beta} A'_{\alpha\beta} \tag{2.16}$$

$$\bar{g} = g + \tfrac{2}{3} \sum_{\alpha,\beta} S_{\alpha\beta}\, g'_{\alpha\beta} \tag{2.17}$$

We now have that the measured hyperfine spacing (and the g-factor) in a mesophase when the director is parallel to the magnetic field is calculated as the sum of an isotropic component and an anisotropic component that is given by the product of the ordering matrix that describes the molecular orientational ordering and the anisotropy of the hyperfine tensor (and the **g** tensor) [11]. Measurement of the experimental hyperfine splitting $\bar{a}$ or $\bar{g}$ and a knowledge of the anisotropic tensors **A′** and **g′** obtained from the solid state spectrum allows the ordering matrix **S** to be determined for the spin probe dissolved in the mesophase.

The ordering matrix is diagonal with principal components S_{11}, S_{22} and S_{33} in a coordinate system that contains the director. For a biaxial spin probe in a uniaxial phase only two of these components are independent and equations 2.16 and 2.17 reduce to

$$\bar{a} = a + S_{11} A'_{11} + 1/3\, (S_{22} - S_{33})\, (A'_{22} - A'_{33}) \tag{2.18}$$

with a similar expression for $\bar{g}$

$$\bar{g} = g + S_{11}\, g'_{11} + 1/3\, (S_{22} - S_{33})\, (g'_{22} - g'_{33}) \tag{2.19}$$

Equations 2.18 and 2.19 may be solved to obtain the two independent components of **S**: the major order parameter S_{11} and the biaxial order parameter $(S_{22} - S_{33})$. There is no evidence of biaxiality in any of the mesophases studied in this Thesis.

We can simplify further if the spin probe is cylindrically symmetric, for then the ordering matrix **S** is characterised by the single parameter S_{11} (see section 1.5) and equation 2.16 reduces to:

$$\bar{a} = a + S_{11} A'_{11} \tag{2.20}$$

in which S_{11} and A'_{11} are the orientational order parameter for the molecular long axis and the component of the anisotropic hyperfine tensor along the molecular long axis respectively. The ordering matrix **S** is assumed to have cylindrical symmetry in all of the mesophases studied in this Thesis. Given that the nitrogen hyperfine tensor also has cylindrical symmetry, but about the axis *3*, the orientational order for the molecular long axis S_{11} ($\equiv \bar{P}_2$) can be related to the orientational order for the axis *3* and the hyperfine splitting in a mesophase is given by

$$\bar{a} = a - \bar{P}_2 A'_{33} / 2 \tag{2.21}$$

in which A'_{33} is the component of the anisotropic hyperfine tensor along the axis *3* parallel to the axis of the $2p_z$ orbital in cholestane and is easily obtained from the solid state spectrum (see section 2.8). When using cholestane, the spacing between the hyperfine lines decreases at the transition from an isotropic phase to an orientationally ordered phase.

2.6 Angle dependence of Liquid Crystal spectra

We consider now the changing spectrum as the magnetic field is rotated relative to the director. The measured values of A and g when the magnetic field is parallel to the director in a uniaxial mesophase are given by relations 2.16 and 2.17. If the magnetic field is rotated so as to make an angle of 90° with the director then the direction cosines in equations 2.16 and 2.17 reflect this change. Recalculation now gives the observed values of the hyperfine and **g** tensors as

$$\bar{a}\,(90°) = a - \tfrac{1}{3} \sum_{\alpha,\beta} S_{\alpha\beta} A'_{\alpha\beta} \tag{2.22}$$

$$\bar{g}\,(90°) = g - \tfrac{1}{3} \sum_{\alpha,\beta} S_{\alpha\beta}\, g'_{\alpha\beta} \tag{2.23}$$

In summary, rapid rotation of the probe molecule about its long axis and fluctuation of the molecular long axis about the director in a uniaxial mesophase transforms the effective principal axis system for the hyperfine and the **g** tensors from their true axis systems within the molecule to that of the average orientation of the molecule itself and in doing so, they take on an axially symmetric form about the director. When the magnetic field is parallel to the director, the hyperfine splitting and *g*-factor are those given by equations 2.16 and 2.17 and correspond to one of the principal components of the (partially-averaged) $\tilde{\mathbf{A}}$ and $\tilde{\mathbf{g}}$ tensors, and are normally denoted $\tilde{A}_{\parallel}$ and $\tilde{g}_{\parallel}$. The tilde denotes an effective principal axis system due to partial averaging because of the rapid molecular rotation in a uniaxial phase. When the magnetic field is perpendicular to the director, the appropriate principal components given by 2.22 and 2.23 are denoted by $\tilde{A}_{\perp}$ and $\tilde{g}_{\perp}$. The effective $\tilde{\mathbf{A}}$ and $\tilde{\mathbf{g}}$ tensors in these effective principal axis systems are:

$$\tilde{\mathbf{A}} = \begin{pmatrix} \tilde{A}_{\perp} & 0 & 0 \\ 0 & \tilde{A}_{\perp} & 0 \\ 0 & 0 & \tilde{A}_{\parallel} \end{pmatrix} \qquad \tilde{\mathbf{g}} = \begin{pmatrix} \tilde{g}_{\perp} & 0 & 0 \\ 0 & \tilde{g}_{\perp} & 0 \\ 0 & 0 & \tilde{g}_{\parallel} \end{pmatrix} \qquad (2.24)$$

For some intermediate angle ξ between the magnetic field and the director, the effective hyperfine splitting and the *g*-factor is given by [8]

$$\bar{a}(\xi) = (\tilde{A}_{\parallel}^{2}\,\tilde{g}_{\parallel}^{2}\cos^{2}\xi + \tilde{A}_{\perp}^{2}\,\tilde{g}_{\perp}^{2}\sin^{2}\xi)^{½} \,/\, \bar{g}(\xi)^{½} \qquad (2.25)$$

$$\bar{g}(\xi) = (\tilde{g}_{\parallel}^{2}\cos^{2}\xi + \tilde{g}_{\perp}^{2}\sin^{2}\xi)^{½} \qquad (2.26)$$

and this allows calculation of the angle ξ corresponding to a given hyperfine splitting and *g*-factor if the principal components of $\tilde{\mathbf{A}}$ and $\tilde{\mathbf{g}}$ or even just $\tilde{\mathbf{g}}$ are known. The anisotropy in the $\tilde{\mathbf{g}}$ tensor is usually small for the nitroxide spin probes and equation 2.25 can be simplified, and is simplified in this Thesis where used, to

$$\bar{a}(\xi) = (\tilde{A}_{\parallel}^{2}\cos^{2}\xi + \tilde{A}_{\perp}^{2}\sin^{2}\xi)^{½} \qquad (2.27)$$

and this allows calculation of the angle ξ corresponding to a given hyperfine splitting if just $\tilde{A}_{\parallel}$ and $\tilde{A}_{\perp}$ are known. Although $\tilde{A}_{\perp}$ can be difficult to obtain experimentally, measurement of the isotropic hyperfine splitting a allows calculation of $\tilde{A}_{\perp}$ *via* the trace of the hyperfine tensor:

$$3\,a = (\tilde{A}_{\parallel} + 2\tilde{A}_{\perp}) \qquad (2.28)$$

Overall then, the EPR experiment treats processes that occur in the fast and slow motion limits separately while the nature of the motion need not be specified other than whether it is fast or slow on the EPR timescale. Since molecular motions with respect to the director are rapid on the EPR timescale they occur in the fast motion limit. Thus, they determine the principal components of the partially-averaged $\tilde{\mathbf{A}}$ and $\tilde{\mathbf{g}}$ tensors which can be used to study the orientational order of the spin probe dissolved in the mesophase. This is dependent in part on the strength of the interactions between the paramagnetic solute and the liquid crystal solvent discussed in section 1.5 (Chapter 1), but it is often useful to have a knowledge of the orientational order within the mesophase and this is reflected in, if not exactly matched by, the orientational order of the spin probe dissolved in the mesophase. This proves useful in this Thesis. At the other extreme, motions of the director and the diffusion of the spin probe between regions of the sample in which the director orientation may differ are slow on the EPR timescale and therefore occur in the slow motion limit. In all of the experiments in this Thesis, use is made of the fact that the components of the $\tilde{\mathbf{A}}$ and $\tilde{\mathbf{g}}$ tensors seen in the spectrum are influenced by, and therefore can be used to determine, the director orientation in the mesophase which is only minimally disrupted by the presence of the trace quantities of spin probe (10^{-5} M) needed to obtain a spectrum. The EPR experiment therefore naturally handles the description of the orientational order in a mesophase with respect to a laboratory axis system in two stages as we chose to do throughout Chapter 1: the first stage describing the orientational order of the molecules with respect to the director and the second stage relating the behaviour of the director to a laboratory axis system. In what follows we consider this second stage in some more detail.

This section has considered the angular dependence of the EPR spectrum of a monodomain liquid crystal sample. When the director distribution is not uniform, the situation is similar to that of the powder spectrum for the polycrystalline sample considered earlier with two important differences. First, the component subspectra are now determined by the orientations of the principal axes of the partially-averaged $\tilde{\mathbf{A}}$ and $\tilde{\mathbf{g}}$ tensors with respect to the magnetic field and second, the weighting factor for each of these subspectra is determined by the orientational distribution of the director $f(\Omega)d\Omega$ with respect to the magnetic field (in the polycrystalline case $f(\Omega)d\Omega$ was the orientational distribution of the molecular-fixed principal axes with respect to the magnetic field). Formally, equation 2.12 is modified to

$$h(B) = \sum_{r} \int L\,(B, \tilde{B}_r, T_2^{-1})\ f(\xi)d\xi \tag{2.29}$$

in which $\tilde{B}_r$ in the lineshape function indicates that the resonant fields are now determined by the partially-averaged $\tilde{A}$ and $\tilde{g}$ tensors. In an isotropic distribution of the director, which gives a three-dimensional powder spectrum,

$$f(\xi)d\xi = \sin\xi\ d\xi \tag{2.30}$$

in which ξ is the single angle needed to define the respective orientations of the magnetic field and the director in some part of the sample (Just as a single angle was all that was required to specify the orientation of a cylindrically-symmetric particle with respect to the director in a uniaxial mesophase in figure 11c, Chapter 1).

In the general case in which the director distribution is unknown, it is clear that although the position of lines in each of the subspectra are governed by the angular fluctuations with respect to the director, their respective intensities in the sample spectrum are governed by the director distribution function $f(\xi)d\xi$ and therefore, in principle, the spectrum contains information that can be used to back-calculate $f(\xi)d\xi$. In practice, it is usually simpler to assume a form for $f(\xi)d\xi$ and to calculate the spectra using this distribution of the director. This is discussed shortly.

2.7 Lineshapes and linewidths

The previous sections have dealt with the factors that govern the position of lines in the EPR spectrum. This section explores the information that is present in the linewidths and lineshape functions of equations 2.12 and 2.29. Resonances in EPR are typically of the order of several Gauss wide (1G = 10^{-1} mT). Wide lines such as these and those seen in the NMR of solids are often detected by phase sensitive methods which detect the first derivative, that is, the slope of the absorption lineshape. $L(B, \tilde{B}_r, T_2^{-1})$ is the lineshape function which is most commonly a lorentzian

$$L\,(B, \tilde{B}_r, T_2^{-1}) = \frac{T_2}{\pi} \cdot \frac{1}{1 + T_2^2\,(B - \tilde{B}_r)^2} \tag{2.31}$$

or a gaussian

$$L\,(B, \tilde{B}_r, T_2^{-1}) = \frac{T_2}{\sqrt{2\pi}} \cdot \exp\!\left(-\tfrac{1}{2}.T_2^2\,(B - \tilde{B}_r)^2\right) \tag{2.32}$$

in which T_2^{-1} is a measure of the linewidth (formally, T_2^{-1} has the units of frequency, but in this Thesis, values for T_2^{-1} are reported with the units of magnetic field strength, a reflection of the fact that we record the spectrum by measuring the absorption of fixed frequency rf radiation as a function of the applied magnetic field). When all couplings are resolved the natural lineshape for solution spectra is lorentzian but in the spectra of crystalline solids and in situations in which weak interactions between magnetic species leads to unresolved couplings, the gaussian lineshape is also common [5, 11]. The lineshapes of spin probes dissolved in a liquid crystal solvent are often a mixture of the two. The normalized lorentzian and gaussian lineshapes are shown in figure 3 in the absorption and first derivative modes. The same linewidth T_2^{-1} is used in each case. It is noticeable that the lorentzian line is much more intense in the wings.

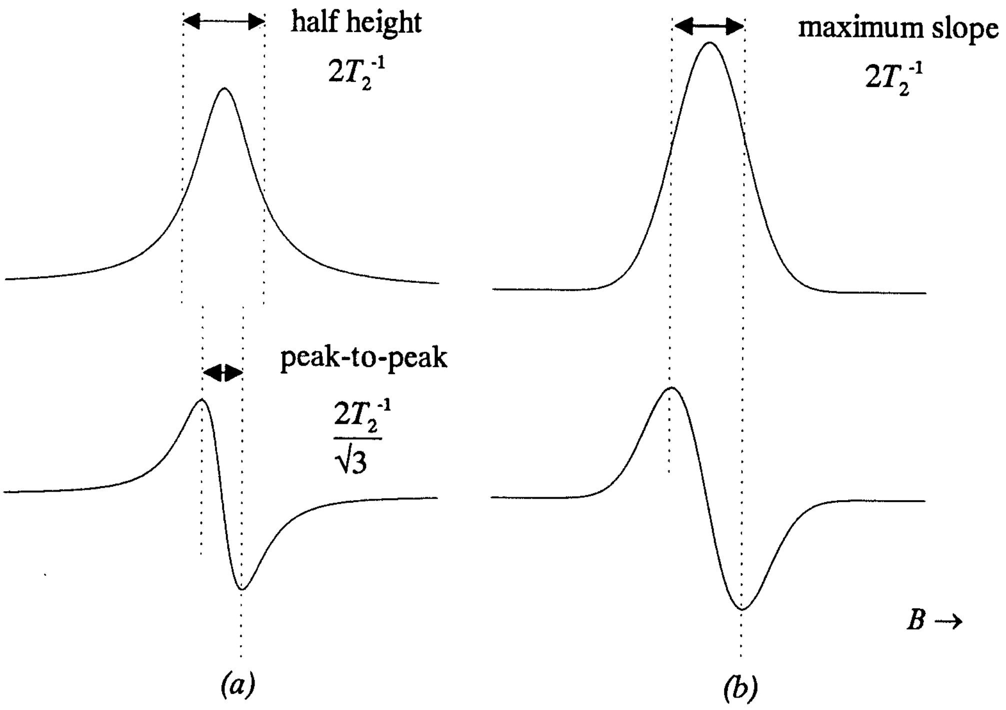

Figure 3 Line shapes of (a) the lorentzian line and (b) the gaussian line in the absorption (top) and first derivative modes, as a function of the magnetic field.

The linewidths contain dynamic information about the system under study [13, 14]. In the limit of very rapid molecular motion in solution all hyperfine lines have an identical linewidth. If molecular motion is slowed slightly on the EPR timescale, then the width of the resonance is related to the nuclear spin quantum number m_I associated with each hyperfine line and is given by

$$T_2^{-1} = A + B\,m_I + C\,m_I^2 \qquad (2.33)$$

In a mesophase the coefficients A, B and C are predicted to depend upon the angle ξ between the director and the magnetic field, this dependence is predicted to be

$$A(\xi) = A_0 + A_2 P_2(\cos\xi) + A_4 P_4(\cos\xi) \qquad (2.34)$$

with similar expressions for B and C. This makes the (reasonable) assumption that both electron and nuclear spins are quantized along the laboratory magnetic field. The angle-dependent linewidth coefficients are dependent upon the orientational order and the rotational dynamics of the spin probe in the mesophase. These coefficients can be used to calculate the order parameter $\overline{P}_4$ and the rotational correlation times for the spin probe in the liquid crystal [13, 14].

Having introduced all of the basic equations that govern the appearance of the EPR spectra of spin probes dissolved in a mesophase, it is instructive to consider a real example, which we do in the next section.

2.8 The EPR spectrum as a function of experimental conditions: an example.

We now bring together the different strands of the previous sections and consider the changing form of the spectrum as a polycrystalline liquid crystal sample containing a cholestane spin probe is heated *via* a smectic phase and a nematic phase into an isotropic phase. This demonstrates how the spectrum changes in different motional regimes. The sample is cooled into the nematic phase in which the director is uniformly aligned parallel to the magnetic field. The nematic phase is then spun, at first slowly, and then more rapidly, about an axis orthogonal to the magnetic field. This produces a change in, first, the director orientation, and then the director distribution, and this serves to illustrate how the EPR spectrum of the spin probe dissolved in the mesophase depends upon the orientation and the distribution of the director with respect to the magnetic field, that is, the form of $f(\xi)d\xi$ in equation 2.29. The sample spinning is stopped and after some time the monodomain spectrum is recovered indicating that the director has realigned along the magnetic field. The nematic phase is then cooled into an aligned smectic A phase in the magnetic field of the spectrometer and the angle dependence of this spectrum is considered. The changes in the spectra that are observed during this sequence of experiments also show how magnetic fields and the history of the sample influence the behaviour of the director in various mesophases.

The spectrum of the polycrystalline sample is shown in figure 4a. Molecular motion is quenched and therefore in the slow motion regime the spectrum contains resonances across the full range of the fields given by the principal components of the nitrogen hyperfine tensor and the **g** tensor which are set in the probe molecule. The relative intensities and shapes of the different peaks in this so-called three-dimensional powder spectrum reflects the fact that these principal axis systems make every possible angle with the magnetic field, just two angles are needed to specify the orientation of the principal axis system with respect to the magnetic field direction and therefore $f(\Omega)d\Omega=\sin\theta d\theta\, d\phi$ in equation 2.12. As the temperature is increased, the polycrystalline sample melts into a smectic A phase; now the molecular motion is no longer quenched, rapid rotational motion of the spin probe (and of the mesogen molecules themselves) in the uniaxial smectic A phase means that the nitrogen hyperfine tensor and the **g** tensor take on partially-averaged forms $\tilde{\mathbf{A}}$ and $\tilde{\mathbf{g}}$ with cylindrical symmetry about the local director. However, the director is randomly oriented over the whole sample on melting a polycrystalline sample as the magnetic field is insufficient to reorient the smectic layers. The three-dimensional powder spectrum of the smectic A phase shown in figure 4b is now given by equation 2.29 in which $f(\xi)d\xi = \sin\xi d\xi$ to reflect the uniform orientational distribution of the director with respect to the magnetic field. Upon further heating, a transition to the nematic phase occurs, the hyperfine and **g** tensors remain partially-averaged, but now the magnetic torque is sufficient to align the director parallel to the magnetic field (in a material with a positive $\Delta\tilde{\chi}$) and so the spectrum of the monodomain sample consists of just three hyperfine lines separated by a spacing $\tilde{A}_{\parallel}$ centred on a magnetic field calculated by substituting $\tilde{g}_{\parallel}$ in equation 2.4. The orientation of the director is reflected in the form of $f(\xi)d\xi$ which is a delta function centred on $\xi=0°$. The hyperfine spacing in the monodomain nematic phase, $\tilde{A}_{\parallel}$, changes as a function of the orientational order and therefore as a function of temperature and can be used to determine the orientational order parameter for the spin probe in the nematic phase, $\overline{P}_2$, using equation 2.21. The orientational order vanishes at and above the clearing temperature, and the spectrum of the isotropic phase contains three lines separated by the isotropic hyperfine splitting, a, centred on a magnetic field given by the isotropic g-factor, g. The spectra of the nematic and of the isotropic phase are shown in figure 4c and 4d. A comparison of the spectra in figure 4a, b and d show the spectra that result when all orientations of the spin probe with respect to the magnetic field are equally probable in the different motional regimes of the spin probe.

The sequence of figure 5 shows a selection of EPR spectra of the same sample during cooling. As the sample is cooled into the nematic phase, the spectrum of figure 4c is recovered and is shown in figure 5a. Continuous slow rotation of the sample about an axis orthogonal to the static magnetic field, as occurs in some viscosity measurements on the nematic phase (see Chapter 5), causes the director to adopt an equilibrium orientation that lies at some angle to the magnetic field so as to balance the torques on the director due to the magnetic field and the rotation of the sample. Figure 5b shows the case in which the director makes an angle of 30° with the magnetic field direction at some spinning speed and magnetic field strength. The hyperfine splitting, $\overline{a}(30°)$ and g-factor, $\overline{g}(30°)$ are given by equations 2.25 and 2.26 and the distribution function $f(\xi)d\xi$ is a delta function centred on $\xi=30°$. More rapid rotation of the nematic sample leads to the formation of a so-called two-dimensional powder pattern in which the director adopts an isotropic distribution in the plane normal to the spinning axis and containing the magnetic field. The two-dimensional powder spectrum shown in figure 5c shows a continuous distribution between the line positions given by $\tilde{A}_{\parallel}$ and $\tilde{A}_{\perp}$ as evidenced by the appearance of an apparent absorption lineshape of the high and low field lines in the spectrum displayed in the first derivative mode. This distribution is reflected in the form of $f(\xi)d\xi$ which simply equals $d\xi$. The parallel and perpendicular features in figure 5c are of very similar intensity, indicating that the proportions of the director that are parallel and perpendicular to the magnetic field are identical in the two-dimensional director distribution. This spectrum should be compared with that of the three-dimensional powder spectrum of the smectic phase formed on heating the polycrystalline sample and shown in figure 4b to emphasize the relationship between the director distribution and the EPR spectrum. If the nematic-smectic transition is of low entropy, then the principal components of the (partially-averaged) $\tilde{\mathbf{A}}$ and $\tilde{\mathbf{g}}$ tensors are similar either side of the transition, as these are a function of the orientational order of the spin probe with respect to the local director. The three-dimensional powder spectrum of the multidomain smectic and the two-dimensional powder pattern of the rapidly spinning nematic show roughly the same line positions. However, the different intensities of the same basic components in the spectra are a consequence of the different director distributions in the two cases: the three-dimensional powder spectrum clearly shows much stronger perpendicular features as a larger proportion of the director lies at a larger angle to the magnetic field in the three-dimensional case. In this Thesis we are often interested in the orientation and/or orientational distribution of the director in various experiments and therefore the form of $f(\xi)d\xi$. If the sample spinning is stopped, then the director experiences only the magnetic torque and after some time a monodomain nematic phase is recovered with the director lying parallel to the magnetic field. Careful cooling of this aligned sample can be used to from a monodomain smectic A phase. Now it is possible to observe the angle dependence of the EPR spectrum simply by rotating the sample to a different position and acquiring the EPR spectrum: although the director orientation (distribution in the more general case) within the sample remains unchanged (because the magnetic field is insufficient to reorient the smectic layers) rotation changes the director orientation (distribution) with respect to the magnetic field and it is this orientation (distribution) that determines the EPR spectrum. The hyperfine splitting is again predicted for a given angle by equation 2.25. Figure 5d shows the changing spectrum as the sample is rotated through 180°: the apolar character and high viscosity of the smectic A phase is shown by the fact that the spectrum at an angle ξ is equivalent to that at an angle $(180°-\xi)$.

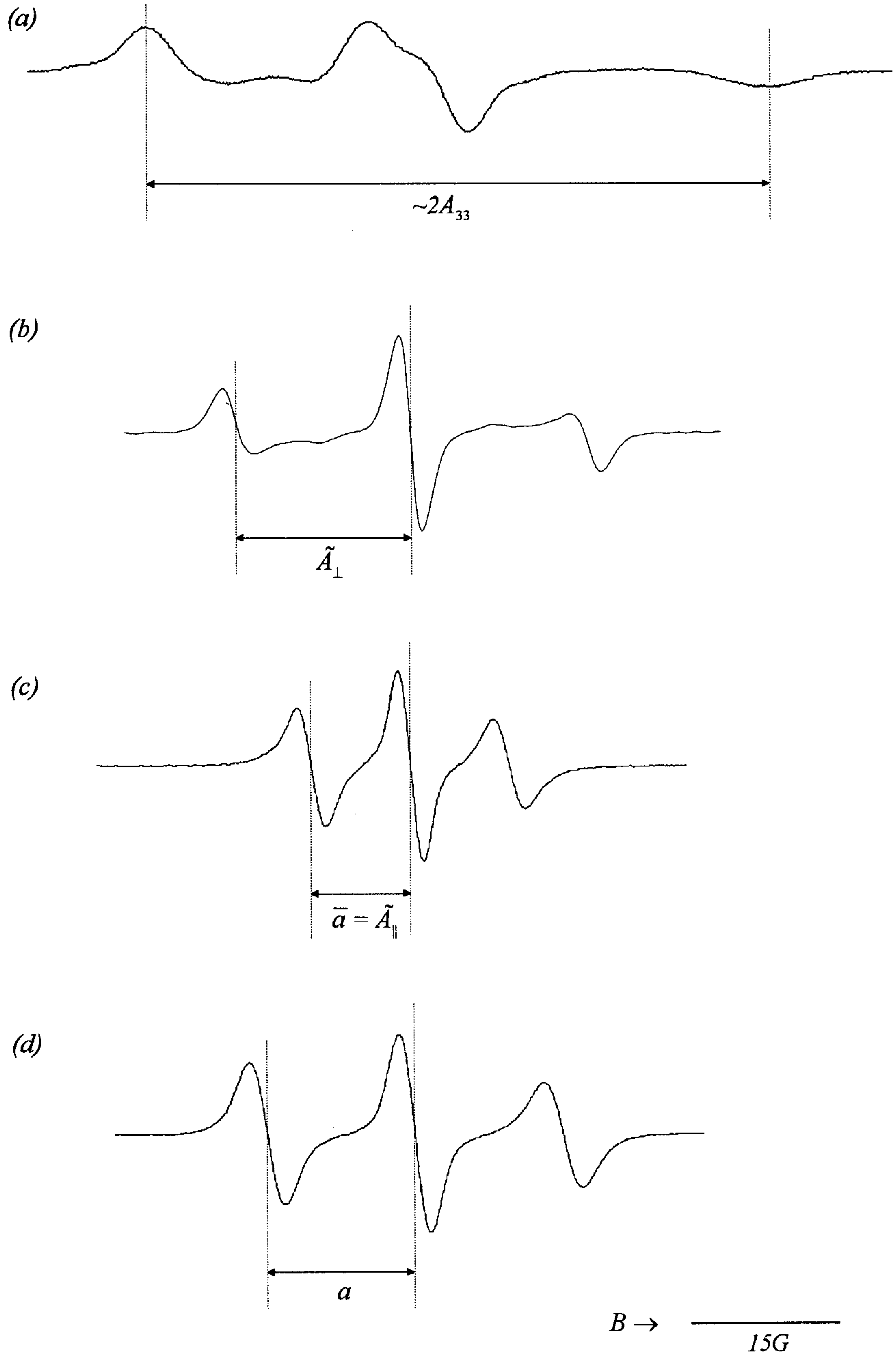

Figure 4 The spectrum of the cholestane spin probe in a liquid crystal dimer as a function of temperature during heating: (a) the polycrystalline powder, (b) a multidomain smectic A phase, (c) the nematic phase and (d) the isotropic phase.

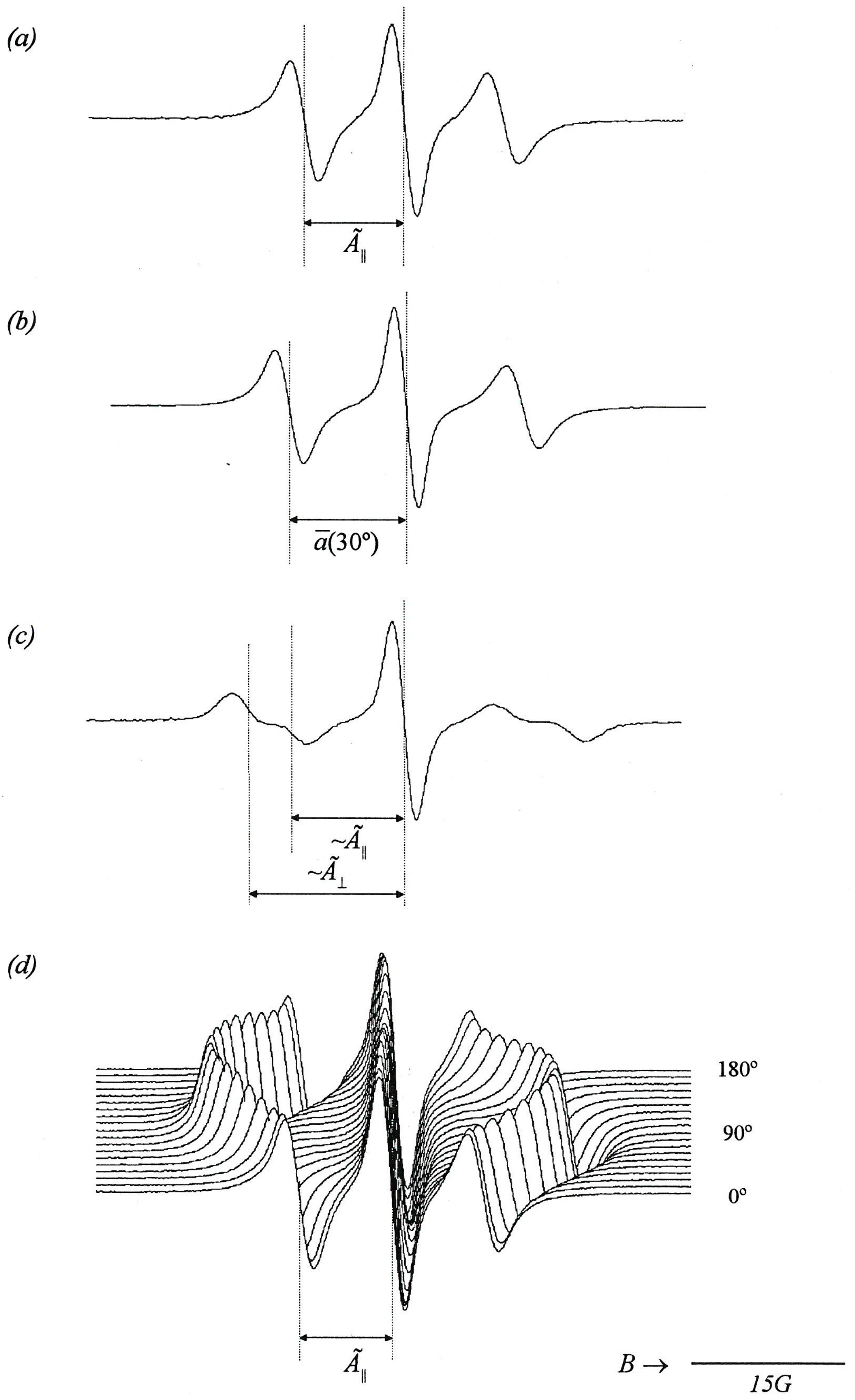

Figure 5 The spectrum of the cholestane spin probe in a liquid crystal dimer as a function of temperature during cooling: (a) the nematic phase (b) during slow rotation of the nematic phase (c) during rapid rotation of the nematic phase and (d) the angle dependence of the spectrum of the aligned smectic A phase.

2.9 Simulation of EPR spectra

In this Thesis we are concerned with the director orientation and/or distribution with respect to the magnetic field and wish to know $f(\xi)d\xi$. In Chapters 5 and 6 the interpretation of the experiments is based on comparisons between the experimental EPR spectra and their simulated counterparts, which are calculated assuming particular distributions of the director. The background to these simulations is now described. The equation for the EPR spectrum of a spin probe dissolved in a mesophase was given in 2.29 in which $f(\xi)d\xi$ describes the orientational distribution of the director with respect to the magnetic field. In the simulations the sample spectrum is calculated as a weighted sum of a series of i subspectra calculated at a discrete number of magnetic field values. The integration over the relevant angles ξ that appears in 2.29 is here approximated by a summation over the same angles as this is particularly amenable to the numerical approach we use to fit the experimental spectra. Therefore, in our calculations, the expression that is evaluated is

$$h(B) = \sum_{\text{angles i}} \sum_{\mathrm{r}} L(B, \widetilde{B}_{\mathrm{r}}(\mathrm{i}), T_2^{-1}(\mathrm{i})\,)\, \mathrm{f}_{\mathrm{i}} \tag{2.35}$$

in which $\sum_{\mathrm{r}} L(B, \widetilde{B}_{\mathrm{r}}(\mathrm{i}), T_2^{-1}(\mathrm{i})\,)$ represents a particular subspectrum and f_{i} the weighting factor in the summation. The set of coefficients f_{i} which are sought contain the same information as is contained in the integration over $f(\xi)d\xi$. Each of the subspectra corresponds to a different angle ξ (in the range 0 to 90°) between the director and the magnetic field. This separation of the sample spectrum into a weighted sum of i subspectra means that the description of the orientational distribution of the director with respect to the magnetic field, contained within the set of coefficients f_{i}, can be treated independently of the factors which influence each of the subspectra. Each of the i subspectra is calculated independently using the hyperfine splitting, *g*-factor and the linewidths which vary with the angle ξ as previously described (in Chapter 6, the set of subspectra also implicitly include the effect of a magnetic field gradient which introduces the extra dependence B(i), this is discussed in Chapter 6).

2.10 Instrumental

The EPR spectrometers that are used in this Thesis operate at X-band, with typical microwave frequencies of the order of 9.4GHz and resonant magnetic fields for the nitroxide spin probe in the range of 3300-3400G depending slightly upon the experiment (the presence of a quartz heating jacket for variable temperature work lowers both the resonant magnetic field and the microwave frequency in the spectrometer). The experiments described in Chapters 3 to 5 use a Bruker ECS 106 spectrometer, while that described in Chapter 6 uses a Bruker ESP 300 spectrometer: the only notable difference between the two is that the latter is fitted with gradient coils that provide for a field gradient of up to 300Gcm^{-1} in the region of the sample (this is discussed in Chapter 6). For convenience, this description of the basic principles of spectrometer operation is developed assuming that the magnet is not fitted with gradient coils and the spectrometer is operating in the more common field-sweep mode although the same guiding principles also hold more generally.

A block diagram of the essential components of an EPR spectrometer is shown in figure 6. The spectrometer consists of two main blocks, the magnet and the signal channel, both of which are run under the control of the a console and have a number of embellishments which maximise the efficiency of spectral acquisition. The sample is positioned inside a microwave cavity (an amplifier for weak EPR signals from the sample) situated in a homogeneous magnetic field and is bathed in fixed frequency microwave radiation generated by the microwave bridge (a klystron valve) which is channelled to and from the cavity by waveguide [2, 7]. The spectrum is obtained by sweeping the magnetic field. When there is no EPR signal, a standing wave is set up in the microwave cavity and no microwave radiation is reflected back from the cavity to the detector. At some magnetic field values, the resonance condition is satisfied and microwave radiation is absorbed by the sample, the coupling of the cavity with the waveguide is destroyed, and microwave radiation is reflected back from the cavity and is detected as an EPR signal.

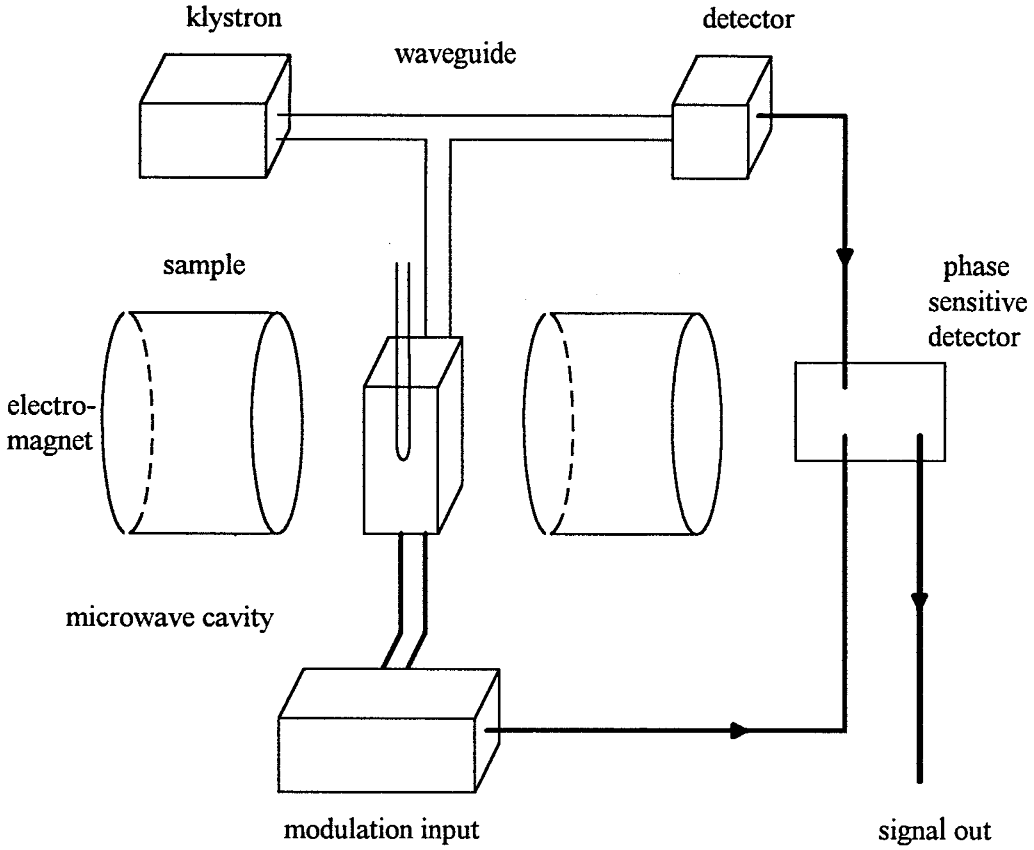

Figure 6 A block diagram of an EPR spectrometer.

Phase sensitive detection is one of several refinements that are used to improve the sensitivity of signal detection [2, 7]. As the magnetic field is swept, the applied field is modulated sinusoidally at a modulation frequency and modulation amplitude that are set by the user. For an EPR signal which is approximately linear over an interval as wide as the modulation amplitude, the EPR signal is transformed into a sine wave with an amplitude proportional to the slope of the absorption signal, hence the common appearance of the detected EPR spectrum as the first derivative of the absorption spectrum. The phase sensitive detector (or lock-in detector) produces a DC signal proportional to the amplitude of the modulated EPR signal and compares the modulated signal with a reference signal having the same frequency and phase as the field modulation. The signal channel is only sensitive to signals with the same frequency as the field modulation and so this encoding enhances the recognition of the real EPR signal and suppresses other signals such as noise and electrical interference. Higher modulation amplitudes increase the intensity of the detected EPR signals, however, if the modulation amplitude is too large then the detected signal becomes broadened and distorted. The modulation amplitude should be set to a value considerably less than the linewith so as not to distort the detected signal. The modulation frequency has less effect upon the measured spectrum in the experiments in this Thesis and a value of 100kHz is used throughout.

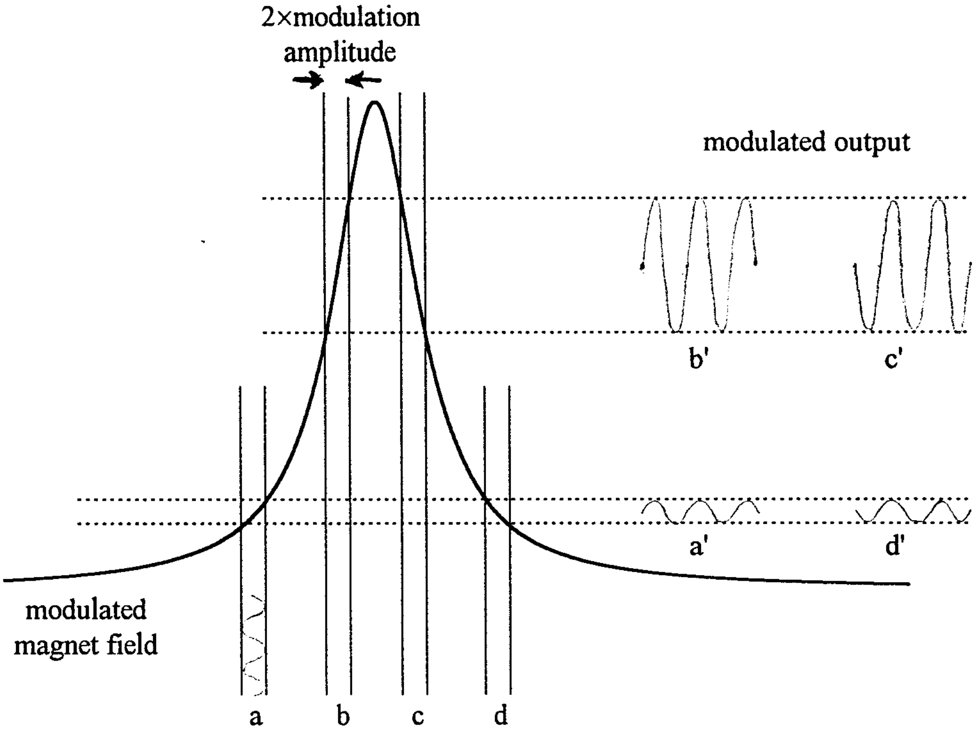

Figure 7 Using phase sensitive detection, the detected signal is proportional to the amplitude of the absorption signal, shown for four values of the magnetic field across the spectrum.

The signal-to-noise ratio in the detected signal is also dependent on a user-set parameter called the time constant, this is the time period over which the detector collects signal which determines the response time of the spectrometer. The noise level decreases as the time constant is increased, but beyond a certain point the time constant will also start to filter out the real EPR signal and distort the shape and position of a resonance. The combination of the time constant and the time taken to sweep through the magnetic field (acquisition time for the spectrum) should be set so that the time taken to sweep through a peak is greater than ten times the time constant.

The modulation amplitudes, time constant and sweep time vary in the experiments in the following Chapters according to the spin probe that is used (and therefore, the resultant linewidths), the experiments that are being performed and the range over which the spectrum extends.

In making up samples for EPR experiments, careful sample preparation is important to ensure that the spectral parameters (lineshapes and linewidths) truly reflect the properties of the spin probe in the mesophase and that the spin probe itself causes minimal perturbation to the properties of the mesophase. For example, the addition of the chiral cholestane spin probe to a nematic phase can induce a cholesteric phase which has a very different macroscopic behaviour. In practice, both of these potential difficulties are overcome by working with a minimal concentration of the spin probe in the mesophase ($\sim 10^{-5}$ M) so that the magnetic interactions between different probe molecules can be ignored: this also ensures that, when using the cholestane spin probe dissolved in an otherwise nematic phase, even small external fields induce a cholesteric-nematic transition. Low concentrations of the spin probe in the samples studied in this Thesis are introduced by adding a small quantity of a stock solution of the spin probe in a solvent to a quartz sample tube. The solvent is then removed and the liquid crystal added. The sample is then degassed using a freeze-thaw cycle, to remove any dissolved oxygen, and then sealed under vacuum. This ensures that extra line broadening due to unresolved fine coupling between the spin probe and paramagnetic oxygen is minimised.

The behaviour that we observe in the thermotropic systems studied in this Thesis is a function of temperature and therefore the control of the sample temperature is an important part of the experiments (although less so in Chapter 5). The temperature control system for the ECS 106 spectrometer is based on a Eurotherm controller interfaced to the spectrometer. The sample tube is positioned inside a tubular quartz dewar that fits inside the microwave cavity. A stream of air (or nitrogen, for low temperature work) blows over a combined thermocouple/heater located just below the bottom of the sample tube which regulates the sample temperature to within ±0.2°C (for a sample of typical size).

2.11 References

[1] ATHERTON, N.M., *Electron Spin Resonance: Theory and Applications*, John Wiley, 1973.

[2] AYSCOUGH, P.B., *Electron Spin Resonance in Chemistry*, Butler and Tanner, 1967.

[3] ATKINS, P.W., Chapter 20, *Physical Chemistry*, 3rd edition, Oxford University Press, 1987.

[4] SLICHTER, C.P., *Principles of Magnetic Resonance*, Harper and Row, 1963.

[5] CARRINGTON, A. and MCCLACHLAN A.D., *Introduction to Magnetic Resonance*, Harper and Row, New York, 1967.

[6] BERLINER, L.J. and various authors, *Spin Labeling: Theory and Applications*, Academic Press, 1976.

[7] POOLE, C., *Electron Spin Resonance*, John Wiley Interscience, 1967.

[8] NORDIO, P.L., Chapter 2, *Spin Labeling: Theory and Applications*, ed. L.J. Berliner, Academic Press, 1976.

[9] see, CARRINGTON, A. and MCCLACHLAN A.D., Appendix D, *Introduction to Magnetic Resonance*, Harper and Row, New York, 1967, or DE JEU, W.H., Appendix, *Physical Properties of Liquid Crystalline Materials*, Gordon and Breach, 1980, for a brief discussion of tensor algebra.

[10] HOATSON, G.L. and LEVINE, Y.K., Chapter 1, *The Molecular Dynamics of Liquid Crystals*, eds. G.R. Luckhurst and C.A. Veracini, Kluwer, 1994.

[11] LUCKHURST, G.R., Chapter 7, vol. 2, *Liquid Crystals and Plastic Crystals*, eds. G.W. Gray and P.A. Winsor, Ellis Horwood, 1974.

[12] SEELIG, J., Chapter 10, *Spin Labeling: Theory and Applications*, ed. L.J. Berliner, Academic Press, 1976.

[14] LUCKHURST, G.R., SETAKA, M. and ZANNONI, C., *Mol. Phys.*, **28** 49, 1974.

[15] LUCKHURST, G.R., SMITH, S.W. and SUNDHOLM, F., *Acta Chemica Scandinavica*, **A41** 218, 1987.

Chapter 3

Viscoelastic properties of nematic Phase V measured using an EPR technique

3.1 Introduction

The elastic properties of a body or substance describe its tendency to return to its original size and shape after being subject to deforming stresses. The viscosity of a conventional fluid determines its resistance to flow. It is normal to associate elasticity measurements with solids and viscosity measurements with liquids. The dynamic and equilibrium behaviour of anisotropic fluids is governed by so-called viscoelastic properties which combine elements of both the elastic and the viscous properties of the system. In this respect, anisotropic materials such as liquid crystals, and especially those of low molar mass, are rather unique, as both elasticity and viscosity measurements can be obtained and a physical and technological importance ascribed to them both: for example, the response time of a liquid crystal display is proportional to the twist viscosity coefficient γ_1 [1, 2] (also called the rotational viscosity coefficient). It is clear that a better understanding of the mechanism of the physical response of a liquid crystal to changes in external conditions assists in optimising their application by, for example, influencing display design or switching patterns.

In this Chapter we study the viscoelastic properties of Phase V, a low molar mass nematic liquid crystal, using EPR spectroscopy. It is useful to begin by introducing ideas about the viscosity of simple liquids and to understand in a qualitative sense several observations about the dependence of viscosity on structural types and external conditions. Viscosity measurements of isotropic liquids relate to the rate of movement of the centres of mass of the particles of the fluid under a shear stress which can be applied in various ways. Section 3.3 discusses how these ideas are extended to liquid crystals where more controlled conditions are required to obtain comparable and meaningful measurements of shear viscosities because of the complicating influence of the director. The twist viscosity of liquid crystals is introduced in section 3.4, this relates to the dynamics of orientational or reorientational processes of the director without any associated movement of the centres of mass of the anisometric molecules of the liquid crystal and obviously has no isotropic counterpart. Sections 3.5 and 3.6 outline the theory and practical measurement of the rate of director reorientation which is proportional to the twist viscosity coefficient γ_1 under certain conditions. The results of our experiments are then reviewed, analysed and discussed in sections 3.7 to 3.9.

3.2 Viscosities of simple liquids [3]

In isotropic liquids, viscosity measurements describe the dynamics of the response to a shearing stress, applied for example during pouring. The properties of the constituent molecules that confer the viscous properties on a fluid depend upon the intermolecular potential, which is determined by particle size, shape and specific intra- and intermolecular interactions. The details of the intermolecular potential are not fully understood except in the simplest cases, but their effects can be quantified indirectly by viscosity measurements that deal with the dynamic responses of liquids.

The intermolecular forces that hold molecules together in a bulk flowing liquid may be likened to the frictional forces μ that operate at the interface between two solids when one is moved relative to the other. This similarity is seen in figure 1. Figure 1a shows the frictional forces between the surfaces of two solids as they are moved relative to each other, figure 1b shows the equivalent case for a sandwich of liquid lying between and adhering to the surfaces of two plates moved relative to each other.

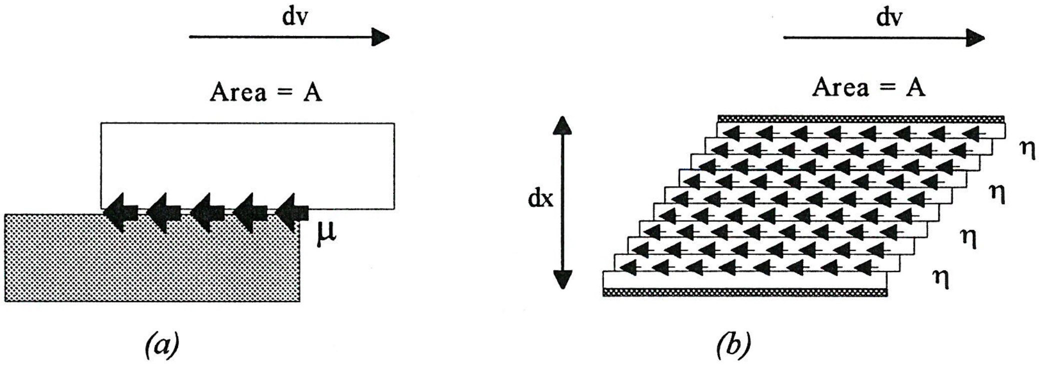

Figure 1 Schematic representation of the frictional forces (a) between two solids and (b) in a sandwich of liquid between two solids. In each case the bottom plate is stationary as the top plate is moved.

The sheared liquid can be regarded as being composed of lamellae normal to the velocity gradient (dv/dx) with forces η akin to frictional forces acting between these lamellae preventing them from sliding freely over each other and resisting the relative movement of the two plates (by analogy with figure 1a). The laminar or streamline flow shown in figure 1b is termed newtonian flow and this sample is said to be behaving as a newtonian fluid; in this case the condition

$$F = \eta \; A \frac{dv}{dx} \tag{3.1}$$

is satisfied for the applied force F required to drag parallel plates of area A separated by a distance dx at a relative speed dv. η represents the viscosity coefficient of the liquid.

The temperature dependence of η can be predicted using the following argument: in order for a molecule to be able to free itself from the influence of its neighbours, it must possess an energy above a certain activation energy E_a needed to overcome the intermolecular forces with those neighbours. The number of molecules with a given amount of energy is described by the Boltzmann distribution and therefore at any temperature the percentage of molecules that possess an energy above E_a can be derived from the Boltzmann distribution. Consequently the viscosity is expected to decrease as the temperature increases according to

$$\eta \propto \exp(E_a/RT) \tag{3.2}$$

and this describes the Arrhenius dependence of η on temperature which is normally observed for simple liquids.

In reality, most liquids are composed of more or less anisometric molecules, but the effect of the anisotropic shape does not usually cause a significant departure from the newtonian behaviour of equation 3.1. However, departures do occur, most frequently when the liquid is composed of rod-like molecules: a force applied to an isotropic liquid of such particles can cause shear alignment at each of the notional lamellar boundaries within the liquid layer. This alignment of rod-like molecules along the shear direction leads to a lowering of the measured viscosity when compared to that predicted by equation 3.1. This can be understood simply by considering that the rods may slide more easily over each other in the side-to-side configuration than in a random relative configuration; this is pictured in figure 2.

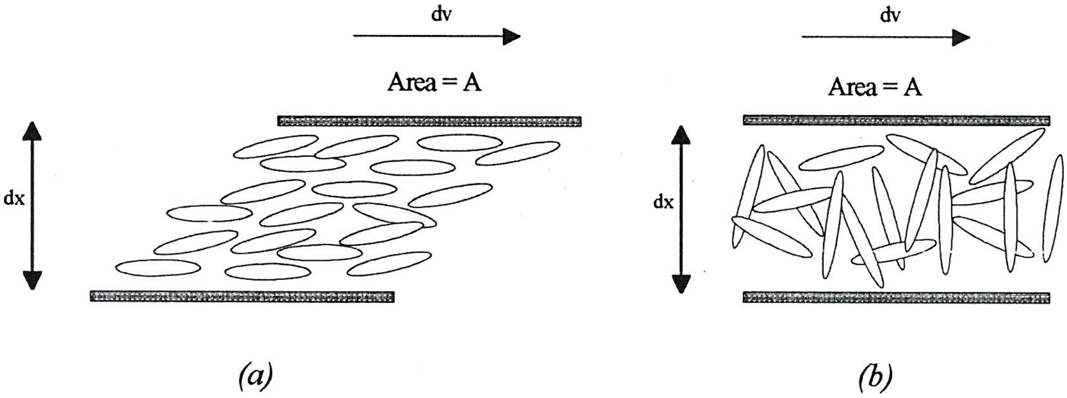

(a) (b)

Figure 2 Elongated molecules slide over each other more easily in a (a) side-to-side than in a (b) random relative orientation.

This demonstrates that molecular orientation and especially correlations in orientation between neighbouring molecules are important in determining the measured viscosity. Rod-like molecules and orientational order are defining characteristics of mesophases and so experiments that measure the shear viscosity of liquid crystals must take account of the mutual dependency between the measured viscosity and the degree or orientation of any alignment that may exist or evolve during an experiment. The next section discusses how this is done.

3.3 Shear viscosities of Nematic Liquid Crystals

The alignment of neighbouring rod-like molecules in a nematic liquid crystal means that some degree of molecular reorientation, and therefore director reorientation, is bound to occur during a shear experiment similar to that described, this makes it difficult to measure a meaningful viscosity in the event that there is an equation for the motion of the director as well as that for the individual particles to consider. However, controlled and reproducible measurements can be made if the director reorientation can be prevented while the system is under shear. This can be achieved by pinning the director, that is, by imposing a uniform and invariant director on the sample and maintaining this orientation throughout the shear experiment. This can be done using a strong external field (see Chapter 1). For a liquid crystal situated between parallel plates there are three values of the so-called Miesowicz viscosity coefficients for the shear experiment which are associated with the three limiting orientations of the pinned director with respect to the shear direction and the velocity gradient that can be envisaged. These three geometries are pictured in figure 3. If the experiment is not conducted with the sample lying between parallel plates then a further stretch type of distortion may occur and this is also pictured in figure 3d.

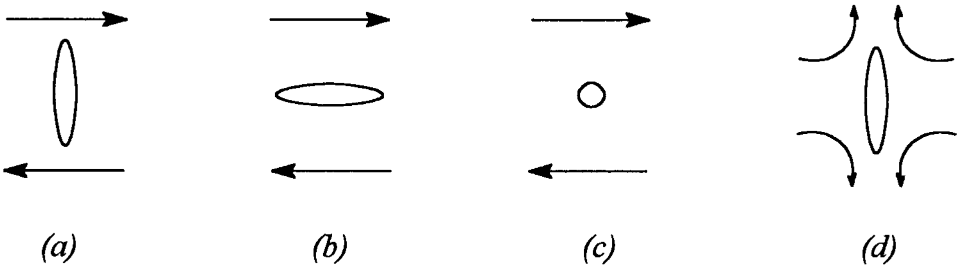
(a) *(b)* *(c)* *(d)*

Figure 3 The experimental geometries using a unique pinned director direction for measurement of the three Miesowicz coefficients (a) η_1 (b) η_2 (c) η_3 and the geometry for the measurement of (d) η_{12} in which the director orientation varies across the sample.

There have been many experimental measurements of the Miesowicz viscosity coefficients η_i of liquid crystals [4] and of the single viscosity coefficient η above the clearing temperature. The results for 4-methoxybenzylidene-4'-*n*-butylaniline (MBBA) demonstrate some typical features [5]. The relative values for η_1, η_2 and η_3 can be understood relatively easily. At any temperature η_1 has the largest value reflecting the fact that in this geometry the neighbouring lamellae are effectively interlocked because of the average molecular orientation and are prevented from sliding easily over each other. η_2 has the lowest value, in this geometry the director is closest to the orientation seen when shear-induced alignment lowers the effective viscosity of isotropic fluids composed of rod-like molecules, and so η_3 is decreased for the same reasons. η_3 behaves like a continuation of the single isotropic viscosity coefficient η. This is to be expected as in this configuration, shown in figure 3c, there is no anisotropy in the plane defined by the shear and velocity gradient direction as the anisotropy that characterises the nematic phase is only apparent outside of the shear plane. The results for MBBA show that the dependence of the isotropic viscosity and of the Miesowicz coefficients η_1 to η_3 deep in the nematic phase is Arrhenius-like (that is, is well described by equation 3.2) but the behaviour of η_1 to η_3 in the vicinity of the nematic-isotropic transition is more complex. In addition to the temperature dependence of a general viscosity coefficient predicted by equation 3.2, it is anticipated that a contribution to the viscosity will be introduced by the dependence of the viscosity on the orientational order which is also temperature dependent. The precise form for this dependence has been the subject of numerous investigations [see,for example, 6, 7, 8, 9].

Thus far, we have described viscosity coefficients that relates to a sample subjected to a shearing stress and can measure a viscosity that relates to the relative movement of the centres of mass of particles at different points in the fluid. In this respect the measurements of the Miesowicz viscosity coefficients for liquid crystals are analogous to those of isotropic liquids, the only refinement being that the measurements on liquid crystals relate to a specific orientation of the shear plane with respect to the director. In the next section, we consider a case in which the hydrodynamic behaviour of the liquid crystal has no isotropic counterpart but to which some of the ideas developed here can also be applied.

3.4 Liquid Crystal viscosities relating to director motion

In anisotropic fluids, a completely different type of drag acts on the response of the director to a distorting force that does not involve (in principle at least) any movement of the centres of mass of the particles of the fluid, in contrast with the shear viscosities which are all concerned with the movement of the centres of mass. If the restriction of a fixed orientation of the director is lifted, then an equation of motion for the director must be considered which was deliberately discounted in the previous experiments. This opens up the possibility of exploring the dynamics and forces on the director itself rather than those on the molecules of the liquid crystal. In considering the equations of motion for the director, two independent terms with the units of viscosity arise, these material parameters are the twist viscosity coefficients γ_1 and γ_2 (also frequently referred to as rotational viscosity coefficients) [5, 10]. In this Chapter we consider the viscoelastic behaviour of a low molar mass nematic liquid crystal in an experiment to measure γ_1. Several methods have been used to measure γ_1 of liquid crystals, based on the response of the director to instantaneous changes in the orientation of an aligning field or to a continuously rotating magnetic field to name but two [10]. The techniques used to monitor the state of the system are many and include optical studies, measurements of mechanical torque, magnetic susceptibility, dielectric properties and using magnetic resonance spectroscopies (see the Discussion, this Chapter). The next section develops the essential theory and assumptions for the experiment to measure γ_1 in which an aligned sample is subject to an instantaneous change in the orientation of a magnetic field, and applies irrespective of how the response of the director is monitored. In our experiments, the director response was monitored by EPR spectroscopy. More specific details relating to this follow in section 3.6, for now, it is noted that EPR as we use it here, and magnetic resonance in general, has the advantage that it allows us to follow both the orientation of the director and its state of alignment as it realigns in the magnetic field. This feature is not common to all of the techniques that have been used to follow the reorientation process or detect the equilibrium director orientation (in the case of rotating field experiments).

3.5 Theory

In section 3.2 we saw that shear-induced alignment of rod-like molecules of an otherwise isotropic fluid could lead to departures from predicted behaviour. Similarly, coupling of rotational and translational motions of the molecules of a liquid crystal introduces complications to the theory underlying experiments intended to measure the twist viscosity in anisotropic systems. However, under certain conditions the translational and orientational motions of molecules in a liquid crystal are decoupled and can therefore take place independently [5]. In this section we consider the theory of a case in which pure rotations of the director occur without producing any simultaneous translational motions of the particles of the fluid.

The equations of classical mechanics can be applied to the purely rotational motion of the director [11]. A simple equation for the rotational motion of the director in a magnetic field can be considered,

$$I\,\frac{\mathrm{d}^2\xi}{\mathrm{d}t^2} = T_\mathrm{B} + T_\mathrm{visc} \tag{3.3}$$

ξ is the angle between the director and the magnetic field. Assuming that the angular acceleration is constant the left hand side of equation 3.3 represents an inertial term which is normally neglected [5]. The T_B term on the right hand side represents a force on the director due to magnetic forces (equivalently T_E would represent the force on the director in an electric field), the second term T_visc represents a viscous term due to frictional forces which will tend to damp any response. A balance exists between torques due to the external, for example, magnetic forces and the internal forces due to the viscosity that oppose them.

In the case considered here an external magnetic field acts on the liquid crystal, using equation 1.4 from Chapter 1 the orientation-dependent magnetic free energy F_B is given by:

$$F_\mathrm{B} = -\frac{1}{3\mu_0}\Delta\tilde{\chi}\, B^2 P_2(\cos\xi) \tag{3.4}$$

in which ξ is the angle between the magnetic field and the director. This gives rise to a magnetic torque,

$$T_\mathrm{B} = -\frac{\mathrm{dF}}{\mathrm{d}\xi} = -\frac{1}{\mu_0}\,\Delta\tilde{\chi}\, B^2 \sin\xi\cos\xi \tag{3.5}$$

This is balanced by the viscous torque, given by

$$T_{\mathrm{visc}} = -\gamma_1 \frac{d\xi}{dt} \tag{3.6}$$

Now, neglecting the inertial terms in equation 3.3 and considering a torque balance, the equation of motion of the director is formulated as [12]

$$\gamma_1 \frac{d\xi}{dt} = -\frac{1}{\mu_0} \Delta\tilde{\chi} B^2 \sin\xi \cos\xi \tag{3.7}$$

this has the solution

$$\tan\xi_t = \tan\xi_0 \exp\left(\frac{-t}{\tau_r}\right) \tag{3.8}$$

in which ξ_0 is the initial angle made by the director and the magnetic field and ξ_t its subsequent value after time t. The time constant τ_r given by

$$\tau_r = \gamma_1 \mu_0 / \Delta\tilde{\chi} B^2 \tag{3.9}$$

represents a time constant for the magnetic field-induced director reorientation.

From equation 3.8, it is clear that any technique for monitoring the angle ξ between the director and the magnetic field as a function of time allows a determination of τ_r. A knowledge of the characteristic response time τ_r at a given magnetic field strength allows calculation of the ratio $\gamma_1/\Delta\tilde{\chi}$ and, if $\Delta\tilde{\chi}$ is known, the twist viscosity γ_1 can be calculated. Equation 3.9 gives the dependence of τ_r on γ_1 and on $\Delta\tilde{\chi}$ at a given field strength. In practice, values for $\Delta\tilde{\chi}$ are not easy to obtain, however $\Delta\tilde{\chi}$ has all the characteristics of an orientational order parameter and scales as the order parameter P_2 of the liquid crystal (see Chapter 1). In this EPR study we can only actually measure the orientational order parameter for the spin probe in the mesophase, however it is reasonable to assume that this reflects the orientational order of the liquid crystal host and is therefore also proportional to the value of $\Delta\tilde{\chi}$ for the mesophase. Later we use the order parameter measured for the spin probe in place of $\Delta\tilde{\chi}$ in our calculations of the product $\tau_r P_2$ which we use in place of γ_1 in our discussions of the temperature dependence of the twist viscosity of the liquid crystal.

The theory of equations 3.3 to 3.9 is based on the premise that the rotational and translational motions of the director and of the particles of the liquid crystal are decoupled and in particular that the director remains aligned during the relaxation process. This is sketched in figure 4 which indicates in an idealised form the various orientations of the director in a cross-section of the cylindrical sample at different stages of the experiment. Figure 4a represents the state of the aligned sample prior to the rotation of the director with respect to the magnetic field which was a necessary part of our experiment and is described later. Figure 4b shows the director lying at an angle ξ_0 to the magnetic field immediately following rotation of the sample tube through ξ_0, while figures 4c and 4d show the director orientations at various times during the subsequent relaxation of the director. In figure 4e the relaxation is complete and the director again lies parallel to the magnetic field. Throughout the experiment, the director is represented as being macroscopically aligned, the equations of motion of the director that ultimately give the twist viscosity assume that this is the case and that it is solely the director orientation with respect to the magnetic field that changes during the relaxation as predicted by equation 3.8 and shown in figure 4.

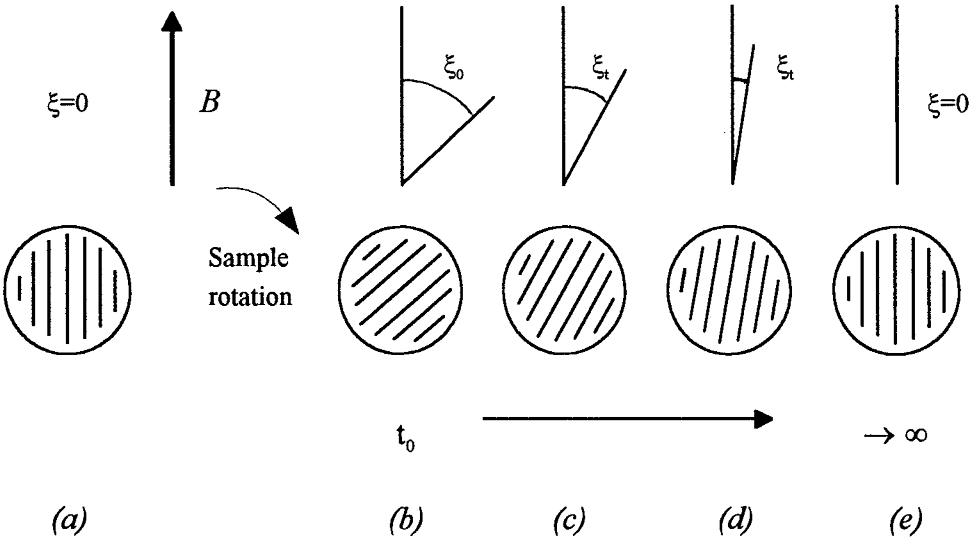

Figure 4 A schematic view of the rotation-relaxation experiment. A monodomain sample is formed using an external magnetic field in (a), (b) shows the sample immediately after rotation through an angle ξ_0 and (c) and (d) show the subsequent relaxation of the director, in (e) the sample director has again aligned with the magnetic field.

Breakdowns of the theory stem from breakdowns in the macroscopic alignment of the director. Previous work [13, 14, 15, 16] suggests that the modes of director relaxation, that is, its spatial distribution during relaxation, are dependent upon the initial angle ξ_0 through which the director is rotated. For initial angles of rotation ξ_0 less than 45°, there is direct experimental evidence that the director retains its alignment during the relaxation process and it is under these conditions that the theory of equations 3.5 to 3.9 predicts that the twist viscosity γ_1 can be measured [5, 10]. For initial angles of rotation ξ_0 greater than 45°, the director alignment is lost and the director becomes non-uniform during the relaxation, subsequently certain portions of the sample director relax quickly whilst in other regions the director remains at an angle to the magnetic field for longer than is suggested by the above theory. This has been explained by the breakdown of the decoupling between the rotational and translational motion of the particles of the fluid. Overall, this changed relaxation mode leads to a lesser effective viscosity for initial angles of rotation in the range 45 - 90° than would be predicted by the above theory and presumably leads *via* a pathway with a lower activation energy toward a more rapid relaxation of the bulk of the sample director.

3.6 The Rotation-Relaxation Experiment

3.6.1 Background

In these experiments, the value of the angle ξ is monitored using EPR spectroscopy by measuring the changing hyperfine splitting of a trace amount of a paramagnetic spin probe dissolved in the liquid crystal [17]. The static magnetic field of the EPR spectrometer provides the external magnetic field that tends to align the director. In principle, the rotation-relaxation experiment required by the above theory is very simple as was sketched in figure 4. A sample tube containing an aligned liquid crystal is rotated about an axis orthogonal to a static magnetic field; the director is then no longer aligned along the field and so experiences a magnetic torque tending to realign the director with the magnetic field (see Chapter 1). The reorientation of the director is slowed by the viscous forces in the liquid crystal which are determined in this experiment by the twist viscosity coefficient γ_1. The director orientation relative to that of the magnetic field is monitored as a function of time by observing the evolution of the EPR spectrum and in particular by observing the changes in the resolved component along the magnetic field of the partially-averaged nitrogen hyperfine tensor of a paramagnetic solute dissolved in the nematic phase. The reorientation of the director is slow on the intrinsic EPR timescale (see Chapter 2) and the exchange of the paramagnetic solute between regions of the sample in which the director would vary if not uniformly aligned is negligible on the EPR timescale. The EPR spectrum of the whole sample is therefore a superposition of the spectra from each of the probe molecules sampling the director in different regions of the sample; (assuming, quite reasonably, that the spin probe is well-distributed throughout the sample). Such a spectrum reflects the distribution of the different orientations of the director across the sample, and, importantly, enables us to identify when the director orientation is uniform across the sample and when changes to the distribution occur. It is noted that the EPR spectrum is sensitive only to the distribution of director orientations across the sample and does not give us any spatial information regarding changes in any translational motions of individual molecules or of microdomains if they develop.

In principle, the experiment requires only the observation of the temporal evolution of the EPR spectrum of the sample following rotation. In practice, there are a number of factors that need to be considered in order to measure the temporal evolution of the spectrum with the necessary detail. In the introduction to the EPR experiment of Chapter 2, we suggested that the EPR spectrum of a sample was acquired using a constant microwave frequency as a function of the applied magnetic field, which was swept across the range of interest. This is referred to as field-sweep mode and is commonly used. For our present purposes, the field-sweep mode imposes a rather stringent instrumental limitation on our ability to resolve the spectral evolution with sufficient detail. The director relaxation in the nematic liquid crystal used in this experiment largely occurs during the first 0.3s following rotation. During this period the spectrum is evolving most rapidly and the most discriminating information regarding the changing hyperfine splitting can be acquired. Thereafter, the spectral evolution is less rapid and information regarding changing hyperfine splitting is less informative. This is compounded by the non-linear dependence of the observed hyperfine splitting on the angle ξ_t in equation 3.8 which means that small changes in the angle ξ early in the relaxation produce very large changes in the spectrum. This dependence also means that similar absolute errors in the hyperfine splitting measured later in the relaxation introduce a disproportionately large error to the calculated angle ξ_t. The requirement is therefore to be able to acquire a large number of spectra in the first 0.3s of the relaxation at exactly known times after the rotation. Ideally, each of these spectra should be acquired in as short a time as possible, as it considerably simplifies the analysis if the director orientation can be regarded as static during the acquisition of each spectrum. Although the Bruker ECS 106 spectrometer allows for rapid acquisition of a single spectrum in the field-sweep mode, the instrumental delay between acquisition of successive spectra is too long to characterise the relaxation accurately.

The approach considered thus far has been to acquire details of the time evolution of the spectrum by building up a matrix of changing spectral intensity with time from a succession of field-sweep spectra acquired at different times following the rotation. In this (two-dimensional) matrix magnetic field forms one dimension and time the other. However, in principle, an exactly equivalent set of data can be acquired using the spectrometer in its time-sweep mode and instead performing a series of rotation-relaxation experiments, each at a single fixed magnetic field strength. There are both advantages and disadvantages to this alternative method of acquiring the temporal evolution of the spectrum demanded by the experiment. The essential advantage is that it offers an easy route to obtaining the spectral information required, with good time resolution throughout the relaxation, but also during the rotation that precedes it (see later) and could in principle be applied to systems with much shorter relaxation times. The principal disadvantage is that we must assume, or be able to verify, that the repeated rotation-relaxation process is synchronised and exactly reproducible. Fortunately, we are able to do this as abnormal rotations give a substantially different time-sweep.

3.6.2 Sample Preparation

Two samples of nitroxide spin probes dissolved in nematic Phase V were prepared. Different spin probes were used to enable us to demonstrate that the relaxation process observed is a property of the nematic solvent and is independent of the choice of spin probe. The spin probes used in this study, (3-spiro-[2'-N-oxyl-3',3'-dimethyl-oxazolidine])-5α-cholestane [18], and 2,2,6,6-tetramethyl-4-piperidine-N-oxide were purchased from the Aldrich Chemical Company and used without further purification. They are hereafter referred to as the cholestane and the tempone spin probe respectively. Their structures were shown in figure 13, Chapter 1. Phase V is a eutectic mixture of two disubstituted azoxybenzenes, each of which exists in two isomeric forms. The structures of these components are shown in figure 5 together with the composition and transition temperatures for the mixture. Phase V was obtained from E Merck (Darmstadt) and used without further purification.

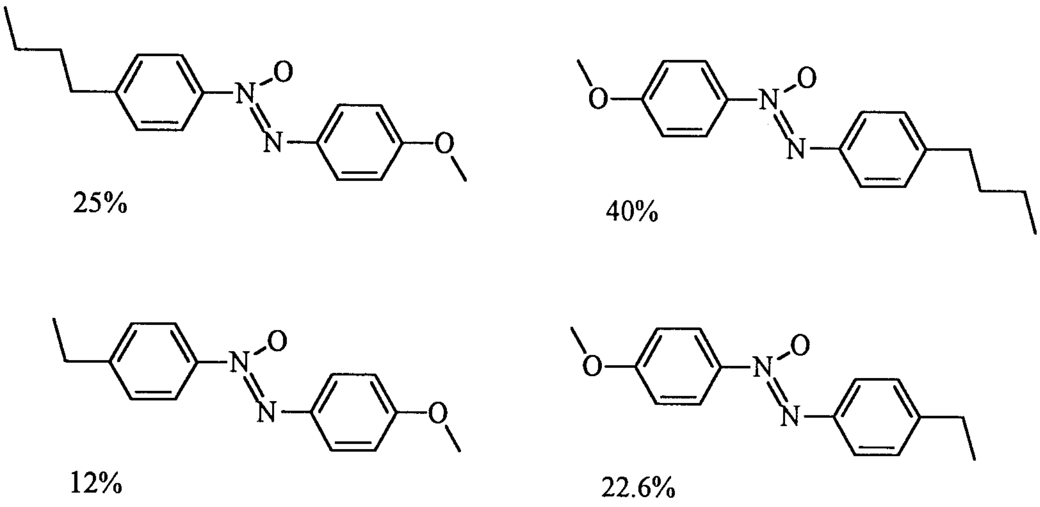

$$\mathrm{Cr} \xrightarrow{-5°\mathrm{C}} \mathrm{N} \xrightarrow{75°\mathrm{C}} \mathrm{I}$$

Figure 5 The structure of the components and the composition and transition temperatures for nematic Phase V.

EPR experiments were carried out in precision made quartz tubes (i.d. 3mm). The spin probe was first dissolved in dichloromethane and added to the sample tube, the solvent was then removed and then ~50mg of Phase V was added. The sample was heated into the isotropic phase in a vacuum and then degassed, to remove dissolved oxygen, by a repeated freeze-thaw cycle before being sealed under vacuum.

3.6.3 Experimental

A schematic diagram of the experimental set-up used is shown in figure 6. The rotation of the sample was achieved by using a rotary solenoid. Two rotary solenoids were used in this series of experiments, these produced rotation of the drive shaft and sample through fixed angles of 45° and 95°. The EPR tube containing the sample was attached to the drive shaft of the rotary solenoid (RS cat. nos. 439-997 and 440-004) by a pvc sleeve so that the sample tube lay along the axis of the drive shaft. The solenoid was mounted over the poles of the spectrometer magnet so as to position the sample in the centre of the cavity of the spectrometer.

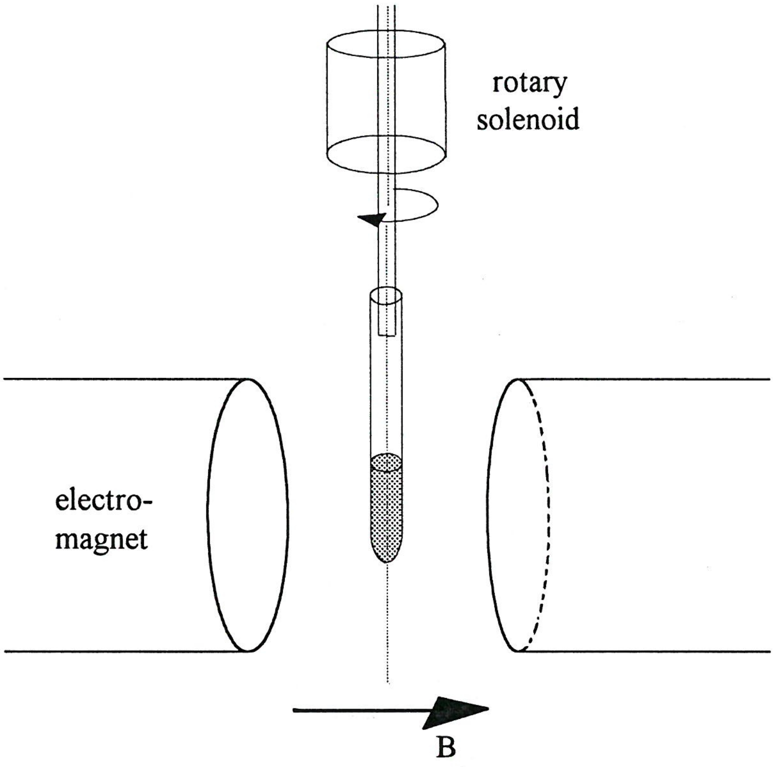

Figure 6 A schematic view of the apparatus used in the rotation-relaxation experiment.

The rotary solenoid of choice for the experiment was powered independently of the spectrometer by its own (home-built) power supply. The switching of the current in either solenoid was controlled by an output from the spectrometer, allowing switching to occur during the acquisition of data. The coil voltage in the rotary solenoids was set to ~6V in the 'current on' position which produced a rotation of the drive shaft and sample tube from the 0° to the 45° position in ~0.03s, the drive shaft subsequently remained in the 45° position while the current was left on. When the solenoid coil current was switched off the solenoid drive shaft was returned to its 0° or 'off' position by the action of a spring attached to the shaft. This return movement took ~0.05s. The Bruker ECS 106 spectrometer fitted with the (rectangular) TE_{102} [19] cavity forms a highly coupled system, as such, rather small differences in the resonance frequency can lead to detuning of the cavity, with concomitant lost of spectral sensitivity. To check that the sample was optimally positioned in the spectrometer cavity, field-sweep spectra were also recorded of the relaxed sample in the 0° and then in the 45° (or 95°) positions. The fact that these two spectra are identical confirms that the sample is optimally positioned and that the sample tube is aligned with the axis of the drive shaft of the solenoid.

For variable temperature work, the Bruker ECS 106 spectrometer cavity is fitted with a quartz jacket which surrounds the sample. The sample is heated by a stream of compressed air (or nitrogen for low temperature work) which blows over a combined heating element and temperature sensor which is positioned just below the sample. This gives a temperature stability of ±0.2°C across the sample at typical working temperatures. Prior to the main rotation-relaxation series of experiments, a series of field-sweep spectra was acquired over a range of temperatures ranging from above the isotropic-nematic transition, through the transition and deep into the nematic phase. A similar set of spectra were again recorded following completion of the whole experiment. These spectra serve as a set of reference spectra and can be checked against the reconstructed spectra built up by the time-sweep method during the rotation-relaxation experiment. Although the latter set show lower resolution along the field axis they serve as a check that the sample had fully relaxed following rotation-relaxation at one field value before the field was increased to a new value and the rotation-relaxation repeated.

The rotation-relaxation experiment was carried out by rotation through an angle ξ_0 of 45° at four different temperatures on nematic Phase V doped with the spin probe cholestane. These were: 73.5, 63.5, 53.5 and 43.5°C. In addition, the rotation-relaxation experiment was later repeated at 43.5°C using the second solenoid which rotates the sample through 95°. The 45° rotation-relaxation experiment was also carried out on the sample of tempone in Phase V at temperatures of 62.5, 53.5 and 42.5°C. At each temperature the sample was left to equilibrate. The range of magnetic fields for which the time-sweep during the rotation-relaxation was acquired were chosen so that just over one-half of the normal field-sweep range is reconstructed, this compromise allows for the hyperfine splitting to be measured but considerably reduces the time required for the experiment at each temperature.

3.6.4 Instrumental Parameters

Some of the spectrometer settings were common to both the field-sweep and time sweep acquisitions, thus the spectrometer operating frequency (~9.38GHz), modulation frequency (100kHz), receiver gain (2×10^4) and microwave power (12mW) were constant throughout. The spectrometer parameters that were varied during the acquisition of spectra for both samples during the initial variable temperature scan and the subsequent rotation-relaxation experiments are listed in Table 3.1.

Table 3.1 The spectrometer parameters used in the acquisition of spectra.

Sample →	cholestane in Phase V		tempone in Phase V	
spectrometer operating mode	field-sweep	time-sweep	field-sweep	time-sweep
modulation amplitude / G	0.55	0.55	0.113	0.127
number of data points acquired	1024	1024	1024	1024
sweep width / G	60	0	60	0
sweep time / s	10.243	2.621 (# 5.243)	20.972	2.621
time constant / ms	20.480	2.560	5.120	10.240
point interval / G	60/1024	0.2	60/1024	0.05

\# - sweep time used in 95° rotation-relaxation experiment
A single time-sweep is recorded at each field value.

After the sample had been equilibrated at each temperature the acquisition of the full field-time data set during the rotation-relaxation experiment was controlled by an automation routine programmed into the spectrometer. In the following protocol the field was stepped through i values, x takes the value 1 to i:

1. Solenoid current off.
2. $t = 0.0$s : commenced time-sweep acquisition at fixed field strength B_x.
3. $t = 0.3$s : driver pulse output from spectrometer switched solenoid current on.
4. $t = 2.621$s : time sweep ends, spectrum written to disk.
5. Switch solenoid current off.
6. Wait 3.0s : set magnetic field to new field strength B_{x+1}.
7. x = x+1, steps 2 to 6 were repeated i times.

In a variant on the above format the time-sweep was also acquired prior to, during, and following the solenoid current being switched off. However the synchronisation of the rotation was poorer in this case and these spectra were not used in the analysis.

3.6.5 Processing of Results

The series of time-sweeps at each temperature were linked in WIN-EPR (the spectrometer analysis software) into a single two-dimensional stack plot in which time forms one dimension and magnetic field strength the other. This presented no problem as the rotations were synchronised to occur at the same time into each time-sweep. The software allows the data to be viewed along either the time or field dimension. The hyperfine splittings were measured from reconstructed spectral slices viewed along the field direction using a 'distance' feature within the WIN-EPR program. A grid was overlaid on the spectrum to aid pinpointing of peak positions. The 'distance' feature gives a readout of the separation between the positions of two cursors which are placed as judged by eye at the peak positions of the low-field and centre peaks of the spectrum of the nitroxide spin probe (A peak-picking routine in the WIN-EPR program which picks the data points closest to the maxima in the integrated spectrum was found to introduce a significant rounding error to measurements of the hyperfine splitting because of the poorer resolution of the reconstructed spectra: 85-200 data points over 34G). In all there are 1024 reconstructed field sweep spectra at each temperature, which represents the full field-time spectrum of the appropriate spin probe over 2.621s; of these, the first 117 slices (0.3s) are of the aligned system prior to rotation and may be used to check the accuracy to which a constant hyperfine splitting can be reproducibly measured using the reconstructed spectra. Thereafter the hyperfine splitting of every tenth slice (0.025s) is measured manually and used to calculate a value for ξ_t from which $\tan\xi_t$ is obtained.

3.7 Results

3.7.1 Cholestane in Phase V

Figure 7 shows a stack plot of the spectrum of cholestane in Phase V recorded as a function of temperature with the spectrometer operating in field-sweep mode.

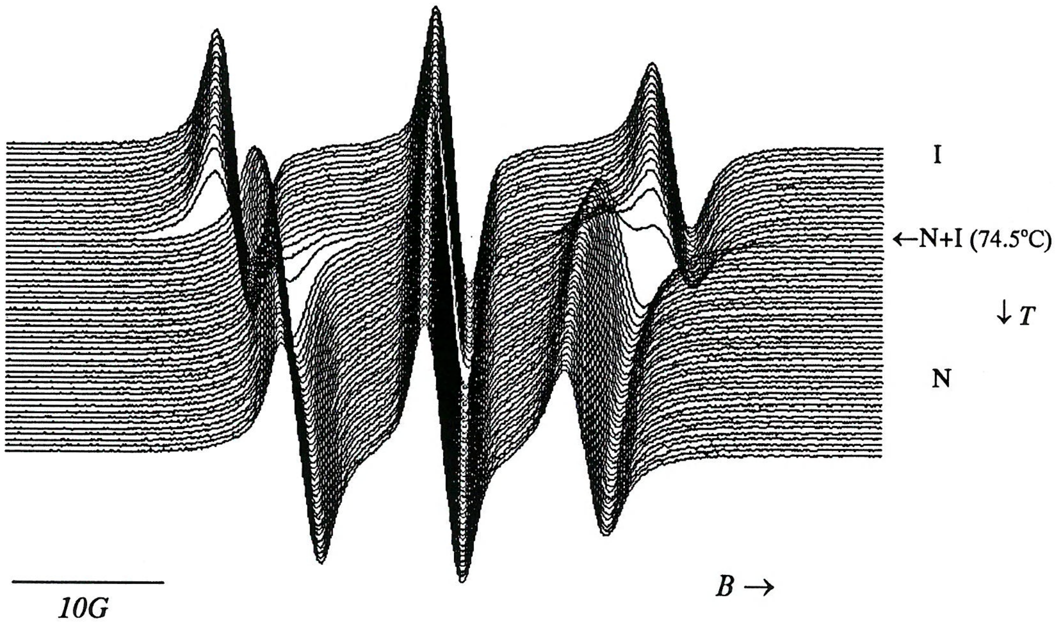

Figure 7 The EPR spectrum of cholestane in Phase V as a function of temperature.

In this case the resolution of field swept spectra along the magnetic field axis is much higher (1024 data points across the 60G spectral width); this enables the peak-picking routine to be used to pinpoint peak positions without introducing any significant rounding error. Using the measured hyperfine splittings $\tilde{A}_{\parallel}$ taken from the spectra in figure 7 the orientational order parameter $\overline{P}_2$ for the cholestane spin probe in Phase V can be calculated as a function of temperature using the relation [17],

$$\overline{P}_2 = -2.(\tilde{A}_{\parallel} - a)/A'_{33} \tag{3.10}$$

in which the value of A'_{33} for the cholestane spin probe is 18.3G (based on the value of A_{33} for the cholestane spin probe dissolved in *ortho*-terphenyl and the isotropic hyperfine splitting a).

Figure 8(a) and (b) show the hyperfine splitting $\tilde{A}_{\parallel}$ and the calculated orientational order parameter $\overline{P}_2$ as a function of temperature for the set of spectra shown in figure 9. Figure 8 shows more clearly than figure 7 that the isotropic-nematic transition temperature of pure Phase V is depressed slightly (~0.5°C) by the presence of the spin probe in the sample and also shows the existence of a narrow biphasic region in the vicinity of the transition. This stems from the presence of the small quantity of the spin probe in the Phase V sample and/or the existence of a small temperature gradient across the sample (see Chapter 1).

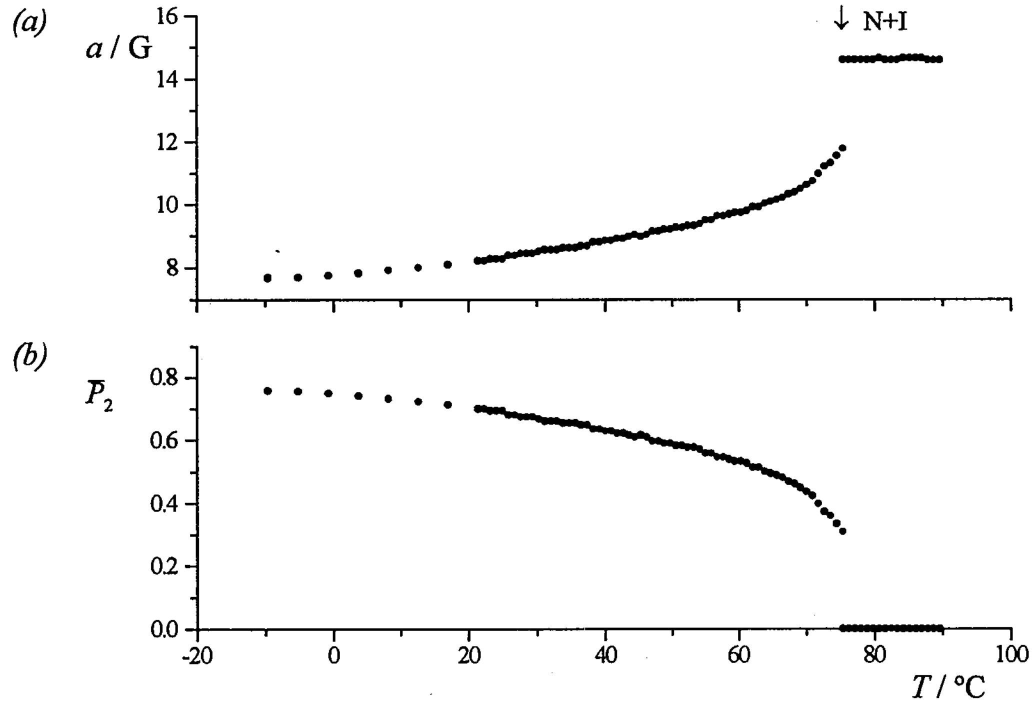

Figure 8 Temperature variation of (a) the hyperfine splitting and (b) the orientational order parameter P_2 for the cholestane spin probe in Phase V.

Turning to the rotation-relaxation experiment, figure 9 shows two typical time-sweep acquisitions that comprise part of the overall two-dimensional field-time spectrum. These examples are taken from the 45° rotation-relaxation experiment at 53.5°C. The triggering of the rotary solenoid by the spectrometer is indicated by a dotted line. Figure 10 shows the complete two-dimensional stack plot for the sample at a temperature of 53.5°C, the resolution along the time axis (1024 points) is clearly greater than along the field axis (85 points). The time axis has been reversed so that the evolution of the spectrum is more easily seen. Figure 11 shows the two-dimensional stack plots for the 45° rotation-relaxation experiment for the sample of cholestane dissolved in Phase V at all four temperatures when transformed and viewed along the magnetic field axis (figure 11d corresponds to the stack plot shown in figure 10). The period of the time-sweep prior to director rotation is clearly visible as is the time taken for the rotation itself to occur. The slower relaxation of the director as the temperature is decreased is clearly obvious.

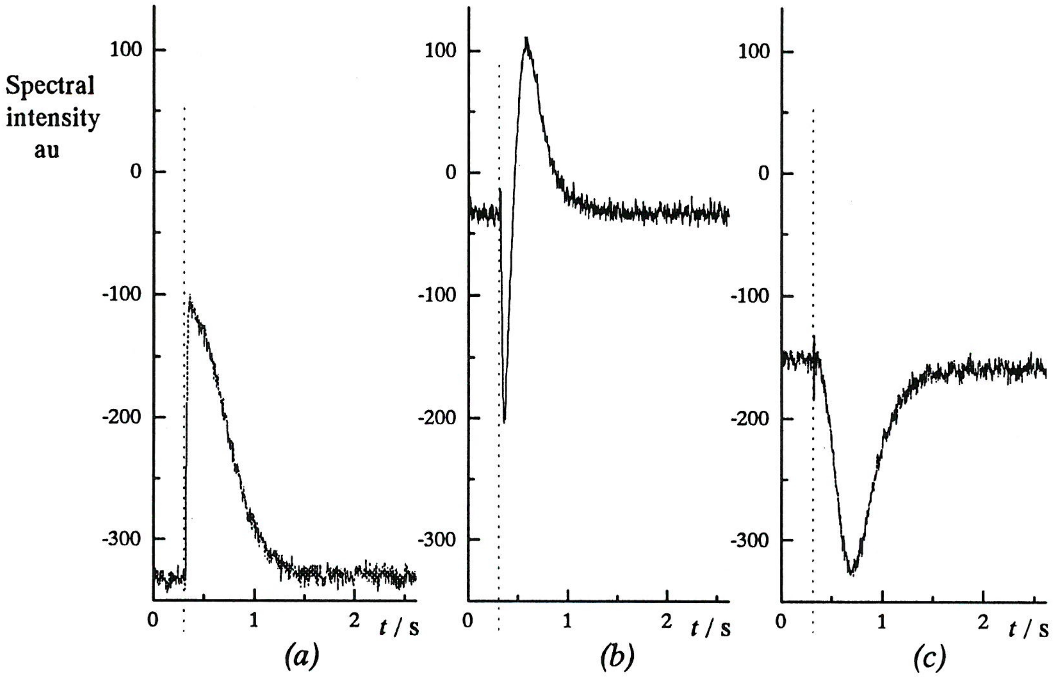

(a) (b) (c)

Figure 9 Typical time-sweep acquisitions for the cholestane spin probe in Phase V at a temperature of 53.5°C: the magnetic field strengths shown are (a) 3331.8G (b) 3335.8G and (c) 3337.8G.

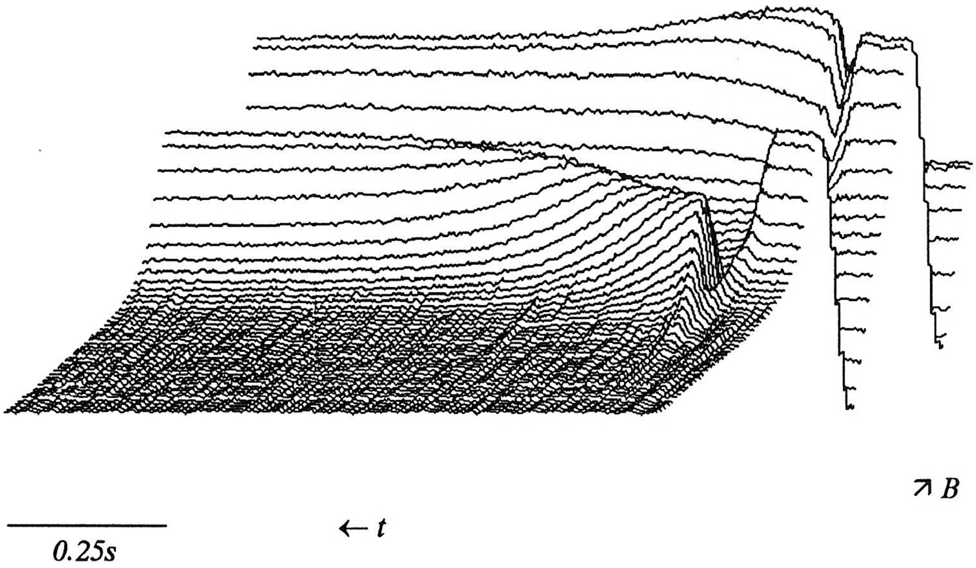

Figure 10 Reconstructed two-dimensional stack plot for the 45° rotation-relaxation experiment for the cholestane spin probe in Phase V at 53.5°C.

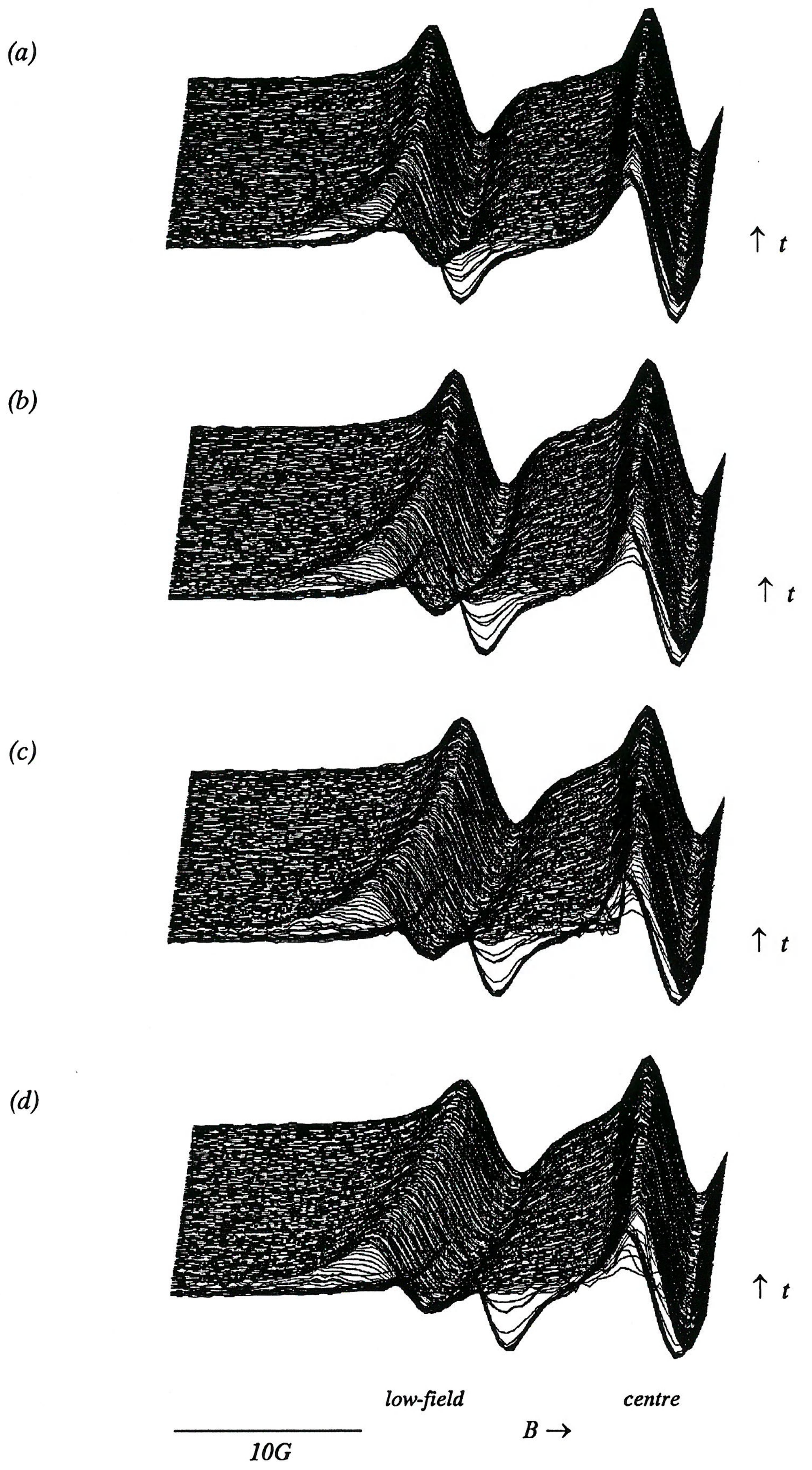

Figure 11 Two-dimensional stack plots for cholestane in Phase V at (a) 73.5°C (b) 63.5°C (c) 53.5°C and (d) 43.5°C.

Figure 12 shows the two-dimensional stack plot for the 95° rotation-relaxation experiment at 43.5°C when expanded and viewed along the reversed time axis and then transformed and viewed along the magnetic field axis. The full spectrum has been reconstructed in this case, showing all three hyperfine lines of the cholestane spin probe.

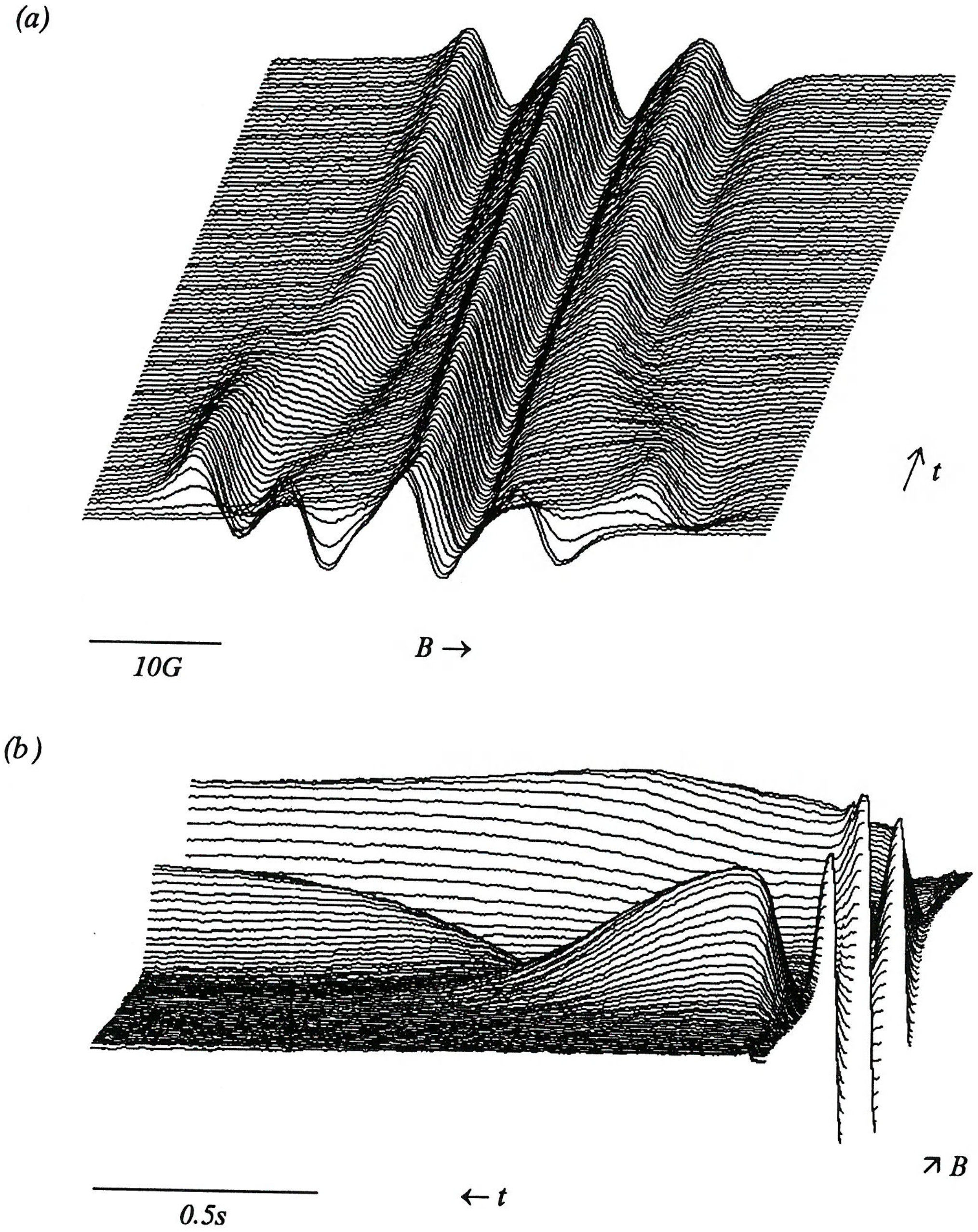

Figure 12 The two-dimensional stack plot for the 95° rotation-relaxation experiment for cholestane in Phase V at 43.5°C looking along (a) the reversed time axis and (b) the magnetic field axis.

The reconstructed field-sweep spectra of the early part of figures 11 and 12 correspond to the unchanging spectrum of the relaxed sample prior to rotation. The antisymmetric lineshapes in both figures indicates fast motion of the spin probe and macroscopic alignment of the director while the measured values of the hyperfine splitting at each temperature indicate that the director lies parallel to the magnetic field. The behaviour of the spectrum at each temperature during the rotation of the sample by the solenoid is discussed in greater detail later. However, the hyperfine splitting and the lineshapes in the spectrum of the sample a short time after the rotation indicate a uniform director lying at an angle of approximately 45° to the magnetic field in figure 11 and approximately 80° in figure 12. This is roughly consistent with the director having been rotated through the same angle as the sample tube. Thereafter, the subsequent evolution of the spectrum was qualitatively different according to the angle through which the sample was rotated: the two cases are shown in figure 13a and b which shows a selection of spectra extracted from figures 11d and 12b at various (non-uniform) intervals during the relaxation phase of the 45° and 95° rotation-relaxation experiments respectively, both at a temperature of 43.5°C. The spectra taken from the 95° experiment have been expanded to show the behaviour of just the low-field and central hyperfine lines to emphasize the contrast with those from the 45° experiment. The hyperfine splitting immediately following rotation of the director is of course different in the two cases, the larger splitting reflecting the larger angle between the director and the magnetic field after rotation to the 95° position, but this is not the central point here, where it is the qualitative differences in the subsequent relaxations that are emphasized. Following a rotation to the 45° position, the two reconstructed hyperfine lines remain but the splitting between them decreases with time until the initial spectrum prior to rotation is recovered. The constancy of the two antisymmetric lines indicates that the director remains uniform throughout the relaxation while the changing hyperfine splitting between them is indicative of the progressive realignment of the director with the magnetic field from the 45° position. The dotted line follows the position of the low-field line during the director reorientation to indicate this. Following rotation to the 95° position, the behaviour of the low-field hyperfine line is very different: no dotted line could be drawn to follow the position of the low-field line at all times during the relaxation process. The loss of the antisymmetric lineshape of the low-field line early in the relaxation indicates the development of a non-uniform distribution of the director within the sample and not solely a changed orientation with respect to the magnetic field. This aspect of the sample behaviour is discussed in greater detail in the discussion section, for now it is noted that the theory underlying the measurement of τ_r and the calculation of the twist viscosity is based upon the assumption that the director remains uniformly aligned within the sample during the relaxation: therefore the results of the 95° rotation-relaxation experiment can not be interpreted using this simple model.

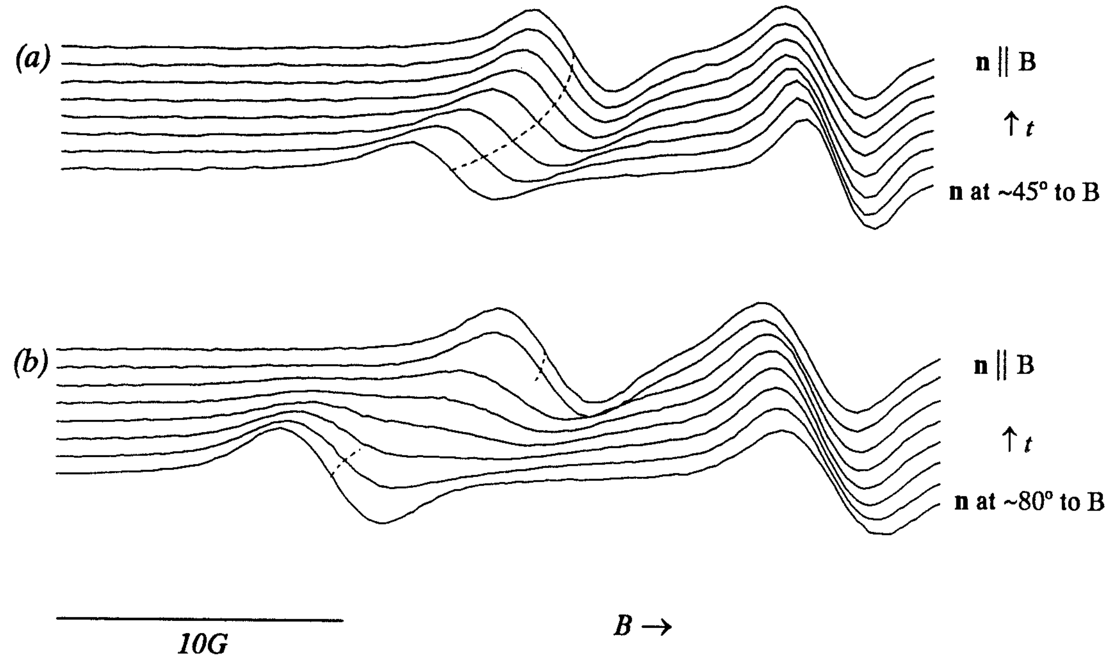

Figure 13 Extracted spectra from the (a) 45° and (b) 95° rotation-relaxation experiments at 43.5°C during the period of director relaxation.

3.7.2 Tempone in Phase V

Figure 14 shows a selection of the set of field-sweep spectra of tempone dissolved in Phase V and figure 15, the temperature variation of the hyperfine splitting and of the orientational order parameter $\overline{P}_2$ for the full set of field-sweep spectra.

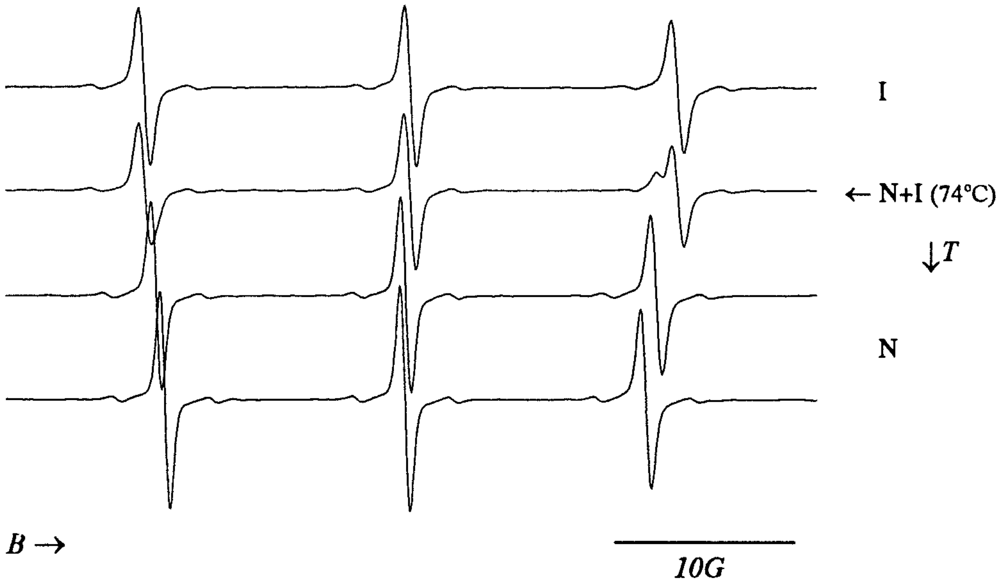

Figure 14 The EPR spectrum of tempone in Phase V as a function of temperature.

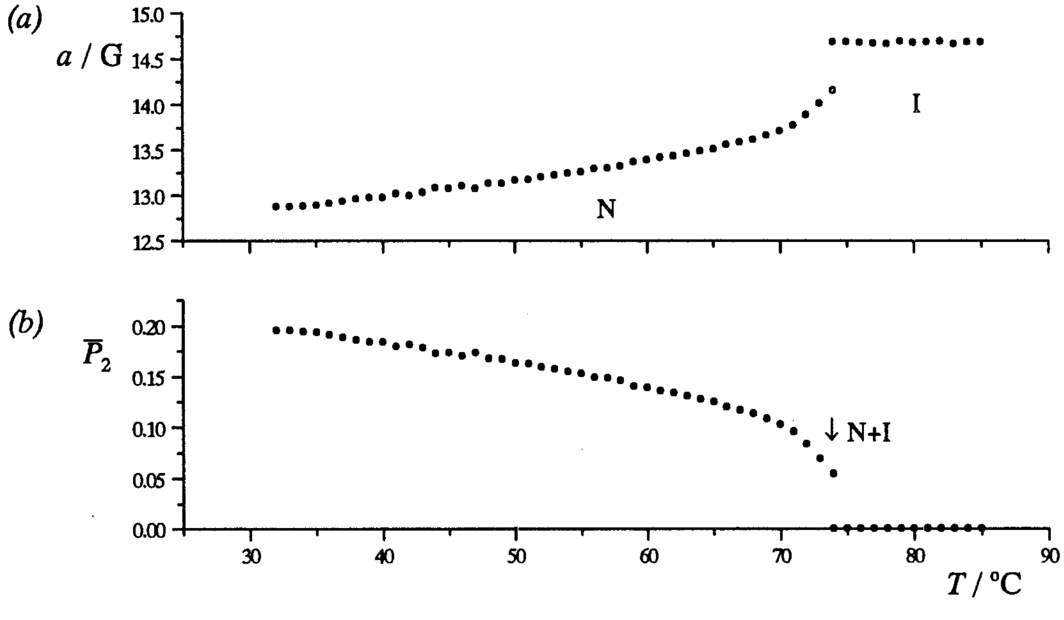

Figure 15 Temperature variation of the (a) hyperfine splitting and (b) order parameter $\overline{P}_2$ for the tempone spin probe in Phase V.

The spectra of tempone in Phase V indicate the same general behaviour of the sample as described in the previous section. Thus, the isotropic-nematic transition temperature is depressed slightly by the presence of the spin probe and a biphasic region in which nematic and isotropic phases coexist is evident in the data shown in figure 15. Subsequently, the hyperfine splitting decreases slowly with temperature as the orientational order of the nematic phase increases. However there are some differences. The principal difference is that the magnetic interactions in the spectra of tempone in nematic Phase V are characterised by a weak anisotropy (most obviously, a smaller difference $\tilde{A}_{\perp}-\tilde{A}_{\parallel}$). This reflects the weaker orientational ordering of the less anisometric tempone spin probe in nematic Phase V as compared with that of the more anisometric cholestane spin probe at a given temperature. The range of hyperfine splittings is therefore narrower for the tempone spin probe than for the cholestane spin probe. The spectra of tempone are also characterised by a narrower linewidth which reflects the very rapid rotational motion of tempone in Phase V. Partly for this reason, some additional hyperfine coupling to ^{13}C nuclei ($I=\frac{1}{2}$) is evident in the appearance of a ^{13}C satellite line either side of the three nitrogen hyperfine lines (these are also prominent because of the chemical structure of tempone, which places six C nuclei in close proximity to the unpaired electron).

The two-dimensional stack plot of figure 16 shows a selection of slices from the field-time spectrum of tempone dissolved in Phase V reconstructed using the 45° rotation-relaxation experiments at 42.5°C. The difference between the spectra during the director rotation and the subsequent relaxation is more difficult to observe qualitatively for the reasons just discussed and for this reason just a selection of the reconstructed field-sweep spectra are shown. The spectra of tempone in Phase V during the rotation-relaxation experiment indicate the same qualitative behaviour of the director as those of the cholestane spin probe in the 45° rotation-relaxation experiment discussed previously; this is seen more clearly in the expansion of the spectrum in the region of the low-field hyperfine line shown in figure 16b. Thus the apparent disadvantages of the weak anisotropy of the magnetic interactions of tempone in Phase V are mitigated by the effects of the narrow linewidths and consequently, we are able to disentangle the components of the changing spectrum during director rotation and relaxation very accurately.

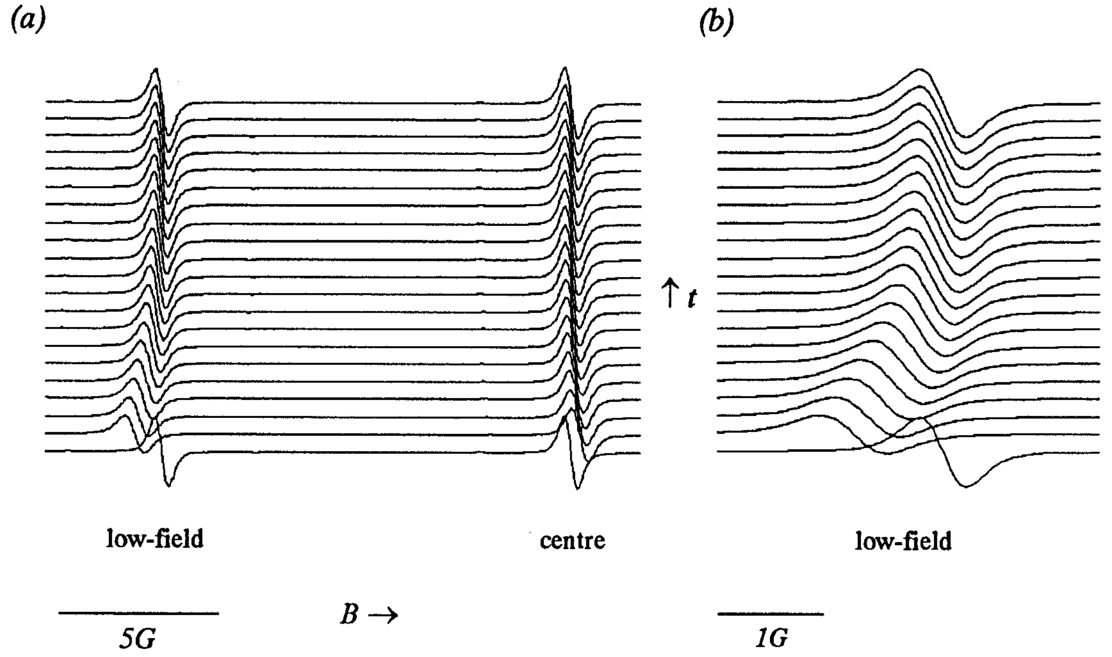

Figure 16(a) A selection of reconstructed field-sweep spectra taken from the two-dimensional stack plot for tempone in Phase V at 42.5°C, the low-field line is expanded in (b).

3.8 Analysis

3.8.1 Calculation of τ_r

The 45° rotation-relaxation experiments which show relaxation with a macroscopically aligned director were used to calculate the time constant τ_r which is proportional to the twist viscosity γ_1. There are two ways in which the changing hyperfine splittings from the spectra in figures 11 and 16 were analysed to obtain τ_r. In the first of these the hyperfine splittings were used to calculate the angle ξ_t between the director and the magnetic field, and then this angle was substituted into a linearized equation 3.10,

$$\ln(\tan \xi_t) = \ln(\tan \xi_0) - t/\tau_r \qquad (3.11)$$

A plot of $\ln(\tan\xi_t)$ at each temperature against time should yield a straight line if equations 3.8 and therefore 3.11 are valid. This line is characterised by a gradient of $-1/\tau_r$ although the intercept on the y-axis does not correspond to $\ln(\tan\xi_0)$ in our experiment because of the delay between the start of the time-sweep and attainment of ξ_0. Additionally, because of the dependence of the hyperfine splitting on the angle ξ_t, small errors (notably rounding errors) distort the straight line at small values of the angle ξ_t, small errors (notably rounding errors) distort the straight line at small values of the angle ξ_t, that is, at longer times t, as $\overline{a}(\xi_t)$ approaches $\tilde{A}_\parallel$. For this reason some of the data points are omitted from the calculation of the gradient and some data points can not be defined (because ln(0) is not defined) on the logarithmic plot. A linear regression was used to calculate the best straight line through the indicated data points. The calculated values of τ_r are shown in Table 3.2. Figure 17 shows the comparison between the experimental data and the fitted straight line for the sample of cholestane dissolved in Phase V. The fitted data closely follows the experimental data in the region in which the spectrum is rapidly evolving, but diverges at longer times due to the propagation of errors in the logarithmic plot. This is emphasized by the error bars shown on several of the data points in figure 17. Table 3.2 also lists the product $\tau_r \overline{P}_2$ which is proportional to the twist viscosity coefficient γ_1, this is discussed later.

Table 3.2 The analysis for the cholestane and tempone spin probes in Phase V.

Spin probe	T / °C	$\tilde{A}_\parallel$ / G	$\tilde{A}_\perp$ / G	$\overline{P}_2$	$(-1/\tau_r)$ / s^{-1}	τ_r / s	$\tau_r \overline{P}_2$ / s
cholestane	73.5	11.2	16.3 †	0.37	-9.55	0.105	0.039
cholestane	63.5	10.0	16.9 †	0.50	-5.85	0.171	0.085
cholestane	53.5	9.45	17.2 †	0.56	-4.24	0.236	0.132
cholestane	43.5	9.0	17.45 †	0.62	-2.92	0.343	0.213
tempone	62.5	13.4	15.3 ‡	0.14	-6.61	0.151	0.021
tempone	53.5	13.2	15.4 ‡	0.16	-4.26	0.235	0.037
tempone	42.5	13.0	15.5 ‡	0.18	-2.85	0.351	0.064

† - calculated using a = 14.6 G for the cholestane spin probe.
‡ - calculated using a = 14.65 G for the tempone spin probe.

The estimated errors (standard deviation) in the calculated values of τ_r are approximately 0.01s at the highest temperature, decreasing to 0.005s at the lowest temperature and do not depend upon the choice of spin probe. It is emphasized that this linear regression necessarily uses only a subset of the total data for the reasons already mentioned.

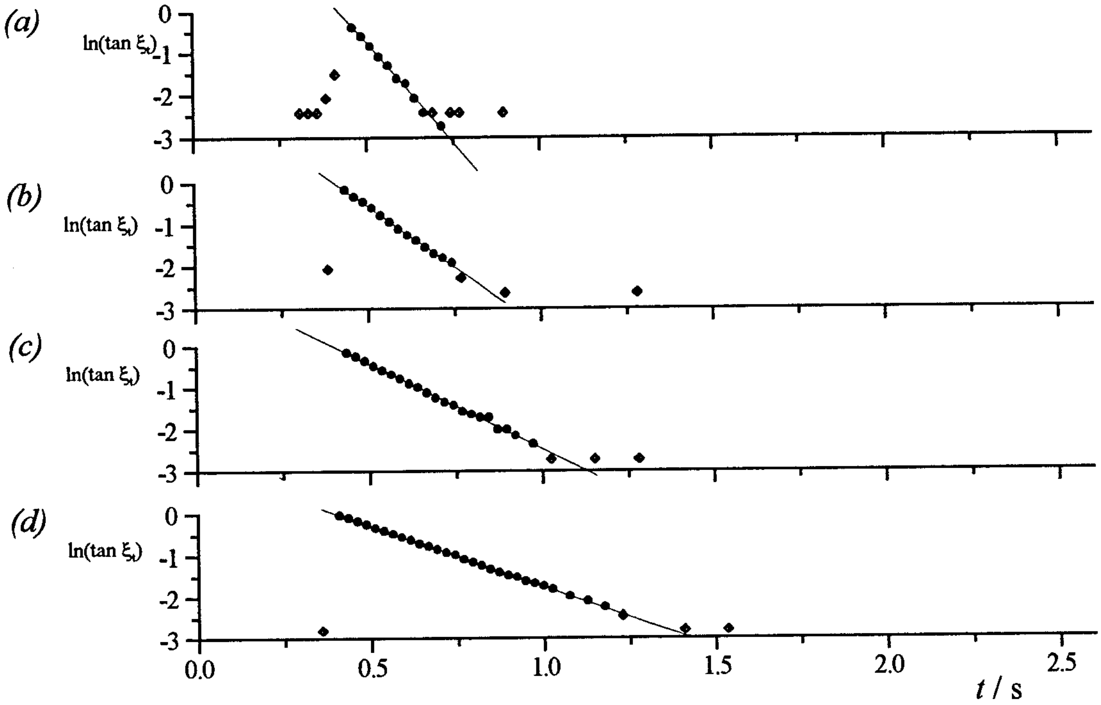

Figure 17 ln(tan ξ_t) *against t for cholestane in Phase V at (a) 73.5°C (b) 63.5°C (c) 53.5°C and (d) 43.5°C.* ◆ *indicates points not used in the fitting process.*

The same spectral data can also be analysed in an alternate manner using the hyperfine splittings directly. Combining equations 3.8 and equation 2.27 (Chapter 2) describing the angular dependence of the hyperfine splitting, we obtain equation 3.12 describing a direct correlation between the observed hyperfine splitting $\bar{a}(\xi_t)$ and the time t following the rotation. This method avoids the problems of the linearized equation in which, as t increases, small errors in the measured hyperfine splitting introduce a disproportionately large error in the fitted straight line. Additionally, the hyperfine splitting is always defined, thus this method avoids the problem of the logarithmic plot on which some points were undefined. This alternative equation is shown below:

$$\bar{a}(\xi_t) = \left(\frac{\tilde{A}_{\parallel}^2 + \tilde{A}_{\perp}^2 . \tan^2\xi_0 . \exp(-2.t/\tau_r)}{1 + \tan^2\xi_0 . \exp(-2.t/\tau_r)} \right)^{½} \qquad (3.12)$$

This assumes that the director begins its relaxation at time 0, however, for fitting purposes this must be modified to take account of the delay between the start of the time sweep and the time by which the director has been rotated to ξ_0. In equation 3.13 this delay is indicated by the time t_0.

$$\bar{a}(\xi_t) = \left(\frac{\tilde{A}_{\parallel}^2 + \tilde{A}_{\perp}^2 . \tan^2\xi_0 . \exp(-2.(t-t_0)/\tau_r)}{1 + \tan^2\xi_0 . \exp(-2.(t-t_0)/\tau_r)}\right)^{1/2} \qquad (3.13)$$

Figure 18 shows the plots of $\bar{a}(\xi_t)$ as a function of time for the cholestane spin probe in Phase V. In each of these figures, the whole duration of the time-sweep is shown, this includes a period of 0.3s before the sample was rotated and the period of approximately 0.1s which the sample director took to rotate. During the period of director rotation no meaningful hyperfine splitting can be measured, as the uniform director alignment is lost before being recovered soon after the rotation. This is considered further in the discussion section.

Equation 3.13 can be fitted using a least squares fitting routine programmed into MicroCal Origin. To fit the data requires that each of the quantities in equation 3.13 except $\bar{a}(\xi_t)$ and t are treated as either parameters to be fitted or constants. $\tilde{A}_{\parallel}$ and $\tilde{A}_{\perp}$ were measured directly and calculated respectively and treated as constants. However, the combination of initial angle of rotation ξ_0 and the corresponding value of t_0 to use is less certain because of the slight loss of coupling between the rotation of the sample tube and of the director: although the sample tube itself was rotated through 45°, the largest measured hyperfine splitting did not correspond to the director having moved through 45°. In the worst case (at the highest temperature) the director was rotated through only 35°, in the best case (at the lowest temperature) the director was rotated through 44°. This was tackled by treating the values of $\tan\xi_0$ and the corresponding time t_0 as constants and assigning values according to the time t corresponding to the maximum measured hyperfine splitting $\bar{a}(\xi_t)$ following sample rotation when the lineshape clearly indicates a uniform director orientation.

The values of the constants and the results of the fitting process using equation 3.13 are shown in Table 3.3. The table also includes, in brackets, the values of τ_r obtained from the earlier linear regression and the value of the product $\tau_r P_2$ discussed later (for tempone, $\tau_r P_2$ has been calculated based on the value of P_2 for the cholestane spin probe at the appropriate temperature, this too is discussed later). The values of τ_r are in good agreement with those calculated in Table 3.2 using the linearized equation. Comparisons between the fitted data and the experimental data for $\bar{a}(\xi_t)$ in figures 18 and 19 show that the fitted data closely reproduces the experimental data at all times following rotation of the director. The estimated errors in the calculated values of τ_r are approximately 0.025s at the highest temperature, decreasing to 0.003s at the lowest temperature.

Table 3.3 Fitting parameters for equation 3.13.

Spin probe	T / °C	$\tilde{A}_\parallel$ / G	$\tilde{A}_\perp$ / G	tan ξ_0	t_0 / s	τ_r / s	(τ_r(l.r.)/ s	$\tau_r \bar{P}_2$ / s
cholestane	73.5	11.2	16.3 †	0.68	0.49	0.11	(0.105)	0.04
cholestane	63.5	10.0	16.9 †	0.85	0.46	0.17	(0.171)	0.085
cholestane	53.5	9.45	17.2 †	0.87	0.44	0.24	(0.236)	0.13
cholestane	43.5	9.0	17.45 †	0.97	0.42	0.343	(0.343)	0.21
tempone	62.5	13.4	15.3 ‡	0.82	0.30	0.16	(0.151)	0.08
tempone	53.5	13.2	15.4 ‡	0.89	0.29	0.238	(0.235)	0.13
tempone	42.5	13.0	15.5 ‡	0.95	0.29	0.353	(0.351)	0.22

† - calculated using a = 14.6 G for the cholestane spin probe.
‡ - calculated using a = 14.65 G for the tempone spin probe.

Equation 3.9 gives the dependence of τ_r on γ_1 and on $\Delta\tilde{\chi}$ for a given magnetic field strength. In this study we use the fact that $\Delta\tilde{\chi}$ scales as the order parameter $\bar{P}_2$ measured for the relevant spin probe in Phase V. Neglecting the small difference in the values of B^2 (~1%) throughout the experiment one obtains $\tau_r \propto \gamma_1 / \bar{P}_2$ and therefore $\gamma_1 \propto \tau_r \bar{P}_2$. The calculated values of $\bar{P}_2$ and the products $\tau_r \bar{P}_2$ have been included in both Tables 3.2 and 3.3 for the purposes of analysing the thermal dependence of γ_1 in the next section. As a final point, but very importantly, it is noted that the values of $\bar{P}_2$ calculated using the hyperfine splittings measured from the reconstructed spectra of the aligned sample are in very good agreement with those values calculated using the hyperfine splittings taken from the reference set of field-sweep spectra. This is important as it establishes that the quality and resolution of the reconstructed spectra is sufficient to allow an accurate determination of the hyperfine splitting.

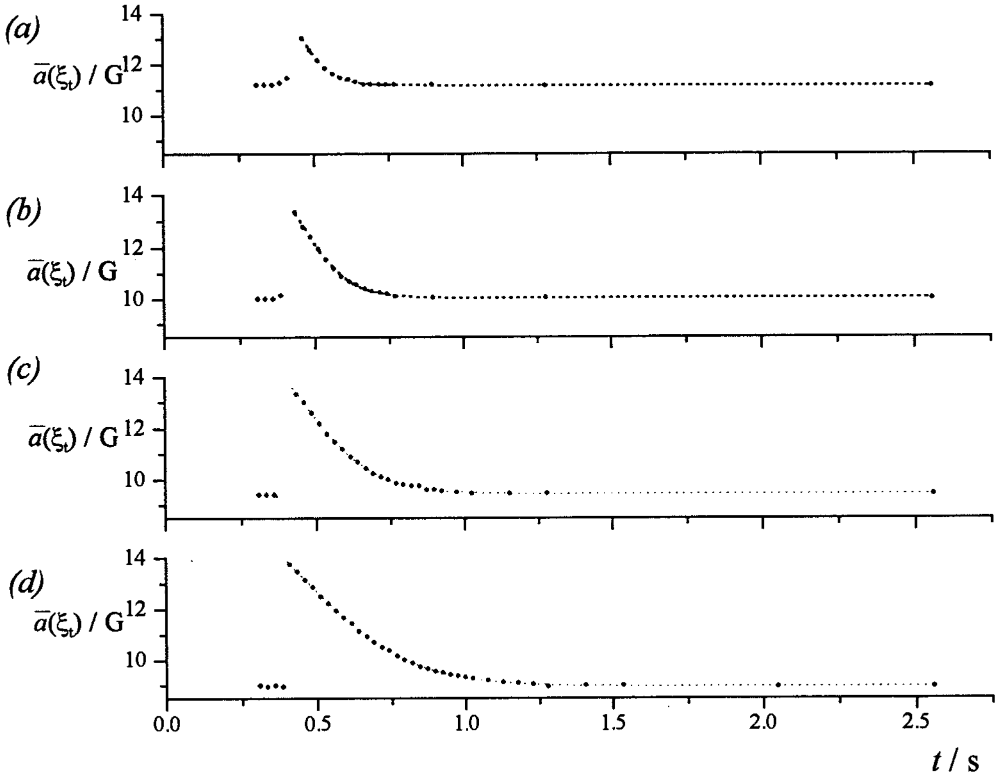

Figure 18 Fitted data, ----, using the experimental data • for $\bar{a}(\xi_t)$ against time for cholestane in Phase V at (a) 73.5°C (b) 63.5°C (c) 53.5°C and (d) 43.5°C. ♦ indicates experimental data points not used in the fitting process.

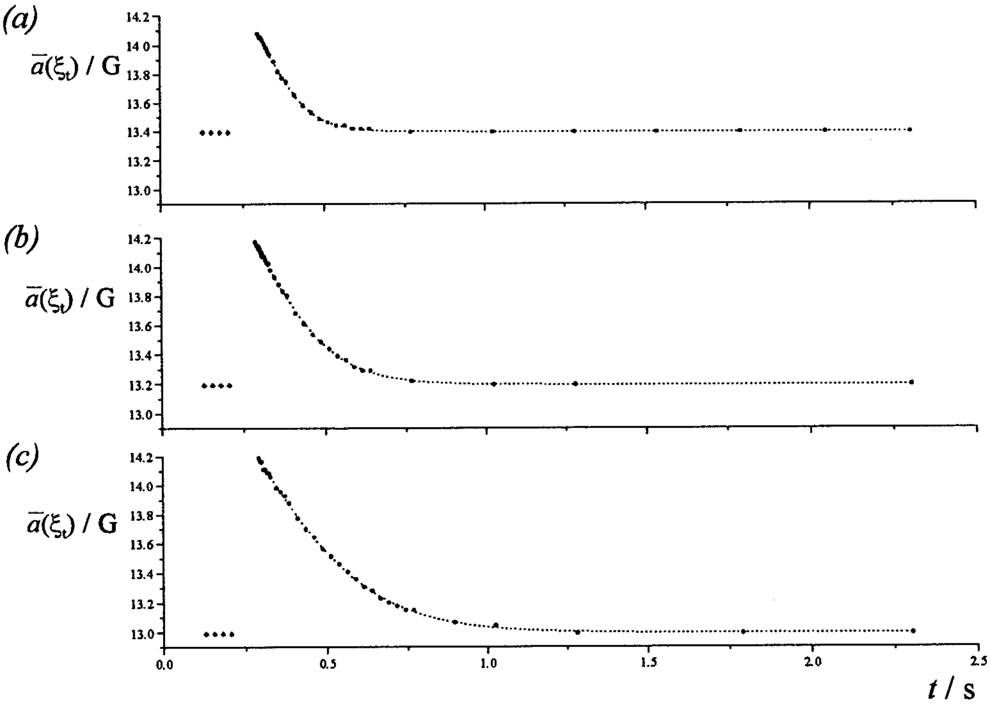

Figure 19 Fitted data ---- using the experimental data • for $\bar{a}(\xi_t)$ against time for tempone in Phase V at (a) 62.5°C (b) 53.5°C and (c) 42.5°C. ♦ indicates experimental data points not used in the fitting process.

3.8.2 Temperature dependence of γ_1 and τ_r

The analysis for the 45° rotation-relaxation experiment can be used to study the temperature dependence of γ_1 and of τ_r. Substituting the twist viscosity γ_1 for the general viscosity η in equation 3.2 we obtain:

$$\gamma_1 \propto (\gamma_1)_0 \exp(E_a/RT) \qquad (3.14)$$

this ignores the dependence of γ_1 on the order parameter of the liquid crystal, which has been the subject of many experimental studies and theoretical treatments but has not been clearly resolved [20, 21]. Equation 3.14 may be linearized,

$$\ln(\gamma_1) = \mathrm{A} \ln(\gamma_1)_0 + E_a/RT \qquad (3.15)$$

in which a number of constants are gathered in the term A. We use the product $\tau_r \overline{P}_2$ to represent the scaled value of the twist viscosity, and should strictly use the value of $\overline{P}_2$ for Phase V, rather than that measured for a spin probe in Phase V which is dependent upon solute-solvent interactions (see Chapter 1, section 1.5). In this analysis we use the value of $\overline{P}_2$ measured, or anticipated, for the cholestane spin probe in the calculation of $\ln(\tau_r \overline{P}_2)$ which is plotted against T^{-1} in figure 20. This is valid as the differences in the constants of proportionality that relate the measured order parameters for the different spin probes to that of Phase V serve only to determine the position of the otherwise separate lines, but do not affect their gradients. This serves the purpose of collapsing the points onto a single line so that points from the two different spin probes can be used in the calculation of the activation energy E_a.

The plot in figure 20 shows evidence of curvature at low values of T^{-1} (that is, close to the nematic-isotropic transition where the orientational order is strongly temperature dependent) as seen previously in a study by Flanders [22] and in other measurements of the viscosity coefficients of mesophases [20]. It is difficult to pinpoint the onset of the curvature with so few points on the graph. However, the upper portion of the graph largely coincides with the linear region of the graph which was used to obtain the activation energy in the study of Flanders. In our calculation, the lowest point is omitted from the calculation of the activation energy as this corresponds to a region in which the plot is not linear. Using the remaining points, we calculate a value of 41.3±1.8kJmol^{-1} for the activation energy of the twist response of Phase V.

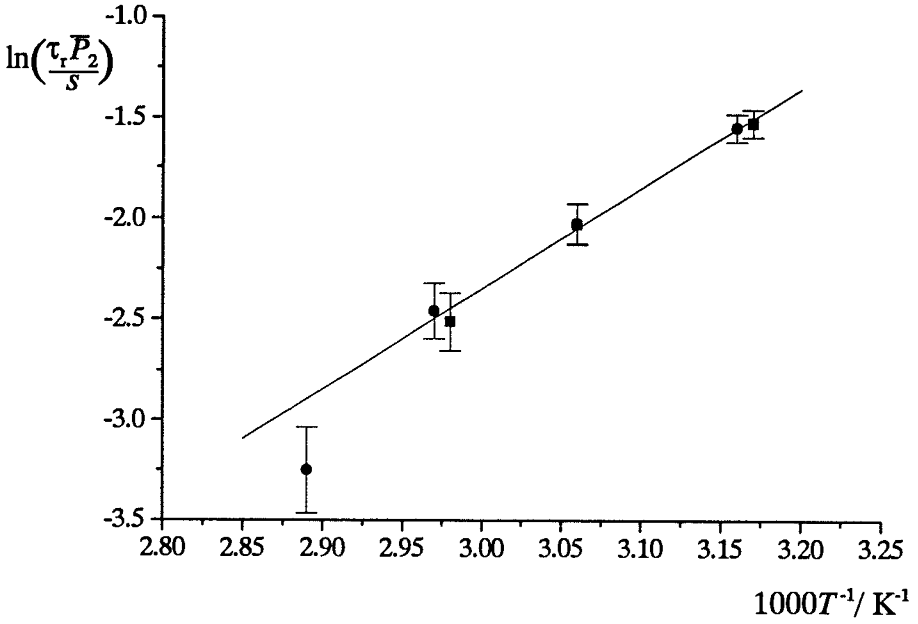

Figure 20 $\ln(\tau_r \overline{P}_2/\mathrm{s})$ *against inverse temperature for Phase V,* ● *and* ■ *indicate data points from the cholestane and tempone experiments respectively, typical error bars are shown on the plot.*

We now consider the behaviour of the time constant τ_r. According to the theory of relaxation processes [3], τ_r is a rate constant which characterises the director reorientation. The temperature dependence of this rate constant can be evaluated by substitution of τ_r for γ_1 in equation 3.14. With this substitution we obtain

$$\tau_r \propto (\tau_r)_0 \exp(E_a/RT) \qquad (3.16)$$

This may also be linearised to give

$$\ln(\tau_r) = A' \ln(\tau_r)_0 + E_a/RT \qquad (3.17)$$

in which a number of constants are gathered in the preexponential term A′.

Figure 21 shows the plot of $\ln(\tau_r)$ against inverse temperature for Phase V. The fact that this plot yields a straight line indicates that the dependence of the relaxation rate constant τ_r (which is proportional to $\gamma_1/\overline{P}_2$) upon temperature is Arrhenius-like, at least in the range of temperatures used in this study and the order parameter of the mesophase at these temperatures. That this plot yields a straight line also indicates that the dependence of the viscosity coefficient γ_1 on temperature and on order parameter is well described by the general form

$$\gamma_1 \propto \overline{P}_2 \exp(E_a/RT) \qquad (3.18)$$

this dependence is one that has previously been observed for some other liquid crystals [5, 9] although our data set does not justify excluding other possibilities. The gradient of this plot is equal to E_a/R and so can be used to calculate the activation energy E_a for the director reorientation in Phase V.

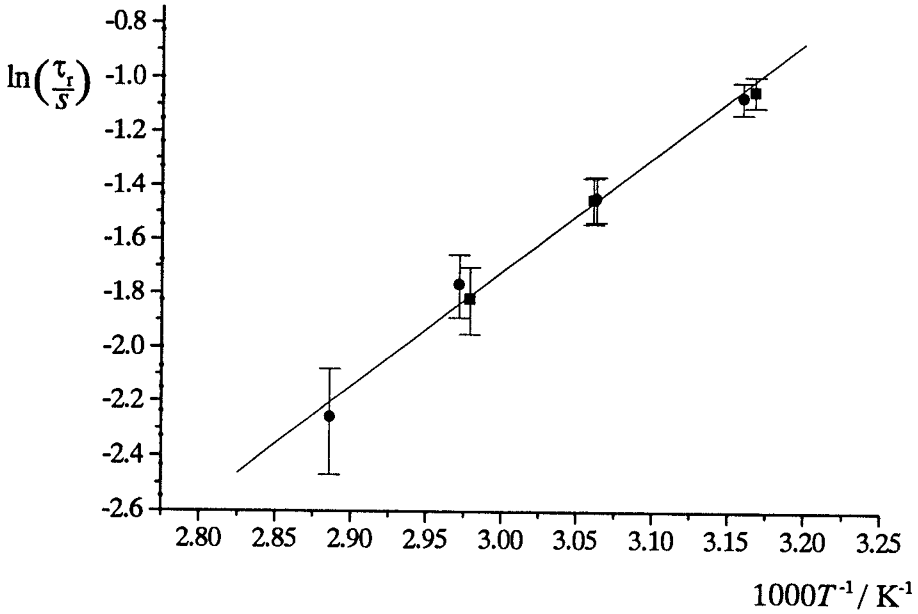

Figure 21 ln (τ_r / s) *against inverse temperature for Phase V,* • *and* ▪ *indicate data points from the cholestane and tempone experiments respectively, typical error bars are shown on the plot.*

The best straight line through the points in figure 21 gives an activation energy of 34.4 ± 1.5kJmol^{-1} for the relaxation response of Phase V assuming Arrhenius behaviour of the relaxation.

3.9 Discussion

By way of introduction to the discussion of the experimental results and their analysis it is first useful to consider briefly the place of the twist viscosity coefficient γ_1 in the overall scheme of the material parameters that characterise the dynamic response of liquid crystals under different conditions. γ_1 is one of six coefficients with the units of viscosity that have been identified for a liquid crystalline material: the four viscosities for a liquid crystal under shear η_1, η_2, η_3 and η_{12} and the two twist (rotational) viscosities γ_1 and γ_2 [5, 10] (in the treatment of Leslie extended by the work of Parodi

[23, 24], these have been identified as having their basis in combinations of six independent underlying material parameters, the Leslie coefficients α_1 to α_6, of which five are independent). Where we are dealing with the reorientation of an aligned director, the time constant τ_r for the relaxation at a given magnetic field strength is defined simply in terms of the twist viscosity coefficient γ_1 and the diamagnetic anisotropy $\Delta\tilde{\chi}$. In contrast, where we are dealing with behaviour of the director that involves the loss of uniform alignment and a distribution of director orientations develop throughout the sample, the treatment required is more complex and involves elastic terms and other viscosity coefficients in addition to γ_1 [13, 14, 15]. Since the EPR spectrum is dependent upon the distribution of the director within the sample with respect to the magnetic field, it reports upon both the orientation of the director and its state of alignment and therefore points directly to which areas of theory should be used for the interpretation of our different experimental observations. This ability of the EPR experiment to detect both the orientation and state of director alignment allows us to easily identify two main areas for discussion. Initially, we focus on the quantitative analysis of the measurements of the magnetic field-induced reorientation of an aligned director of the Phase V sample, that is, on the results of the 45° rotation-relaxation experiments. The second part of the discussion relates to all those occasions on which the EPR experiment revealed that the director was not uniformly aligned across the sample. This was observed during the director relaxation phase of the 95° rotation-relaxation experiment as noted in the results section, and during the pulsed rotation of the director in both the 45° and the 95° experiments prior to observation of the subsequent field-induced director relaxation.

The 'simple' theory which we have outlined which underlies the experiments used to measure γ_1 assumes that the macroscopic alignment of the director within the sample is retained and that it is solely the director orientation with respect to a laboratory axis system that is changed. We now turn to the results of the 45° rotation-relaxation experiment in which this condition is satisfied and consider the relaxation times and activation energy obtained from our experiments on Phase V compared with those of previous studies. The rotating field experiment of Flanders makes use of mechanical torque measurements to determine the director orientation in a sample held stationary and subjected to a rotating magnetic field [22, 25]. Flanders reports an activation energy for the twist viscosity of Phase V of 36.6 kJ mol^{-1} (estimated ±3.5 kJmol^{-1}, actually quoted as $E_a/R = 4.4 \pm 0.5 \times 10^3$ K) calculated using the linear portion of the plot of $\ln(\gamma_1/\rho)$ against T^{-1}. This compares with the value of 41.3 ± 1.8 kJ mol^{-1} calculated from our results using the linear portion of the plot of $\ln(\tau_r \bar{P}_2)$ against T^{-1}. A previous EPR study by McFadden *et al.* using a time-sweep technique followed the director in a similar rotation-relaxation experiment to ours by observing the changing amplitude:linewidth ratio of hyperfine lines of probe molecules dissolved in Phase V [26]. However, the fact that the EPR spectrum was not reconstructed means that we must assume that the changing amplitude:linewidth ratio is due to a change in the director orientation with respect to the magnetic field but does not explicitly exclude the possibility that the changed amplitude:linewidth ratio could be due to a change in the director distribution in which case more complex theory is required. In McFadden's study, relaxation times τ_r falling in the range 2s to 23s were measured over a temperature range -23°C to -3°C (250 to 270K) in which there is little variation of the order parameter. From a plot of $\ln(\tau_r)$ against T^{-1} the activation energy was calculated as 61.6 ± 1.7 kJ mol^{-1} assuming a simple Arrhenius dependence of τ_r on temperature. It was noted briefly that similar measurements above 0°C (273K) yielded an activation energy of 46.1 kJ mol^{-1}, again neglecting the dependence of order parameter on temperature in a regime in which the dependence is stronger. If simple Arrhenius behaviour is assumed, the trend is toward a lower calculated activation energy using higher temperatures. This compares with the activation energy calculated from our experimental results of 34.4 ± 1.5kJmol^{-1} at higher temperatures with relaxation times τ_r in the range 0.1s to 0.35s. It is noted that the experiments of both Flanders and of McFadden are unable to provide any direct evidence that confirms the state of director alignment during their experiments.

All of the experimental measurements of τ_r and of γ_1 fall into one of two categories which illustrate two strategies for obtaining measurements of the twist viscosity coefficient. Firstly, those that study the position of the equilibrium that exists when a sample is subject to one or more external constraints: the position of the equilibrium or the director fluctuations within the equilibrium state depends in part upon the twist viscosity of the liquid crystal. Secondly, those that study the dynamic response to a non-equilibrium state imposed on the liquid crystal by some change in external conditions: the time taken for the response depends in some way upon the twist viscosity of the liquid crystal. The rotating field method used by Flanders and considered in Chapter 5 is one example from the former category while the rotation-relaxation experiment used by McFadden and which we consider in this Chapter falls in the latter category. Within these two categories the orientation or dynamics of the director have been monitored by a wide variety of techniques, for example, optically [27, 28, 29, 30], using light scattering [31], measurements of the reflection of ultrasound [32], by studying the motion of inversion walls [33], mechanical torque measurements [7, 22], magnetic susceptibility measurements [34], dielectric measurements [35], and using magnetic resonance spectroscopies [36, 37, 38, 39]. Some of these techniques detect only the average director orientation while some, notably magnetic resonance, are also sensitive to the director distribution and provide direct experimental confirmation of the state of director alignment.

The agreement between the twist viscosities obtained from many experiments which were collected and reviewed [5] for MBBA is surprisingly good, and was independent of whether the study involved an equilibrium or a dynamic state of the system. The agreement is more dependent upon whether the experiments lead to departures from uniform director alignment, whether this is detected, and therefore whether the correct theoretical models are applied to the interpretation of experimental observations. Experimental techniques for monitoring the director such as EPR which give direct evidence of the state of director alignment are obviously useful as they indicate when certain theoretical models are inappropriate. For example, departures from expected behaviour are seen under certain conditions in rotating field experiments which EPR spectroscopy is able to attribute to breakdown in the uniform alignment of the director [40] but which had not been predicted from the torque balance equations and which is not obvious from mechanical torque measurements.

This brings us to our second major area of discussion which considers those cases in which the director alignment is not uniform across the sample. We discuss first the behaviour of the sample and of the EPR spectrum during the period of director rotation that is used to prepare a macroscopically aligned director lying at an angle ξ_0 to the magnetic field (prior to observing the magnetic field-induced director reorientation which has already been discussed). Figures 22 and 23 show a selection of the reconstructed EPR spectra of cholestane in Phase V during the period (~0.07-0.13s) of director rotation immediately following the rotation of the sample tube through angles of 45° and 95°. At the bottom of each figure the two reconstructed lines of the three-line spectrum of cholestane indicate a monodomain sample with the director lying parallel to the magnetic field before the sample is rotated. Moving up the sequence of spectra in each figure, the spectra show that the macroscopic director alignment is lost immediately following the rotation of the sample tube by the solenoid, but that the bulk of the director is eventually refocused at the same angle to the magnetic field. This is indicated by a return to the two lines of the three-line spectrum shown at the top of each figure in which the different splittings correspond to the different angles between the director and the magnetic field in the two cases. However, the maximum observed hyperfine splitting in each set of spectra does not correspond to the director having been rotated through the same angle (45° or 95°) as the sample tube itself. The maximum angle ξ_0 through which the director rotates when the sample tube is rotated through 45° is 44° at 43.5°C (but is only 35° at 73.5°C) and when rotated through 95° at 43.5°C is only 80°.

The theory surrounding the dynamic behaviour of director distributions is complex and has not been fully developed, and a detailed analysis of these observations during the rotation of the director is beyond the scope of this study. Here we make several remarks and suggestions about the likely course of director rotation given our experimental observations. As a way of introducing an explanation for the behaviour we have described, we consider the behaviour that would be expected if two simple extremal descriptions applied to the sample and director rotation. First, if the mesophase is very viscous, then the sample tube, mesophase and director rotate as a rigid body, and rotation of the sample tube through a particular angle would be reflected by an identical rotation of the macroscopically aligned director with respect to the magnetic field. This would be obvious from looking at the EPR spectrum. Alternately, if the sample has very low values of the viscosity coefficients then rotations of the sample tube and of the director become uncoupled and so rotation of the sample tube would have no effect upon the orientation of the director with respect to the magnetic field. In this case no change would be observed in the EPR spectrum.

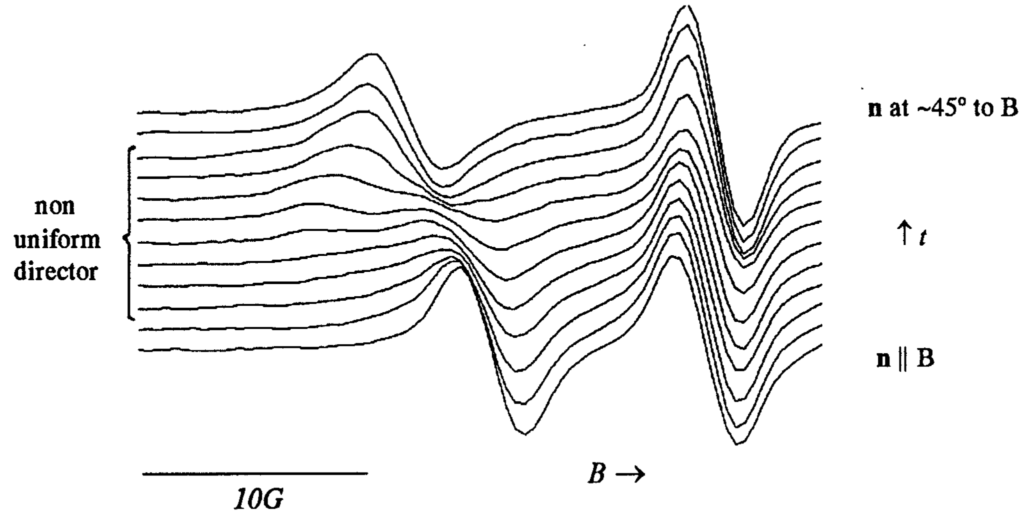

Figure 22 Reconstructed field-sweep slices of the spectrum of cholestane in Phase V at 53.5°C following rotation of the sample through 45°.

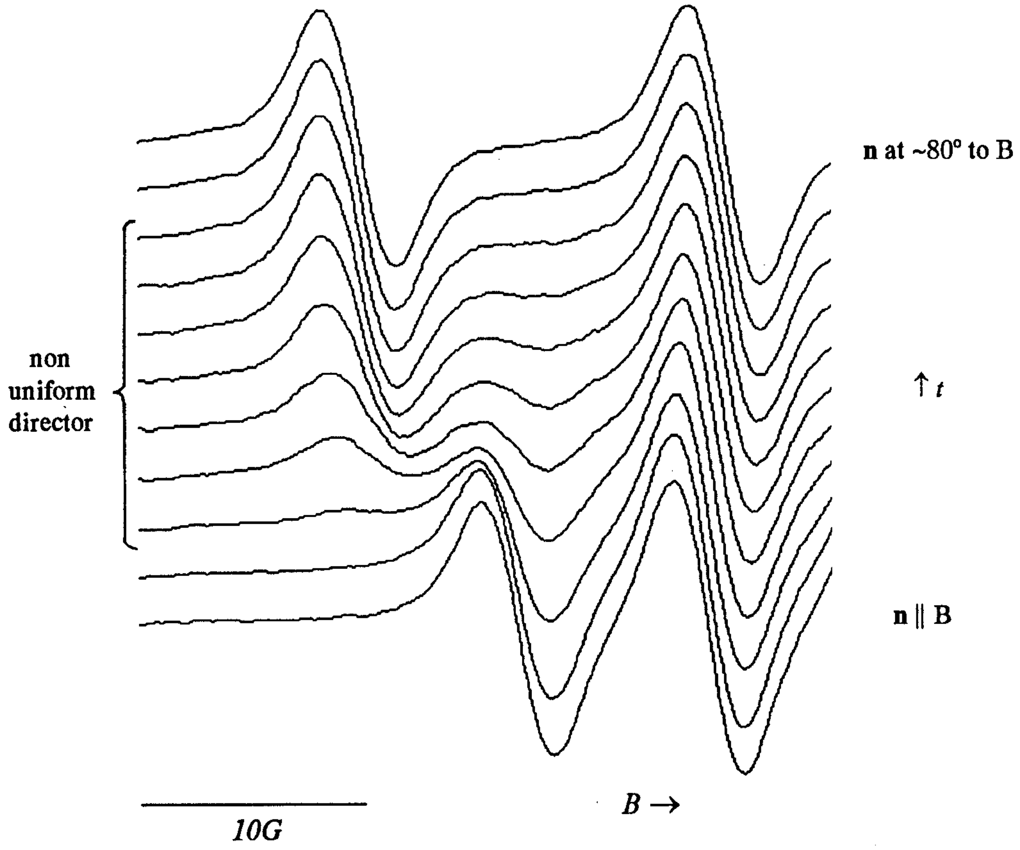

Figure 23 Reconstructed field-sweep slices of the spectrum of cholestane in Phase V at 43.5°C following rotation of the sample through 95°.

The situation we have observed would appear to lie between these two extremes: although the rotation of the sample tube is basically transferred into the rotation of the director, this process is not instantaneous and clearly proceeds *via* a distribution of director orientations. For samples of intermediate viscosity it is envisaged that regions of the nematic phase and the director close to the walls are rotated with the sample tube, but that the nematic phase and the director towards the centre of the tube remain unaffected, at least in the period immediately following rotation of the sample tube. In-between the centre of the sample and the walls of the sample tube there is presumably a continuum of intermediate director orientations between these extremes. This is sketched in figure 24b, which represents the range of director orientations across the circular cross-section of the sample just after rotation of the tube. In this state, there is some shear of the mesophase in going from figure 24a to b and an elastic deformation of the director across the sample tube following rotation (in figure 24b the sample can be imagined to be composed of concentric cylindrical shells, in each shell the director orientation is uniform but is rotated slightly with respect to the director in neighbouring shells). Presumably because of the anchoring of the mesophase to the walls of the sample tube, the most efficient way of relieving the elastic deformation of the director is by a gradual transfer of the orientation of the director close to the walls of the tube to the central part of the sample. This is represented in figure 24c and d before we observe that the director refocuses into a monodomain in figure 24e in which the director has been rotated through approximately the same angle as the sample tube, which is what we observe experimentally. Exactly how this transfer occurs is uncertain but it could again involve rotation of the director coupled with flow (that is, shear) of the mesophase. Throughout this process a magnetic torque acts on all of the director which is not oriented parallel to the magnetic field, this would both retard the transfer of the director orientation from the edges of the sample to the middle of the sample, while at the same time also tending to start the process of the field-induced reorientation of the director close to the walls of the tube. At higher temperatures, all of the viscosity and elasticity coefficients are smaller and so the field-induced reorientation of the director in the outer portion of the sample will be more rapid while the transfer of the director orientation from the outside to the centre of the sample is less efficient. Thus at higher temperatures, we observe that the monodomain refocuses with the director lying at a smaller angle to the magnetic field than the angle through which the sample tube has been rotated.

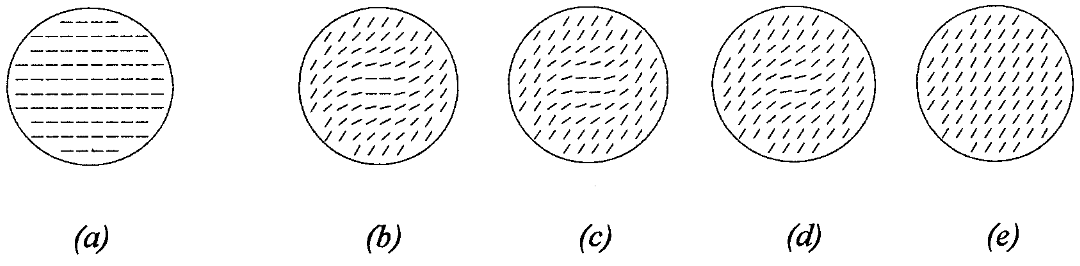

Figure 24 The proposed director distribution across the circular sample cross-section (a) prior to and during rotation of the director (b)-(d) through 45° before the director refocuses at 45° to the magnetic field (e).

The other situation in which we have observed a breakdown in the macroscopic alignment of the director is during the field-induced director relaxation that follows after the director had refocused at an angle of 80° to the magnetic field in the 95° rotation-relaxation experiment. This was highlighted in the results section and in the comparison between figure 13a and b which indicates that the mechanisms of director reorientation are clearly different in the 45° and 95° rotation-relaxation experiments. A detailed analysis of the relaxation that proceeds *via* a non-aligned director has been beyond the scope of this study. Here we summarize the main results to date of work that has looked into this difficult area. Optical experiments on thin cells [16, 29], and experiments that correlate the NMR spectrum of a polymer sample with the optical texture of a section of the sample [14], have shown that the breakdown in the macroscopic director alignment is seen when the field-induced director reorientation occurs through angles of greater than 45°. In such cases, a systematic spatial variation in the director orientation is coupled with translational motion of the particles of the fluid (backflow) which logically must have the effect of lowering the effective viscosity of the sample, at least in the early stages of the relaxation. The director orientation, and in fact the sense of director rotation, varies across the sample normal to the direction of the magnetic field in which the sample is realigning, but is invariant parallel to the magnetic field. The optical texture of the reorienting sample is characterised by a pattern of stripes parallel to the new magnetic field direction. The effective viscosity in this case is given by a different combination of the basic Leslie coefficients which must also involve the shear viscosity coefficients and some aspects of the behaviour must also depend upon elastic terms. As a final note, although this behaviour is qualitatively different from that which we have described during the period of director rotation, the dynamics of both situations are dependent upon many of the same material parameters.

3.10 Conclusions

Using EPR spectroscopy, we have been able to follow the magnetic field-induced reorientation of the director in a low molar mass liquid crystal. Since the EPR experiment is sensitive to the director distribution with respect to the magnetic field of the spectrometer, we are able to determine the degree of director alignment as well as its average orientation with respect to the magnetic field which is important in determining the applicability of theory to the interpretation of sample behaviour. In these experiments we have followed reorientations of the macroscopically aligned director at different temperatures through angles of approximately 45° which are characterised by time constants τ_r in the range 0.1s to 0.35s. The temperature dependence of the time constant τ_r has been considered and has been used to obtain a measure of the twist viscosity coefficient γ_1 and to calculate activation energies for the reorientation response of an aligned director in Phase V which are in reasonable agreement with the results of previous studies. Following rotation of the director through a larger angle, ~80°, the macroscopic alignment of the director is lost during the subsequent magnetic field-induced reorientation. This is consistent with the results of other experiments which show that a coupling occurs between director rotation and a backflow so that a spatial periodicity develops in the director orientation. It has been suggested elsewhere that this lowers the effective viscosity so that the initial director relaxation occurs more rapidly and that this process is most prevalent in those systems, for example, main-chain liquid crystal polymers, in which the shear viscosity coefficients are small in relation to the twist viscosity coefficients.

3.11 Further Work

Further studies could concentrate on a proper quantitative analysis of the director dynamics during the periods in which the director is not uniformly aligned across the sample, with a view to obtaining more detailed information about the viscoelastic behaviour of a range of low molar mass liquid crystals, for which EPR experiments of this type are ideally suited. The results of these experiments could be compared with the equivalent experiments on polymers for which more data already exists. These periods of non-uniform director orientation across the sample include the short period of director rotation following rotation of the sample tube as well as during the field-induced relaxation of the director that follows rotation through large angles. More recent experiments in our laboratory have investigated the behaviour of the director in sample tubes of different diameters [41]. These have shown that the director follows the rotation of the sample tube very closely in sample tubes of small diameter but that a much greater distribution of director orientations follows the rotation of a sample tube of large diameter although the director subsequently refocuses at a single angle to the magnetic field. An imaging experiment similar to that used in Chapter 5 could potentially give a very interesting insight into the coupling between director rotation and, indirectly, the translational motion of the particles of the fluid at all stages of these experiments.

3.12 References

[1] Jakeman, E. and Raynes, E.P., *Physics Lett.* A, **39** 69, 1972,

[2] γ_1 and λ_1 have been used interchangeably in the literature to describe the twist viscosity coefficient, here we use γ_1.

[3] see any standard university physics text, or for example, Atkins, P.W., *Physical Chemistry*, 3rd edition, Oxford University Press, 1987.

[4] Gähwiller, Ch., *Mol. Cryst. Liq. Cryst.*, **20** 301, 1973.

[5] de Jeu, W.H., Chapter 7, *Physical Properties of Liquid Crystalline Materials*, Gordon and Breach, 1980.

[6] Diogo, A.C. and Martins, A.F., *Mol. Cryst. Liq. Cryst.*, **66** 133, 1981.

[7] Dörrer, H., Kneppe, H., Kuss, E. and Schneider, F., *Liq. Crystals.*, **1** 573, 1986.

[8] Kneppe, H., Schneider, F. and Sharma, N.K., *J. Chem. Phys.*, 77 3203, 1982.

[9] Prost, J., Sigaud, G. and Regaya, B., *Le Journal de Physique - Lettres*, **37** L-341, 1976.

[10] de Gennes, P.G., Chapter 5, *The Physics of Liquid Crystals*, Clarendon Press, Oxford, 1974.

[12] Fan, S.M., Luckhurst, G.R. and Picken, S.J., *J. Chem. Phys.*, **101** 3255, 1994.

[13] Martins, A.F., Esnault, P. and Volino, F., *Phys. Rev .Lett.*, **57** 1745, 1986.

[14] Esnault, P., Casquilho, J.P., Volino, F., Martins, A.F. and Blumstein, A., *Liq. Crystals.*, 7 607, 1990.

[15] Casquilho, J.P., Goncalves, L.N. and Martins, A.F., *Liq. Crystals*, **21** 651, 1996.

[16] Lonberg, F., Fraden, S., Hurd, A.J. and Meyer, R.B., *Phys. Rev. Lett.*, **52** 1903, 1984.

[17] Chapter 2, this Thesis, or Luckhurst, G.R., Chapter 7, vol 2, *Liquid Crystals and Plastic Crystals*, eds. G.W.Gray and P.A.Winsor, Ellis Horwood, 1974.

[18] also known by the non-systematic name 3β-DOXYL-5α-cholestane.

[19] Poole, C., *Electron Spin Resonance*, John Wiley Interscience, 1967.

[20] see, for example, refs. 4-9 and refs therein.

[21] for example, Osipov, M.A. and Terentjev, E.M., *Z. Naturforsch.*, **44a** 785, 1989.

[22] Flanders, P.J., *Mol. Cryst. Liq. Cryst.*, **29** 19, 1974.

[23] Parodi, O., *J. Phys.*, **31** 581, 1970.

[24] de Jeu, W.H., *Phys. Lett.*, **69A** 122, 1978.

[25] alternately, in many experiments the sample is rotated in a stationary magnetic field, see Chapter 5.

[26] McFadden, P.N., Shannon, J.M., Bruno, G.V. and Eastman, M.P., *Mol. Cryst. Liq. Cryst.,* **54** 183, 1979.

[27] Kuzma, M.R., *Phys. Rev. Lett.,* **57** 349, 1986.

[28] McClymer, J.P., Labes, M.M. and Kuzma, M.R., *Phys. Rev.* A, **37** 1388, 1988.

[29] Hurd, A.J., Fraden, S., Lonberg, F. and Meyer, R.B., *J. Physique,* **46** 905, 1985.

[30] Wu, S-T. and Wu, C-S., *Phys. Rev.* A, **42** 2219, 1990.

[31] Taratuta, V.G., Hurd, A.J. and Meyer, R.B., *Phys. Rev. Lett.,* **55** 246, 1985.

[32] Martinoty, P. and Candau, S., *Mol. Cryst. Liq. Cryst.,* **14** 243, 1971.

[33] Leger, L., *Solid State Commun.,* **11** 1499, 1972.

[34] Fuhrmann, F., Dries, Th., Fischer, E.W. and Ballauff, M., *J. Pol. Sci.* B, **30** 1199, 1992.

[35] Faetti, S., Gammaitoni, L., Martinelli, M. and Rolla, P.A., *Liq. Crystals.,* **9** 133, 1991.

[36] Wise, R.A., Olah, A. and Doane, J.W., *J. de Physique-Colloque,* **36** C1-117, 1975.

[37] Magnuson, M.L. and Fung, B.M., *J. Chem. Phys.,* **100** 1470, 1994.

[38] Fan, S.M., Luckhurst, G.R. and Picken, S.J., *J. Chem. Phys.,* **101** 3255, 1994.

[39] Ciampi, E., Emsley, J.W., Luckhurst, G.R., Timimi, B.A., Kothe, G. and Tittelbach, M., *J. Chem. Phys.,* **107** 5907, 1997.

[40] Carr, S.G., Luckhurst, G.R., Poupko, R. and Smith, H.J., *Chem. Phys.,* 7 278, 1975.

[41] Ionescu, D. and Luckhurst, G.R., private communication.

Chapter 4

Viscoelastic properties of the nematic phase of an odd and an even liquid crystal dimer measured using an EPR technique

4.1 Introduction

In this Chapter, the method of following the director reorientation using the rotation-relaxation technique developed and tested in the previous Chapter will be applied to measuring the rate of director reorientation in the nematic phase of two members of the series of symmetric liquid crystal dimers, the *α,ω*-bis(4-*n*-alkylanilinebenzylidene--4'-oxy) alkanes **1**, specifically *α,ω*-bis(4-hexylanilinebenzylidene-4'-oxy)nonane and *α,ω*-bis(4-hexylaniline-benzylidene-4'-oxy)decane. These shall hereafter be referred to as the odd dimer and the even dimer respectively or, from the acronym *m*.O*n*O.*m* coined for this series, as 6.O9O.6 and 6.O10O.6. The *m*.O*n*O.*m* series may be considered the dimeric analogues of the *n*O.*m* monomers **2** [1], which have been extensively studied.

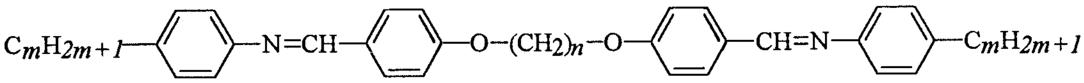

1

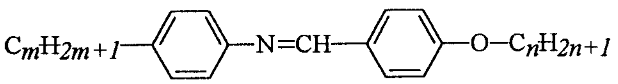

2

A comparison is made between the rate of director reorientation measured for 6.O9O.6 and 6.O10O.6 and that determined for the monomer 4-pentyloxybenzylidene-4'-hexylaniline, 6.O5, which may be thought of as the basic mesogenic building block for these two dimers. The importance and behaviour of liquid crystal dimers is considered in section 4.2. The experimental section 4.3

describes the synthesis of these compounds, the preparation of samples for study by EPR and various aspects of the EPR experiment that is used to obtain the data that is required for a measurement of the director reorientation response from which the twist viscosity coefficient γ_1 is calculated. The more general background to this experiment was previously covered in Chapter 3, sections 3.5 and 3.6. The results of the rotation-relaxation experiments are reviewed and analysed in section 4.4. The discussion of section 4.5 covers the points of comparison between the results in the light of the very different properties for the three compounds tested. Sections 4.6 and 4.7 outline the conclusions of this series of experiments and propose areas for further study.

4.2 Liquid Crystal Dimers

The first dimer liquid crystals were synthesized some 70 years ago by the group of the German chemist Vorlander [2]. In the intervening period there is no published record of their synthesis until 1980 when Griffin *et al.* reported the synthesis of several members of the (symmetric) series of α,ω-bis(4-*n*-alkoxybenzoyloxy-4'-phenoxy)-alkane dimers [3]. Since then, dimeric liquid crystals have attracted renewed interest [4]: initially as a by-product of the drive to produce, understand and use polymeric liquid crystals in technological applications such as data storage but more recently, as their own important and interesting properties have been recognised. Dimeric liquid crystals show elements of the behaviour of both low molar mass and polymeric liquid crystals, thus they have a degree of simplicity that is lost in polymers but possess a chemical link between two mesogenic groups that imposes constraints on their relative orientations which is a feature of polymeric liquid crystals [5]. This gives rise to their interesting combination of properties: they exhibit a wide variety of mesophase types, including some rare phases and some interesting and subtle modifications of more common phases [6, 7] (also see Chapter 6). Their simple molecular structure as compared with those of polymers makes them far more tractable and testable model systems for theorists and theories seeking to explain the underlying reasons for different behaviour. In addition, for good practical reasons, many experiments are more easily carried out on dimers than on polymers. For example, the removal of lower molar mass oligomers to prepare monodisperse polymers for experiment or in manufacturing is often difficult while the presence of such 'impurities' in a sample can have the effect of destabilising or destroying some of the mesophases exhibited by a monodisperse polymer or significantly modifying their properties. Frequently, pure polymers require considerable heating to attain the high temperatures at which mesophases form and, although this is sometimes an essential feature for their application [8], at these higher temperatures there is a greater risk of thermal degradation. This may be overcome by studying the mesophases of a solution of the polymer in a solvent which form at lower temperatures [9]. However, dissolution affects the extent to which polymer-polymer interactions dictate mesophase behaviour and may change molecular properties such as spacer conformations which are often important in determining some aspects of sample behaviour. In comparison, the preparation of dimer samples of high purity is more straightforward: such samples exhibit, for example, sharp transitions and clearly defined phase behaviour at accessible temperatures, which are features of low molar mass mesogens. Consequently, the mesophases of many dimers can be studied as pure thermal systems in which mesophase behaviour is seen as a function of temperature and in which there is less risk of thermal degradation. The development and understanding of structure-property relationships is put on a firmer footing in such cases where there is no interference or attenuation of dimer-dimer interactions by the presence of a solvent. Having outlined the reasons for the study of dimers, we now review some of the properties of dimers relevant to the present investigations using the example of the *m*.O*n*O.*m* series.

The transitional properties and phase behaviour of the *m*.O*n*O.*m* series have previously been the subject of extensive study [6]. General observations about the *m*.O*n*O.*m* dimer series include a rich and varied smectic polymorphism and a universal tendency towards increased stability of smectic phases as the terminal chain length is increased for a given spacer length. The dependence of the transition temperatures and transitional entropies on the parity and length of the spacer group is marked and follows a common trend for dimers ([10], also see section 1.4, Chapter 1). This is evident in figure 1 which shows the transition temperatures and transitional entropies for the homologous series of 6.O*n*O.6 dimers which includes 6.O9O.6 and 6.O10O.6 that are the subject of this study. Thus, there is a pronounced odd-even alternation in the clearing temperatures as the parity of the spacer is altered which is attenuated as the length of the spacer is increased and an odd-even alternation in the entropy changes at the clearing transition which does not attenuate as the spacer length is increased. The dimers with an even spacer have the larger values of both the clearing temperatures and clearing entropies which stems from the more elongated shape and the parallel orientations of the mesogenic groups in the even dimer (see Chapter 1). This is shown in figure 2 in which 6.O9O.6 and 6.O10O.6 are shown in the fully extended all-*trans* conformation of the spacer. The clearing temperatures of all of the 6.O*n*O.6 dimers are considerably higher than those of the 'constituent' monomer 6.O5 which is also shown in figure 2. The entropy changes at the clearing transition for the odd dimers are comparable with those of the *n*.O*m* monomers while those of the even dimers are considerably higher than those of the odd dimers and the monomers. In Chapter 1, this was explained in terms of the many conformations of the even spacer, in addition to the all-*trans* conformation, that are favoured in an anisotropic environment and that preserve the parallelism of the mesogenic groups and therefore maintain high orientational order in the nematic phase. In contrast, there remains a large angle between the mesogenic groups in all but the very high energy conformations of an odd spacer, as in the all-*trans* conformation pictured in figure 2, and so neither the orientational order nor the conformational order is as high as in the mesophase formed by an even dimer. Consequently the entropy change associated with the loss of this weaker order at the clearing transition is far less.

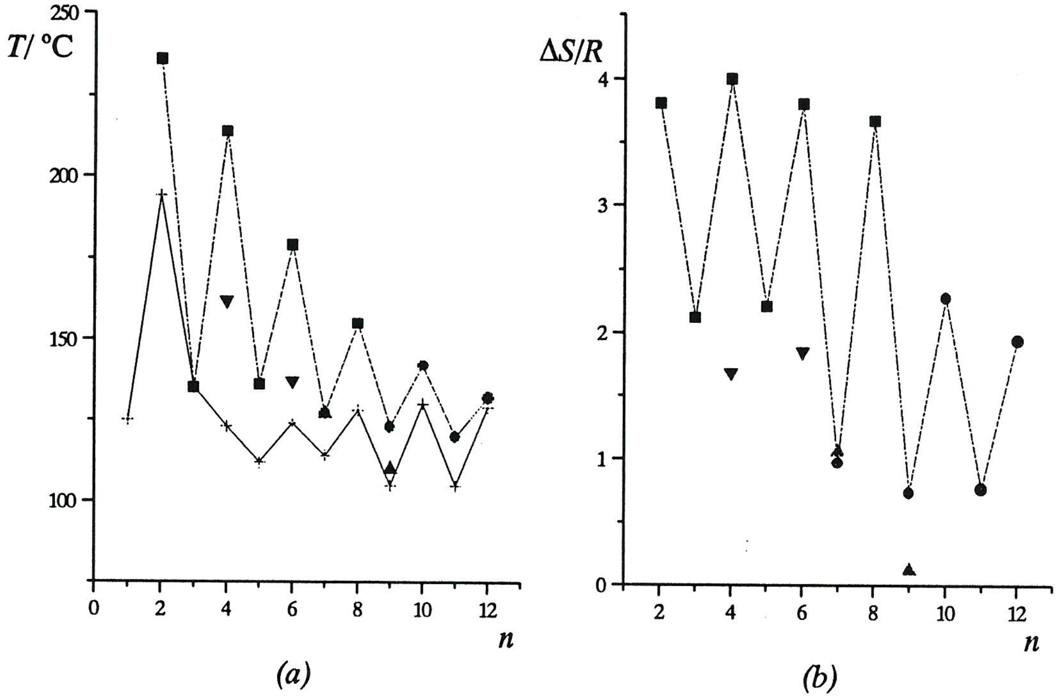

Figure 1 The (a) transition temperatures and (b) transition entropies for the series of 6.OnO.6 dimers. ● = N-I, ■ = SmA-I, ▲ = SmA-N, ▼ = SmF-SmA, + = melting transition. The clearing transitions have been linked on both plots and the melting entropies have been omitted for clarity.

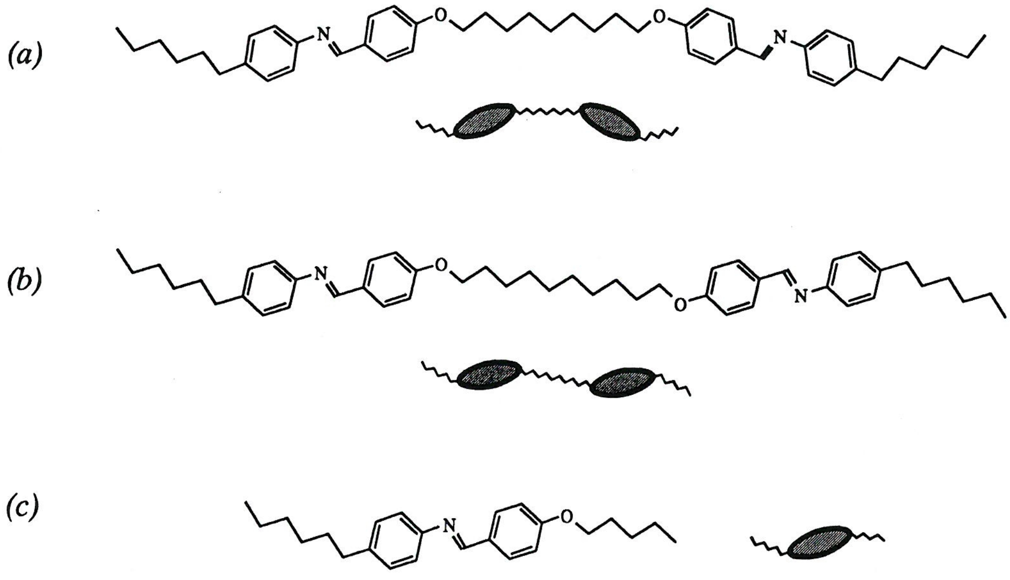

Figure 2 Caricatures of the chemical structure and molecular shape of (a) the odd dimer 6.O9O.6 (b) the even dimer 6.O10O.6 and (c) the monomer 6.O5.

Thus far, the odd-even alternation in the transitional properties of dimers has been explained in terms of the alternation in the orientational order in their respective mesophases. There is one other important difference in the molecular organisation within a nematic phase composed of elongated molecules and one composed of bent molecules that has not been considered explicitly up until now. The suggested molecular organisation within a monodomain nematic phase formed by an odd and an even dimer is sketched in figure 3 [11, 12, 13]. In the nematic phase formed by the even dimer, all of the mesogenic groups tend to align along the director whereas the mesogenic groups tend to be tilted with respect to the director in the nematic phase formed by the odd dimer. This is shown in the different orientations of several elongated solute molecules (such as cholestane) dissolved in the nematic phase which simply reflect the average orientations of the mesogenic groups which surround them. It is convenient to introduce the concept of a local director $\boldsymbol{n}_l$ to describe the different organisations in the two cases. In the even dimer the local director is oriented parallel to the global director $\boldsymbol{n}_G$ throughout the sample. In the odd dimer, the mesogenic groups are *on average* aligned along a direction that defines a global director. However, locally there is some orientational order about a direction which defines $\boldsymbol{n}_l$ which is tilted with respect to $\boldsymbol{n}_G$ by a fixed angle β determined by the bend in the odd dimer, and is tilted in different directions with respect to $\boldsymbol{n}_G$ at different points in the sample. Assuming for the odd dimer, that there is cylindrical symmetry about $\boldsymbol{n}_l$ as there is about $\boldsymbol{n}_G$, then the orientational order of the mesogenic groups about the global director, S_G^{odd} (which is what is measured in an EPR experiment, in this context we use S rather than P_2 for the ease of the notation involving subscripts and superscripts) can be related to the local orientational order, S_l^{odd}, by the simple geometrical relationship,

$$S_G^{\text{odd}} = S_l^{\text{odd}} P_2(\cos\beta) \qquad (4.1)$$

Thus the measured orientational order is less than the local orientational order that exists in the nematic phase formed by the odd dimer. If we also make the more drastic assumption that the local orientational order S_l is identical for the odd and the even dimers (that is, $S_l^{\text{odd}} = S_l^{\text{even}}$) we also obtain,

$$S_G^{\text{odd}} = S_l^{\text{even}} P_2(\cos\beta) \qquad (4.2)$$

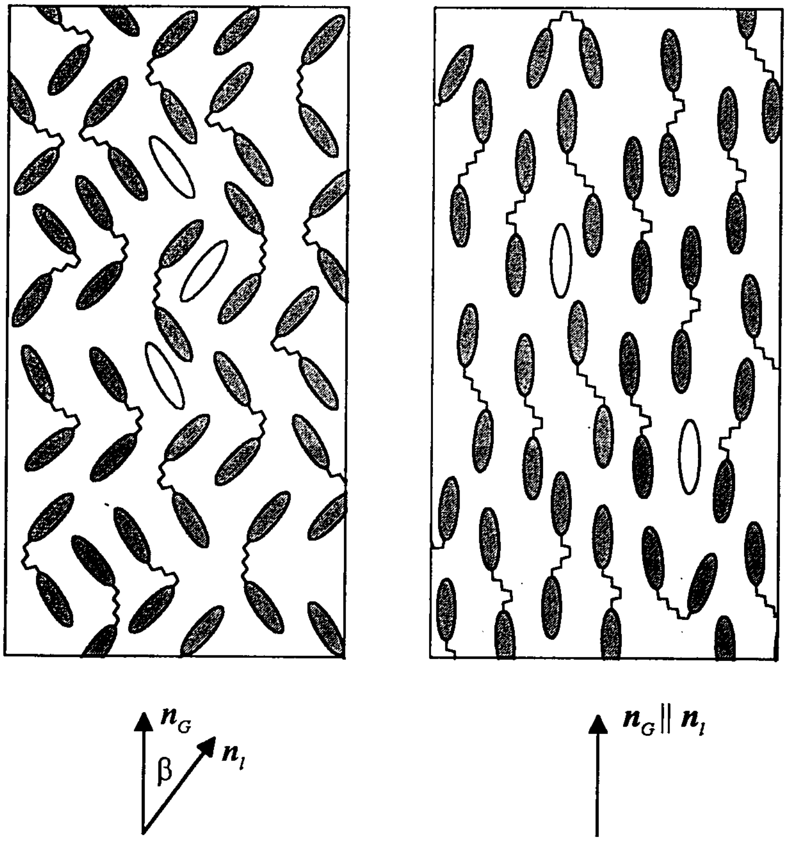

Figure 3 A snapshot in two-dimensions of the different molecular organisations in the nematic phase of (a) an odd and (b) an even dimer. The locations and orientations of several elongated solute molecules are also shown.

This result can be understood in the following way. Part of the reason why the measured orientational order of the odd dimer is lower than for the even dimer is because the local directors are tilted with respect to the global director whereas, in the even dimer, the local director is everywhere parallel to the global director. This model for the nematic phase of liquid crystal dimers suggests subtly different molecular organisations depending upon the parity of the spacer. The even dimers form a true macroscopic monodomain. The odd dimer also forms a macroscopic monodomain with a defined direction for the global director but on an intermediate scale the structure has some similarity to that of a multidomain in that the (local) director orientation varies from point-to-point in the sample. However, this degree of freedom of the local director with respect to the global director is limited to an undefined tilt direction around the global director as the tilt angle β remains fixed (by the molecular geometry). We digress slightly to note that, in some respects, this degree of freedom is similar to that in a smectic C phase in which an external field defines only the orientation of the layer normal but not the tilt direction within a layer. In contrast, the uniform orientation of the local directors in the even dimer is similar to that in a monodomain sample of an orthogonal smectic phase, for example, a smectic A phase. The different degrees of director alignment has a very noticeable effect upon the rates of director reorientation that are observed in smectic phases in certain experimental circumstances (see Chapter 1 and the Discussion, this Chapter), but it is not clear what effect these differences in the molecular organisation of the nematic phase will have on the rates of director reorientation in our experiments.

Thus far we have only considered some of the static and transitional properties of the *m*.O*n*O.*m* series and have noted in particular a pronounced odd-even dependence of these properties upon the parity of the spacer which we have attributed to the differences in the macroscopic orientational order within these systems. Similar trends might be expected in other material parameters and in the dynamic properties of different members of the series. In this Chapter, we measure the relaxation time τ_r for the field-induced director reorientation in the nematic phases of 6.O9O.6 and 6.O10O.6 and of the related monomer 6.O5. Differences in the rate of director reorientation are expected not least because of the dependences of τ_r, considered in the previous Chapter, on the twist viscosity coefficient γ_1, the diamagnetic anisotropy $\Delta\tilde{\chi}$, and on the absolute temperatures which are different for the nematic mesophases of the different compounds for some of the reasons we have already outlined. From the discussion of the previous paragraph, there is also a possibility of a dependence of τ_r upon the different local structures in the nematic phases formed by dimeric liquid crystals that can not apply to monomeric systems. In the discussion of the results from this series of experiments, the different transitional properties have an important bearing on how we compare the results of our measurements for different systems. For now, we turn to the details of the experimental method.

4.3 Experimental

4.3.1 Compound Preparation

These compounds were synthesized according to established procedures and recrystallized from ethyl acetate (EtOAc) [6]. They were analysed by optical microscopy, DSC, IR and NMR prior to sample preparation for EPR and the results found to be consistent with literature values where listed (optical microscopy, DSC) and the structures proposed where full literature details were not available (NMR, IR).

The phase behaviours and transition temperatures of these compounds are as follows:-

6.O9O.6 : $\mathrm{Cr} \overset{105^{\circ}\mathrm{C}}{\text{———}} \mathrm{SmA} \overset{110^{\circ}\mathrm{C}}{\text{———}} \mathrm{N} \overset{123^{\circ}\mathrm{C}}{\text{———}} \mathrm{I}$

6.O10O.6 : $\mathrm{Cr} \overset{130^{\circ}\mathrm{C}}{\text{———}} \mathrm{N} \overset{142^{\circ}\mathrm{C}}{\text{———}} \mathrm{I}$

6.O5 : $\mathrm{SmB} \overset{51^{\circ}\mathrm{C}}{\text{———}} \mathrm{SmC} \overset{53^{\circ}\mathrm{C}}{\text{———}} \mathrm{SmA} \overset{61^{\circ}\mathrm{C}}{\text{———}} \mathrm{N} \overset{73^{\circ}\mathrm{C}}{\text{———}} \mathrm{I}$

Just the higher transition temperatures are recorded here for 6.O5, in the literature [1], two unidentified smectic phases are reported for 6.O5 below the smectic B phase.

4.3.2 Sample Preparation for EPR

Sample preparation was carried out as for the Phase V samples in the previous Chapter. Cholestane (shown in figure 13, Chapter 1), obtained from the manufacturer (Aldrich) and used without further purification, was used as the spin probe in this study. The samples were exhaustively degassed using a freeze-thaw cycle, in particular to remove dissolved paramagnetic oxygen (which contributes to line broadening and may promote sample degradation) and then sealed under vacuum. In particular, careful preparation of samples of the dimers proved to be essential as degradation, indicated by a sample discolouration and a loss of spectral intensity, proved to be more of a problem over the experimental timescales at the elevated temperatures used in this series of experiments as compared with those of the previous Chapter.

4.3.3 EPR

The method of following the director reorientation by EPR following a step rotation of the sample was described in the previous Chapter. The basic requirement is to be able to follow the rate of reorientation of a uniformly aligned director (throughout the sample) into an aligning magnetic field. The 45° rotary solenoid was used in these experiments to rotate the sample and produce a non-equilibrium orientation of the director lying at an angle to the magnetic field. Under these conditions, the rate of the subsequent reorientation of the macroscopically aligned director, characterised by the time constant τ_r, can be simply interpreted in terms of the twist viscosity coefficient γ_1, the anisotropy in the magnetic susceptibility $\Delta\tilde{\chi}$,and the magnetic field strength B, that is, $\tau_r = \gamma_1 \mu_0 / \Delta\tilde{\chi} B^2$ [14].

4.3.4 Instrumental

The experimental setup of the sample tube attached to the 45° rotary solenoid under the control of the Bruker ECS 106 EPR spectrometer and the assembly of the apparatus to control the sample temperature was the same as that used in the previous Chapter. The temperature dependence of the EPR spectrum was first recorded for each sample using the EPR spectrometer operating in field-sweep mode. The temperature range in each case was chosen so as to include several spectra of the sample in the isotropic phase prior to cooling through the isotropic-nematic transition and into the nematic phase. This set of spectra contain information about the variation of the orientational order parameter $\overline{P}_2$ with temperature. They could also be checked against spectra acquired in the field-sweep mode prior to and following the rotation-relaxation experiment at each temperature which served as a check for any sample degradation during the experiment that would lead to a depression of the clearing temperature [15]. The relaxation times of the different samples (being less than ~10s) are such that the evolution of their spectra must again be followed by acquiring the evolution of the EPR signal as a series of time-sweeps at different magnetic field strengths during the rotation-relaxation experiment. Typical parameters appropriate for the cholestane spin probe dissolved in these sytems were used in the acquisition of both the initial set of field-sweep spectra and the time-sweeps (microwave power: 12.6mW, modulation amplitude: 1.01G, time constant: 20.48ms, field sweep acquisition time: 10.486s for 60G sweep, time-sweeps acquired every 0.4G over a 30G range). The width of the spectrum reconstructed using the time-sweep data, when viewed along the field dimension, does not span the full width of the spectrum of the cholestane spin probe that would normally be acquired if the spectrometer was operating in field-sweep mode. The information that we obtain from the spectrum in these studies is essentially the changing hyperfine splitting although we also seek to verify that the macroscopic alignment of the director is maintained during the director relaxation. The minimum information that we need to obtain this measurement and verify this condition is contained in the position of the centre line and the position and lineshape of either the high or low-field hyperfine line. This information is duplicated in the spectrum spanning all three hyperfine lines. To minimise the time that the sample must spend at an elevated temperature just over half of the spectrum is reconstructed. We acquire the portion of the spectrum in the range from the centre line down to the low-field line as the low-field line is narrower and therefore better defined and this allows the evolution of the director orientation to be followed more accurately (It is noted that this is actually more of a problem when studying other more viscous systems in which the high-field line may be substantially broader than the low-field line).

4.4 Results

Figure 4 shows the variation with temperature of the spectrum, acquired in the field-sweep mode, of cholestane dissolved in the odd dimer, the even dimer and the monomer, that is, in the compounds 6.O9O.6, 6.O10O.6 and 6.O5 respectively. The temperature variation of the order parameter $\overline{P}_2$ for the long axis of the spin probe is calculated from the observed hyperfine splitting using relation 2.21 substituting the relevant values for the isotropic hyperfine splitting for the cholestane spin probe dissolved in these three samples, which are: 14.8, 14.7 and 14.6G. The anisotropic portion of the total hyperfine tensor A'_{33} is calculated from the measured isotropic hyperfine splitting together with the measured value of A_{33} for a sample of the cholestane spin probe dissolved in a glass *of ortho*-terphenyl.

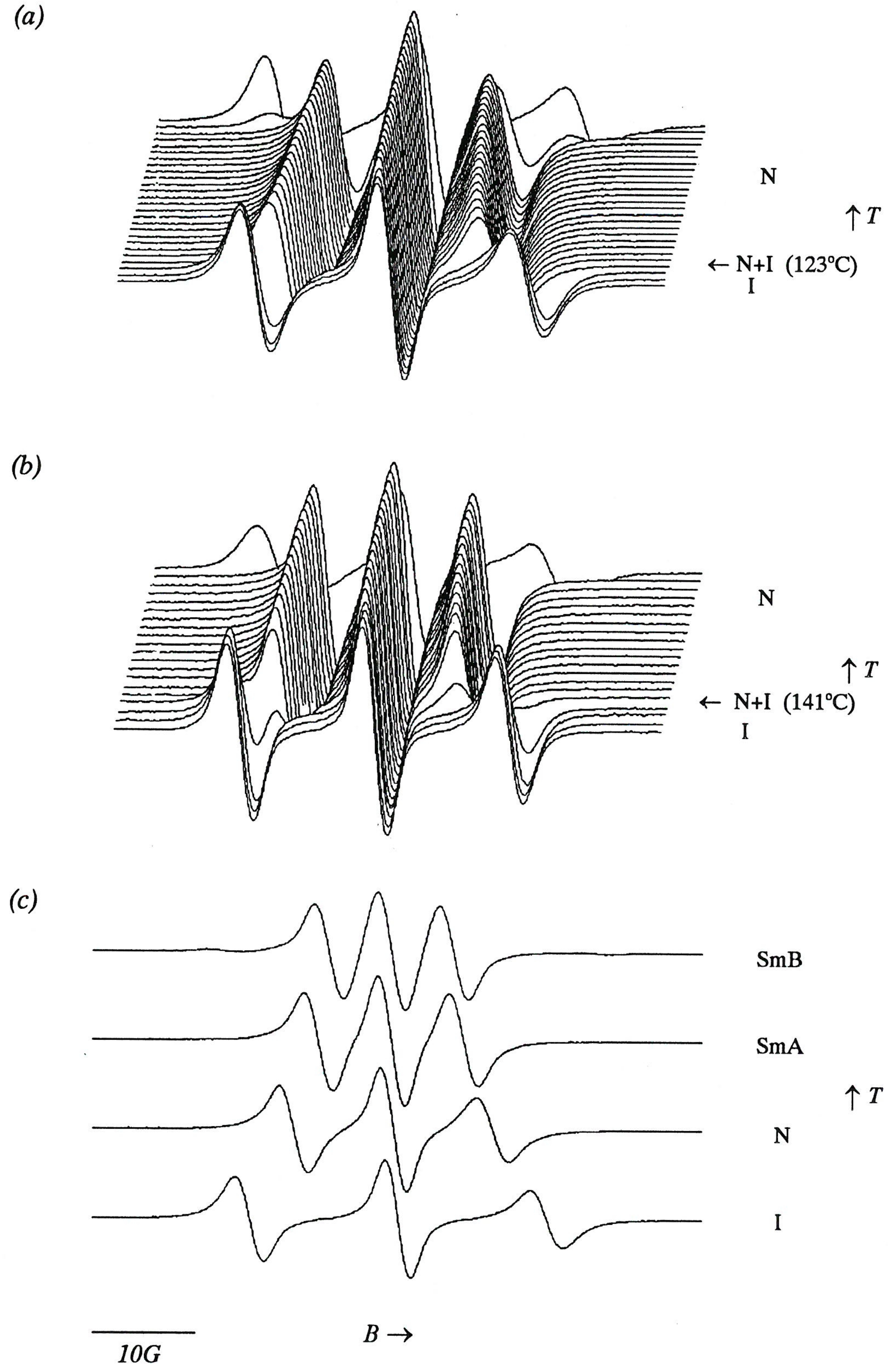

Figure 4. The spectrum of cholestane in (a) 6.O9O.6, (b) 6.O10O.6 and (c) 6.O5 as a function of temperature.

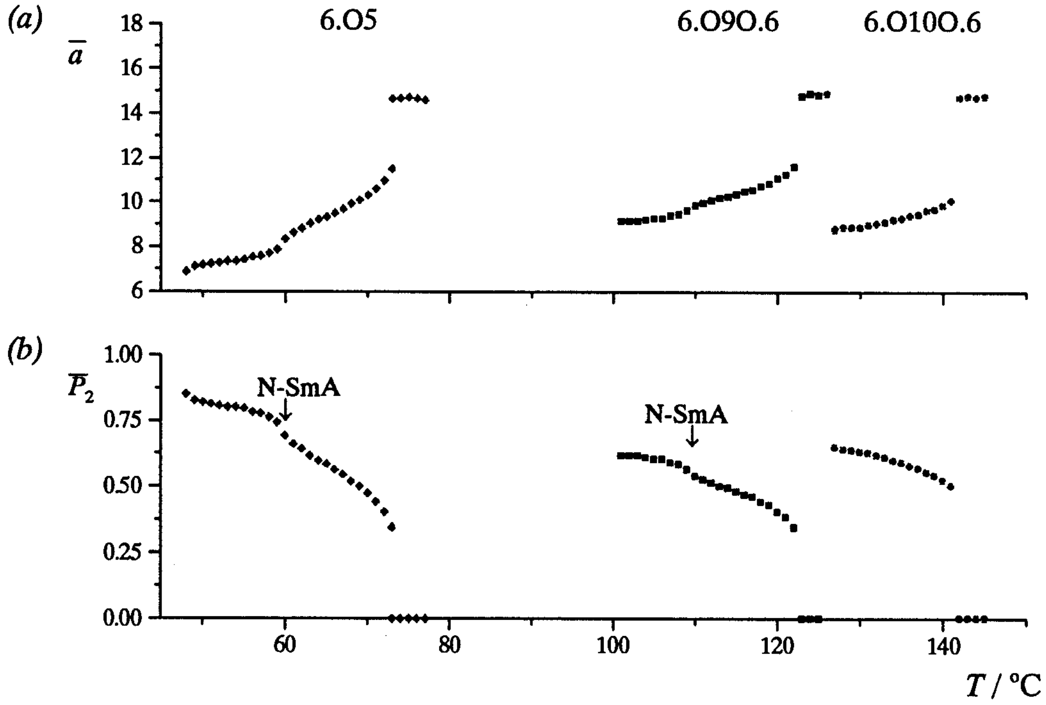

Figure 5. The variation of (a) the hyperfine splitting and (b) the order parameter $\overline{P}_2$ as a function of temperature for cholestane in 6.O9O.6, 6.O10O.6 and 6.O5.

We shall first describe the temperature dependence of the spectrum of cholestane in the even dimer. Upon cooling, the spectrum of cholestane in 6.O10O.6 in figure 4b shows a dramatic change in the hyperfine splitting at the nematic-isotropic transition, this is clearly seen in the plot of figure 5. A similarly dramatic change in the orientational order parameter $\overline{P}_2$ for the spin probe dissolved in the mesogen is consistent with the large entropy change associated with this transition ($\Delta S/R$=2.28). Upon subsequently decreasing the temperature of the mesophase, the hyperfine splitting decreases gradually and this reflects a gradual increase in the orientational ordering of the spin probe in the mesophase and of the mesophase itself. The spectrum of cholestane in the isotropic sample and in the nematic phase shows three well-separated hyperfine lines with an antisymmetric lineshape which is indicative of fast rotational motion of the spin probe (and of the dimer molecules themselves) at the temperatures at which the isotropic phase and the nematic phase exist. The spectrum then changes abruptly as the sample crystallised and takes on a form rather like the isotropic spectrum, except that now the lines are much broader and the antisymmetric lineshape of the outer lines is lost. This indicates that the spin probe is still mobile in the crystal.

The spectrum of cholestane in 6.O9O.6 also shows a dramatic change in the hyperfine splitting and of the calculated orientational order parameter at the nematic-isotropic transition calculated using the sequence of spectra shown in figure 4a. However the decrease in the hyperfine splitting and the jump in the orientational order parameter at this transition was less than that observed for the even dimer, as is clear from figure 5. This is consistent with the lower entropy change that occurs at the nematic-isotropic transition for the odd dimer for the reasons outlined in section 4.2 ($\Delta S/R$=0.74). There is subsequently a stronger temperature dependence of the (decreasing) hyperfine splitting and the (increasing) order parameter as the temperature of the nematic phase was decreased. 6.O9O.6 also exhibits a smectic A phase below the nematic phase. The transition to the smectic A phase was accompanied by another small decrease in the hyperfine splitting consistent with the smaller entropy change at this transition ($\Delta S/R$=0.12) as expected for a compound that possesses a reasonably long (13°C) nematic range. This is indicated in figure 4b and figure 5.

In comparing figures 4a and 4b, the spectra of the even dimer are indicative of a large increase in the orientational order at the nematic-isotropic transition and then a rather weak dependence on temperature of the orientational order on further reducing the temperature. In contrast, the spectra of the odd dimer show a lesser jump at the onset of orientational order at the nematic-isotropic transition but thereafter a stronger dependence of the orientational order as the temperature of the mesophase is decreased. It is noted that the measured orientational order of the odd dimer is never as high as that of the even dimer, even after a substantial decrease in the temperature of the mesophase. These observations are consistent with the arguments outlined in section 4.2 and Chapter 1. The temperature variation of the spectrum of cholestane dissolved in 6.O5 is shown in figure 4c. The temperature range of these spectra indicate the lower transition temperatures for the monomer in relation to those of the dimers. This fits with the universal trend that the transition temperatures of monomers are observed to be lower than those of the dimers for a given mesogenic group. The similar linewidths observed for the spin probe in the monomer to those observed for the spin probe dissolved in the dimers indicate that this system too is in the fast motion limit. The orientational order parameter P_2 for cholestane in the nematic phase of 6.O5 varies between that observed for the odd dimer at low values of the shifted temperature $T_{NI}-T$ and the even dimer at higher values of the shifted temperature. Thereafter, there is an almost linear dependence of the orientational order parameter on temperature in the smectic A phase formed below the nematic phase. At lower temperatures, 6.O5 forms a very highly ordered smectic B phase. The small separation of the inner pair of lines $\tilde{A}_{\parallel}$ in this five-line spectrum is indicative of high orientational order in the smectic layers, whilst the larger splitting $\tilde{A}_{\perp}$ between the weaker outer features come from some of the spin probe which has been expelled from the smectic layers, and lies with its long axis perpendicular to the layer normal and the magnetic field.

Having considered the temperature dependence of the spectra of the different samples we now turn to their behaviour in the rotation-relaxation experiment. The Bruker WIN-EPR software was used to combine and manipulate the time-sweep acquisitions. The three-dimensional plot of spectral intensity as a function of magnetic field and of time can be manipulated so as to view either individual time sweeps, the reconstructed (field-sweep) spectrum at a particular instant or in a stack plot which shows the evolution of the field-sweep spectrum. The temporal evolution of the partially reconstructed spectra of the cholestane spin probe dissolved in 6.O9O.6 at temperatures of 121°C and 116°C is shown in figure 6. Those for cholestane in the even dimer, 6.O10O.6, at temperatures of 139°C and 129°C are shown in figure 7. Figure 8 shows the equivalent spectra for cholestane in 6.O5 at 69°C.

The inferences about the director orientation and distribution that can be drawn using the two reconstructed hyperfine lines are identical to those that can be drawn if all three hyperfine lines had been measured. The aim of this section is to describe the behaviour of the director in the sample unambiguously, and to show how this is inferred from the changes in the spectra that we have observed.

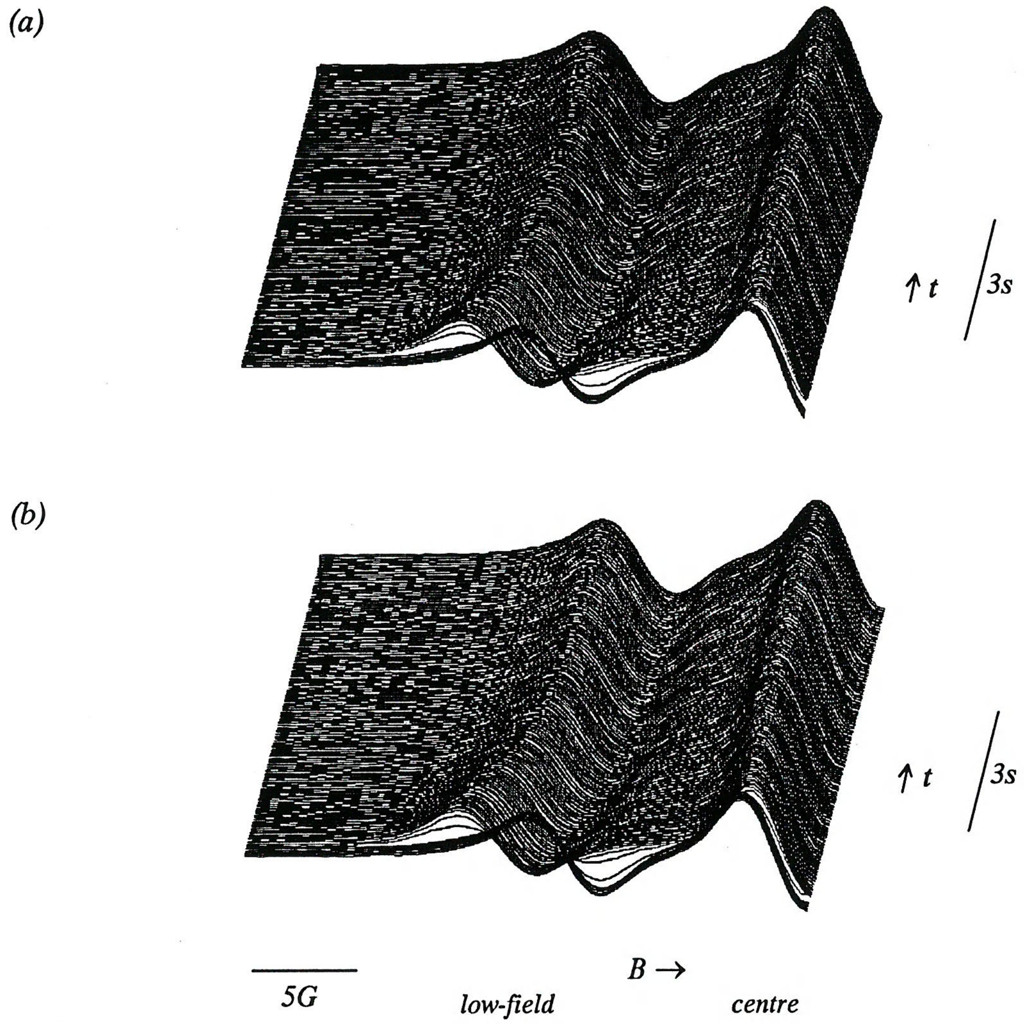

Figure 6 The temporal evolution of the partial spectrum of cholestane in 6.O9O.6 at (a) 121°C and (b) 116°C during the 45° rotation-relaxation experiment

The qualitative behaviour of the spectrum is the same for all of the samples and at any temperature. Specifically, prior to sample rotation, the two lines of the partially-reconstructed spectrum separated by a hyperfine splitting of $\tilde{A}_{\parallel}$ indicate that there is a uniform alignment of the director parallel to the magnetic field throughout the sample. Following the rotation of the sample tube through 45° by the rotary solenoid triggered 0.50s into each of the time-sweep acquisitions, the uniform alignment of the director is lost between 0.52s and 0.60s which is indicated most obviously by the splitting of the low-field line. This line is split by the anisotropy in the hyperfine interaction and, to a much smaller extent, by the small anisotropy in the

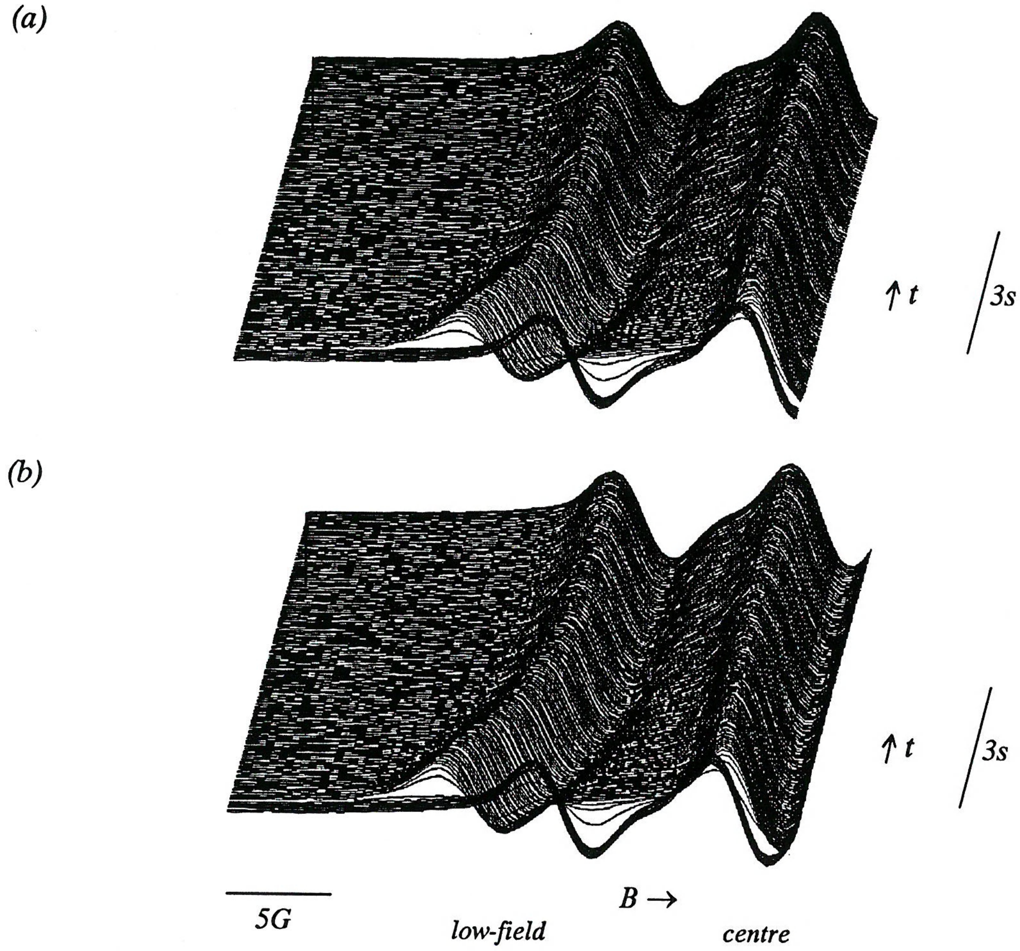

Figure 7 The temporal evolution of the partial spectrum of cholestane in 6.O10O.6 at (a) 139°C and (b) 129°C in the 45° rotation-relaxation experiment.

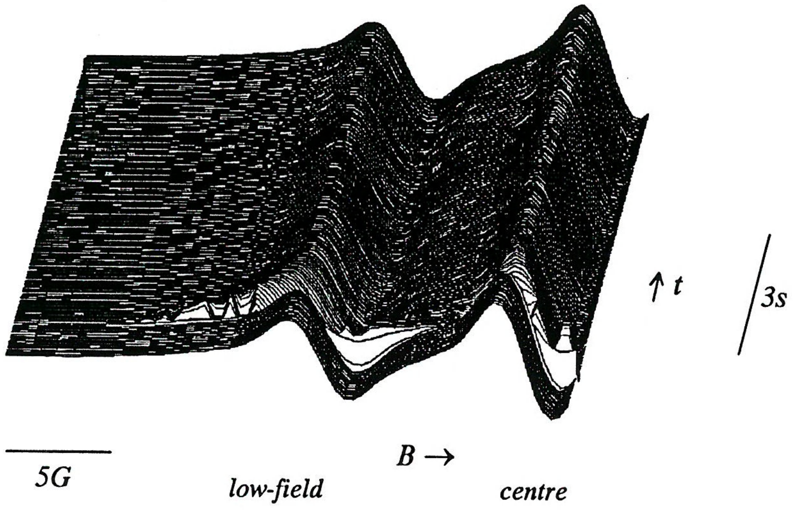

Figure 8 The temporal evolution of the partial spectrum of cholestane in 6.O5 at 69°C during the 45° rotation-relaxation experiment.

partially-averaged $\tilde{g}$ tensor (the small change in the shape and position of the central line, due to the g-anisotropy, is just noticeable). The loss of the uniform alignment of the director during this stage of the experiment was discussed in relation to the Phase V samples in the previous Chapter. Subsequently, in each case the two line spectrum is recovered by a time corresponding to ~0.60s into each of the time-sweep acquisitions (that is, ~0.10s after the rotation of the sample tube was triggered). This indicates a return to an aligned director throughout the sample, although now the larger hyperfine splitting between the two lines indicates that the director is oriented at some 45° to the magnetic field. Although the rotation of the sample tube and of the director do not occur simultaneously, the overall effect of rotation of the sample tube is to rotate the director through approximately the same angle although there is a time lag following rotation of the sample tube before the director reaches this new orientation. Thereafter, the magnetic torque acting on the director causes the relaxation of the director back into alignment with the magnetic field, the progress of this reorientation is reflected by the change in the hyperfine splitting as it decreases towards the initial value prior to the rotation. The rate of director reorientation is interpreted simply in terms of the twist viscosity of the liquid crystal in cases, as here, where the persistence of the two-line spectrum indicates that the director remains aligned *within* the sample, and simply rotates with respect to the magnetic field (see Chapter 3). If the whole spectrum of the cholestane spin probe with its three hyperfine lines had been reconstructed, then the behaviour of the high-field line would have largely mirrored that of the low-field line [16].

A series of 1024 reconstructed field-sweep spectra represent the changing state of the director alignment and orientation over a ten second period, covering the period prior to and during sample rotation and during the magnetic field-induced director reorientation that follows. The hyperfine splittings between the low-field line ($m_I=+1$) and the central hyperfine line ($m_I=0$) of the reconstructed spectra corresponding to the state of the sample at 0.10s intervals during the director relaxation are measured using the cursor and a distance feature within the WIN EPR program (see Chapter 3). The hyperfine splittings measured as a function of time following the rotation of the samples through 45° are then fitted using expression 4.3 programmed into MicroCal

Origin to obtain the time constant τ_r that characterises the field-induced director reorientation in each case,

$$\bar{a}(\xi_t) = \left(\frac{\tilde{A}_{\parallel}^{2} + \tilde{A}_{\perp}^{2} . \tan^{2}\xi_0 . \exp(-2.(t-t_0)/\tau_r)}{1 + \tan^{2}\xi_0 . \exp(-2.(t-t_0)/\tau_r)} \right)^{½} \qquad (4.3)$$

As in Chapter 3, the fitting of equation 4.3 requires input of $\tilde{A}_{\parallel}$, $\tilde{A}_{\perp}$, and the time t_o as a reference time at which the director has been rotated to make a defined angle ξ_0 (~45°) with the magnetic field after which realignment of the director by the magnetic field commences. $\tilde{A}_{\parallel}$ is measured directly from the spectrum of the relaxed sample under each different set of experimental conditions. $\tilde{A}_{\perp}$ was calculated by substitution of the measured value of $\tilde{A}_{\parallel}$ and the isotropic hyperfine splitting, *a*, into relation 2.28 (see Chapter 2). The time t_0 is obtained from the spectra during the rotation-relaxation experiment as the time (following rotation of the sample) at which the measured hyperfine spitting is at its greatest and in which the spectrum shows that the director is uniformly aligned throughout the sample. This value of the hyperfine splitting is used to calculate the values of the angle ξ_0 and $\tan\xi_0$. Figures 9 to 11 show the measured hyperfine splittings and those obtained by fitting expression 4.3 to the experimental data for each of the different samples and temperatures. The constants and parameters used to obtain these fits are shown in table 4.1.

Table 4.1 The experimental conditions, hyperfine parameters and fitting parameters substituted in equation 4.3.

sample	T / °C	a / G #	$\tilde{A}_{\parallel}$ / G	$\tilde{A}_{\perp}$ / G ‡	τ_r / s
6.O9O.6	121	14.8	11.2	16.6	1.20
6.O9O.6	116	14.8	10.5	16.9	1.39
6.O10O.6	139	14.7	9.7	17.2	1.02
6.O10O.6	129	14.7	8.9	17.6	1.325
6.O5	69	14.6	9.9	17.0	0.345

= as measured between the low-field and centre peaks of the spectrum.
‡ = calculated value.

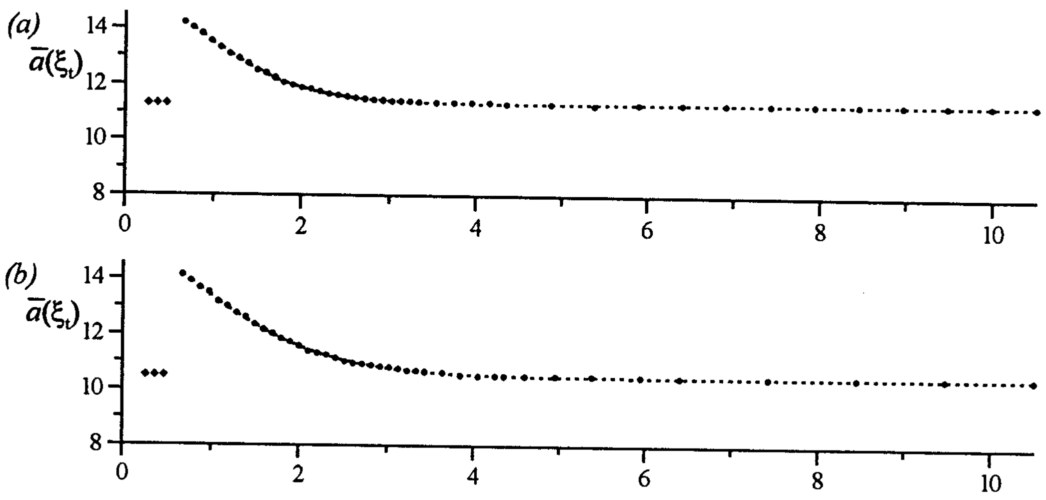

Figure 9 Experimental, •, and fitted values, ---, of the hyperfine splitting for the cholestane spin probe in 6.O9O.6 during the 45° rotation-relaxation experiments at temperatures of 121°C and 116°C, ♦ indicates experimental data points not used in the fitting process.

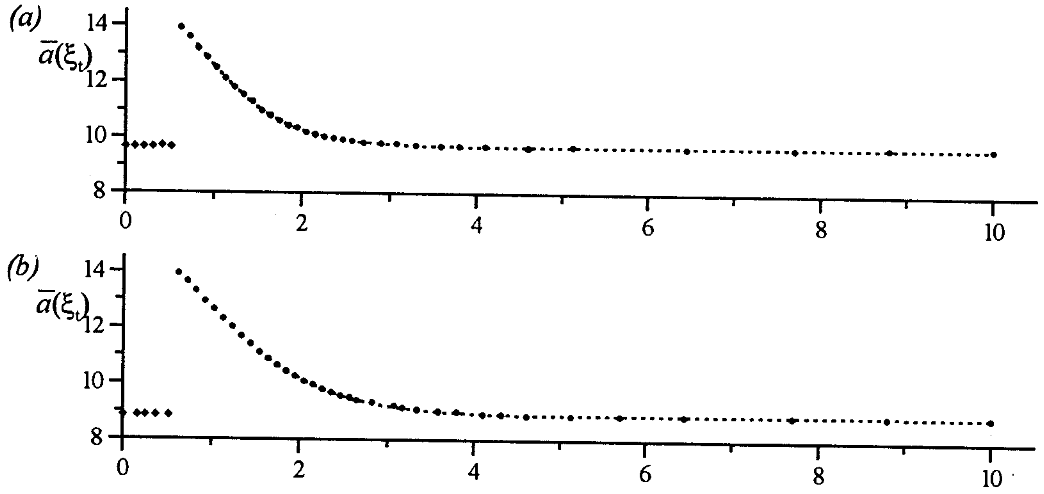

Figure 10 Experimental, •, and fitted values, ---, of the hyperfine splitting for the cholestane spin probe in 6.O10O.6 during the 45° rotation-relaxation experiments at temperatures of 139°C and 129°C, ♦ indicates experimental data points not used in the fitting process.

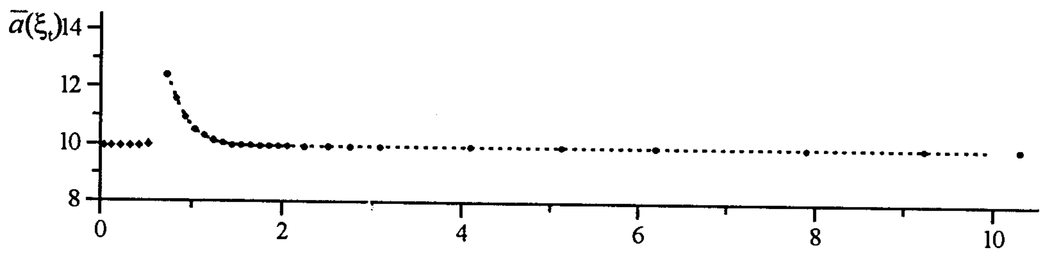

Figure 11 Experimental, •, and fitted values, ---, of the hyperfine splitting for the cholestane spin probe in 6.O5 during the 45° rotation-relaxation experiments at a temperature of 69°C, ♦ indicates experimental data points not used in the fitting process.

4.5 Discussion

In this review of the results of the previous section we shall seek to explain the role that the spacer has in influencing the director relaxation time constant τ_r and the twist viscosity coefficient γ_1 in the dimers 6.O9O.6 and 6.O10O.6, and to compare these results with those obtained for the monomer 6.O5. The difficulty of identifying the precise role played by the odd and even spacer in determining the relaxation time and twist viscosity of dimers is emphasized by the fact that there is at present no complete understanding of the dependence of twist viscosity on the basic parameters of temperature and orientational order in monomeric systems [14, 17, 18, 19, 20]. These difficulties are exacerbated by the large differences in the static and transitional properties of monomers and of odd and even dimers that were outlined in Chapter 1 and in the introduction to the behaviour of dimers earlier in this Chapter.

Given the absence of a universally applicable model for the behaviour of the twist viscosity on temperature and on the orientational order parameter, it is not certain what, if any, temperature scale should be used to compare the results we have for different materials. We therefore consider our results using an absolute temperature scale and a shifted temperature scale T_{NI}-T. Different models suggest that both of these temperatures have some significance in determining γ_1 and τ_r [21, 22].

In these experiments, we have measured the relaxation time τ_r for the field-induced director reorientation directly. Rearrangement of equation 3.9 gives an expression for the twist viscosity coefficient γ_1 in terms of τ_r,

$$\gamma_1 = \frac{\tau_r \Delta\tilde{\chi} B^2}{\mu_0} \tag{4.4}$$

In the right hand side of this expression, only $\Delta\tilde{\chi}$ is dependent upon temperature. We know of no measurements of $\Delta\tilde{\chi}$ for these systems, however, as we saw in Chapter 1, $\Delta\tilde{\chi}$ has the properties of an orientational order parameter [23]. In fact, $\Delta\tilde{\chi}$ should be proportional to the orientational order parameter $\overline{P}_2$ for the mesogenic groups in the mesophase and therefore also to the orientational order parameter $\overline{P}_2$ measured for the long axis of the cholestane spin probe dissolved in the nematic phase formed by these systems. The product $\tau_r\overline{P}_2$ (calculated using the measured orientational order for the spin probe) should therefore be proportional to γ_1 and, for our purposes, contains the information necessary to enable us to examine the relative behaviour of γ_1 for the monomer and dimers that we study. Table 4.2 shows the values of τ_r and $\tau_r\overline{P}_2$ on the different temperature scales that we consider and other relevant information to enable a comparison of properties to be made.

Table 4.2 The temperature dependences of τ_r and $\tau_r\overline{P}_2$ from table 4.1.

sample	T / °C	T_{NI} / °C	T/T_{NI}†	T_{NI}-T/ °C	M_N	$\overline{P}_2$	τ_r / s	$\tau_r\overline{P}_2$ / s
6.O9O.6	121	123	0.995	2	686	0.39	1.20	0.46
6.O9O.6	116	123	0.982	7	686	0.47	1.39	0.65
6.O10O.6	139	141	0.995	3	700	0.55	1.02	0.56
6.O10O.6	129	141	0.971	13	700	0.64	1.325	0.84
6.O5	69	73	0.988	4	351	0.51	0.345	0.18

† = calculated using Kelvin temperatures.

Figure 12 shows the data for τ_r and $\tau_r\overline{P}_2$ as a function of absolute temperature. From the data presented in table 4.2 and shown in figure 12 the most striking result is the

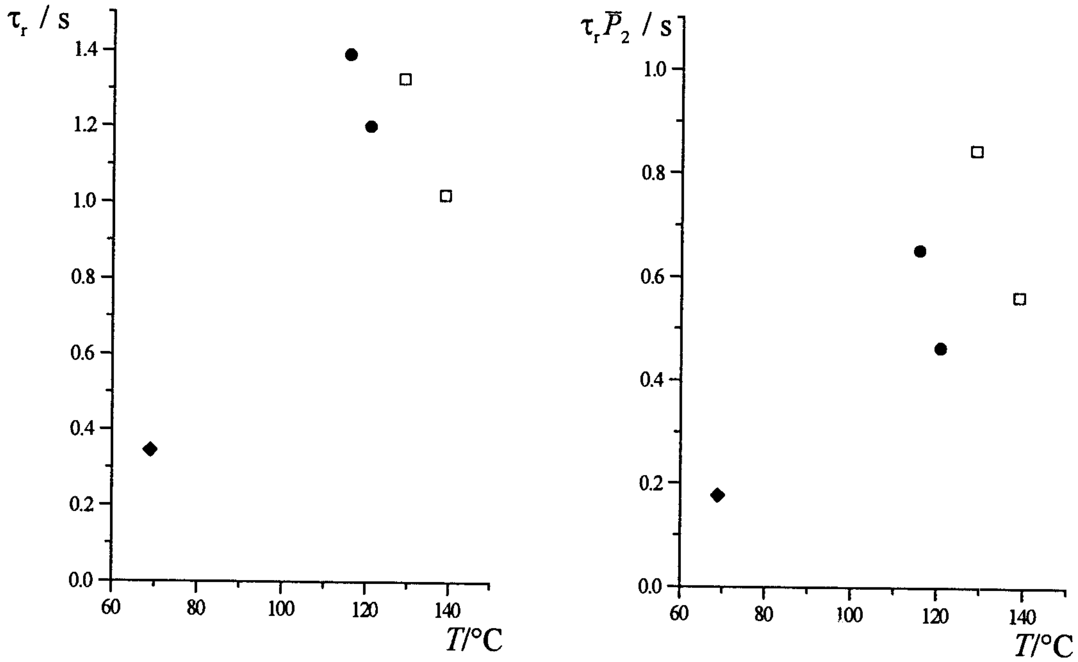

(a) *(b)*

Figure 12 (a) τ_r and (b) $\tau_r\overline{P}_2$ for the odd dimer, ●, the even dimer, □, and the monomer, ◆, against temperature.

very different values of τ_r and $\tau_r\overline{P}_2$ for the monomer and for the dimers, irrespective of spacer parity in the dimer. The relaxation times for the odd and the even dimers are rather similar (falling in the range 1.0-1.4s) but are much higher than that for the monomer measured at a much lower temperature (0.35s at 69°C). In isotropic systems, higher shear viscosities are associated with higher molecular weights of members in a homologous series [24], but in an anisotropic environment it could be argued that a slower reorientation of the director might be expected at the much lower temperatures at which the monomer forms a nematic phase as compared with either of the dimers. We shall consider the relaxation times shortly, but first we turn to a consideration of the relative values of $\tau_r\overline{P}_2$ as a precedent for this behaviour already exists.

In fact, the behaviour we have described for $\tau_r\overline{P}_2$ is qualitatively in accord with theory developed for the nematic phases formed by elongated main-chain polymers in which the twist viscosity coefficient is predicted to be proportional to $\overline{M}_N^2$ (that is, $\gamma_1 \propto \overline{M}_N^2$) in which $\overline{M}_N$ is the average molecular weight of the polymer [25]. For an elongated polymer, $\overline{M}_N$ is proportional to the length-to-breadth ratio l/b and therefore γ_1 should also be proportional to $(l/b)^2$. Experimental work on a (lyotropic) poly-γ-benzyl glutamate (PBG)/solvent system suggests that this dependence is followed for polymers of higher molecular weights (DP in the range 320-1000 with l/b in the range 32-100) [26]. Work on a thermotropic system suggests that this dependence broadly extends to monomers and an even dimer as well as applying to (even) main-chain polymers of higher molecular weights (containing the same mesogenic group), if the twist viscosity coefficients are compared at the same value of the reduced temperature T/T_{NI} (=0.9) [27]. It should be noted, however, that this dependence applies better for longer oligomers and polymers and that the correspondence between the twist viscosities of the monomer and the dimer was less well described by this relation.

Returning to our results, the reduced temperatures T/T_{NI} for which we have data are, first, similar, but not identical, for the different systems we have studied and, second and more importantly, much closer to 1 (see Table 4.2) and so correspond to a region in which the orientational order in the nematic phase has the strongest temperature dependence which is different for each system. Comparisons at a lower reduced temperature (where the order parameter is less variable) presumably factor out the different dependences of orientational order on temperature, but closer to the nematic-isotropic transition, this is less likely to be the case. Thus, the influence of the different dependences of the orientational order on temperature in our different materials will affect the measured values of $\overline{P}_2$ for the dissolved spin probe and this will have a different effect on the calculated values of $\tau_r\overline{P}_2$ for each compound. That said, a plot of $\tau_r\overline{P}_2$ against M_N is shown in figure 13. The dotted line shows the predicted values of $\tau_r\overline{P}_2$ based on the value for 6.O5. From the limited amount of data which we have available, the value of $\tau_r\overline{P}_2$ for either of the dimers is less than would be predicted from the value of $\tau_r\overline{P}_2$ for 6.O5 using the theory for extended polymers; the only point that falls above the projected line using the value of $\tau_r\overline{P}_2$ for the monomer is for the even dimer and corresponds to a lower value of T/T_{NI}. However, a discrepancy of a similar magnitude was also seen in the relative values of the twist viscosities of a monomer and its associated dimer in the previous study cited [27], although in an opposite sense, in that the twist viscosity coefficient of the (even) dimer was higher than that predicted using the value for the monomer. We merely note that, given the different values and limited range of values of T/T_{NI} for which we have data, the relative values of $\tau_r\overline{P}_2$ for monomer and dimers are broadly in accord with this model.

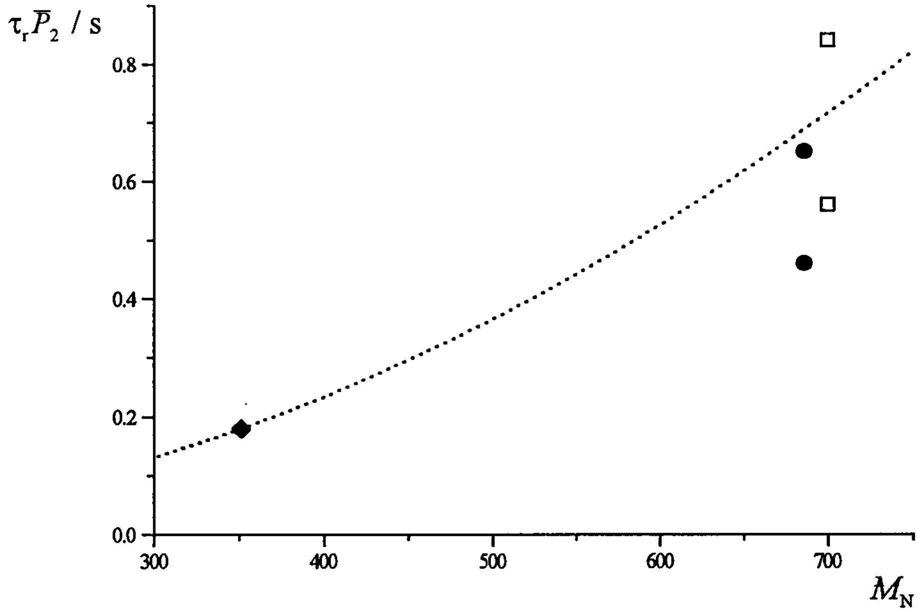

Figure 13 $\tau_r\overline{P}_2$ *against* M_N *for 6.O9O.6, ●, 6.O10O.6, □, and 6.O5, ◆. The dotted line shows the calculated value of* $\tau_r\overline{P}_2$ *based on the value for 6.O5 assuming* $\tau_r\overline{P}_2 \propto M_N^2$.

Having commented upon the relative values of $\tau_r \overline{P}_2$ for monomer and our two dimers we turn to a comparison of the results for the odd and the even dimer using this simple model. For the data that we have, the points for 6.O9O.6 and 6.O10O.6 do not appear to lie on the same curve; the value of $\tau_r \overline{P}_2$ for 6.O10O.6 is greater than would be predicted using this model and the value of $\tau_r \overline{P}_2$ for 6.O9O.6 scaled by the factor $(700/686)^2$ to account for the greater molecular weight of the even dimer (at very similar values of the reduced temperature T/T_{NI}). Alternately, 6.O9O.6 gives a lower value of $\tau_r \overline{P}_2$ than would be predicted based on the value of $\tau_r \overline{P}_2$ for 6.O10O.6 scaled to account for the lesser molecular weight. This is less surprising when we recall that this theory was formulated for elongated polymers which implies that $\overline{M}_N \propto l/b$, which is not the case when we consider an odd and an even dimer (although this is the case when we consider sets of odd dimers and sets of even dimers separately). Removal of a single methylene group from the ten atom spacer of the elongated even dimer leads to the pronounced bent shape of the conformationally averaged structure of the odd dimer; this leads to a considerably smaller value of the l/b ratio for the more biaxial odd dimer in comparison with that of the even dimer than is suggested by the small difference in their respective molecular weights. It is not clear that we should consider only the shapes of the conformationally averaged structures in determining the ratio l/b, but a lower value of l/b for a bent odd dimer is consistent with the experimental finding that $\tau_r \overline{P}_2$ is lower for 6.O9O.6 than for the more elongated 6.O10O.6 (This is also more consistent with general discussions of the behaviour in liquid crystal systems, in which molecular geometry is seen as the primary factor in determining whether a mesophase is formed and/or the properties of such a mesophase, see Chapter 1). Therefore it is suggested that the even dimer has the greater twist viscosity when viewed on this temperature scale as a consequence of its more elongated shape rather than due to its slightly greater molecular weight.

We return now to the relaxation times for 6.05, 6.O9O.6 and 6.O10O.6 as a function of temperature shown in figure 12. The differences in τ_r between the monomer and the dimers follow from the very different twist viscosities due to the differences in the molecular weights but primarily in the molecular aspect ratios which have already been commented on. The general similarity of τ_r for odd and even dimers at the temperatures for which we have data has already been noted, here we examine the subtleties in more detail. Inasmuch as we are justified in referring to trends with so few data points and no temperature range over which odd and even dimers both exhibit a nematic phase, the pattern appears to be that, at a given temperature, if a measurement can be made, the relaxation time τ_r for the even dimer is longer than for the odd dimer. So, referring to the data points on the plot, we have measured a longer relaxation time for 6.O10O.6 at a higher temperature and for greater orientational order (T=129°C, $\overline{P}_2$=0.64) than for 6.O9O.6 (T=121°C, $\overline{P}_2$=0.39) when both the higher temperature and the higher orientational order would tend to suggest that the director reorientation would occur more rapidly in the nematic phase formed by 6.O10O.6 if the intrinsic twist viscosity was the same for both dimers. Therefore, the fact that we have observed a slower relaxation for 6.O10O.6 suggests that the process of director reorientation is inherently less efficient in this nematic phase than in that formed by 6.O9O.6.

This suggestion is confirmed when the behaviour of $\tau_r\overline{P}_2$ for the dimers on an absolute temperature scale is reconsidered. Not surprisingly, given the greater orientational order for the even dimer and the narrow range of values for τ_r that have been measured, the difference in the trends of the values of τ_r is amplified in the product $\tau_r\overline{P}_2$. $\tau_r\overline{P}_2$ for the even dimer, and therefore presumably the coefficient γ_1 of the nematic phase, is predicted to be considerably greater than that for the odd dimer at a given temperature if a measurement can be made. Therefore, on both the reduced and an absolute temperature scale we arrive at the same conclusion: that 6.O10O.6 appears to have a greater intrinsic twist viscosity. The fact that we have happened to observe a narrow range of relaxation times for dimers in our investigations would appear to be because both the necessarily higher temperatures and the greater orientational order largely compensate for the higher intrinsic twist viscosity of the even dimer. What remains in the larger relaxation times for the even dimer that we predict at a given temperature is due to the residual effects of the higher intrinsic γ_1 of the even dimer. Possible reasons for the higher twist viscosity of the even dimer are discussed later in this section.

The use of an absolute temperature scale allows for the influence of molecular kinetic energy but not for the influence of orientational order when comparisons of the field-induced relaxation times and the twist viscosities are made between different systems. Use of the reduced temperature scale is one way of taking some account of the influence of orientational order in comparing the results for different systems [28]. Another temperature scale which is often used to take account of the influence of orientational order is the shifted temperature T_{NI}-T. The use of this scale has met with some success, for example, γ_1 measurements for the nematic phase of 1O.4 (4-methoxybenzylidene-4'-butylaniline, MBBA) spanning approximately an order of magnitude and collected over a wide range of temperatures and pressures have been collapsed onto a universal curve when plotted on a temperature scale analogous to the shifted temperature T_{NI}-T [22]. This suggests that a quantity very similar to the shifted temperature T_{NI}-T exerts a large influence on the twist viscosity and certainly should be considered when the behaviour of the twist viscosity is being investigated. The values for τ_r and $\tau_r\bar{P}_2$ from table 4.2 are plotted on a shifted temperature scale in figure 14.

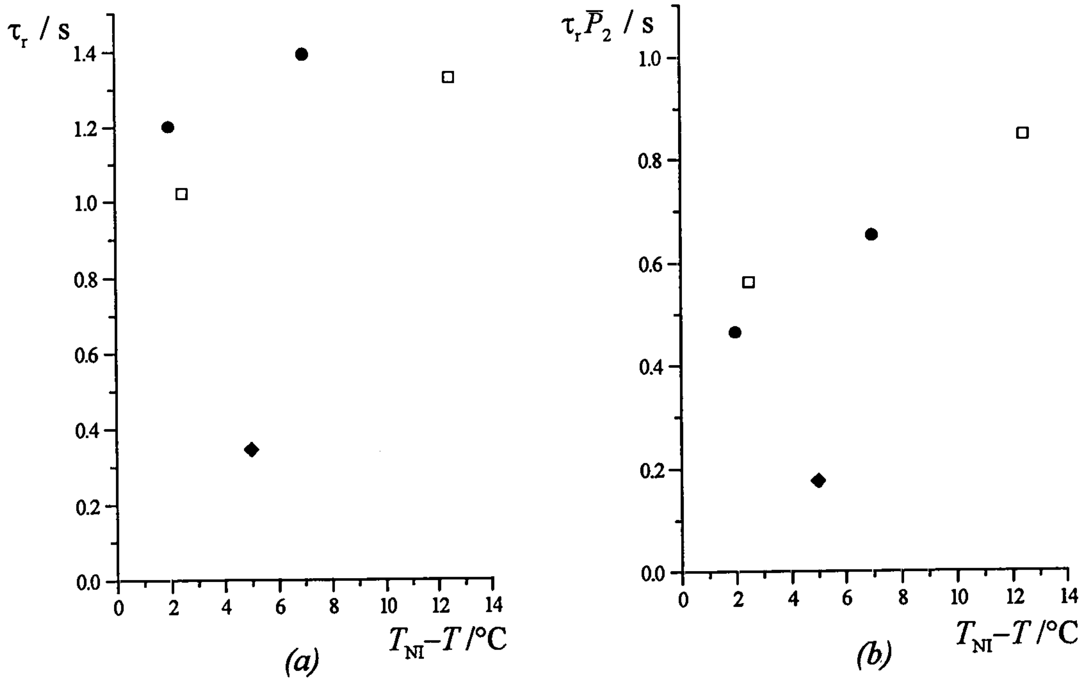

Figure 14 (a) τ_r and (b) $\tau_r\bar{P}_2$ against shifted temperature for 6.O9O.6, ●, 6.O10O.6, □, and 6.O5, ◆.

From figure 14, at similar values of the shifted temperature the data points for 6.O5 and for the two dimers fall in very different areas of the respective plots. The reorientation of the monomer is much faster than that of the dimers which can be attributed mainly to the very much lower twist viscosity of the monomer at similar values of T_{NI}-T or indeed on any temperature scale. This again emphasizes the very different viscoelastic properties of monomers and dimers. Turning to the relative values of τ_r and $\tau_r \overline{P}_2$ for the two dimers in figure 14, there is very little difference between the twist viscosities of 6.O9O.6 and 6.O10O.6 at the same shifted temperature, as judged by the very similar values of $\tau_r \overline{P}_2$, but we observe a faster director reorientation in 6.O10O.6. This is in agreement with expectations: for a similar twist viscosity for both dimers on a shifted temperature scale, we would expect a faster reorientation of the director in 6.O10O.6 when we recall that both the temperature and the orientational order are higher in this system (in this respect, the shifted temperature scale is unable to compensate fully for the naturally greater orientational order in the mesophase formed by an even dimer). The fact that we observe comparable twist viscosities for these two dimers on the shifted temperature scale, when the results for 6.O10O.6 were acquired at a higher temperature, is consistent with our earlier suggestion that the twist viscosity of 6.O10O.6 is intrinsically higher. Therefore the interesting feature about the display of this data on the shifted temperature scale is that it gives very little dependence of the twist viscosities on the parity of the spacer in the dimer. If this is universally the case, then this temperature scale is useful in the interpretation of the twist viscosities and relaxation times of dimers. If this is not universally the case, but is observed here only because of the particular relationship between the twist viscosities and the relative transition temperatures of 6.O9O.6 and 6.O10O.6, then this temperature scale is less useful: considerably more experimental work using a range of dimer systems would be needed to ascertain whether this is part of a general pattern of behaviour.

A principal aim at the outset of this series of experiments was to investigate the effect of spacer parity in dimers on their relaxation times and twist viscosity: the comparison between the results for monomers and dimers was initially of secondary interest. Given that the dependence of the twist viscosity on temperature and order parameter is not clearly established for monomers [14], as far as possible, we wished to remove the need to use a detailed model to allow for differences in temperature in our interpretation of the relaxation times and twist viscosities for odd and even dimers. The choice of the liquid crystals for these experiments was based partly on the fact that the differences in the transition temperatures for 6.O9O.6 and 6.O10O.6 are less than for many other odd-even dimer pairs (although, it is not possible to entirely eliminate the differences in the static and transitional properties of odd and even dimers which follow from their different molecular shapes). However, one unfortunate consequence of our choice of materials was that their nematic ranges are rather narrow. This means that we are unable to compare results for τ_r and $\tau_r\overline{P}_2$ over an extended temperature range to confirm that the observations we have made form part of a more general pattern of behaviour for dimers, or to test our results against some of the more detailed models which attempt to separate the effects of orientational order and of temperature on the twist viscosity [18, 19, 20]. Testing of some of these models requires a knowledge of the isotropic shear viscosity as it has been suggested that the underlying Arrhenius dependence of the isotropic shear viscosity is a major factor in determining the twist viscosity of the nematic phase [21]. Such measurements call for the use of the more conventional techniques for measuring viscosity; although EPR experiments are ideal for determining director orientations and distributions in mesophases, they are not the appropriate means for investigating isotropic properties. To the best of our knowledge, the temperature dependence of the isotropic shear viscosity and the activation energy in the expression for the thermal behaviour of the shear viscosity has not been measured for these systems.

Given that there are difficulties in establishing the precise criteria for comparisons of the results of our experiments, the rest of this discussion considers the central result to emerge from this experimental work: that the even dimer appears to have a greater intrinsic twist viscosity then the odd dimer. As we have seen, this result is in accord with the expectations for an athermal system, in which a higher twist viscosity for an even dimer would be expected to follow as a result of its more anisometric shape. However, the fact that our results on a thermotropic system broadly agree with a model that regards the nematic phase as being composed of rigid rods with different length-to-breadth ratios raises a number of interesting points. In the athermal

PBG/solvent system to which we have already referred and to which this model has been applied (that is, $\gamma_1 \propto \overline{M}_N^2 \propto (l/b)^2$), the PBG polymer folds into an α-helix which approximates very closely to a rigid elongated rod with a very clearly defined length-to-breadth ratio. Each of these rigid rods approximates to an 'ideal' monomer molecule for the purposes of describing for example, the orientational distribution function in the mesophase. In calamitic thermotropic low molar mass liquid crystals, the mesogenic groups form part of smaller, densely packed molecules which possess varying degrees of internal flexibility. The orientational distribution functions are different but interrelated for different portions of the molecule. The importance of quite specific short range interactions such as dipole-dipole interactions, packing considerations and local short range order is demonstrated by their influence on, for example, both the local structure and the overall structure of a mesophase and its properties (see section 1.4, Chapter 1, section 4.2, this Chapter and Chapter 6 [29]). Consequently, it is far from clear that even the conformationally-averaged shapes of these molecules can or should be approximated by an elongated rod-like shape if we wish to understand and formulate structure-property relationships for the viscoelastic properties of thermotropic systems. The proposal for the different molecular organisations within the nematic phase of liquid crystal dimers is one result of trying to take a more realistic view of at least some aspects of real thermotropic systems. This model has already been successful in explaining at least one unexpected experimental finding [11, 13] and could also suggest an explanation for our experimental observations. That said, it should be emphasized that the detailed mechanism by which director reorientation occurs even in simple monomeric systems is not understood (although some models of the expected temperature and order parameter dependence incorporate some of the features likely to be important, for example, free volume [18]) and so the following arguments should be viewed in this context).

In introducing the model for the molecular organisation in the nematic phase, a degree of similarity was noted between the distribution of director orientations in the odd dimer and that in a smectic C phase when the layer normal and tilt angle are defined, but in which the tilt direction remains undefined. A similarity was also noted between the director distribution in the even dimer and that in a smectic A phase, in that the local directors all lie parallel to the global director. We digress briefly to describe the effect this has on the behaviour that is seen in smectic phases. In a smectic C phase, either with the distribution of director orientations we have described, or in which the tilt direction is constant from layer to layer, it is observed that there is very little barrier to the rotation of the local directors about the layer normal, that is, changing the tilt direction but retaining the same tilt angle (see Chapter 1 [30]). The local directors in different layers can rotate relatively independently of each other without disrupting the layered structure. Consequently, two mechanisms of director reorientation can be identified. First, those as we have described that involve changes in the tilt direction within the existing layer structure that can occur rapidly even in small external fields. A director reorientation of this type is pictured in figure 15a. Second, those that involve changes in the tilt angle which occur *via* disruption or reorientation of the smectic layers which occur only in much larger external fields. The smectic A phase provides a better example of the latter type for our present purposes and this is pictured in figure 15b. In a smectic A phase, the director orientation is defined by the layer normal and *vice versa*. The director is therefore not free to rotate without causing reorientation of the layers themselves, which involves considerable disruption of the layered structure during rotation and which is therefore strongly resisted by the intermolecular forces which promote smectic phase formation. This provides a large barrier to any rotations of the director in a smectic A phase which therefore occur only in large external fields, with the result that we are able to observe the angle dependence of the EPR spectrum of a smectic A phase using a magnetic field of ~0.33T without changing the director orientation within the sample.

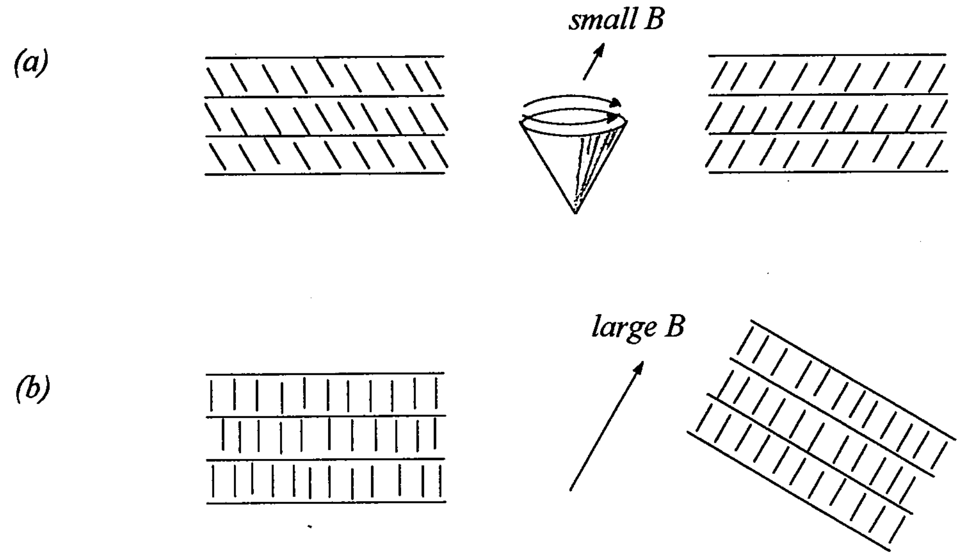

Figure 15 Director reorientations that involve (a) changes in the tilt direction in a smectic C phase occur easily in a small external field whereas (b) those that involve reorientation of the layers in a smectic A phase occur only in much larger external fields.

These analogies should not be taken too far (for example, there is by definition no permanent layered structure in the nematic phase) but certain similarities to the processes that may occur in the nematic phases formed by dimeric liquid crystals can be noted. In the proposed structure of the nematic phase formed by the odd dimer, long range forces do not correlate the local director orientations of microdomains over large distances, other than to maintain the 'tilt' angle β between $\boldsymbol{n}_l$ and $\boldsymbol{n}_G$, as these are dominated by the geometrical constraints on the relative orientations of neighbouring microdomains acting over much shorter distances due to the bend in the odd dimer. As the local director in each microdomain has a degree of freedom from the global director and the longer range intermolecular forces, we might imagine that each microdomain is much freer to reorient in an external field as in doing so, it only has to reach an accommodation of the geometrical constraints with its immediate neighbours to which it is linked by spacers (although the nearest neighbours must also reach an accommodation with their other nearest neighbours). Bearing in mind the natural fluidity of the nematic environment, with molecular tumbling, fluctuations in orientation and conformational changes (especially in the nematic phase formed by the odd dimer in which the distribution of conformations of the spacer is more uniform) this may be easily achieved. As more of the microdomains reorient in an external magnetic field this is progressively reflected in the reorientation of the global director, which is simply defined by the average orientation of the local directors throughout the sample. So, similar to the unhindered director rotations about the layer normal that we described in the smectic C phase, we can imagine that the process of director reorientation in the odd dimer can be achieved by a series of relatively unhindered local fluctuations without significant disruption of the local or macroscopic structure.

In the model for the nematic phase of the even dimer, long range forces act together with short range forces to correlate the local directors throughout the sample and create a true monodomain. We have also seen that a synergy exists between the high orientational order of the mesogenic groups and the selection of elongated conformers which enhances the anisotropy and the thermal stability of the mesophase. The selectivity of elongated conformers and the high macroscopic orientational order that is maintained by a combination of short and long range intermolecular forces implies that the system is highly coupled. The reorientation of the director in the even dimer would therefore seem to require a cooperative reorientation of many molecules as the average shape and orientation of each is strongly dictated by and sensitive to the orientation of all of its neighbours, both near and far. Alternately, this could be taken to imply that reorientation of the director occurs *via* a disruption of the local and macroscopic forces which promote high conformational and macroscopic orientational order as features of the nematic phase formed by the even dimer. To return to the analogy with the smectic A phase; these forces play the same role, though to a far lesser extent, in inhibiting and slowing director reorientation in the nematic phase as the forces that maintain the layered structure which prevent director rotations in the smectic A phase except in large external fields.

Again, it is not certain how far these analogies should be carried, but an interesting experimental finding that appears consistent with these ideas is provided by some of the viscoelastic behaviour seen in the series of unsymmetric CB.O*n*O.*m* dimers **3**. These dimers have previously attracted attention because of their tendency to form some interesting smectic phases [7]. Some members of the series form an interdigitated smectic A phase ($\mathrm{SmA_d}$) in which the average layer spacing is approximately 1.7-1.9 times the all-*trans* molecular length (that is, $d/l \sim 1.7\text{-}1.9$). Of greater interest for our purposes is the observation that some other members of the series form an intercalated smectic A phase (SmA_c) in which the interlayer distance is approximately 0.5 times the all-*trans* molecular length, that is, individual molecules span two adjacent smectic layers ($d/l \sim 0.5$). The molecular organisation in the intercalated smectic A phase is sketched in figure 16. The relaxation times for the director reorientation in the nematic phases that form above these smectic phases have been measured using the EPR method described in this and the previous Chapter [31]. In general it proved difficult there, as here, to present the results in a way that showed a clear dependence of either τ_r or $\tau_r\overline{P}_2$ on the parity of the spacer or any other molecular features. However, it was noted that, on a plot of τ_r against temperature, almost all of the even dimers fell on to a single curve. In general, the odd dimers did not fall on to a single curve, but could be regarded as being grouped in one region of the plot. The clear exception among the odd dimers was CB.O11O.10, which forms an intercalated smectic A phase below the nematic phase and presumably exhibits some pretransitional intercalated smectic ordering in the nematic phase. The data points for CB.O11O.10 fall towards the curve followed by the even dimers. Although the measured orientational order for the intercalated smectic A structure formed by the odd dimer is rather low (but not atypical for an odd dimer), the existence of some locally intercalated structure in the nematic phase would be expected to force the overall director reorientation to occur *via* a concerted reorientation of the local directors. This is what was predicted for the nematic phase formed by the even dimer and therefore the position of the data points for this compound away from those of the odd dimers and towards those of an even dimer is consistent with these ideas.

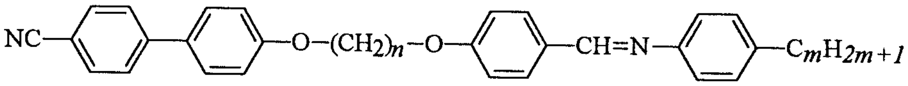

3

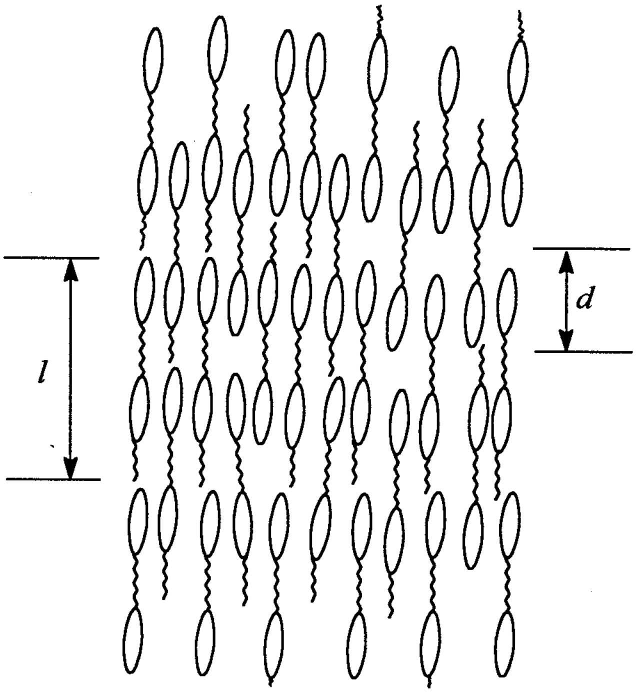

Figure 16 A sketch of the molecular organisation in the intercalated smectic A phase, SmA_c, in which the interlayer repeat distance d is approximately half the molecular length l.

4.6 Conclusions

The twist viscosity and the time constant for the director reorientation and their temperature dependences are very important in determining the suitability of materials for many applications, for example, the response time for a display is proportional to γ_1 [32]. The rotation-relaxation experiment in which both the state and the orientation of director alignment is monitored using X-band EPR spectroscopy has proved to be a very useful tool in the study of the director reorientation and twist viscosity of low molar mass liquid crystals. This stems partly from the strength of the magnetic field (~0.33T) which is an integral part of the EPR experiment which serves to align or realign the director of typical low molar mass liquid crystals on a timescale which can be followed accurately by the EPR experiment. The present studies have revealed large differences between the time constant for the director reorientation in a monomer and in related dimer liquid crystals: the monomer relaxation occurs much more rapidly even at a significantly lower temperature, indicating that it possesses a lower twist viscosity.

This is in agreement with a model developed for elongated polymers. The interpretation of the results for odd and even dimers is complicated by differences in the static properties (the order parameter and the transition temperatures) which make it difficult to make a simple comparison of τ_r and γ_1 measured under identical conditions. This is exacerbated by the lack of a universal theory which allows proper account to be taken of differences in the transition temperatures and orientational order so that we can access and compare the underlying twist viscosities for different systems. We have considered the results of the current study using both an absolute and a shifted temperature scale which a previous study has suggested is how the comparison should be made. No firm conclusions about the relative behaviour of odd and even dimers can be made from the results plotted on the same shifted temperature scale. An interesting result from plotting the results on the same absolute temperature scale has been explored in some detail: the director in the even dimer is seen to relax more slowly at a higher temperature and a measured value of the order parameter than the odd dimer at a lower temperature and measured value of the orientational order. We propose that this result fits with a previous model which describes different local structure in the nematic phase of odd and even dimers. In the odd dimer, natural fluctuations in the local structure provide an efficient mechanism for the reorientation of the bulk sample director *via* relatively independent reorientations of microdomains which are formed as a simple consequence of the bend in the molecule of the odd dimer. In the even dimer, the combination of high local orientational order and long range correlations in orientational order mean that the reorientation has to occur in a more coherent manner throughout the sample, while at the same time removing a mechanism for this to occur. Consequently, director reorientation in the even dimer involves more disruption of the local and macroscopic order, which is reflected in the greater intrinsic twist viscosity.

4.7 Further Work

A simple variation of the present EPR experiment has the potential for measuring other viscoelastic parameters of similar compounds. It remains to be seen how effective these are in enabling the measurement of the other liquid crystal viscosity coefficients beyond the twist viscosity coefficient that we have considered in some detail in this Thesis. However, in principle, the information that is obtained from these experiments can be subjected to the sort of rigorous analysis which has been applied to the results of analogous NMR experiments on the reorientation of polymeric liquid crystals and which are not available from practical NMR experiments on low molar mass materials at the present time. A complete understanding of the viscoelastic behaviour of low molar mass liquid crystals will prove useful in putting the behaviour of polymeric materials in a new context. In particular, those material properties which are a consequence of polymeric rather than liquid-crystalline character can be identified. The dimer systems present elements of both types of behaviour which may prove useful for their future application, in addition, they provide a useful intermediate between these two extremes which may contribute to a better understanding of the different influences on the behaviour of both types of material. The apparent differences in the dependences of viscosities on order parameter and on temperature for various low molar mass materials were cited earlier: The concepts involved in explaining dimer behaviour may provide a more universally applicable insight into the interrelationships between the different factors which influence viscoelastic behaviour.

References 4.8

[1] Smith, G.W., Gardlund, Z.G. and Curtis, R.R., *Mol. Cryst. Liq. Cryst.*, **19** 327, 1973.

[2] Vorlander, D., *Z. Phys. Chem.*, **126** 449, 1929.

[3] Griffin, A.C. and Britt, T.R., *J. Am. Chem. Soc.*, **103** 4957, 1981.

[4] see, for example, Imrie, C.T. and Luckhurst, G.R., Chapter X, vol. 3, *Handbook of Liquid Crystals*, eds. D. Demus, J.W. Goodby, G.W. Gray, H.-W. Spiess and V. Vill, Wiley-VCH, 1998, and references therein.

[5] Luckhurst, G.R., Chapter 7, *Recent Advances in Liquid Crystalline Polymers*, ed. L.L. Chapoy, Elsevier, 1985.

[6] Date, R.W., Imrie, C.T., Luckhurst, G.R., and Seddon, J.M., *Liq. Crystals.*, **12** 203, 1992.

[7] Attard, G.S., Date, R.W., Imrie, C.T., Luckhurst, G.R., Roskilly, S.J., Seddon, J.M. and Taylor, L., *Liq. Crystals*, **16** 529, 1994.

[8] Shibaev, V.P., Kostromin, S.G., Platé, N.A., Ivanov, S.A., Vetrov, V.Y. and Yakovlev, p. 345, *Polymeric Liquid Crystals*, ed. A. Blumstein, Plenum Press, 1985.

[9] see, for example, Fan, S.M., Luckhurst, G.R. and Picken, S.J., *J. Chem. Phys.*, **101** 3255, 1994.

[10] see, for example, Ferrarini, A., Luckhurst, G.R., Nordio, P.L. and Roskilly, S.J. *Chem. Phys. Lett.*, **214** 409, 1993.

[11] Heeks, S.K. and Luckhurst, G.R., *J. Chem. Soc. Faraday Trans.*, **89** 3289, 1993.

[12] Luckhurst, G.R., *Ber. Bunsenges. Phys. Chem.*, **97** 1169, 1993.

[13] Barnes, P.J., Douglass, A.G., Heeks, S.K. and Luckhurst, G.R., *Liq. Crystals*, **13** 603, 1993.

[14] de Jeu, W.H., Chapter 7, *Physical Properties of Liquid Crystalline Materials*, Gordon and Breach, 1980.

[15] see, for example, Chapter 1, this Thesis, or De Jeu, W.H., Chapter 2, *Physical Properties of Liquid Crystalline Materials*, Gordon and Breach, 1980.

[16] Thus, we would have a three-line spectrum and hyperfine splittings of $\tilde{A}_{\parallel}$ from the stationary sample prior to rotation, a large splitting of both the low and high field lines during the period of director rotation when the uniform alignment is lost.

This would be followed by a refocusing into a three-line spectrum with large hyperfine splittings corresponding to an angle of ~45° between the magnetic field and the director, and then a subsequent decrease in the hyperfine splittings between these three lines as the aligned director reorients in the magnetic field.

[17] PROST, J., SIGAUD, G. and REGAYA, B., *J. Phys. Lett. Paris*, **37** L-341, 1976.

[18] DIOGO, A.C. and MARTINS, A.F., *Mol. Cryst. Liq. Cryst.*, **66** 133, 1981.

[19] KNEPPE, H., SCHNEIDER, F. and SHARMA, N.K., *J. Chem. Phys.*, 77 3203, 1982.

[20] BOCK, F.-J., H., KNEPPE, and SCHNEIDER, F., *Liq. Crystals*, **1** 239, 1986.

[21] OSIPOV, M.A. and TERENJEV, E.M., *Z. Naturforsch.*, **44a** 785, 1989.

[22] DÖRRER, H., KNEPPE, H., KUSS, E. and SCHNEIDER, F., *Liq. Crystals*, **1** 573, 1986.

[23] DE JEU, W.H., Chapter 3, *Physical Properties of Liquid Crystalline Materials*, Gordon and Breach, 1980.

[24] see, for example, the viscosities of the *n*-alcohols, Chapter 6, *CRC Handbook of Chemistry and Physics*, ed. D.R. Lide, CRC Press, 1997.

[25] MEYER, R.B., Chapter 6, *Polymer Liquid Crystals*, eds. A. Ciferri, W.R. Krigbaum and R.B. Meyer, Academic Press, 1982.

[26] LEE, S-D. and MEYER, R.B., *Liq. Crystals*, 7 15, 1990.

[27] HEATON, N., REIMER, D. and KOTHE, G., *Ber. Bunsenges. Phys. Chem.*, **97** 1320, 1993.

[28] for example, Maier-Saupe Theory predicts a universal dependence of orientational order on T/T_{NI} which is broadly correct for many liquid crystals, see Chapter 1, or DE JEU, W.H., Chapter 1, *Physical Properties of Liquid Crystalline Materials*, Gordon and Breach, 1980. This is further improved by taking extra terms in the expansion of f(β), see LUCKHURST, G.R., Chapter 7, vol. 2, *Liquid Crystals and Plastic Crystals*, eds. G.W. Gray and P.A. Winsor, Ellis Horwood, 1974.

[29] GRAY, G.W. AND GOODBY, J.W., *Smectic Liquid Crystals: Textures and Structures*, Leonard Hill, 1984.

[30] MEIBOOM, S. and HEWITT, R.C., *Phys. Rev. Lett.*, **34** 1146, 1975.

[31] DUNN, C.J., LE MASURIER, P.J. and LUCKHURST, G.R., in preparation.

[32] JAKEMAN, E. and RAYNES, E.P., *Phys. Lett.*, **39A** 69, 1972.

Chapter 5

The use of field gradient EPR in the study of rotating Nematic Liquid Crystals

5.1 Introduction

In this Chapter the technique of spectral-spatial imaging by EPR spectroscopy is used to investigate the spatial distribution of the director in a spinning sample of a nematic liquid crystal. Information about the distribution is obtained by acquiring the EPR spectrum of the sample in the presence of a known magnetic field gradient applied across the sample.

Section 5.2 of this Chapter concentrates on the theoretical description of the director behaviour in spinning nematic liquid crystals. Section 5.3 shows how this behaviour and the deviations from this predicted behaviour are revealed in the appearance of EPR spectra, although some EPR spectra are shown, these are intended to indicate the fundamental magnetohydrodynamic behaviour of the sample itself and not merely the behaviour observed in an EPR experiment. Section 5.4 introduces the concept of spectral-spatial imaging and explains how the deliberate application of a magnetic field gradient can yield extra information about the spatial characteristics of a sample. The earlier part of this section is applicable to magnetic resonance in general although the treatment provided will be aimed increasingly towards the EPR experiment. In section 5.5 the background to the simulations of field gradient EPR spectra is described as are the results of some early simulations that were used to assess the viability of field gradient EPR spectroscopy as a means for studying the director distribution in spinning nematic samples. Sections 5.6 and 5.7 describe the experiment and its results which are then subjected to a more detailed analysis in section 5.8. The conclusions of this work are collected together in section 5.9.

5.2 The theory of rotating Nematic Liquid Crystals

This section deals with the physical behaviour of a sample of a nematic liquid crystal in the presence of an external magnetic field and introduces the concept of magnetohydrodynamics of liquid crystals. In the equilibrium state, a bulk sample of a nematic liquid crystal which is not subject to any strong external fields possesses partial orientational ordering of the molecules with respect to the local director, S_l (see Chapter 1), however the macroscopic order, S_G, over the whole sample is zero as macroscopically the director has no preferred orientation. If the sample is a nematogen with a positive anisotropy of diamagnetic susceptibility ($\Delta\tilde{\chi}$) and is subject to a sufficiently strong magnetic field, the equilibrium state is a monodomain in which the liquid crystal director lies parallel to the magnetic field direction and S_l=S_G (see section 1.3, Chapter 1). As the magnetic field is increased from zero, or if its direction is altered, there is a continuum of non-equilibrium states in which the director experiences a magnetic torque tending to align the director with the magnetic field direction, but in which the director response is damped by viscous forces within the liquid crystal. In consequence, director reorientation from the stable isotropic state when no magnetic field is present to the stable monodomain in a magnetic field is a non-instantaneous process. The magnetic field imposed on the sample can be varied, for example, instantaneously or continuously, or increased gradually, and the resulting competition between magnetic torque and sample viscosity can be used to probe the viscous response of the liquid crystal. Specifically, because of the motion of the director during reorientation, it is the twist viscosity γ_1 that is probed [1, 2]. The term magnetohydrodynamics describes the response of the liquid crystal to an external magnetic field which we consider here, but a response to other external forces could also be envisaged, for example, to ac or dc electric fields or to surface alignment.

The effect of manipulating either the director or the magnetic field so that the two are no longer parallel was discussed in Chapter 3 and 4 and was used as a basis for measuring the twist viscosity coefficient γ_1 of the nematic phase: in those experiments the sample was rotated instantaneously with respect to the external magnetic field and then held in this new position. The director was observed to rotate back into the magnetic field direction taking a characteristic time τ_r that is proportional to the ratio

$\gamma_1/\overline{P}_2$ of the liquid crystal. In those experiments, a dynamic, non-equilibrium situation was created and the dynamics of the subsequent relaxation was used as a measure of the twist viscosity. Using the same experimental geometry, in a related experiment, the sample may also be rotated continuously with respect to the magnetic field, as shown in the schematic experimental setup pictured in figure 1. This formulation of the experiment, which we use in this study, is one variant of the rotating field method, the other being the case in which the magnetic field is rotated about a stationary (or nearly stationary) sample. Rotating field methods have been widely used for measuring the twist viscosity coefficients of liquid crystals [3, 4, 5]. In the rotating field experiments an equilibrium situation is created, and it is the position of the equilibrium which is determined in part by the twist viscosity of the liquid crystal.

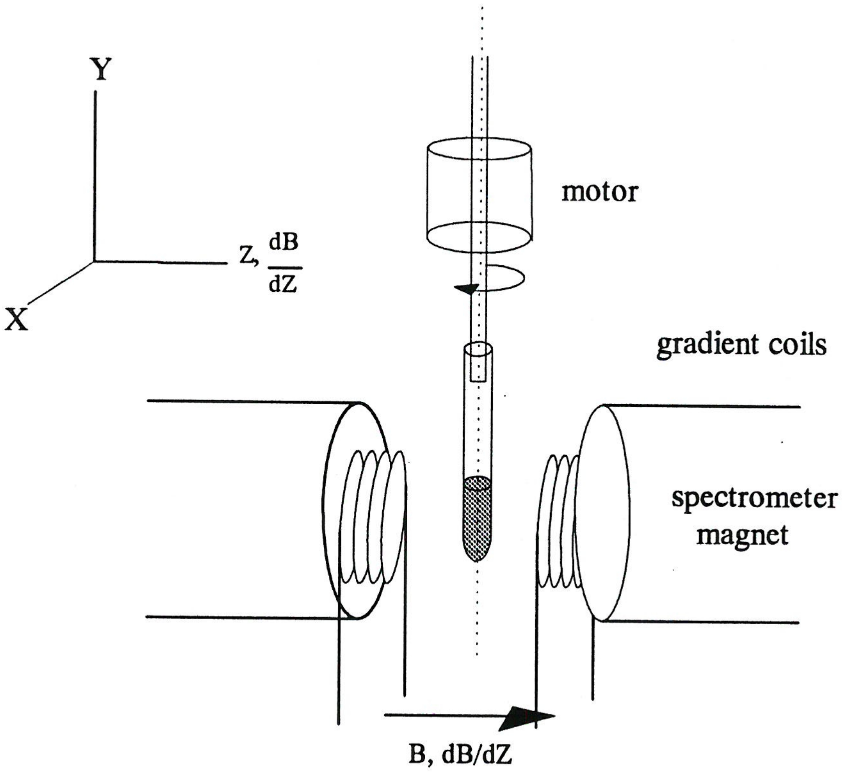

Figure 1 The arrangement of sample, magnetic field and sample spinning axis used in the rotating field method to measure the twist viscosity coefficient γ_1 of a liquid crystal. The sample is spun about the spinning axis with an angular velocity Ω. The gradient coils used to produce a magnetic field gradient across the sample in this series of experiments are also shown.

Continuum theory has been used to predict the behaviour of the director experiencing a continuously rotating magnetic field [6]. In the geometry pictured in figure 1 the essential result from the continuum equations is that:

$$I \frac{d^2\xi}{dt^2} - \gamma_1 \left(\frac{d\xi}{dt} - \Omega \right) + \Delta\tilde{\chi} B^2 \mu_0^{-1} \sin\xi \cos\xi = 0 \qquad (5.1)$$

in which I is the inertial tensor associated with the director, Ω is the angular velocity of sample rotation and the third term represents the magnetic torque on the director as a function of the angle ξ between the magnetic field and the director (see Chapter 1). The case of Ω=0 corresponds to a stationary monodomain sample in which ξ=0 as described earlier. The director inertia term I in equation 5.1 is often neglected [2]. In considering the solutions to equation 5.1 it is convenient to describe the behaviour of the director as a function of the reduced angular velocity Ω/Ω_c, in which Ω_c is a critical spinning speed. When the reduced spinning speed is less than 1, that is, the sample is spun at a speed below Ω_c, the director is predicted [6] to lie at a constant angle ξ to the magnetic field given by the relation:

$$\sin 2\xi = \Omega/\Omega_c \qquad (5.2)$$

in which

$$\Omega_c = -\frac{\Delta\tilde{\chi} B^2}{2 \mu_0 \gamma_1} \qquad (5.3)$$

The angle ξ can therefore be used to calculate the twist viscosity coefficient γ_1 at a given magnetic field strength if $\Delta\tilde{\chi}$ is known.

At spinning speeds above Ω_c the solution of equation 5.1 suggests that the director is not static but actually rotates about the axis of rotation of the sample at an average angular velocity ω given by [6]

$$\omega = (\Omega^2 - \Omega_c^2)^{1/2} \qquad (5.4)$$

The behaviour of the director as predicted by equations 5.2 and 5.4 is pictured in figure 2.

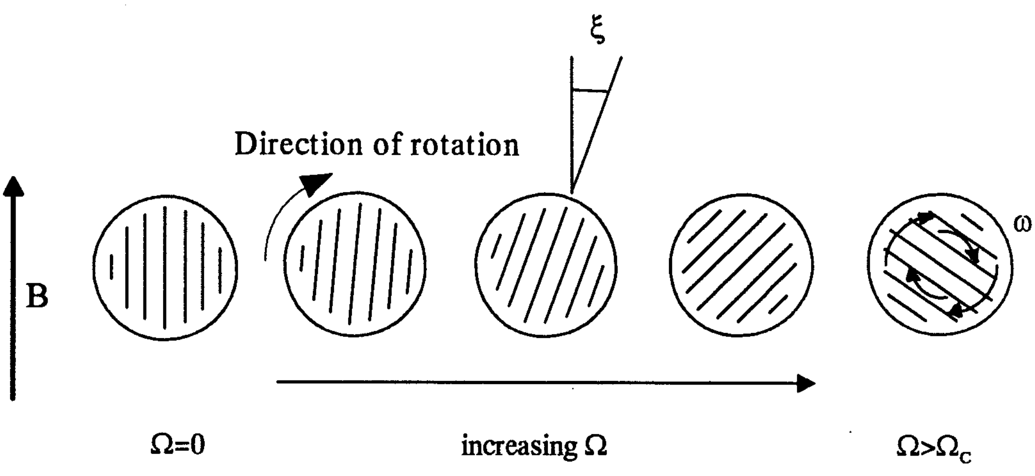

Figure 2 A schematic view of the behaviour of the director as a function of spinning speed Ω as described by equation 5.2 and 5.4.

5.3 Experiments on rotating Nematic Liquid Crystals

Many different experimental measurements have been made on liquid crystals using the generic rotating field geometry pictured in figure 1, usually with the aim of obtaining γ_1 but also studying more general behaviour. These include techniques based on mechanical torque measurements and optical methods in which the sample is held stationary and it is the magnetic field that is rotated [7]. Magnetic resonance experiments lend themselves more easily to experiments in which the stationary magnetic field of the spectrometer itself provides the external magnetic field, and where it is the sample itself that is rotated [8, 9, 10, 11]. It should be noted that there is good agreement between the results obtained with the magnetic field rotated about a stationary sample or *vice versa*. It should also be noted that experimental measurements of γ_1 made using either of the rotating field approaches that study the system at equilibrium are in agreement with those made using the dynamic, non-equilibrium, rotation-relaxation method as used in Chapters 3 and 4 [12].

A schematic view of the behaviour of the director in a cross-section of a cylindrical sample spinning at different spinning speeds Ω was shown in figure 2. However, several experiments indicate that the director behaviour is not completely described by equations 5.2 and 5.4 and figure 2. Observations of resonance linewidths in EPR experiments at intermediate spinning speeds, $0 < \Omega/\Omega_c < 1$, show that a progressive fanning out of the director occurs as Ω/Ω_c is increased towards 1 [9]: equation 5.2 is typically only obeyed when Ω/Ω_c lies below approximately 0.9. In this regime, the apparent fanning out of the director is pictured schematically in figure 3a showing the angular distribution function as a function of spinning speed Ω: the position of the maximum of the distribution is equal to the angle ξ predicted by equation 5.2 but the shape of the distribution clearly changes as a function of Ω.

Equation 5.4 predicts a rotation of the director at an average angular velocity ω for spinning speeds above Ω_c [6]. In EPR experiments this would be predicted to give a time-dependent spectrum in which the hyperfine spacing changes with the angle ξ (according to equation 2.24). Experimentally, this is observed only transiently before the spectrum takes on an invariant two-dimensional powder form indicating that the director adopts an isotropic distribution in the plane containing the magnetic field and orthogonal to the spinning axis [9]. In NMR experiments (which use lower frequencies and stronger magnetic fields) rapid sample spinning is needed to produce the two-dimensional powder spectrum, but also visible in the spectrum are rotational satellite lines separated by ω from the two-dimensional powder spectrum, indicating that the director continues to rotate within the sample [10]. Such satellite lines are not observed in the two-dimensional powder EPR spectrum, as separations of the order of ω at the typical spinning speeds attainable in experiments are lost in the large natural linewidth of EPR resonances.

One empirical approach to account for the observed behaviour is to describe the director of the stationary monodomain sample (prior to rotation) by a delta function, that is, the sample director is defined by a single direction and lies parallel to the magnetic field. As the sample is spun, at first slowly, the sample director is no longer described by a delta function. Simulations have shown that the director distribution in this case is well represented by an elliptical distribution with a high eccentricity and with the semi-major axis of the ellipse lying at the angle ξ to the magnetic field direction predicted by equation 5.2 [9, 10]. As the spinning speed is increased the eccentricity of the ellipse that best describes the director distribution decreases until, by Ω_c, the eccentricity is 1 and the ellipse has evolved into a circle. This reflects the isotropic in-plane orientational director distribution which is reflected by the two-dimensional powder pattern found in magnetic resonance experiments. The evolution of the description of the distribution from the delta function to the two-dimensional powder pattern *via* the ellipse is pictured schematically in figure 3b. It should be noted that the distributions shown in figure 3 make no statement about whether the sample has a static director or a mobile director, both could equally fit this model, but the experimental results show that the director distribution *is* static with respect to the magnetic field.

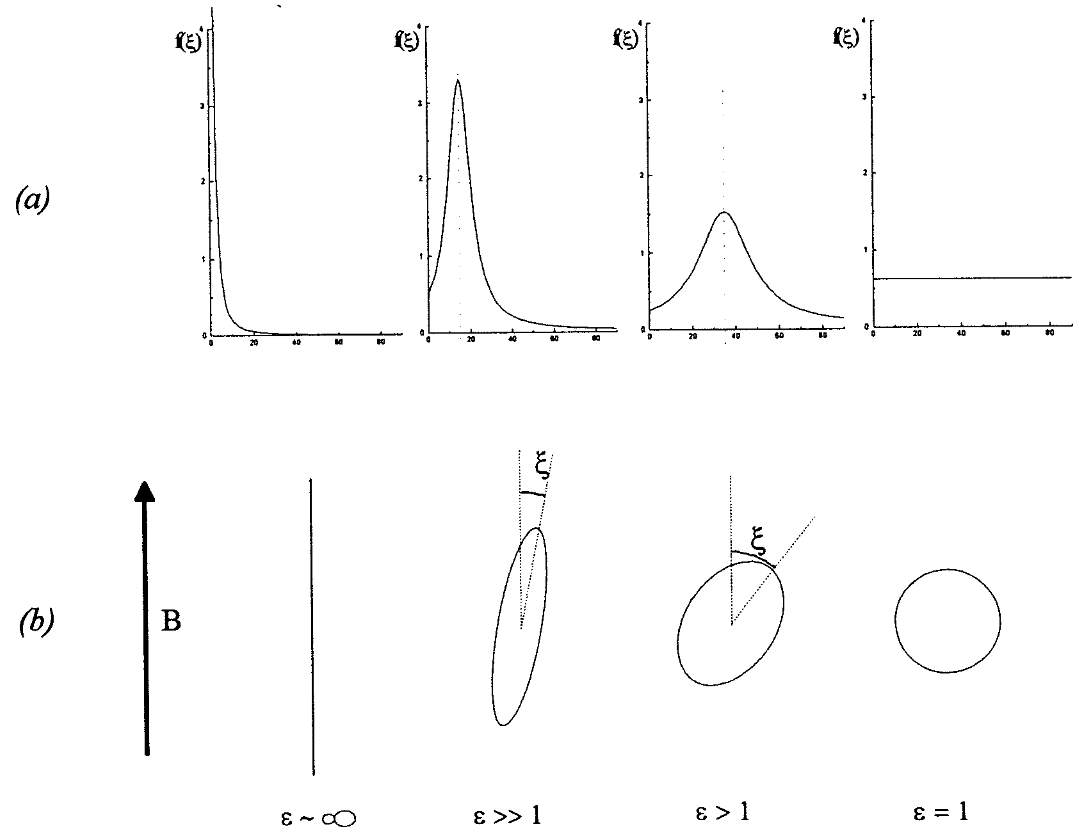

Figure 3 (a) The behaviour of the angular distribution function and (b) the corresponding description of the director behaviour using an elliptical function as the spinning speed is increased from Ω=0 *to above* Ω_c.

Figure 3 provides a view of the overall distribution of the director across the whole sample. In the case of a stationary sample, a monodomain with the director lying along the magnetic field direction is a unique and identifiable case. In a sample spun above Ω_c, many possible spatial variations in the director across the sample can be envisaged that would lead to the observed two-dimensional powder pattern. It is the spatial structure of the director distribution of the two-dimensional powder pattern that we seek to elucidate in this study by an EPR imaging experiment.

5.3.1 The EPR spectra of rotating Nematic Liquid Crystals

The previous section dealt with the physics of the behaviour of nematic liquid crystals when they experience a continuously rotating external field with no consideration as to how this behaviour is explored. We shall now examine how this behaviour has been studied using EPR spectroscopy. Figure 4a shows the EPR spectrum of a stationary sample of the cholestane spin probe dissolved in the nematic phase of the liquid crystal dimer 6.O9O.6 (see Chapter 4) at 112°C. The observed hyperfine splittings $\bar{a}(\xi)$ depend on the angle ξ between the magnetic field and the director as described in section 2.6, Chapter 2. The parallel and perpendicular components of the hyperfine tensor for this spin probe dissolved in this liquid crystal solvent are $\tilde{A}_{\parallel}$ =10.0G and $\tilde{A}_{\perp}$=17.0G. In figure 4b the spectrum of the spinning sample is shown as a function of Ω.

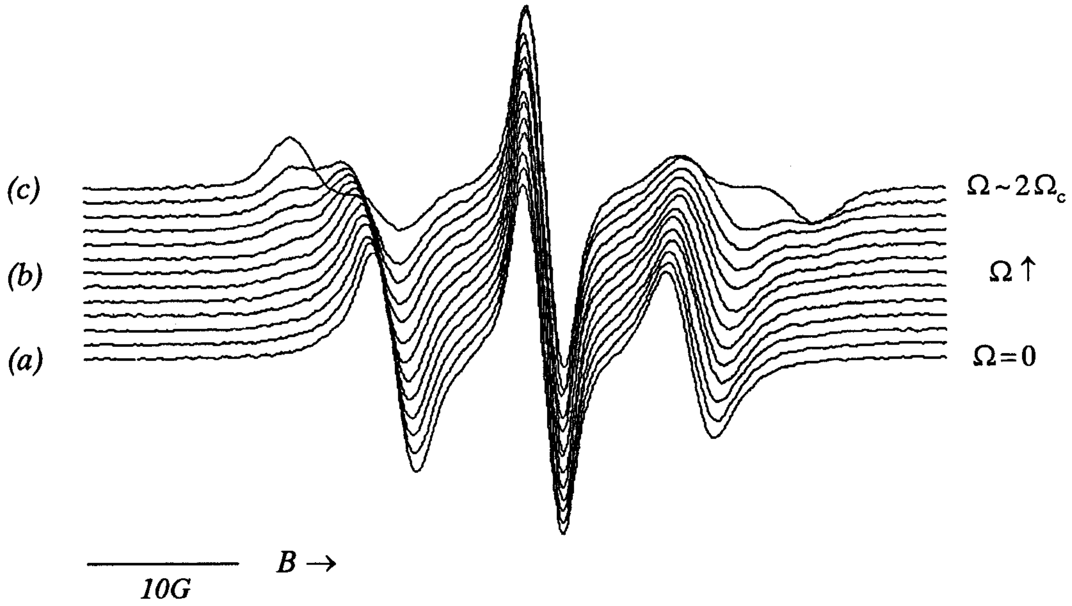

Figure 4 The spectra of a cholestane spin probe dissolved in nematic 6.O9O.6 for (a) a stationary sample and as a function of increasing spinning speed (b) below Ω_c and (c) above Ω_c. Ω_c for this sample is approximately 0.05 rads s^{-1}.

We can see in figure 4a that the spectrum corresponding to the stationary sample shows the antisymmetric lineshapes and the hyperfine splitting $\tilde{A}_{\parallel}$ which indicate that the sample forms a monodomain in which the director lies parallel to the magnetic field. As Ω is increased the hyperfine splitting progressively increases and the outer lines broaden and become less antisymmetric: the increasing hyperfine splitting is indicative of an increase in the angle ξ between the director and the magnetic field and the broadening indicates that there is a distribution of director orientations in the spinning sample. Figure 4c shows a spectrum recorded at higher spinning speeds and now spectral features corresponding to the director lying parallel and perpendicular to the magnetic field are clearly apparent. The apparent absorption lineshapes of the high and low field hyperfine lines indicate that there is a continuous distribution of director orientations between the extremes of the director lying parallel and perpendicular to the magnetic field whilst the similar intensity of the parallel and perpendicular features indicates that the director is uniformly distributed in a plane containing the magnetic field direction. The hyperfine splittings taken from figure 4 were used to calculate the variation of ξ with spinning speed Ω and to determine the validity of equation 5.2: if this is valid then a plot of sin(2ξ) against Ω should yield a straight line with gradient Ω_c^{-1}. Figure 5 shows the plot of sin(2ξ) against Ω for the spin probe cholestane dissolved in 6.O9O.6 corresponding to the spectra shown in figure 4.

As can be seen from figure 5, at low spinning speeds there is a linear correlation between sin(2ξ) and Ω indicating that the behaviour is that predicted by equation 5.2. However, it is clear that this correlation does not persist up to a spinning speed of Ω_c as predicted. This deviation along with evidence of the distribution of the director at intermediate Ω has been observed previously and is well-fitted by the elliptical model for the director distribution [9].

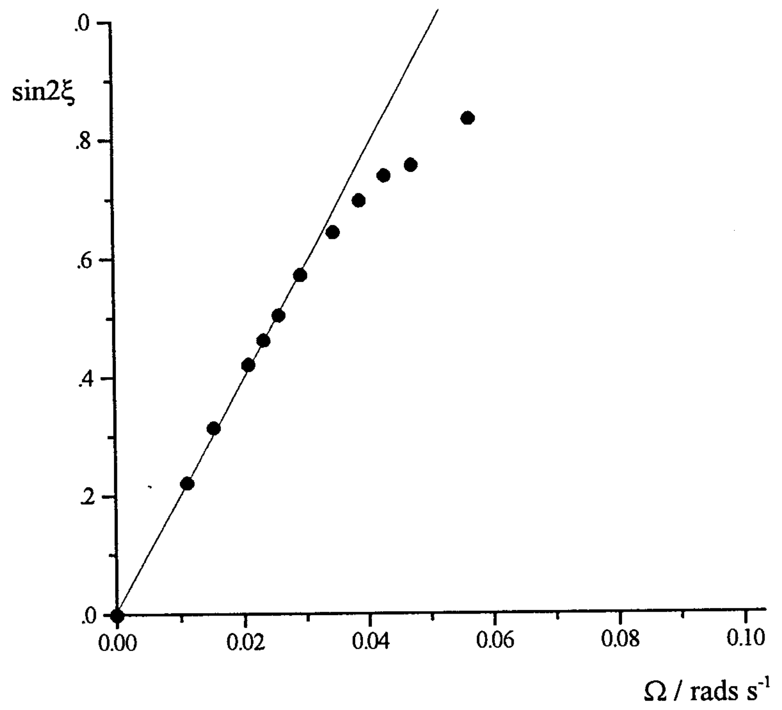

Figure 5 $\sin(2\xi)$ *against* Ω *for the cholestane spin probe dissolved in the nematic phase of 6.O9O.6 .*

These experimental spectra show that the spectrum formed at spinning speeds above Ω_c is indicative of a two-dimensional powder in which the director adopts an isotropic distribution in the plane normal to the spinning axis. However, this analysis of the powder spectrum does not give the spatial arrangement of the director across the sample, it is merely known to be consistent with an overall two-dimensional isotropic distribution. There are, in principle, an infinite number of possible patterns that may be envisaged for the director in space which would lead to the same observed powder spectrum although certain of them can probably be discounted on the grounds of their lack of symmetry. The aim of the experimental work in this Chapter is to determine the actual spatial distribution of the director in the spinning sample that gives rise to the static two-dimensional powder EPR spectrum.

The schematic appearance of the director distribution across the sample of three director distributions is shown in figure 6 in which lines indicate the orientation of the director field at different points in the sample. In this figure the sample spinning axis is orthogonal to the page and the cylindrically shaped sample is assumed to have a circular cross-section, with the cylinder axis coinciding with the spinning axis. This figure displays three of the many possible patterns that would give rise to a two-dimensional powder pattern. In later discussions these are referred to as the radial, tangential and random director distributions: although these distributions are intended to be regarded as extreme cases, the next section looks at how certain features of these distributions would behave in an EPR imaging experiment.

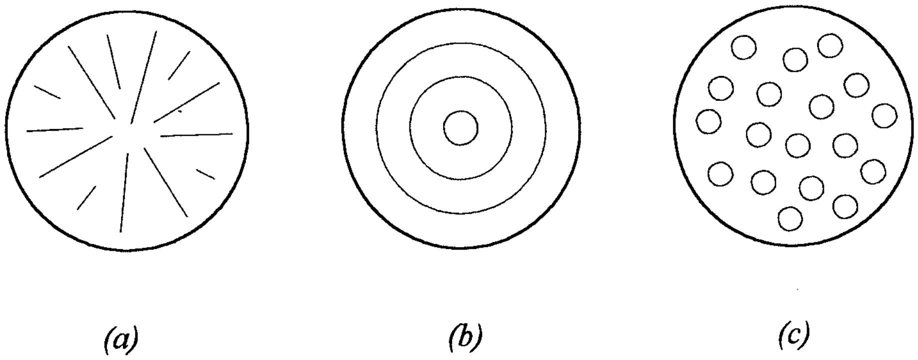

Figure 6 Schematic diagrams for the (a) radial (b) tangential and (c) random director distributions. These pictures show the cross-section of the sample tube with three possible director distributions that would give rise to a two-dimensional EPR powder pattern. The spinning axis lies normal to the page.

In order to distinguish which, if any, of these three distributions approximates to the real behaviour of the director it is necessary to be able to resolve spatially the points in the spinning sample which contribute to specific features in the EPR spectrum, that is, to be able to image the director distribution across the spinning sample. To do this, the EPR spectrum of the sample is acquired whilst it is spun at a spinning speed above Ω_c in the presence of a stationary magnetic field gradient applied across the sample. The theory underpinning this basic imaging experiment using a stationary magnetic field gradient is developed in the next section.

5.4 Magnetic Resonance Imaging

The science of magnetic resonance imaging or MRI, driven largely by its applications in medicine, has made extraordinary progress in recent years, to the extent that it is now routine to be able to produce detailed, whole body images of living systems; MRI is particularly favoured because it is a non-invasive technique. Many of these experiments make use of the proton as the imaging nucleus. The properties of the proton that make it invaluable as a species to image are its wide occurrence, high sensitivity, narrow linewidth and relatively narrow chemical shift range. The narrow linewidth and narrow chemical shift range in particular make pulse techniques routine in the NMR experiment [13]. Imaging using EPR is far less widely applied, largely because of the lesser abundance of suitable paramagnetic species to image but also because the larger natural linewidths coupled with the variability of lineshapes of EPR resonances limits the resolution and complicates spectral analysis [14]. However, by careful and appropriate experimental design, EPR imaging experiments can probe some aspects of the sample character that are not easily accessible by other means. MRI experiments rely on the fact that the observed spectrum depends in some way upon the positions, distributions or dynamics of the species in the sample being imaged. This is achieved by the application of magnetic field gradients to the sample during the experiment, these may be stationary in time and/or space, as we shall use in this series of experiments, or they may be applied transiently as in many of the NMRI applications in which image contrast is determined by changes in dynamics across a sample. Our application of EPR imaging to the study of liquid crystals specifically makes use of the angular dependence of the hyperfine interaction to explore the orientation of the director across our sample and so has no parallel amongst many of the applications of NMRI. A complete account of state-of-the-art MRI would be inappropriate here because of these differences, nonetheless references to some excellent books [14, 15] on the subject are included as they provide very useful background to the principles and techniques of imaging in general, allowing this discussion to concentrate on the features relevant to our specific case. In this account, the magnetic field gradient is always assumed to be stationary in time and space and parallel to the main magnetic field of the EPR spectrometer.

5.4.1 Spectral-spatial imaging

This section sets the scene for the theory underlying the use of a stationary gradient to produce an image of the distribution of a magnetic species. We shall demonstrate the principle here using a single paramagnetic species although what follows applies equally to magnetic nuclei or paramagnetic species. Section 2 in Chapter 2 dealt with the resonance phenomenon in EPR [16]; it was noted then that it is in principle possible to observe the resonance of a single paramagnetic species (for now neglecting any hyperfine interactions) at any frequency provided the magnetic field that it experiences satisfies the resonance condition. If the field experienced by the unpaired electron, B_{exp}, is equal to the applied field, B_{app}, throughout a sample containing a single paramagnetic species, then all of the sample achieves the resonance condition at the same value of the applied field and a single line appears in the spectrum. However, if a magnetic field gradient is applied across the sample during the acquisition of the spectrum, then different values of the applied magnetic field are needed for different points in the sample to satisfy the resonance condition and therefore resonance occurs across a range of values of the applied field. As a consequence, the spectrum recorded in the presence of a magnetic field gradient contains encoded information about the distribution of the paramagnetic species within the sample. This is pictured in figure 7 in which a cylindrical sample and a cuboidal sample respectively present a circular and square cross-section to a magnetic field gradient, for simplicity we assume that both samples contain a uniform concentration of the paramagnetic species which we wish to image (as is the case in a real low molar mass liquid crystal). In figure 7a, the spectrum acquired in zero field gradient is independent of the spatial concentration profile of the paramagnetic species in the sample. When a gradient is applied, as in figure 7b, the field gradient spectrum is dependent upon the concentraion profile of the paramagnetic species in the sample, this relationship is most easily seen in the spectrum displayed in the absorption mode, shown for the sample with a square cross-section. In figure 7c, the effect of a field gradient on a spectrum containing hyperfine splittings is shown.

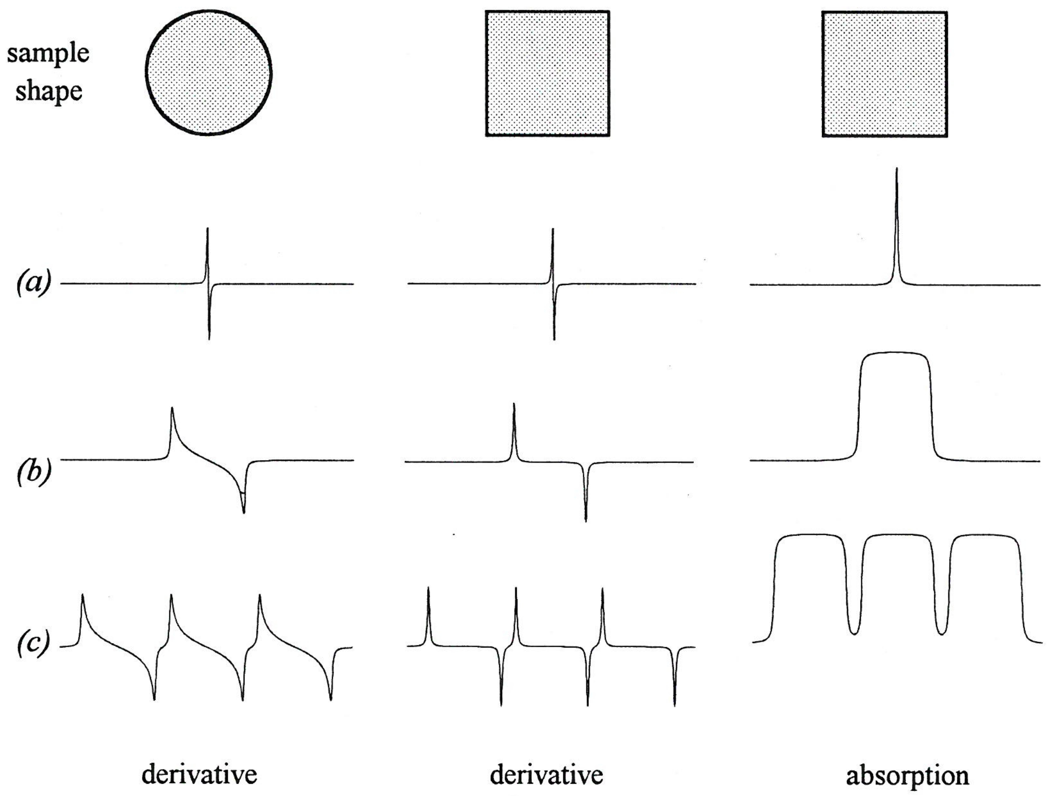

Figure 7 The influence of a field gradient on the sample spectrum, in (a) a single paramagnetic species distributed throughout any sample shape comes into resonance at the same applied field when there is no gradient, when a field gradient is applied, as in (b) and (c) a single species comes into resonance at different applied field strengths and the resulting spectrum reflects the distribution of the paramagnetic species in the sample.

In spectral-spatial imaging the sample is rotated through known angles with respect to the gradient direction and the field gradient spectrum is reacquired. A sample such as that in figure 7 with a square cross-section presents a different concentration profile of the paramagnetic species in the sample to the field gradient direction as it is rotated to different orientations and therefore the spectrum is dependent upon the angle through which the cuboid shaped sample has been rotated. This combined set of spectra are used in projection reconstruction to back-calculate the distribution of the paramagnetic species in the sample, in this case, to calculate that the sample has a square cross-section. It should be noted that rotation of the cylindrical sample which has a circular cross-section produces no change in the projection of the population distribution of the paramagnetic species in the sample onto the gradient direction and no change in the field gradient spectrum. Consequently no new information concerning the shape of the sample and the distribution of the paramagnetic species in the cylindrical sample is obtained by rotating the sample to a new position. Specific use of this fact is made in our experiments because we expressly do not want the field gradient spectrum to depend upon the orientational position of the sample as continuous spinning of the sample is an intrinsic part of the experiment used to produce the sample in a state we wish to image.

In the next part of this discussion we shall outline the relationship between the spectrum of the sample acquired with and without a gradient as this is used in the simulation of the field gradient spectra for one of our model director distributions. Throughout the rest of this discussion of the simulation strategies, the field gradient spectrum is a powder spectrum made up as the sum of a series of subspectra originating from each volume element in the sample. More importantly, for now we shall assume that the shape of the subspectrum emanating from each volume element is identical as it is under this condition that the spectrum in a particular field gradient is dependent only upon the orientation of the sample with respect to the gradient direction. Under this condition, the equation that formally describes the relationship between the spectrum recorded without a magnetic field gradient, $h_0(B)$, and that recorded of the sample in a magnetic field gradient, $h_{fg}(B)$ is [14, 15]:

$$h_{fg}(B) = \int R(\mathrm{r}).C(\mathrm{r})\ (h_0(B - \mathrm{r}.\nabla B)\ )\ \mathrm{dr} \qquad (5.5)$$

in which $R(\mathrm{r})$ represents the distribution of the paramagnetic species in three-dimensional space, $C(\mathrm{r})$ is a function that describes how sensitive the EPR spectrometer is to paramagnetic species at different positions in the microwave cavity (that is, describes the sensitivity distribution of the cavity), ∇B (grad B) describes the magnetic field gradient and the integration is performed over the volume of the sample. If the gradient is assumed to be homogeneous and lies along the Z direction, then equation 5.5 reduces to:

$$h_{fg}(B) = \int R(\mathrm{Z}).C(\mathrm{Z}).\ (h_0(B - \mathrm{Z}.dB/d\mathrm{Z})\ )\ \mathrm{dZ} \qquad (5.6)$$

The integration in equations 5.5 and 5.6 effectively sums over all of the paramagnetic species of the sample and their associated positions, and as a result, the spectrum reflects both their number and position as a concentration profile projected onto the field gradient direction. In equation 5.6, the direction of the magnetic field gradient is constant, therefore the most complete description of the spatial distribution of the paramagnetic species, $R(\mathrm{Z})$, only gives the concentration profile with respect to this single direction. Thus the line integration in equation 5.6 only makes use of the z-coordinate of each of the paramagnetic species in the sample. This is the relationship between the sample shape and the spectra pictured in figure 7.

In the region of an EPR sample in a rectangular cavity the sensitivity of the cavity would be expected to be uniform, therefore $C(\mathrm{r})=1$. The spectrum $h_{\mathrm{fg}}(B)$ is described by a convolution of the spectrum $h_0(B)$ with the concentration profile projected onto the gradient direction, $R(\mathrm{Z})$, which behaves like a weighting function. This is expressed as

$$h_{\mathrm{fg}}(B) = h_0(B) \otimes R(\mathrm{Z}) \tag{5.7}$$

in which $\otimes$ represents convolution. $h_{\mathrm{fg}}(B)$ and $h_0(B)$ are usually known and it is the form of $R(\mathrm{Z})$ that is sought, this can be obtained by the reverse process of deconvolution:

$$R(\mathrm{Z}) = h_{\mathrm{fg}}(B) \otimes h_0(B)^{-1} \tag{5.8}$$

In equation 5.8, $h_0(B)^{-1}$ represents the inverse of $h_0(B)$ such that $(h_0(B))^{-1}\, h_0(B)=1$. Convolution and deconvolution are specific transformations which describe many physical and technical processes. Numerous approaches to convolution and the deconvolution needed to calculate the form of $R(\mathrm{Z})$ have been developed based on, for example, Fourier Transform (FT) algorithms although, in practice, even in ideal conditions this deconvolution is complicated by numerical difficulties, for example, division by zero, and extra subtleties are required [17]. Here we consider only the application of the Fourier Transform to convolution and deconvolution.

5.4.2 Convolution using the FT

The value of the Fourier Transform in calculating the convolution of equation 5.7 makes use of the fact that the Fourier Transform of the convolution of two functions is equal to the product of their Fourier Transforms [14, 15, 18], evaluation of the product is much easier than performing the integration of equation 5.6. Applying this to equation 5.8 we obtain

$$\mathrm{F}(h_{\mathrm{fg}}(B)) = \mathrm{F}(h_0(B)) \,.\, \mathrm{F}(R(\mathrm{Z})) \tag{5.9}$$

from which

$$h_{fg}(B) = \mathrm{F}^{-1}(\ \mathrm{F}(h_0(B))\,.\,\mathrm{F}(R(\mathrm{Z}))\ ) \qquad (5.10)$$

in which F and F^{-1} represent the processes of Fourier and inverse Fourier transformation. This is the technique that is used to calculate the spectra of isotropic samples and from the random distribution of the director in a field gradient, but can not be used for the calculation of spectra for the radial and tangential distributions, as we shall see shortly. The process of deconvolution is more complicated and, as we shall see later, is not applicable to our imaging experiment in which we specifically make use of the fact that the hyperfine splitting is not constant. It is also not useful to us here as the form of $R(\mathrm{Z})$ is of no interest in these experiments and is deliberately defined and invariant.

In spectral-spatial imaging using projection-reconstruction the aim is to obtain the distribution of the paramagnetic species within the sample, that is, the concentration profiles $R(\mathrm{Z})$ are the imaging dimension. For this to be achieved using the methods we have outlined here, the shape of the spectrum emanating from each point of the sample has to be identical as the Fourier Transform uses a single spectrum to represent the spectrum in zero field gradient. Inspection of figure 6 shows that this condition is satisfied for the random trial director distribution in which a two-dimensional powder spectrum emanates from each point in the sample and therefore the Fourier Transform can be used to calculate field gradient spectra for the random distribution. This is not the case for the radial and tangential distributions as there is no single subspectrum $h_0(B)$ that describes the subspectrum in zero field gradient emanating from each point in the sample: each subspectrum depends upon the director orientation at that point (as this determines the angle-dependent hyperfine splitting, g-factor and linewidth) which is not uniform throughout the sample. Therefore, in these cases a different approach is adopted in the calculation of field gradient spectra and this is outlined in the next section. Finally, one last point should be made; as we wish to obtain information about the spatial distribution of the director in a spinning sample we want the director distribution to be the only imaging dimension. We therefore do not want the sample spectrum to depend upon the sample shape in any way. This determines our choice of a cylindrical sample shape and the experimental geometry shown in figure 1 for our experiments so that the concentration profile of the paramagnetic species with respect to the gradient direction is not changed as we spin the sample to produce the director distribution which we wish to study.

5.5 Simulation of field gradient EPR spectra

The simulation of the field gradient EPR spectra corresponding to a more general distribution of the director in our spinning nematic sample is more complex because the subspectra are not homogeneous over the sample in the general case and a different approach must be adopted. In Chapter 2 the conditions for the observation of powder EPR spectra were outlined. In a low molar mass liquid crystal in the fast motion limit (such as the one used in this study) rotations of the probe molecules and of the mesogen molecules with respect to the director are fast but motions of the director are slow on the EPR timescale (~10^{-8}s). Consequently, the nitrogen hyperfine and **g** tensors take on their partially averaged forms with cylindrical symmetry about the director, and the spectrum reflects the director distribution with respect to the magnetic field.

In a stationary magnetic field gradient the spectrum depends upon both the director distribution with respect to the magnetic field and also upon how the director distribution is arranged spatially with respect to the gradient direction. The equation that gives the EPR spectrum of the mesophase when a magnetic field gradient is oriented along the Z-axis is

$$h_{fg}(B) = \sum_{r} \int L(B(\mathrm{Z},\mathrm{d}B/\mathrm{d}\mathrm{Z}), \tilde{B}_r, T_2^{-1})\, \mathrm{f}(\xi)\mathrm{d}\xi \qquad (5.11)$$

in which the spatial encoding is contained within the lineshape function $L(B(Z, dB/dZ), \tilde{B}_r, T_2^{-1})$ and $\mathrm{f}(\xi)\mathrm{d}\xi$ gives the director distribution with respect to the magnetic field. The similarity of equation 5.11 to equation 2.29 in Chapter 2 should be noted, the only modification is the extra term needed to specify the difference between the applied magnetic field and the magnetic field experienced at a point in the sample due to the effect of the field gradient.

For the purposes of our simulations of the spectra of nitroxide spin probes dissolved in the nematic phase corresponding to different distributions of the director, the integral in equation 5.11 is instead evaluated as a sum of subspectra $s_i(B)$ calculated for representative points i in the sample using equation 5.12 in which the simulated field gradient spectrum $S_{fg}(B)$ is given by,

$$S_{fg}(B) = \sum_{\text{sites i}} s_i(B) \qquad (5.12)$$

in which each subspectrum $s_i(B)$ implicitly includes the effect of the field gradient and of the director orientation in the lineshape function,

$$s_i(B) = \sum_{r} L(B(Z_i, dB/dZ), \widetilde{B}_r(\xi_i, \bar{a}(\xi)), T_2^{-1}(\xi)) \qquad (5.13)$$

The angle ξ describes the angle between the magnetic field and the local director defined at each point i which is decided by the director distribution. $B(Z_i, dB/dZ)$ relates the magnetic field experienced by a paramagnetic species with coordinate z_i to the applied field B in the presence of a field gradient dB/dZ, $\widetilde{B}_r(\xi_i, \bar{a}(\xi))$ gives the resonant fields which are calculated from the angle dependence of the g-factor and of the hyperfine splitting using the system of equations developed in Chapter 2 and $T_2^{-1}(\xi)$ describes the angle-dependent linewidth.

This effectively separates the effect of the field gradient from the specification of the director distribution which considerably simplifies the input of the model for the director distribution over the sample. As the sample spectrum is calculated as the sum of representative points in the sample the choice of these points can easily be tailored to reflect the shape of the sample and the concentration profile of the paramagnetic species within the sample. The number of subspectra included in the summation must be large enough to reflect a continuous director distribution over the sample and must not introduce edge effects (However, the number of points included in the summation can easily be varied to check for such distortions, and in the general case, it is easy to modify the summation to simulate the spectrum of any three-dimensional sample rotated about any axis with respect to the gradient). In our case, the distribution of points i for which subspectra are calculated must reflect the uniform concentration of paramagnetic species in the mesophase and their spatial coordinates must reflect the shape of the sample. In the experimental geometry that we consider, the magnetic field gradient lies in the plane in which the director forms a two-dimensional powder pattern and orthogonal to the symmetry axis of the sample. Therefore, the number of points for which subspectra are calculated can be reduced to just those lying within a circle in the plane containing the magnetic field gradient. This reduction assumes that the director orientation is invariant parallel to the axis of the sample tube and is a useful simplification at this preliminary stage.

5.5.1 Simulation of field gradient EPR spectra using EPRIMAGE

Equation 5.12 contains the information necessary to calculate the field gradient spectrum for a particular model for the director distribution including the effects of angle-dependent hyperfine splittings, linewidths and *g*-anisotropy on the spectrum. Equation 5.12 was coded in the program EPRIMAGE, written in Fortran 77 on a PC and compiled using the Salford Compiler. A full program listing is included as Appendix B. Here we describe the operation of the program.

Points lying within a circle on a 50-by-50 square grid in the *XZ*-plane are generated and those lying within a circle are selected to be included in the summation represented by equation 5.12. This is pictured in figure 8a. A director orientation is then assigned to each of these i points depending upon the director distribution that is being modelled for the sample. In figure 8b a tangential distribution is being simulated for the sample.

The Z-coordinate of the point is used to calculate the shift in the magnetic field at a point i with respect to the field experienced at the centre of the circle due to the magnetic field gradient applied along the Z-direction,

$$B_{\mathrm{exp}} = B_{\mathrm{app}} + Z_{\mathrm{i}} \cdot \frac{dB}{dZ} \qquad (5.14)$$

This is shown in figure 8c for one of the i points of the tangential distribution together with the angle ξ between the magnetic field and the local director that is used to determine the angular dependent hyperfine splitting, *g*-factor and linewidth that characterise the subspectrum for this point i. The subspectrum $s_{\mathrm{i}}(B)$ is then calculated as a function of the simulated magnetic field at the origin B_{app} by substituting these quantities into the appropriate lineshape function (see later). The total spectrum for the sample is then calculated as a function of B_{app} by the summation over all sites i indicated in equation 5.12.

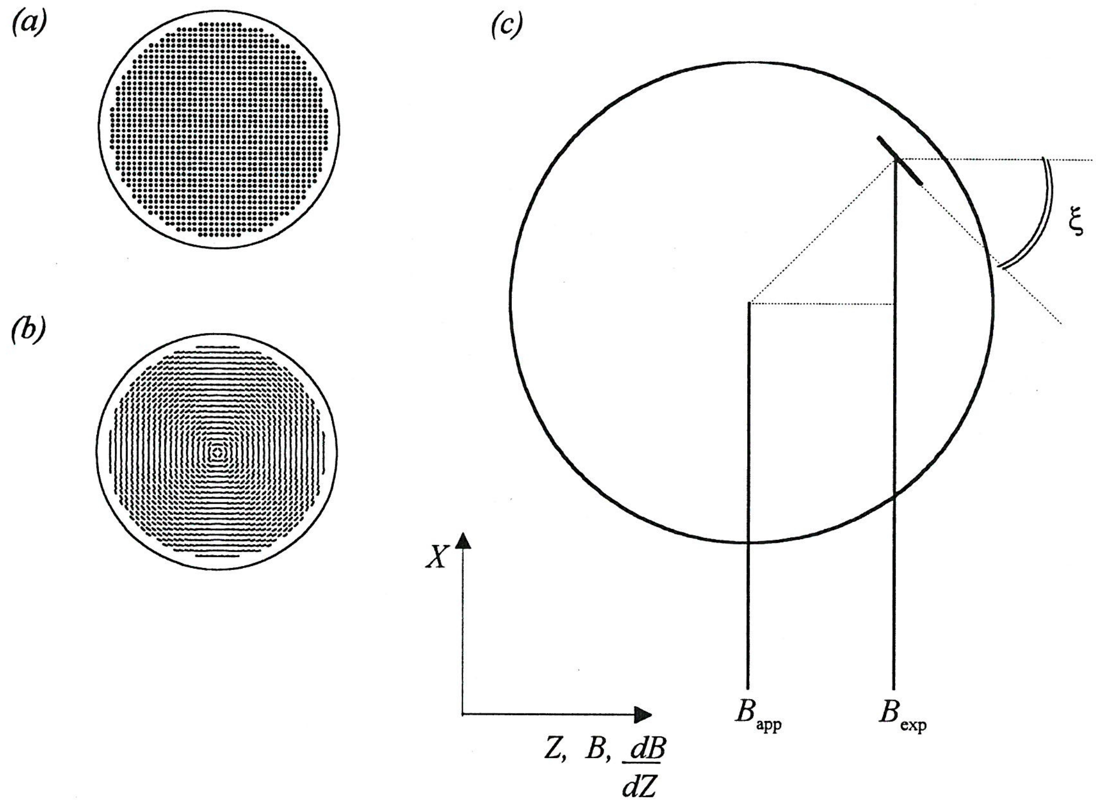

Figure 8 (a) the points for which representative subspectra are calculated (•), (b) the director orientation across the sample imposed by the tangential distribution and (c) the shift in the field due to the gradient and the director orientation at one of the i sites.

5.5.2 Preliminary simulations of field gradient spectra of a spinning nematic sample

In this section we consider the results of some preliminary simulations of field gradient spectra predicted for the radial, tangential and random distributions that had been considered as model director distributions in the nematic phase when the sample is spun above the critical spinning speed Ω_C. It should be noted that we have implicitly made the assumption in considering these model distributions that although the sample itself is spinning, we are treating the director distribution as though it were static with respect to the magnetic field and magnetic field gradient direction. Spectra for the radial and tangential distributions are simulated using EPRIMAGE whilst those for the random distribution are simulated using FT convolution. Spectra were simulated for a number of different values of the field gradient, based on the assumption that the sample tube has an internal diameter of 4mm; the magnitude of the effect of the gradient in G across the sample is then simply given by the product 0.4cm × dB/dZ (in Gcm^{-1}). These simulations for two systems of spin probes dissolved in a nematic phase were intended to help in determining which system and conditions would be most appropriate for the experimental study. Using magnetic parameters based loosely on those of a cholestane and of a tempone spin probe in a low viscosity liquid crystal solvent, simulations for several field gradients for these director distributions are shown in figures 9 and 10. These simulations incorporate only the essential feature that the strength of the hyperfine interaction varies with the angle ξ between $\tilde{A}_{\parallel}$ =10.0G and $\tilde{A}_{\perp}$=17.0G for cholestane and between $\tilde{A}_{\parallel}$ = 12.0G and $\tilde{A}_{\perp}$=16.0G for the tempone spin probe. For now the g-factor is assumed to be isotropic and the linewidths are assumed to have no angle dependence.

From the spectral shapes shown in figures 9 and 10, it is clear that even a moderate field gradient, of $15\mathrm{Gcm}^{-1}$, would allow easy discrimination between spectra arising from the radial, tangential and random director distributions using either spin probe. Some of the features of the simulated spectra in figures 9 and 10 are readily understood, at least on a qualitative level. It is clear that, for small gradients and in this case where an isotropic g-factor is assumed, the centre peak in isolation behaves 'ideally' for the purposes of sample shape determination, with its intensity reflecting the circular sample cross-section projected onto the field gradient direction (see figure 7). This is not the case for the high and low-field peaks because they are also split by the angular-dependent hyperfine splitting.

In examining the outer peaks in figures 9 and 10 there are a number of points to note. For example, it is clear that features corresponding to the director lying parallel to the magnetic field remain relatively intense in the field gradient spectrum of the tangential distribution as compared with the perpendicular features when viewed against the intensity of the central line. This can be understood by a simple consideration of the slice selection that occurs in the one-dimensional imaging experiment. This is represented in figure 11 in which regions that are shaded similarly experience the same magnetic field when the field gradient is applied. The field gradient does not spread out the parallel features over a range of magnetic field values because the tangential distribution places all parallel regions of the director in a slice of the sample

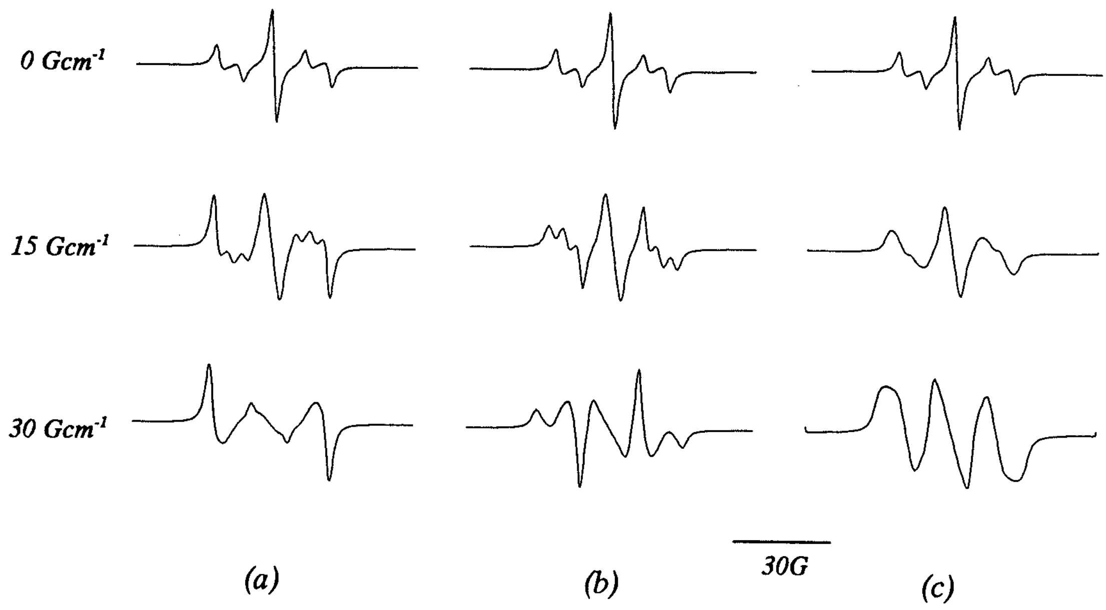

Figure 9 Simulated first derivative spectra for (a) radial (b) tangential and (c) random distributions of the director using parameters typical of a cholestane spin probe for a range of field gradients.

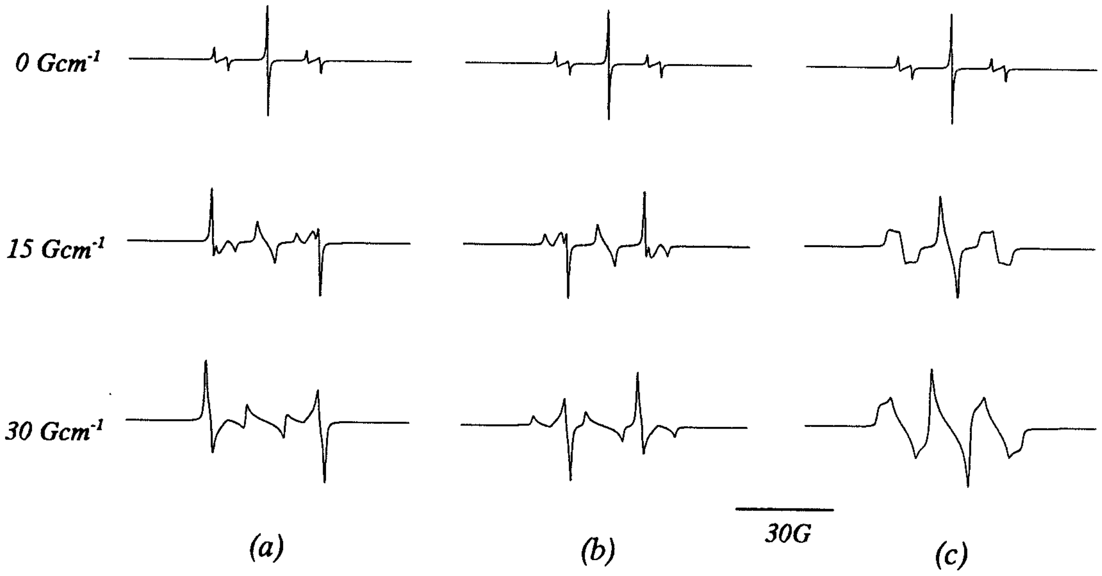

Figure 10 Simulated first derivative spectra for (a) radial (b) tangential and (c) random distributions of the director using typical tempone parameters under the same conditions as in figure 9 for a range of field gradients.

that experiences the same magnetic field and so they come into resonance simultaneously; the effect of the gradient is therefore minimal on these features. Further, the tangential distribution distributes perpendicular regions of the director in the sample so that they experience the most pronounced effect of the magnetic field gradient and this is seen in the simulations in which the perpendicular features of the spectrum are smeared. This is shown in figure 11. In the simulations for the radial distribution the reverse is true, and so it is the parallel features that are smeared out and the perpendicular features that largely retain their intensity as the field gradient is increased. The random distribution calculation shows smearing of both parallel and perpendicular features, this is to be expected as the field gradient acts on both parallel and perpendicular regions as they are both distributed uniformly throughout the sample.

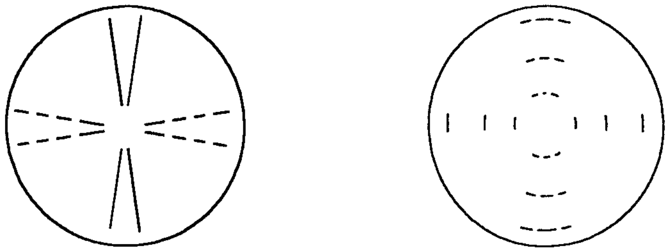

(a) *(b)*

Figure 11 The location of 'parallel' (----) and 'perpendicular' (——) regions of director in the (a) radial and (b) tangential director distributions.

As expected, in zero field gradient there is no difference between the spectra calculated for the radial, tangential and random distributions. As the field gradient is increased the differences between the spectra from the three distributions become more pronounced whichever spin probe is used. It is noted that simulations indicate that the narrower lines of the tempone spin probe leads to better resolution at all field gradients. A comparison of the spectra shown in figures 9 and 10 shows that a larger gradient can be applied to the sample containing the tempone spin probe before overlap of the different hyperfine lines occurs on account of the smaller anisotropy in the hyperfine tensor $(\tilde{A}_\perp - \tilde{A}_\parallel)$ and larger parallel hyperfine splitting $\tilde{A}_\parallel$ for the tempone spin probe, whilst a larger gradient improves our ability to use the spectra to distinguish between the three model distributions. The significance of not overlapping hyperfine lines may prove very important in distinguishing between other, less extreme, distributions than those considered here. In the analysis of the field gradient spectra it is useful that there is no ambiguity as to the origin of each line. This stems from the fact that in this experiment there is only a single imaging dimension, and as such there is no unique transformation that can be applied to the complete spectrum that relates every spectral feature to a particular director orientation at a unique point in the sample. This is shown in figure 12a, the spectrum will identify only the distribution of the director orientation within a notional slice across the sample, which is rather uniform in the highlighted slice for the tangential distribution. However, this alone does not preclude the possibility of other director distributions that could be envisaged, as any allocation of the same distribution within any one slice will also lead to the same observed spectrum: there are therefore many director distributions that are consistent with the observed spectra even in the presence of a gradient. For this reason, it is often preferable to work in the regime in which no overlaps of different hyperfine lines occurs so that a thorough understanding of the origin of each line or feature allows us to discount some of these possibilities immediately. Ideally a two-dimensional image would be produced for which a unique transformation would relate the director orientation at every point to the observed spectrum. However, this is mathematically and technically beyond the scope of the current investigation. This ideal is pictured schematically in figure 12b in which a two-dimensional image would allow us to ascertain the director at a point in two-dimensional space, allowing us to exclude immediately many more of the possible director distributions over the sample.

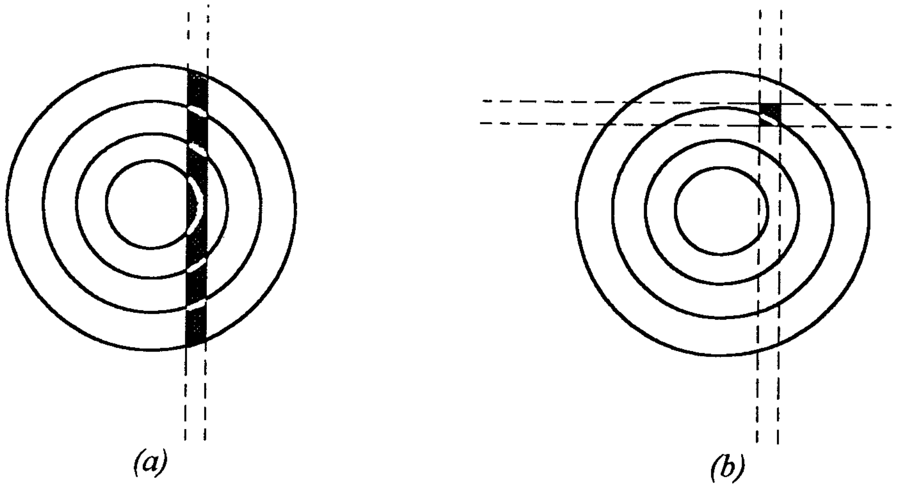

Figure 12 A schematic representation, using the tangential distribution, in (a) a one-dimensional image gives only the director distribution within a slice defined by the gradient direction, in (b) a two-dimensional imaging experiment provides more discriminating information about the director within the sample.

At this point we should repeat that the models of the director distribution so far considered are by no means exhaustive, but they do serve to demonstrate that an imaging experiment using EPR with a single imaging dimension is a useful means of probing the spatial distribution of the director within the two-dimensional powder pattern. For simplicity we have assumed that the director distribution is uniform along the axis of the sample tube. We have also assumed that any dynamics of the director distribution can be ignored by our characterisation of the director distribution in the spinning sample as a fictitious space-fixed distribution. The validity of these assumptions is explored later in the light of experiment.

5.6 Experimental

5.6.1 General

Two samples were prepared. Both samples are made up using the liquid crystal I35, the structure and phase behaviour of I35 is shown in figure 13. Sample 1 uses the cholestane spin probe and Sample 2 uses the tempone spin probe (see Chapter 2).

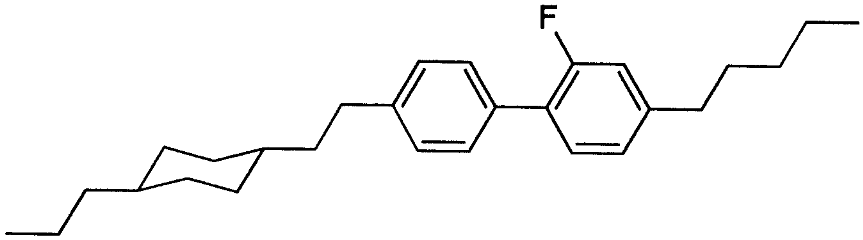

$$\mathrm{Cr}\,\underline{\quad 30^{\circ}\mathrm{C}\quad}\,\mathrm{N}\,\underline{\quad 106^{\circ}\mathrm{C}\quad}\,\mathrm{I}$$

Figure 13 The molecular structure and phase behaviour of the nematic liquid crystal I35 [19].

I35 was chosen because it has a long nematic range and supercools to give a relatively stable nematic phase at room temperature. The long nematic range above room temperature means that any sample heating due to friction during continuing rotation will have a minimal effect on the observed hyperfine splittings. In addition, the orientational order and the individual molecular reorientation times are such that typical nitroxide spin probes dissolved in it give narrow and well-separated hyperfine lines. The twist viscosity of I35 is high and therefore Ω_c is relatively low at room temperature ($\Omega_c \sim 1$rad s^{-1}); thus spinning speeds above Ω_c are easily attainable whilst maintaining tune of the cavity during sample spinning.

The cholestane spin probe is chosen for sample 1 as a standard system as previous work in related experiments has made use of the cholestane spin probe [9]. The tempone spin probe is chosen for sample 2 for a number of reasons: at first glance it might not appear ideal as its nearly spherical shape results in rather weak ordering in a typical nematic liquid crystal and therefore a rather small dependence of the hyperfine splitting on the angle between the magnetic field and the local director. However, the weak anisotropy of probe ordering means that the different hyperfine lines remain separate even in the presence of relatively large (30Gcm^{-1}) field gradients across the sample. This means that different hyperfine peaks in the spectrum remain separated from each other under larger field gradients than is the case for, say, cholestane, that orders more fully when dissolved in a liquid crystal solvent such as I35. In addition, the small size, shape and chemical structure of the tempone spin probe mean that at room temperature in I35 its molecular rotational motions are very rapid which results in narrow hyperfine lines: this too improves the resolution, especially in conjunction with the larger gradients that can be used for this system without overlapping different hyperfine lines.

5.6.2 Experimental Setup

The experiments described here were carried out at the laboratory of Professor G.F. Pedulli in Bologna, Italy [20]. The experiments used a Bruker ESP 300 spectrometer operating at X-band. Gradient coils attached to either side of the TE_{102} rectangular cavity provide for a stationary gradient of up to 300 Gcm^{-1} across the sample, this corresponds to a difference in the field of up to 120 G across the sample inside a narrow-walled quartz EPR tube of inner diameter 4mm. The top of the sample tube was attached by a rubber sleeve to the drive shaft of a synchronous dc motor mounted across the poles of the magnet. The position of the sample was maintained in the centre of the cavity by a guiding dewar situated in the cavity. The motor could bedriven up to a maximum speed of 60 rads s^{-1}. The drive from the motor to the sample was ungeared.

5.6.3 Sample preparation

The inner diameter of the Bruker sample tube was known to high accuracy. A solution of the spin probe in dichloromethane was added to the EPR tube and then a spectrum recorded to check that a sufficient quantity of the spin probe had been added, after which the solvent was removed on a vacuum line. The liquid crystal was then added (~0.2g) to a depth of approximately 2cm in the tube. The sample was then degassed using a freeze-thaw cycle to remove dissolved oxygen. The sample tube was positioned in the cavity so that the rounded bottom of the tube sits outside of the region of the sample from which data was acquired, this is important as in the subsequent simulations a cylindrical sample shape is assumed. This also minimises the influence of surface effects from between the bottom of the tube and the bulk of the sample from which the EPR signal is collected.

5.6.4 Experimental Protocol

The EPR spectrum of a stationary sample of the spin probe in the nematic phase was first recorded in the absence of any field gradient. This spectrum was fully parameterised, that is, the line positions, hyperfine splittings and linewidths of the three hyperfine lines in the spectrum were measured. A field gradient was then applied and the spectrum of the stationary sample was recorded. The field gradient is then switched off whilst the sample was spun with an angular velocity greater than Ω_c to obtain the two-dimensional powder pattern. This spectrum was also parameterised as fully as possible. The spectrum of the spinning sample was then acquired in the presence of the field gradient chosen for the experiment.

5.7 Results

5.7.1 Sample 1: Cholestane in I35

The spectrum of the stationary sample 1 recorded without a field gradient and in a field gradient of 60Gcm^{-1} is shown in figure 14a and b respectively. Figure 15a shows the spectrum for sample 1 rotating at an angular velocity of 15 rads s^{-1} in zero field gradient, and then, in 15b, as a function of increasing magnetic field gradient. The spectrum of figure 15c was acquired in a magnetic field gradient of 60Gcm^{-1} shortly after the sample spinning had begun during a second series of spectral acquisitions.

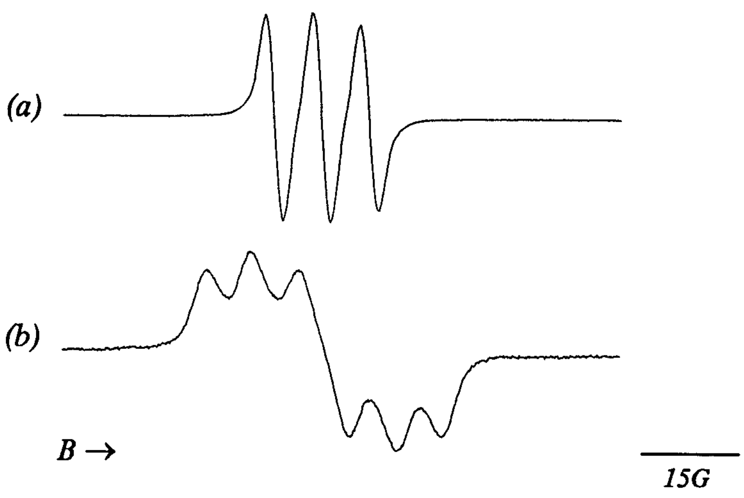

Figure 14 The spectrum of cholestane dissolved in I35 in (a) zero field gradient and (b) 60Gcm^{-1} field gradient.

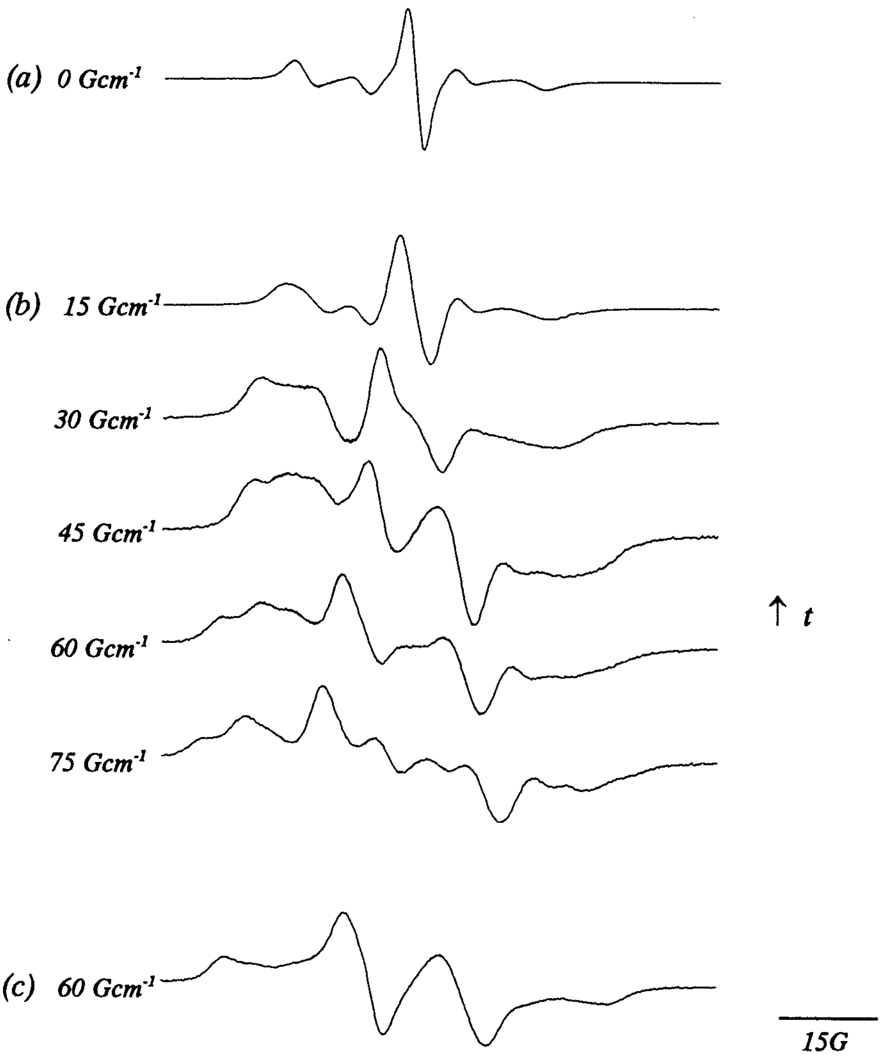

Figure 15 The spectrum of a spinning sample of cholestane in I35 in (a) zero field gradient, (b) as a function of increasing field gradient and (c) repeated at 60Gcm^{-1} field gradient.

5.7.2 Sample 2: Tempone in I35

In the absence of a gradient the spectrum of the stationary sample 2 is shown in figure 16a, the spectrum recorded in a field gradient of 15Gcm^{-1} is shown in figure 16b. Both spectra show the ^{13}C satellites very clearly. Figure 17a shows the spectrum of sample 2 at a spinning speed of 15 rads s^{-1} recorded without a magnetic field gradient. Figure 17b shows the spectrum of the sample during continuous spinning at 15 rads s^{-1} recorded at approximately 5 minute intervals over a 25 minute period using a constant magnetic field gradient of 15Gcm^{-1}. It is important to note that there is no change in experimental conditions during the acquisition of the series of spectra pictured in figure 17b. This is discussed further in the following sections. Figure 17c shows the spectrum of the spinning sample acquired in the presence of a magnetic field gradient of 30Gcm^{-1}. It is clear that this larger field gradient leads to an overlap of the different hyperfine lines as expected.

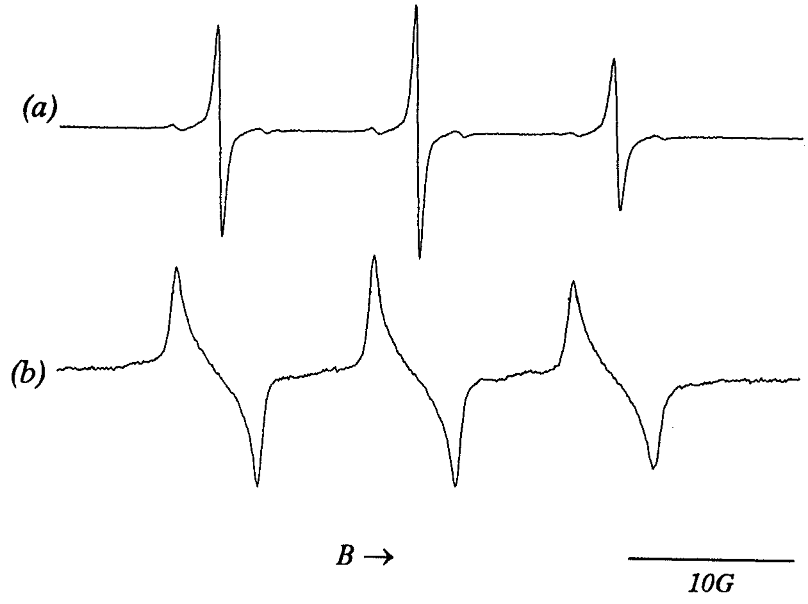

Figure 16 The spectrum of tempone in I35 at room temperature recorded in (a) zero field gradient and (b) in a field gradient of 15Gcm^{-1}.

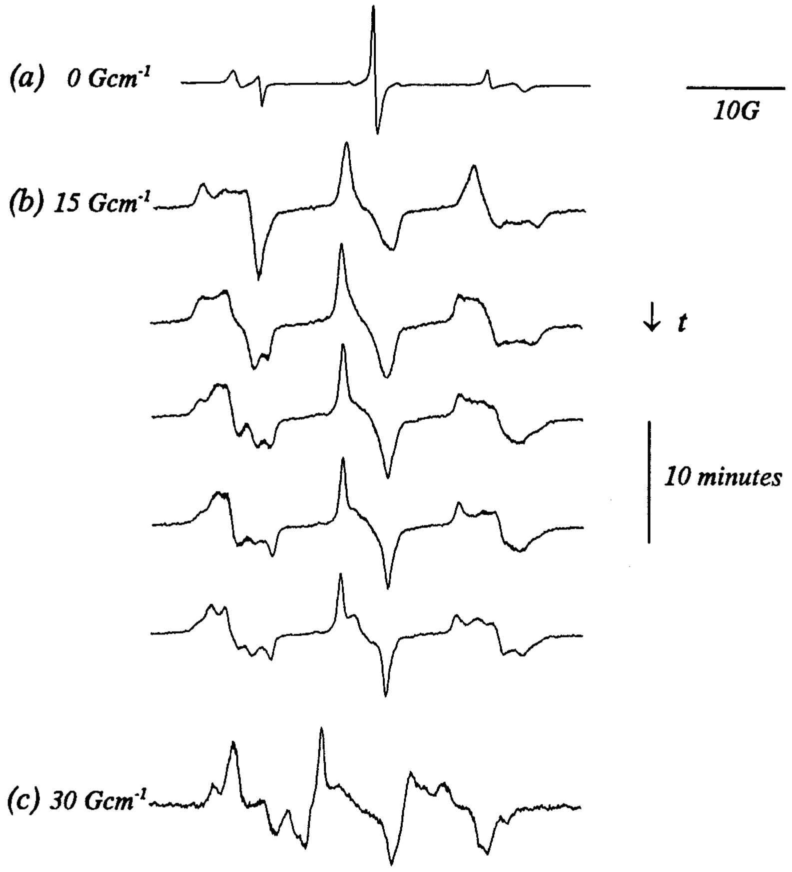

Figure 17 The spectrum of a spinning sample of tempone in I35 at room temperature in (a) zero field gradient, (b) as a function of time in a field gradient of 15Gcm^{-1} and (c) in a field gradient of 30Gcm^{-1}.

5.7.3 Parameterisation of zero field gradient spectra

The spectra of the stationary samples without a magnetic field gradient were analysed by both the Bruker WIN-EPR software which uses a cursor to indicate peak position and by a least-squares fitting routine in Microcal Origin that fits the whole line. The fitting routine required the lineshape function, number of peaks to be fitted and their approximate positions to be input by the user. The hyperfine lines for sample 1 were best fitted by a 50:50 mixture of lorentzian and gaussian lineshapes. The hyperfine lines for sample 2 are well-fitted by a lorentzian lineshape. This analysis yielded the linewidth and, using the calculated peak positions, the parallel splittings, $\tilde{A}_{\parallel}$, between the three hyperfine lines for the spin probe in each sample. In the case of sample 2, the tempone spin probe in I35, the ^{13}C satellite lines were not included as part of the fitting process but their approximate positions were estimated using the cursor in WIN-EPR, the hyperfine coupling to ^{13}C nuclei was estimated from the additional splitting about the central hyperfine line to be 2.63G in the monodomain sample. The parameters for the monodomain samples in the absence of a magnetic field gradient were used to estimate the perpendicular linewidth and hyperfine splitting for the two-dimensional powders in the absence of a gradient. The perpendicular hyperfine splitting was calculated using the calculated parallel hyperfine splitting and the extrapolated isotropic hyperfine splitting using relation 2.28 (that is, $\tilde{A}_{\perp} = \frac{1}{2}(3a - \tilde{A}_{\parallel})$). This can be compared with the perpendicular hyperfine splitting estimated using the cursor in the WIN-EPR program. The perpendicular linewidth in the two-dimensional powder pattern was estimated from the parallel linewidth obtained from the fitting using the ratio of the full-width half-maximum of the perpendicular line to that of the parallel line. The equations that describe the angle-dependence of linewidths were covered previously in Chapter 2. The linewidth coefficients in equations 2.33 and 2.34 are not easily measured directly for either system. However, the values taken from the monodomain spectrum and estimates of the perpendicular linewidth from the two-dimensional powder spectrum were used to calculate linear combinations of the linewidth coefficients. This is sufficient to describe the linewidth for each line separately assuming $P_2(\cos\xi)$ dependence, that is, taking $P_4(\cos\xi)$ terms as zero. This is not an unreasonable approximation given that variations in the trial director distributions have a much larger effect on the simulated spectra.

From the zero gradient spectra of the time-invariant two-dimensional powder spectra of the spinning samples in relation to those of the stationary sample, it is clear that both high and low-field lines are broadened in relation to the central line which has a very similar intensity in the spinning sample to that in the stationary sample. This is simply because the central line is split only by the small effect of the *g*-anisotropy, (~0.4G at ~9.38GHz) while the outer lines are also split by the much larger anisotropy in the hyperfine interaction ($\tilde{A}_{\perp}$-$\tilde{A}_{\parallel}$ ~3.4G for the tempone spin probe in I35). The centre of the spectrum arising from perpendicular regions, and indirectly the *g*-anisotropy, of each sample was calculated from the difference between the parallel and perpendicular peaks of the high and low field hyperfine lines. This calculation neglects the small contribution of the *g*-factor to the hyperfine splitting. This is shown for sample 2 in figure 18.

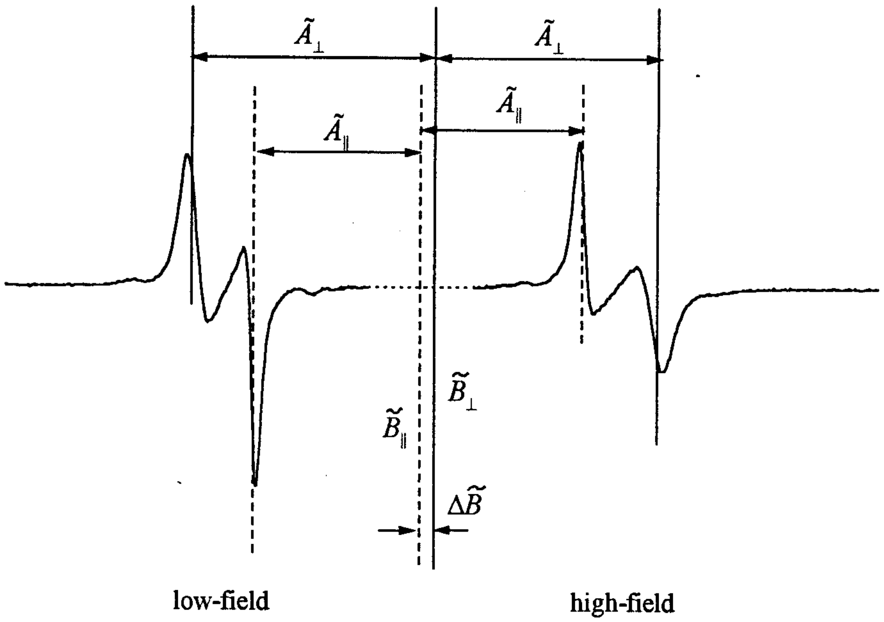

Figure 18 Calculation of the g-anisotropy, shown for tempone dissolved in I35.

The calculated spectral parameters from the fitting using Origin and the additional analysis using WIN-EPR is shown in Table 5.1 and 5.2. The simulated spectra in zero field gradient calculated using these parameters are shown in figures 19 and 20 respectively together with the appropriate experimental spectra from the earlier figures. An isotropic ^{13}C splitting of 2.63G has been added in the simulations of sample 2 spectra shown in figure 20.

Table 5.1 The fitted and calculated parameters for Sample 1 (cholestane spin probe).

hyperfine line	$\tilde{B}_r$ / G	$\tilde{A}_\parallel$ / G	$\tilde{A}_\perp$ / G	T_2^{-1} (‖) / G §	T_2^{-1}(⊥) / G §
$m_I = +1$	3338.6			1.6	1.8
		7.2	18.25 †		
$m_I = 0$	3345.8			1.5	1.5
		7.2	18.25 †		
$m_I = -1$	3353.0			1.7	1.9

§ fitted by a 50:50 mixture of lorentzian and gaussian lineshapes.
† Calculated using an extrapolated value of 14.6G for *a*.

Table 5.2 The fitted and calculated parameters for Sample 2 (tempone spin probe).

hyperfine line	$\tilde{B}_r$ / G	$\tilde{A}_\parallel$ / G	$\tilde{A}_\perp$ / G	$T_2^{-1}(\parallel)$ / G §	$T_2^{-1}(\perp)$ / G §
$m_I = +1$	3333.1			0.34	0.62
		12.3	15.75 ‡		
$m_I = 0$	3345.4			0.32	0.58
		12.3	15.75 ‡		
$m_I = -1$	3357.7			0.42	0.76

§ A purely lorentzian lineshape function provides the best fit for all hyperfine lines.
‡ Calculated using an extrapolated value of 14.6G for a.

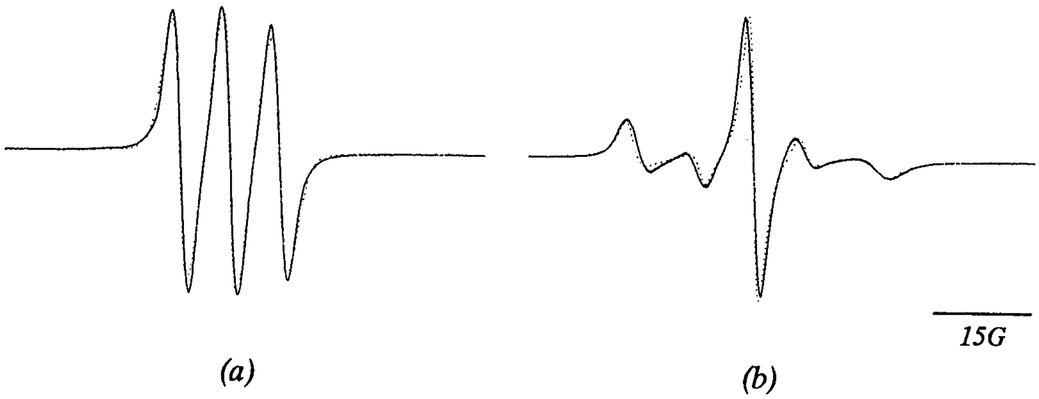

Figure 19 Comparisons between experimental (——) and simulated (·······) spectra of the (a) stationary and (b) spinning sample 1 (cholestane spin probe).

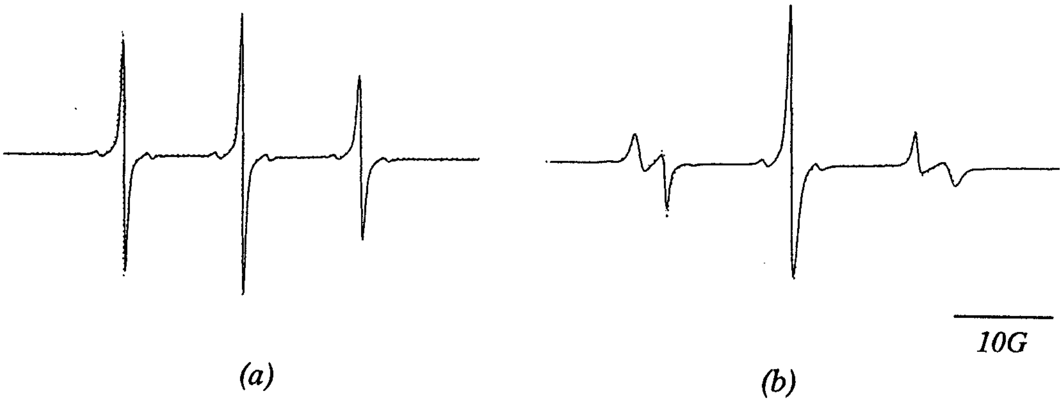

Figure 20 Comparisons between experimental (——) and simulated (·······) spectra of the (a) stationary and (b) spinning sample 2 (tempone spin probe).

The agreement between the calculated and experimental spectra is generally good.

This is important, as good simulations of the spectra obtained when a field gradient is applied rely on a good initial parameterisation of the system. The next section concentrates on the analysis of the spinning samples acquired in non-zero field gradients.

5.8 Analysis

A cursory qualitative analysis of the results obtained using sample 1, cholestane in I35, and compared with the preliminary simulation results shown in figure 9 of section 5.5 shows that even this very crude parameterisation appears to reproduce some of the features that are seen in some of the experimental field gradient spectra of the rapidly spinning sample. However, it is noted that the spectrum of the sample in a field gradient of 60Gcm^{-1} was not constant as seen by the difference between the spectrum of figure 15c and that forming part of the sequence of figure 15b. This is explored further in the spectra of figure 17b which shows a time sequence for the spectrum of sample 2 spinning in a constant magnetic field gradient. This series of spectra show an unexpected temporal evolution of the spectrum which was hinted at by the observation of the two different spectra for sample 1 at a field gradient of 60Gcm^{-1}.

It has been mentioned previously that the EPR spectrum of a spinning sample accelerated from rest recorded in the absence of a field gradient initially evolves rapidly but then subsequently remains static [6]. Any explanation of the subsequent evolution of the director through the series of field gradient spectra shown in figure 17b must therefore also be consistent with the fact that EPR spectra of the same sample acquired without a field gradient over the same period would show no departure from the two-dimensional powder pattern. From this series of spectra, it is clear that the one-dimensional imaging experiment shows evidence of a more complicated behaviour of the director following the initial settling than has been observed in previous experiments that did not use a field gradient [9]. The spectra of the sample showing this evolution of the distribution broadly fall into two categories: those of figures 15c and 17bi which shows rather strong parallel features and the rest which are much more continuous in their variation and show some of the features seen in simulations of the random director distribution. It is clear also that changes in the spectra occur on a relatively slow timescale, of the order of minutes between acquisition of successive spectra, and that there is no significant evolution of the director distribution on the timescale over which a single spectrum is acquired, which is of the order of 1 minute. Evidence for this is the fact that both high and low field portions of any one spectrum show the same features. During the period over which the spectra were acquired (~25 minutes), no repeating pattern was discernable in the appearance of the field gradient spectrum. None of the preliminary models considered earlier made any provision for an evolution of the director distribution. This aspect of the behaviour of the director distribution in the spinning sample is considered in more detail later in the analysis.

Looking beyond the observed time dependence, it is useful at this point to consider again the simulated spectra for the three extreme models suggested earlier and to use these to try and pick out recognisable features in any of the experimental sequence of spectra. In figure 21 several simulated spectra for the radial, tangential and random director distributions are shown again for sample 1, with the simulated field gradient corresponding to that of the experimental dataset. These simulations now make use of the parameters determined in the previous section which, from the similarities seen in figure 19, appear to be a good approximation to the real spectral parameters. For the purposes of this comparison, we make the assumption that our parameterisation of the subspectra is broadly correct. Therefore we assume that deviations of the simulation parameters from the real experimental parameters may cause some cosmetic differences between the simulated and experimental spectra if the director distribution used in the simulations is correct. However, more major discrepancies between the simulated and experimental spectra must be attributed to more significant deviations or failures of these models to represent the real character of the spatial distribution of the director distribution within the spinning sample.

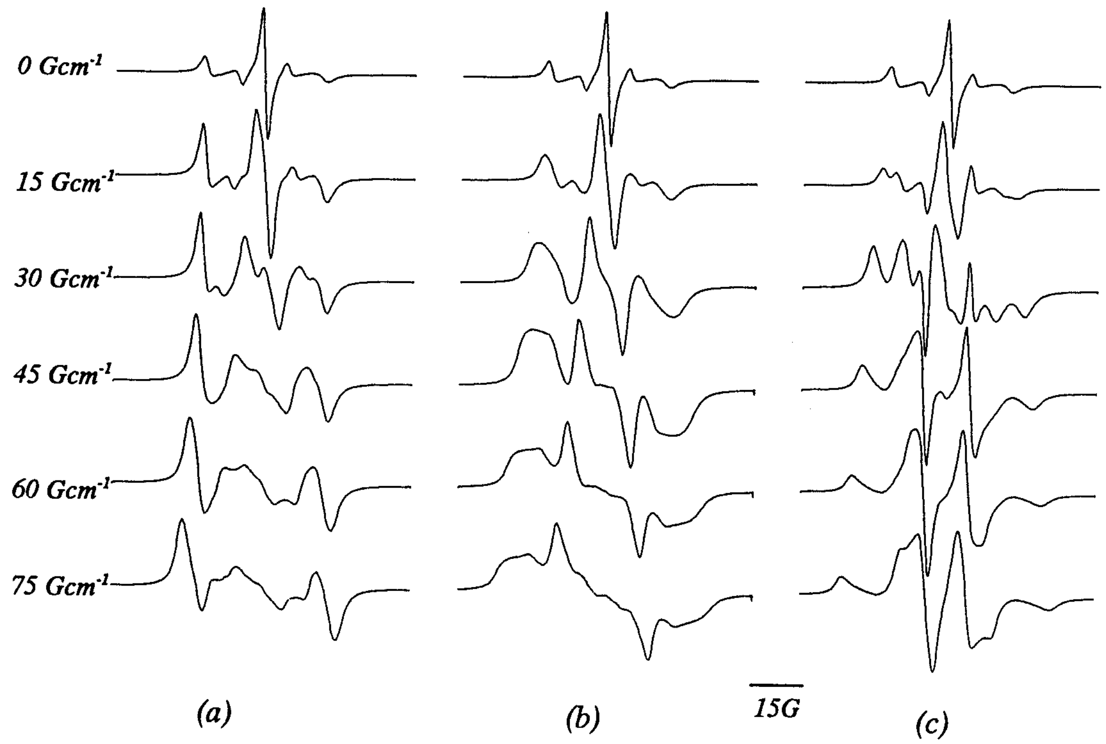

Figure 21 Simulations of sample 1 spectra (cholestane spin probe) for (a) the radial (b) the random and (c) the tangential director distributions in a range of field gradients using the parameters listed in Table 5.1.

None of the simulations in figure 21 fit the experimental spectra obtained for sample 1 exactly. The poorest agreement in this regard is seen for the radial distribution. This distribution concentrates spectral intensity in the perpendicular features when a gradient is applied which disperses much of the spectral intensity away from the centre of the spectrum. The central regions of the experimental spectra clearly contain significant spectral intensity and as a result of this serious failing the radial distribution can largely be discounted. The tangential distribution emphasizes the parallel features which maintains a significant concentration of intensity in the central region of the spectrum as the gradient is increased which is broadly in accord with experiment.

In particular, the tangential distribution introduces a pronounced wave in the central region of the spectrum which also appears in the field gradient spectra of the spinning sample. The random distribution tends to be dominated by the splitting of the central line overlying a weaker, more continuous background modulation of intensity.

For now we simply note that several of the experimental field gradient spectra of figure 15b and c are in broad agreement with both of these patterns.

Relevant simulated spectra for sample 2 using the parameters from table 5.2 are shown in figure 22 for the radial, random and tangential distributions.

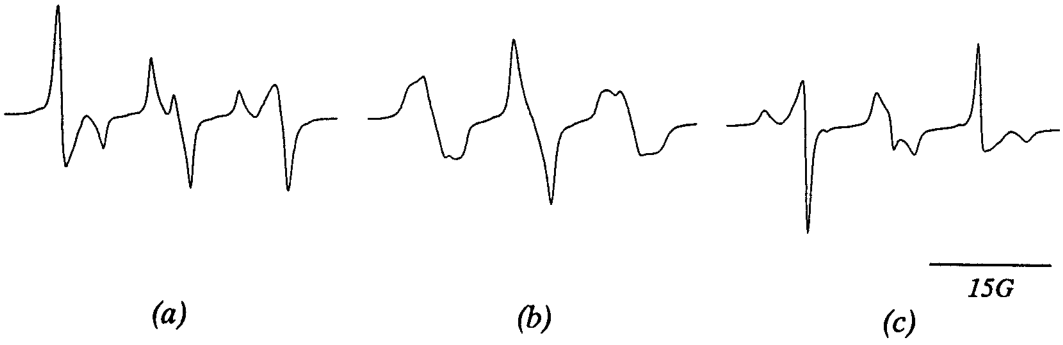

Figure 22 Simulations of sample 2 spectra (tempone spin probe) for (a) the radial (b) the random and (c) the tangential director distributions in a field gradient of 15G cm^{-1} using the spectral parameters listed in Table 5.2.

Focusing attention on the experimental spectrum of figure 17bii to v, it is clear that these spectra show a similarity to the spectrum calculated for the random director distribution and shown in figure 22b. Again, the radial distribution appears to give rise to spectra that are in poor agreement with the experimental spectra for the reasons discussed for sample 1. It is noted that a small peak and an equivalent trough is observed in the centre of the simulations of the radial and tangential distributions respectively: this has been identified as having an origin in the g-anisotropy as it appears as soon as any g-anisotropy is included in the simulation. Nevertheless, a look at the experimental spectrum in figure 17bi shows features similar to those in the spectrum of the tangential distribution in that parallel features are of high intensity, whilst the perpendicular features show intensity smeared along the field axis. However, it is also clear that the experimental spectrum shows parallel features that are weaker and more spread out than would be predicted for a tangential distribution. As a result of the similarities that have been identified between spectra simulated using the random and tangential distributions and the experimental field gradient spectra observed for both samples, we examine in the next section the effect of a locally-defined elliptical distribution function that bridges the gap between the tangential and random distributions.

5.8.1 An elliptic distribution function

The trial distributions considered thus far contain no adjustable parameters in their determination of the director orientation at a particular point in the sample and therefore do not provide a model to which further small adjustments to the distribution can be made to build in those features of the distribution that improve the agreement between simulated and experimental EPR spectra. However, a variation of the elliptical distribution considered in section 5.3 can be parameterised to produce intermediate forms between the random and tangential director distributions and the field gradient spectra for these distributions can be simulated and compared with experiment. It is important to note that here, as in the use of the elliptical distribution to explain the director distribution in the sample spinning below Ω_c, the family of elliptical distributions is being used in an empirical way, as a tool with which to try and understand the features of the distribution, but that any such explanation has no firm basis in theory.

The elliptical distribution function used in this context is exactly the same as that considered earlier to explain the observations of line broadening in the EPR spectrum observed at spinning speeds below Ω_c, except we now introduce one important modification in the frame of reference. At speeds below Ω_c the orientation of the axes of the ellipse that was used to determine the angle-dependence of the director distribution was specified with respect to the externally-fixed magnetic field direction. At speeds above Ω_c a stationary two-dimensional powder pattern is seen even when no gradient is present. This is preserved in this new model by specifying the elliptical intensity distribution function with respect to an internal reference direction set within the sample frame. The dependence of the orientation of the axis set for the ellipse is pictured for two of the i points used to represent the sample in figure 23.
Previously, the eccentricity of the function was used to determine the range of behaviour from a monodomain aligned with the magnetic field, modelled by a very high value for the eccentricity, to a two-dimensional director distribution for an eccentricity of 1. Now, for any constant eccentricity across the sample, the locally-defined elliptic distribution is always consistent with a two-dimensional powder spectrum for the sample if no gradient is present, and it is only when a field gradient is included in the

simulation that the differences in the calculated spectra arise. This modification to EPRIMAGE is coded so that high values of the eccentricity ε approach the tangential distribution, an eccentricity of 1 corresponds exactly to the random distribution, whilst values of the eccentricity close to 0 approach the radial distribution. In this more general model the eccentricity ε is used as the tuneable parameter that defines the model distribution and the fact that the eccentricity can be varied continuously at least fits empirically with the observation of some temporal evolution of the spectrum, although no mechanism is suggested by this model.

The program EPRIMAGE is modified by the additional summation over the angle δ indicated in figure 23 in which the value of the eccentricity and the angle δ is used to determine the weighting function $p(\delta)$ given by

$$p(\delta) = \frac{\varepsilon^2}{2\pi} \cdot \frac{1}{\varepsilon^4 \cos^2(\delta-\delta_0) + \sin^2(\delta-\delta_0)} \qquad (5.15)$$

in which δ_0 is the angle between the magnetic field and the major axis of the ellipse defined at each of the i points. Formally, with this modification EPRIMAGE now evaluates each subspectrum $s_i(B)$ as:

$$s_i(B) = \sum_r \sum_\delta L\left(B(z_i, \frac{dB}{dz}), \tilde{B}_r(\xi(\delta)), T_2^{-1}(\xi(\delta))\right) . p(\delta) \qquad (5.16)$$

The overall sample spectrum $S_{fg}(B)$ is still given by a summation of the subspectra $s_i(B)$ over the i sites. The summation is carried out for δ in the range (0, 90°) at intervals corresponding to 2°. The number of subspectra included in the summation is increased considerably by this modification.

Building upon the similarity of the some of the spectra to those expected to be present in the spectra of the tangential and the random distribution, several simulations were undertaken in which intermediate values of ε between 1 and 4 were used. With a value for $\varepsilon=4$ the field gradient spectrum were rather similar to those of the tangential distribution. The spectra calculated for $\varepsilon=1$ are identical to those calculated earlier for the random distribution (using the FT convolution); the similarities of these spectra to some of the experimental set was discussed earlier. These spectra simulated for sample 1 and sample 2 are shown in figures 24 and 25 for relevant values of the field gradient.

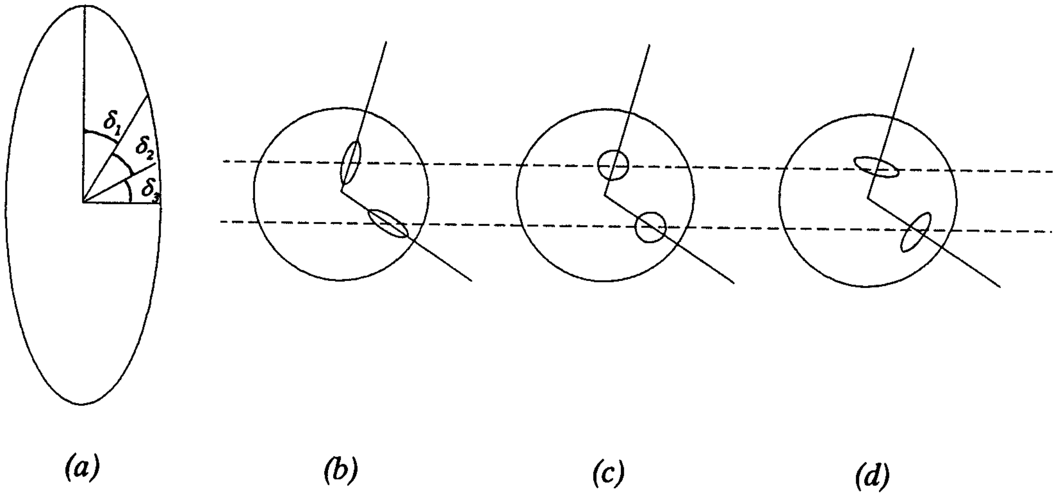

Figure 23 Specification of the intensity distribution in the elliptic distribution for two points in the spinning sample: the orientation of the ellipse depends upon the position of the point i, and the director distribution depends upon the eccentricity ε, (b) the radial distribution results from ε close to zero, (c) the random distribution for ε =1 and (d) the tangential distribution results from high ε.

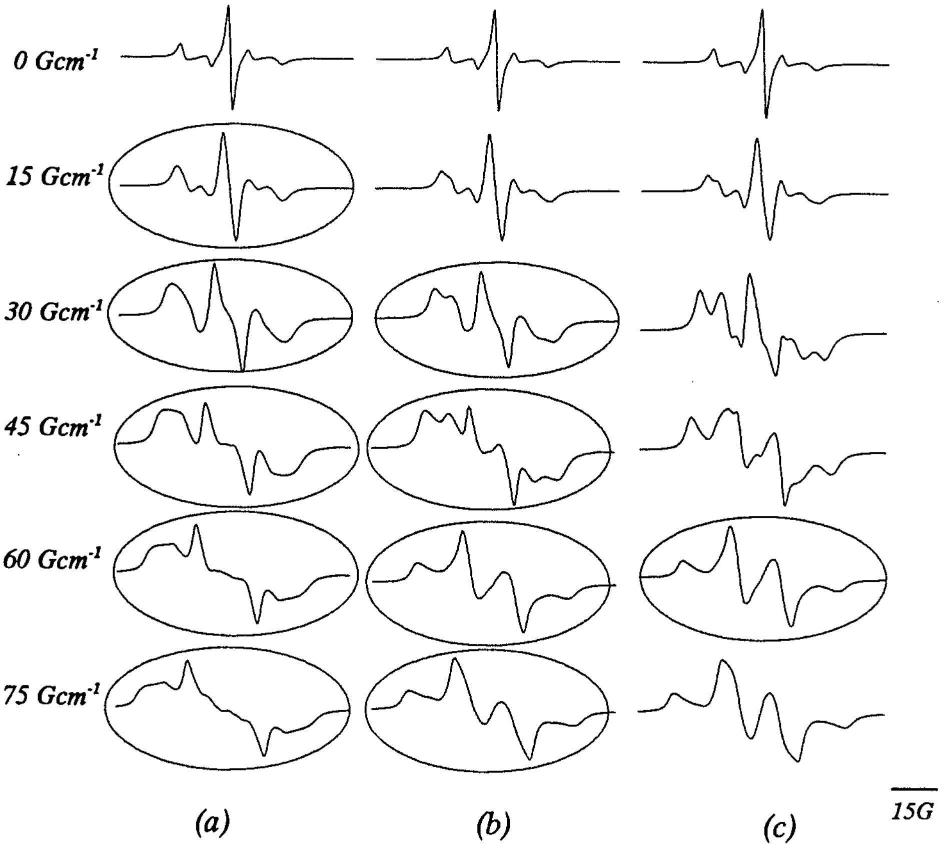

Figure 24 The spectrum calculated for cholestane in 135 in various field gradients using three values for the eccentricity ε. The values used are (a) 1.0 (b) 1.2 and (c) 2. Spectra are highlighted that bear a particular resemblance to any of the experimental set of field gradient spectra.

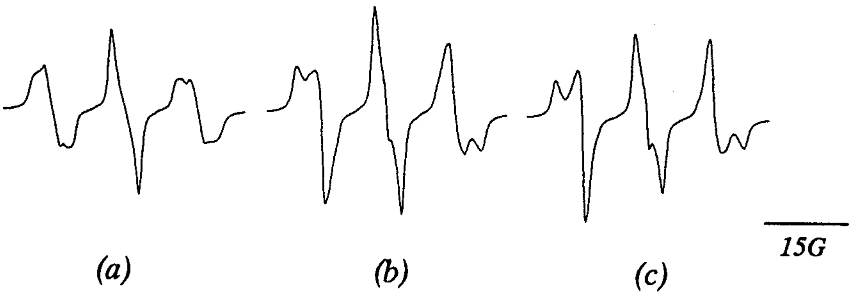

Figure 25 The spectrum calculated for the tempone spin probe in I35 in a field gradient of 15Gcm^{-1} using three values for the eccentricity ε. The values are (a) 1.0 (b) 1.2 and (c) 2.

An examination of the simulated spectra of figures 24 and 25 would suggest that the simulations of the spectra assuming an elliptical director distribution are generally capable of reproducing many of the spectral features that have not been well-fitted in the earlier analyses using the preliminary model distributions. In considering the spectra for sample 1, good agreement with the experimental spectrum shown in figure 15c recorded using a field gradient of 60Gcm^{-1} shortly after the sample started spinning (but after the spectrum in zero field gradient had settled into an invariant two-dimensional powder spectrum) is produced using values for the eccentricity ε of 1.2 and 2. The spectra that form part of the sequence in figure 15b recorded some minutes later using this same gradient and also the higher gradient of 75Gcm^{-1} would appear to contain features that are better fitted by values of ε=1.0 and ε=1.2. Good agreement with the experimental spectra acquired using field gradients of 30 and 45Gcm^{-1} is also reproduced using values of 1.0 and 1.2 for ε, although the former case in particular falls in a regime in which the field gradient spectrum is less discriminating between the different distributions.

Examining the spectra simulated for sample 2, all of which are simulated using a field gradient of 15Gcm^{-1}, it would appear that very small increases in the value of the eccentricity from the value 1.0 which gives rise to the random distribution give rise to spectra which are similar to those of the tangential distribution. A value of ε=1.2 would appear to produce a spectrum with a great deal of similarity to that of figure 17bi which showed the strong parallel features. In particular, values of ε just above 1.0 lead to a filling in of the inverse peak in the centre of the simulated spectrum of the tangential distribution that was introduced by the inclusion of *g*-anisotropy. As was noted previously, most of the other experimental spectra for sample 2 were reasonably fitted by simulations using the random distribution which is just one member of the family of elliptic distributions. The locally-defined elliptical distribution would therefore appear to be able to account for all of the experimental spectra for both samples when suitably parameterised. Although we do not have exactly comparable sets of experimental data for the two samples, this does not exclude us from certain observations about the distributions needed to produce the experimental spectra. Gross features of the experimental spectra for the two samples are modelled by a value of the eccentricity ε in the elliptic distribution between 2.0 and 1.0, that is, the director distribution across the sample ranges from something approaching that of the tangential distribution to that of the random distribution. From the chronological order in which the sequence of spectra for both samples were acquired, those spectra acquired soon after the sample spinning commenced (figure 15c, 17bi) were better fitted by the higher value of the eccentricity, while those acquired after the sample had been spinning for some time were more like those predicted for the random director distribution (for which $\varepsilon=1$).

None of the models we have considered allow for any differences in the director distribution along the axis of the sample tube or across the sample radius. On the latter point, given that the sample tube and the nematic sample within it do not rotate as a rigid body during the early stages of sample rotation (see Chapter 3), some shear-induced alignment of the director tangential to the walls of the sample tube in the plane normal to the spinning axis may be expected in the period shortly after the sample starts spinning. This would be expected to lead to stronger parallel features relative to the perpendicular features in the field gradient spectra for the same reason that the parallel features are dominant in the spectra predicted for the tangential director distribution (shown in figures 9 and 10). However, because the shear-induced alignment is not complete, and because the shear rate is not contant along the radius of the sample, the parallel features are weaker than would be expected for the tangential director distribution (as we have observed in the comparisons between the calculated spectra and the experimental spectra shown in figure 15c and 17bi). During continued spinning, the rotation rates of the sample tube and of the nematic sample equalise and therefore shear-induced alignment becomes progessively less important and eventually zero. This picture is in accord with our simulation results which indicate that the eccentricity of the elliptical distribution that best fits the experimental spectra decreases towards 1 after the sample has been spinning for longer periods. Some more recent results [21] show that if the sample spinning speed is gradually increased from zero to above Ω_C, then the field gradient spectra above Ω_C correspond to those predicted for the random director distribution, without going through a period during which the parallel features are prominent. As no shear-induced alignment occurs in this case, this is consistent with the fact that the strong parallel features in the field gradient spectra correspond to periods during which shear-induced alignment occurs. It is suggested that the temporal evolution which we have observed in this series of experiments is due initially to shear-induced alignment and then to its after-effects.

Despite the successes in fitting many of the experimental spectra, the director distributions we have used do not directly suggest how the director is spatially arranged in a rapidly spinning nematic sample. We therefore briefly review two models for the director structures in the spinning sample that have arisen from other experimental work. In a previous study of spinning nematic side-chain liquid crystal polymers in thin cells, NMR results were correlated with optical studies of the two polymeric samples studied [22]. The NMR spectra show the expected evolution from an initial monodomain spectrum to a two-dimensional powder spectrum over a period which is strongly temperature dependent. Thus, this evolution occurs over some 12 hours at 52°C (325K) but over approximately 4 minutes at 77°C (350K) for a sample of a phenyl benzoate side-group attached to a polysiloxane backbone. Over the same period, the optical texture of the spinning sample was also seen to develop; the final texture, which corresponds to the two-dimensional powder NMR spectrum, shows a pattern of concentric rings around a number of cell-like structures consisting of small microdomains in each of which the director orientation is broadly homogeneous. A mechanism is suggested in which a constant overall two-dimensional powder director distribution is maintained by a dynamic equilibrium in which the director counter-rotates in neighbouring domains which are separated by regions in which a coupled backflow occurs that stabilises the director rotation, as shown in figure 26a. In this figure the directions of flows are indicated by straight arrows and rotations of the director are indicated by curly arrows. The similarity of these convective structures to Williams domains was noted [23]. It is not clear exactly how and if this picture can be translated from the thin cell to the bulk sample which we study but convective cells consistent with a similar pattern of coupled flow and rotation would also fit onto a square grid, as shown in figure 26b. An examination of the optical texture under different polarizing conditions also shows that the regions of the sample close to the surfaces of the cell contain a large number of inversion lines (regions in which the director undergoes a 180° rotation over a small distance). It was noted that the NMR spectrum was not particularly sensitive to defects or these inversion lines in the director structure, as they make up only a small proportion of the volume of the whole sample, but was more sensitive to the director orientations within domains. This same condition also applies in our experiment.

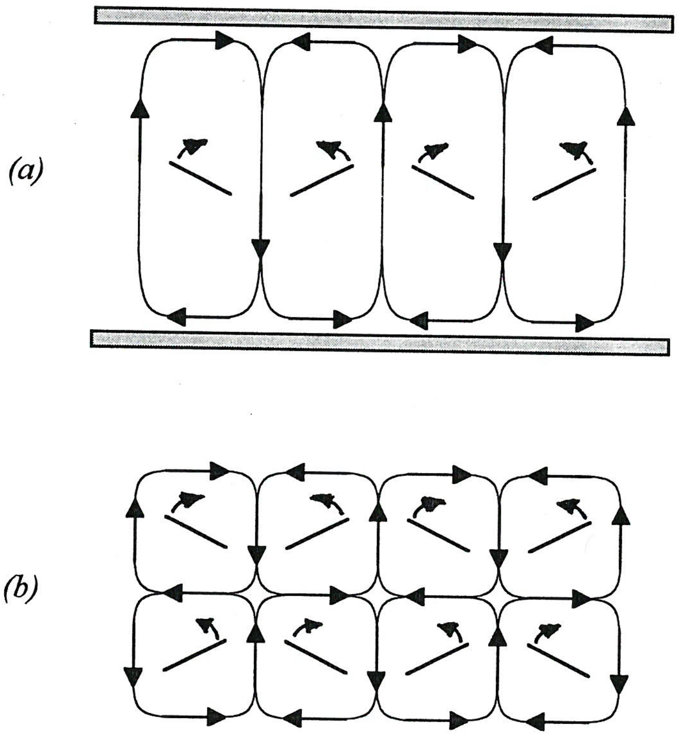

Figure 26 A pattern of coupled flow and director rotation fits into (a) a thin cell or (b) onto a square grid in a bulk sample. The magnetic field rotates in the plane of the page.

A second body of work does not exclude the coupling of flow and director rotation but suggests that the role of defects is more important in determining the director structure in a spinning sample. Thus, when rotating at a spinning speed below Ω_C, after some initial settling, the director distribution remains constant with respect to the magnetic field with the bulk of the director lying at a constant angle ξ to the magnetic field given by equation 5.2 so that the magnetic and frictional torques on the director are balanced. It has been suggested that the dissipation of energy in the rotating field experiment at these slower spinning speeds may be governed by the rates of nucleation, migration and annihilation of orientational defects in the director structure [1]. Such defects may be at points, or along lines or walls. For example, two inversion walls are generated upon rotation of a sample with homeotropic surface alignment of the director through one complete revolution. Unless these can be eliminated then their number will increase linearly with time until they fill the whole sample and the magnetic torque on the director will be decreased. This is not observed experimentally. These walls may be eliminated by the combination of two walls generated at either side of a spinning sample which annihilate each other leading to the restoration of a homogeneous director orientation and thereby maintaining a magnetic torque on the director. When spinning at a speed above Ω_C similar processes may occur. In our experiments the orientation of the director at the sample boundaries is not controlled, but it is suggested that any local defect in the sample, such as a speck of dust, could act as a region of locally increased viscosity [24, 25], in the same way as the enforced homeotropic alignment at the sample walls, and will nucleate inversion lines which then radiate away from the source like ripples. These may combine and annihilate each other in the manner just described for inversion walls generated by the boundaries of the sample but can also be regenerated during each rotation of the sample. In another rotating field study on a thermotropic low molar mass nematogen in a thin cell [24, 25], the development of these structures was seen optically, while, after prolonged rotation, the sample had a stable cell-like optical texture very similar to that described in [22], although it is less clear how the overall two-dimensional powder distribution of the director is maintained in this case.

5.9 Conclusions

It is clear that a one-dimensional EPR imaging experiment provides information about the director distribution in rapidly spinning liquid crystal samples that has not been available in previous EPR experiments. With appropriate experimental design a wealth of information can be gleaned from the system under study because of and not despite the apparent complications of EPR resonances as compared with typical NMR resonances used elsewhere for MRI.

The present series of field gradient EPR experiments have revealed a more complex director distribution in the spinning sample than had been considered in any of the simple guiding models: this is not unexpected. These experiments and the success in simulating some of the spectra are encouraging. Although an unanticipated temporal evolution of the spatial distribution of the director has been seen, this would appear to be temporary and caused as a result of accelerating the sample rapidly from rest as such effects are not observed if the sample is accelerated gradually from rest up to a spinning speed above Ω_C. After some time, the field gradient spectra settle down to those anticipated for the random director distribution throughout the sample.
An elliptical distribution function, which is a modification of a description of the director distribution function in a sample spinning below the critical spinning speed, has been successful in accounting for most of the spectral features and their relative intensities in the experimental field gradient spectra. However, this purely analytical function gives little information about the local director structures in the spinning sample and the reasons for and the mechanisms by which they develop. Further studies should try to ascertain the local dynamics of the director distribution in more detail. The role of the spinning speed relative to the critical spinning speed in influencing the behaviour of the director has not been examined at all in this study. Further studies could examine this as well as the influence of different anchoring conditions between the liquid crystal and the walls of the sample tube on the behaviour of the field gradient EPR spectra.

5.10 References

[1] DE GENNES, P.G., Chapter 5, *The Physics of Liquid Crystals,* Clarendon Press, Oxford, 1974.

[2] DE JEU, W.H., Chapter 7, *Physical Properties of Liquid Crystalline Materials,* Gordon and Breach, 1980.

[3] FLANDERS, P.J., *Mol. Cryst. Liq. Cryst.*, **29** 19, 1974.

[4] KNEPPE, H., SCHNEIDER, F. and SHARMA, N.K., *J. Chem. Phys.*, **77** 3203, 1982.

[5] HEATON, N., REIMER, D. and KOTHE, G., *Ber. Bunsenges. Phys. Chem.*, **97** 1320, 1993.

[6] LESLIE, F.M., LUCKHURST, G.R. and SMITH, H.J., *Chem. Phys.Lett.*, **13** 368, 1972.

[7] DÖRRER, H., KNEPPE, H., KUSS, E. and SCHNEIDER, F., *Liq. Crystals,* **1** 573, 1986.

[8] LUCKHURST, G.R., Chapter 7, vol. 2, *Liquid Crystals and Plastic Crystals,* eds. G.W. Gray and P.A. Winsor, Ellis Horwood, 1974.

[9] CARR, S.G., LUCKHURST, G.R., POUPKO, R. and SMITH, H.J., *Chem. Phys.*, **7** 278, 1975.

[10] EMSLEY, J.W., KHOO, S.K., LINDON, J.C. and LUCKHURST, G.R., *Chem. Phys. Lett.*, **77** 609, 1981.

[11] CIAMPI, E., EMSLEY, J.W., LUCKHURST, G.R., TIMIMI, B.A., KOTHE, G. and TITTELBACH, M., *J. Chem. Phys.*, **107** 5907, 1997.

[12] DUNN, C.J., unpublished results.

[13] DEROME, A.E., *Modern NMR Techniques for Chemistry Research,* Pergamon, 1987.

[14] EATON, G.R., EATON, S.S. and OHNO, K., *EPR Imaging and* In-vivo *EPR,* CRC Press, 1991.

[15] CALLAGHAN, P.T., *Principles of Nuclear Magnetic Resonance Microscopy,* Clarendon Press, Oxford, 1991.

[16] see Chapter 2: implicitly, the applied magnetic field is assumed to be uniform across the sample at a given instant.

[17] for example, the use of window functions, see refs. 14 and 15.

[18] SHAW. D., Chapter 1, Fourier Transform NMR spectroscopy, Elsevier, 1976.

[19] the systematic name for I35 is:

α-(4-*n*-pentyl-2-fluorobiphenyl)-ω-(4-propylcyclohexyl) ethane

[20] full address: Prof. G.F. Pedulli, Dipartimento di Chimica Organica "A Mangini", Università di Bologna, Via S. Donato 15, 1-40127, Bologna, Italy.

[21] PEDRIELLI, P. and LUCKHURST, G.R., private communication.

[22] SCHWENK, N., BOEFFEL, C. and SPIESS, H.W., *Liq. Crystals,* **12** 737, 1992.

[23] WILLIAMS, R., *J. Chem. Phys.*, **39** 384, 1963.

[24] MIGLER, K.B. and MEYER, R.B., *Phys. Rev. Lett.*, **66** 1485, 1991.

[25] MIGLER, K.B. and MEYER, R.B., *Phys. Rev. E,* **48** 1218, 1993.

Chapter 6

The director distribution in the Sm phase of liquid crystal dimers. A study using EPR spectroscopy

6.1 Introduction

In recent years there has been an increase in the number and variety of smectic phases that have been observed [1, 2]. The aim of this study is to investigate the director distribution in two liquid crystal dimers showing an unusual smectic phase using EPR spectroscopy with the expectation that we should be able to propose a structure for this phase, which we denote simply Sm. At the outset it should be pointed out that the length scales over which the director varies in these systems are much smaller than the distances over which the director varied in the previous Chapter. Therefore the imaging experiments of the previous Chapter are unlikely to yield any useful information about the director distribution in these phases and a different approach is considered to extract as much information as possible about the phase from the EPR spectrum. The magnetic fields used in these experiments (3345G) are insufficient to reorient smectic layers, and therefore the angle dependence of the EPR spectrum can be investigated without disturbing the director distribution in the sample. This enables a more complete study of the director distribution to be made than if the spectrum can only be measured for a single orientation of the director distribution with respect to the magnetic field (as is the case, for example, if the director reorients in the field).

In the next section the background to the smectic behaviour of liquid crystals is discussed, including the smectic behaviour of liquid crystal dimers, before the unusual smectic behaviour of the dimers CBO6CB, CB7CB and CBO6CT is introduced. The present EPR experiments are discussed in section 6.3, and the results of those experiments are presented and discussed in sections 6.4 and 6.5. The spectral simulations that form part of a more rigorous quantitative analysis of the experimental spectra follows in section 6.6 and the results of this analysis are discussed in section 6.7. The conclusions of this series of experiments are given in section 6.8.

6.2 The Smectic behaviour of Liquid Crystals

The classical molecular structure of a calamitic liquid crystal is a semi-rigid, anisometric mesogenic moiety to which are attached, or which are joined by, flexible alkyl or alkylene chains [3]. In general the anisometry of the mesogenic group enhances the liquid crystal transition temperature while the presence of flexible or semi-flexible portions of the molecule lowers the melting point [4]. Smectic phase formation in these systems may be regarded as a microphase separation in which the mesogenic portions of the molecule segregate into one microphase and the flexible portions of the molecule form the other. This may be favoured on both energetic and entropic grounds as discussed in Chapter 1. Much of the smectic behaviour of liquid crystals with this classical molecular structure may be rationalised simply in terms of these two factors, although smectic phases are also seen in systems with a different molecular structure [5].

Many systematic studies have been undertaken to understand the structure-property relationships of liquid crystals in more detail; the behaviour across homologous series is particularly instructive in this regard. Smectic phases are prevalent in those systems in which a high degree of inhomogeneity in the molecular structure drives the microphase separation for the reasons just outlined: for example, there is an almost universal tendency towards increased smectic behaviour as the terminal chains are lengthened in both monomers and dimers [4, 6]. For short chains, a nematic phase is presumably preferred because the entropic cost of ordering a short chain may not be too high, while energetically, the core-core interactions may not be too severely diluted by the presence of short chains. The characteristics of the mesogenic group may also be important, thus certain shapes may not pack efficiently and this would reduce the energetic driving force for smectic phase formation. In other cases, the shape may allow a particularly efficient packing arrangement in a smectic phase which maximises the extent to which lateral interactions between the mesogenic groups act to stabilise a layered structure: this is the explanation offered in most of those cases in which a smectic phase is formed by molecules with no terminal chains or short terminal chains [5].

The smectic phases considered in this Chapter are formed by the dimers containing the cyanobiphenyl and cyanoterphenyl mesogenic groups and are considered shortly. These mesogenic groups both possess a strong longitudinal dipole. The properties of the cyanobiphenyl unit as a mesogenic group in the homologous series of monomeric 4'-*n*-alkyl-4-cyanobiphenyls (the K series) and 4'-*n*-alkyloxy-4-cyanobiphenyls (the M series) were discussed in Chapter 1. Both of these series show nematic behaviour for short terminal chains which is increasingly replaced by smectic behaviour as the terminal chain length is increased [4]. The longitudinal dipole in the cyanobiphenyl moiety is known to exert an influence on the layer spacing when these systems form smectic phases [7]. The higher clearing temperatures for the M series and the modest odd-even alternation in the transitional properties of both series was also noted. This alternation was observed to be more pronounced in the K series than in the M series, and this was explained principally in terms of the different geometries of the linking groups between the mesogenic group and the terminal chain (see also [8]). Following from the results of ^{2}H NMR experiments on the K and M series, an angle of 113.5° was estimated for the $C_{ar}\widehat{C}C_{al}$ bond angle in the methylene linking group and the $C_{al}\widehat{C}C_{al}$ bonds in the rest of the alkyl chain, and an angle of 126.4° between the axis of the cyanobiphenyl group and the O-C_{al} bond in the ethylene linking group [8]. The other $C_{al}\widehat{C}C_{al}$ bonds in the rest of the alkyloxy chain were assumed to be 113.5°. It was reasoned that the O atom opens up the angle between the mesogenic group and the terminal chain in the M series (to ~126.4°), creating a more elongated shape, hence the higher clearing temperatures for this series, and this also means that the overall alternation in molecular shape is smaller as the chain length is increased. In the K series, in contrast, the smaller bond angle at the C atom that links the mesogenic group to the terminal chain (~113.5°) creates a less elongated shape and a more pronounced alternation in overall molecular shape as the terminal chain length is increased; these two features are reflected in the lower clearing temperatures and the stronger alternation in the transitional properties in this series.

A much larger odd-even alternation has been observed in the transitional properties of the symmetric dimer series of α,ω-bis(4'-cyanobiphenyl-4-yloxy)alkanes **1** [9], which were plotted in figure 9, Chapter 1, and are listed in table 6.1. The overall change in molecular shape is more dramatic as the parity of the spacer is changed in these systems, the more elongated shape of the even dimers explains the higher transition temperatures and entropies for the even dimers. This series is referred to in this Chapter using the mnemonic CBO(*n-2*)OCB in which *n* is the total number of units in the spacer.

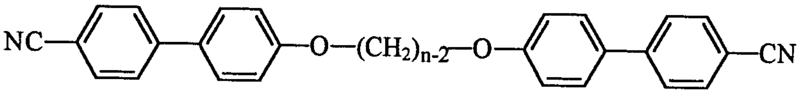

1

Assuming that the bond angles are the same in this series as in the M series, the angle between the mesogenic groups in the all-*trans* conformation of the spacer is alternately 180°(≡0°) and ~139°(≡41°) for the even and odd dimers respectively. This is shown by the caricatures in figure 1 for these and other linking groups discussed later. Although the all-*trans* conformation is only one of many spacer conformations, it serves as a useful guide to the overall molecular geometry. For spacer lengths *n* between 3 and 14, all members of this series exhibit purely nematic behaviour, although, in the case of *n*=3 and *n*=5, the nematic phase is monotropic. The nematic behaviour suggests that the conditions for smectic phase formation are not met in this series, and this can be explained either by the absence of sufficient inhomogeneity in the molecular structure to drive smectic phase formation or by the fact that repulsive forces between neighbouring dipoles in a layered structure lead to the destabilisation of a smectic phase.

In the spirit of extending the argument developed for monomers about the importance of the geometry in determining the extent of the odd-even alternation of transition temperatures in dimers, the transitional properties of two members of the non-symmetric series of α-(4'-cyanobiphenyl-4-yloxy)-ω-(4'-cyanobiphenyl-4-yl)- alkane CBO(*n-1*)CB dimers **2** was examined, specifically CBO5CB and CBO6CB [10, 11]. The transition data for these compounds is also shown in table 6.1.

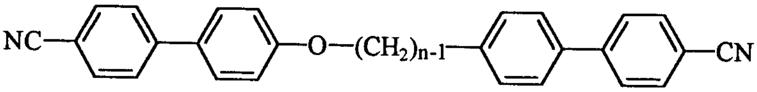

2

Table 6.1 The transitional data for some of the series of CBO(n-2)OCB, CBO(n-1)CB, CBnCB and CBO(n-1)CT series of dimers.

n	T_{CrN} / °C T_{CrI} / °C † T_{CrS} / °C ‡	T_{SmN} / °C	T_{NI} / °C	$(\Delta S_{\mathrm{CrN}}/R)$ $(\Delta S_{\mathrm{CrI}}/R)^{\dagger}$ $(\Delta S_{\mathrm{CrN}}/R)^{\ddagger}$	$(\Delta S_{\mathrm{SmN}}/R)$	$(\Delta S_{\mathrm{NI}}/R)$
CBO(*n*-*2*)OCB series [1]						
3	$144^{\dagger}$		(124)	$9.7^{\dagger}$		-
4	205		265	9.4		1.77
5	$185^{\dagger}$		(170)	$12.0^{\dagger}$		0.54
6	209		250	10.4		1.95
7	137		186	8.8		0.66
8	187		221	12.4		1.98
9	137		181	15.3		0.78
10	175		201	15.2		2.01
11	133		172	13.9		0.94
12	164		184	14.9		2.14
13	123		164	15.8		1.27
14	152		169	19.0		1.92
CBO(*n*-*1*)CB series [2]						
6	175.5		240	8.52		2.18
7	$99^{\ddagger}$	109	154.5	$10.3^{\ddagger}$	0.01	0.47
CB*n*CB series [3]						
4	225		275	8.16		2.21
5	$144^{\dagger}$		(91)	11.19		0.08
6	183		230	9.5		2.61
7	$101^{\ddagger}$	102	115	$7.67^{\ddagger}$	0.31	0.34
CBO(*n*-*1*)CT series [4]						
4	204		380.9	6.51		1.95
5	177.5	(170.5)	270.5	9.49		0.34
6	206.5		339.2	7.65		1.99
7	$152.6^{\ddagger}$	172.2	272.2	$7.9^{\ddagger}$		0.49

[1] = data taken from [9], [2] = data taken from [10], [3] = data taken from [12], [4] = data taken from [13].

In this series, the estimated angle between the mesogenic groups alternates between 167°(≡13°) and 126.5°(≡53.5°) in the all-*trans* conformation of the spacer in the even and odd dimers respectively. These different molecular shapes are also depicted in figure 1. A smaller difference in the clearing temperatures was observed when compared with the results for the CBO(*n-2*)OCB series, as expected for a series in which the overall alternation in molecular shape is made smaller by the different geometry of the linking groups. The even dimer CBO5CB was purely nematic. However, a smectic phase was observed below the nematic phase for the spacer length 7, that is, for the odd dimer CBO6CB. This phase was initially identified by its optical texture [10]: upon cooling, the schlieren texture of the nematic phase is replaced by a poorly-defined focal-conic fan texture just below the nematic-smectic transition, similar to that expected for a smectic A or C. As the temperature of the smectic phase is decreased, the fans become more rounded and the texture becomes more broken. This smectic phase has since been shown to be rather unusual and has been the subject of a number of investigations [10, 11].

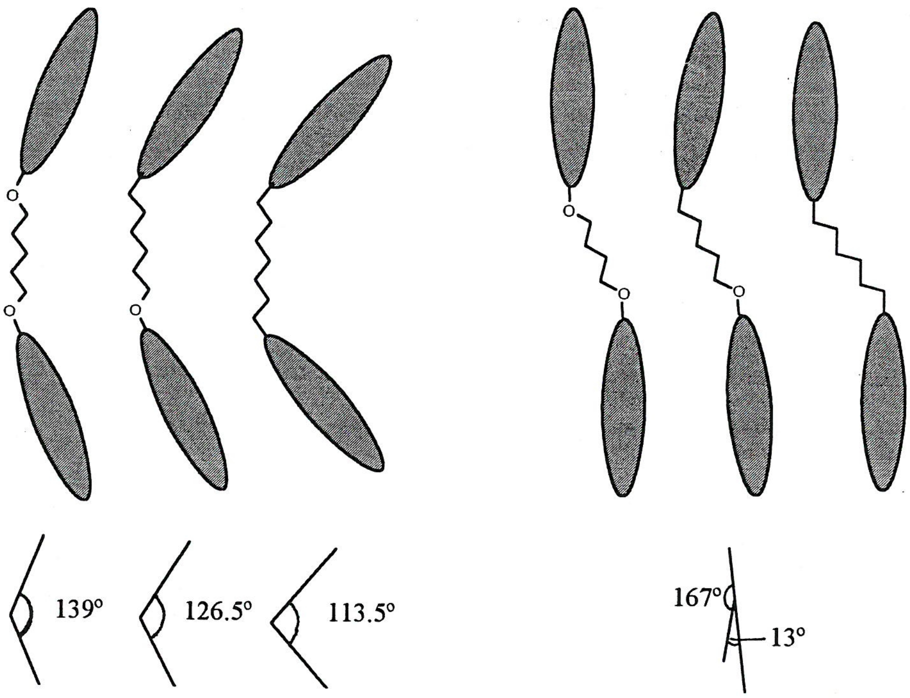

(a)

(b)

Figure 1 The relative orientations of the mesogenic groups in the all-trans conformations of (a) the odd and (b) the even dimers of an ether-linked dimer, a mixed dimer and a methylene-linked dimer.

From a comparative point of view, it was surprising that the inhomogeneity in the molecular structure and/or the efficiency or method of packing in a layered structure in CBO6CB is apparently large enough to drive formation of a smectic phase whereas that of CBO5OCB, also with a spacer length of 7 and with a comparable if not identical geometry, is insufficient to do so, for this compound is purely nematic. Further, it was surprising to see smectic behaviour in the dimer with the odd spacer, CBO6CB. It is expected that the even dimers, specifically CBO5CB in this instance, which have many conformations of the spacer in which the two mesogenic groups in the molecule are parallel, would be better candidates for smectic phase formation because they can align parallel to each other and in doing so can pack efficiently, therefore maximizing the energetic driving force for smectic phase formation. Alternately, it may be precisely this elongated shape which can pack efficiently which maximises the repulsive forces between the dipoles on neighbouring molecules and destabilises a layered structure. The large angle, 126.5°, between the mesogenic cores in the all-*trans* conformation of the odd spacer of CBO6CB, which is reproduced in many other conformations of the spacer, produces a strongly biaxial molecule with a pronounced bent shape. It is not easy to see how such molecules would pack in a smectic phase in general. Thus far, smectic phase formation has been seen as a way of maximising the attractive forces between neighbouring molecules when they are able to pack reasonably efficiently and maximising the entropy of any chains which constitute a less-ordered microphase. In some arrangements of dipolar mesogenic groups, the forces between neighbouring molecules may be predominantly repulsive, and therefore a more unusual arrangement is needed either to minimize the extent of these repulsions, or indeed, to position the dipoles relative to each other so that the forces between them are actually attractive. In either case, it is less surprising that the molecular structure which is able to produce an arrangement of this sort is different from that generally understood to promote smectic behaviour. Hence, an apparently unpromising molecular shape promotes smectic behaviour in CBO6CB and, as the next paragraph discusses, the smectic phase itself has some unusual properties.

There seems little doubt from the optical texture that the phase formed by CBO6CB below the nematic phase is smectic, and it apparently develops normally from the schlieren texture of the nematic phase above it, hence its designation as Sm. The results of DSC show that the N-I transition ($\Delta S/R$=0.47) is associated with the onset of weak orientational ordering in the nematic phase, but this is not atypical for an odd dimer. The entropy change at the N-Sm transition is very small ($\Delta S/R$=0.01), but this is not unexpected: the McMillan ratio $T_{\mathrm{SmN}}/T_{\mathrm{NI}}$ for this compound is 0.87 and it is at precisely this value that McMillan predicts that the N-Sm transition becomes second order (although this theory is usually applied to the nematic-smectic A transition) [14]. The results of X-ray diffraction experiments, which initially appeared difficult to perform because it was doubted that a sufficiently aligned sample had been produced, suggest that the Sm phase possesses an intercalated structure [2], and that significant pretransitional intercalated structure exists in the nematic phase [15]. The X-ray diffraction pattern is characterised by diffuse arcs and spots, indicating that the intermolecular distances are not clearly defined in the nematic or in the Sm phase and therefore the structure is not well ordered, either orientationally in the nematic phase, or orientationally and/or positionally in the Sm phase. This is consistent with the DSC data already described. The results of deuterium NMR (^{2}H NMR) experiments, using both dissolved solutes and deuterium-labelled CBO6CB, are consistent with low orientational order but otherwise show no unexpected behaviour of the major and minor order parameters in this compound either in the nematic phase or in the Sm phase or at the transition between the two [10, 12]. The results of these experiments and those on several homologues from the CBO(*n*-*2*)OCB series fit with the general patterns observed for odd and even dimers in nematic and smectic phases and the orientational order in the nematic phase of these compounds is in accord with the indications that the molecular geometry is important in determining mesophase stability [16]. However, the EPR spectrum of spin probes dissolved in the Sm phase of CBO6CB, which reflects the director distribution in the sample (in a different way from that of the ^{2}H NMR spectrum), shows some entirely unexpected behaviour [10, 11].

The EPR spectra of nitroxide spin probes dissolved in monodomain samples normally contains just three hyperfine lines, separated by a hyperfine splitting that reflects the orientational order of the spin probe in the mesophase (nematic, smectic A) and the angle between the director and the magnetic field (in a tilted smectic phase, or the pulsed-rotation experiment discussed in Chapter 3) as described in Chapter 2. The EPR spectrum of the Sm phase contains five lines, which have a lineshape that indicates that the director in the Sm phase makes a range of angles with the magnetic field between 0° and 90°. This spectrum is shown in figure 2. This behaviour is quite different from that seen or expected at any other transition and in any smectic phase that has been formed, with some care, from a monodomain sample [17]. The study of this phase in two compounds using EPR spectroscopy forms the basis of this Chapter.

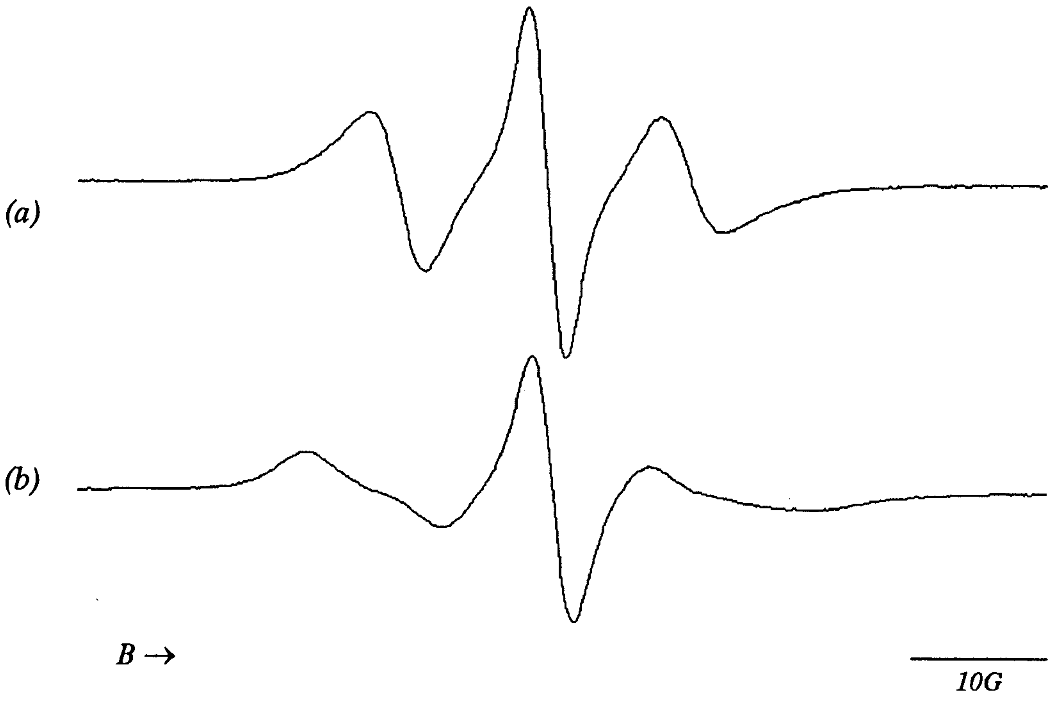

Figure 2 (a) The EPR spectrum of cholestane in CBO6CB changes from (a) a three-line spectrum in the nematic phase to (b) a five-line spectrum in the Sm phase.

The geometry of the linking group and possibly the length of the spacer between the two mesogenic groups would appear to be a critical factor in promoting the formation of a smectic phase in CBO6CB. The behaviour of the α,ω-bis(4'-cyanobiphenyl-4-yl)-alkane dimers, the CB*n*CB series **3**, has also been investigated [12, 18].

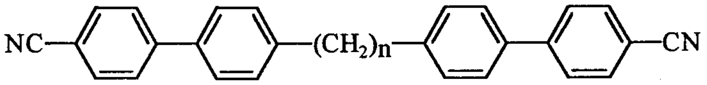

3

The estimated angle between the two mesogenic cores is 180°(≡0°) and ~113.5°(≡66.5°) respectively, in the all-*trans* conformations of the spacer in the even and odd dimers and therefore similar behaviour may be expected in these systems. Uniquely among the CB*n*CB dimers investigated, which are otherwise purely nematic, CB7CB, with a spacer 7 units long and therefore an angle of some 113.5° between the mesogenic groups in the molecule, has both a nematic and a smectic phase. The behaviour of the EPR spectrum of the cholestane spin probe dissolved in this smectic phase shows the same behaviour as was seen in CBO6CB [12]. To add further weight to the argument that this is not unique behaviour, some of the series of the non-symmetric α-(4'-cyanobiphenyl-4-yloxy)-ω-(4'-cyano-p-terphenyl-4''-yl)alkanes, the CBO(*n-1*)CT dimers **4**, were also synthesized and their phase behaviour investigated [13]. The angle between the mesogenic groups in these compounds is the same as that in the CBO(*n-1*)CB series, alternately 167° and 126.5° in the all-*trans* conformations of the even and odd spacers respectively. The even dimers were purely nematic, but CBO4CT, with an odd spacer of length 5, and CBO6CT, with an odd spacer of length 7, also exhibit a smectic phase. Under the microscope this phase has the same poorly-defined focal-conic fan texture as CBO6CB.

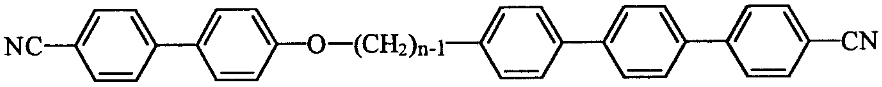

4

Therefore, a particular category of dimeric liquid crystals appear to exhibit a smectic phase that does not form part of the trend towards increased smectic tendency as the molecular inhomogeneity is increased (as homologues with both shorter and longer spacers are purely nematic). The molecular requirements for formation of this phase seem to be rather precise, thus, this phase has been observed for certain of the odd dimers comprising the cyanobiphenyl- and cyanoterphenyl- mesogenic groups linked by an odd spacer group. So far this phase has only been seen in systems with a spacer that is 5 or 7 atoms long. The geometry of the linking groups between the spacer and the mesogenic groups would appear to be important, even though this apparently leads to a molecular shape that is a most unpromising candidate for efficient packing in a smectic phase. The smectic phase so formed has been demonstrated to have only weak orientational and positional ordering, and EPR experiments have indicated that the director distribution in this phase is unusual. In the next section the EPR experiments that are used to probe the director distributions as part of continuing investigations of these unusual systems are described in greater detail.

6.3 Experimental

6.3.1 Synthesis

The dimers CB7CB and CBO6CT were synthesized, by P.J. Barnes and M. Wilson respectively, using procedures described elsewhere [12, 13].

6.3.2 Sample preparation

The following EPR samples with the listed transition temperatures were made up using the procedure described in Chapter 3.

(1) cholestane in CB7CB: $\mathrm{Cr}\ \overset{100^{\circ}\mathrm{C}}{\rule{2cm}{0.4pt}}\ \mathrm{Sm}\ \overset{101^{\circ}\mathrm{C}}{\rule{2cm}{0.4pt}}\ \mathrm{N}\ \overset{114^{\circ}\mathrm{C}}{\rule{2cm}{0.4pt}}\ \mathrm{I}$

(2) cholestane in CBO6CT: $\mathrm{Cr}\ \overset{123^{\circ}\mathrm{C}}{\rule{2cm}{0.4pt}}\ \mathrm{Sm}\ \overset{170^{\circ}\mathrm{C}}{\rule{2cm}{0.4pt}}\ \mathrm{N}\ \overset{\text{not detected}}{\rule{2cm}{0.4pt}}\ \mathrm{I}$

(3) tempone in CBO6CT: $\mathrm{Cr}\ \overset{125^{\circ}\mathrm{C}}{\rule{2cm}{0.4pt}}\ \mathrm{Sm}\ \overset{171^{\circ}\mathrm{C}}{\rule{2cm}{0.4pt}}\ \mathrm{N}\ \overset{\text{not detected}}{\rule{2cm}{0.4pt}}\ \mathrm{I}$

These temperatures are lower than those listed in table 6.1 for the pure compounds because the presence of the spin probe in the EPR samples leads to a slight depression in the transition temperatures. The cholestane spin probe was used in samples 1 and 2 to enable comparisons to be made with the previous experiments using cholestane in CBO6CB, to verify the same unusual behaviour of the EPR spectrum. The tempone spin probe was used in sample 3 to ascertain that the behaviour of the director inferred from the EPR spectrum is independent of the spin probe and is therefore truly a property of the sample in the Sm phase rather than due to some specific interaction between the spin probe and the liquid crystal dimer.

6.3.3 EPR Experimental

In each case the sample tube was loaded into the goniometer which was mounted on to the cavity of the Bruker ECS 106 spectrometer. The goniometer could be operated manually or under the automated control of the spectrometer. Initially the temperature variation of the EPR spectrum of each sample during cooling was measured using appropriate parameters for the respective spin probes. For samples 1 and 2, both of which use the cholestane spin probe, these were: modulation amplitude, ma: 1.01G, time constant, tc: 1.28ms, sweep time 5.243s for 90G sweep. For sample 3 these were: ma: 0.2G, tc: 5.12ms, sweep time 10.486 for 60G sweep. These same parameters were then used in the acquisition of the angular dependence of the spectrum at several fixed temperatures.

The variable temperature sweep for sample 1 (cholestane in CB7CB), over the range 120-50°C, took the sample from the isotropic phase through the nematic phase and into the smectic phase with the sample in the magnetic field of the spectrometer (3345G). The higher nematic-isotropic transition temperature for CBO6CT was unattainable on account of decomposition of the spin probe, therefore the temperature sweep for samples 2 and 3 across the range 175-76°C begun with the sample in the nematic phase and took the sample down into the smectic phase. The experiment was then repeated for each sample, with the angle dependence of the spectrum also recorded at several temperatures. This was done by successively acquiring the spectrum and then rotating the sample tube about its own axis in 10° steps under the automated control of the spectrometer. A complete set of spectra correspond to rotation of the sample through 180°. Spectra of the sample were then recorded in quick succession with the sample in the 270° and the 0° (≡360°) positions, to verify that the director distribution remains unchanged within the sample and does not reorientate in the magnetic field during the acquisition of the angle dependence of the spectrum. This is important because, in the detailed analysis that follows, the director distribution is assumed to remain fixed within the sample after the Sm phase has formed. The sample was only ever cooled in the 0° position. The angle dependence of the EPR spectrum at several temperatures was then recorded by repeating the acquisition-rotation procedure just outlined. In a check on the robustness of the director distribution the sample was also cooled into the smectic phase at various rates and in the highest field attainable in the spectrometer (6600G), after which the angle dependence of the spectrum was recorded. Using the larger magnetic field exerts a four times greater magnetic torque on the director during smectic phase formation (see Chapter 1) and this was intended to indicate whether the application of a greater magnetic torque to the director during cooling into the smectic phase leads to any differences in the director distributions in the three samples.

6.4 Results

In this section, the experimental spectra are presented and interpreted qualitatively in terms of the director distribution in the sample using only the hyperfine splitting and the pattern of intensities in the spectra. Later, a more detailed quantitative analysis is applied and we make use of simulations which include more of the parameters that influence the EPR spectra.

6.4.1 Sample 1: cholestane in CB7CB

The changing spectrum of sample 1 during cooling is shown in figure 3.

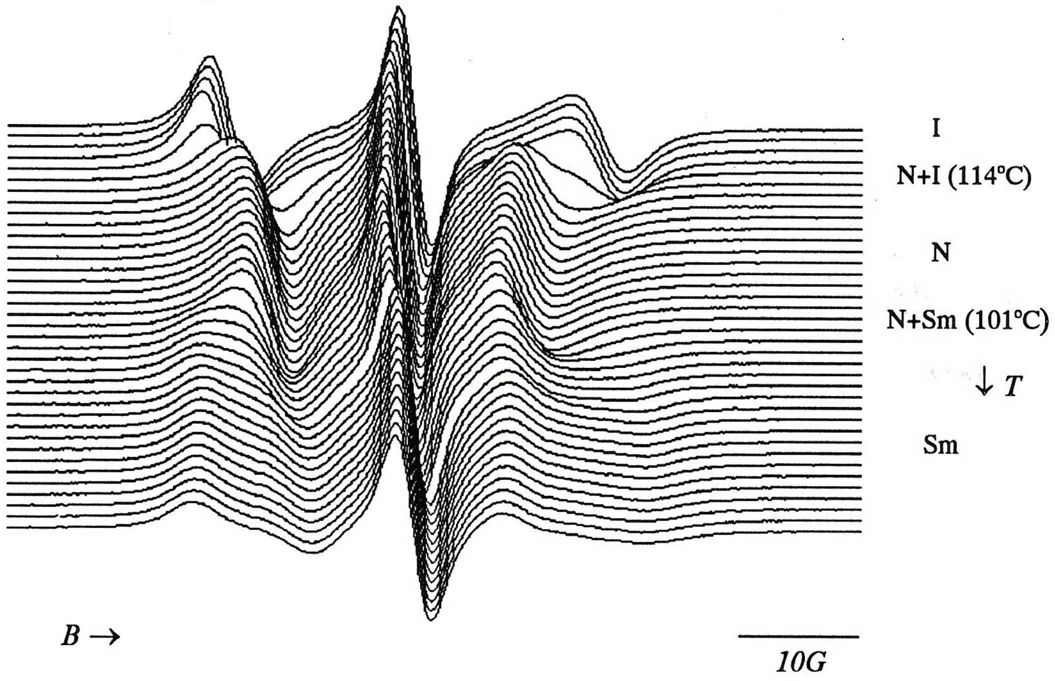

Figure 3 The EPR spectrum of cholestane in CB7CB during cooling from the isotropic phase to the Sm phase.

The appearance and variation of the EPR spectrum of sample 1 with temperature is similar to that described for the cholestane spin probe in CBO6CB. The behaviour of the spectrum upon cooling from the isotropic to the nematic phase follows the pattern observed for the cholestane spin probe dissolved in any low viscosity liquid crystal with a positive $\Delta\tilde{\chi}$ in which the director aligns along the magnetic field in the nematic phase. The spectrum of the sample in the isotropic phase contains three hyperfine lines with an antisymmetric lineshape separated by the isotropic hyperfine splitting a for the nitroxide spin probe. The antisymmetric lineshape indicates that the rotational motion of the spin probe is fast on the EPR timescale. The hyperfine splitting is decreased upon cooling into the nematic phase by an amount that reflects the orientational order of the nematic phase, though the lines are now roughly, but no longer perfectly, antisymmetric; this indicates that in the nematic phase, the rotational motion of the spin probe is slowed somewhat on the EPR timescale. However, using the WIN-EPR software, this splitting can be measured, and can be taken to be close to $\tilde{A}_{\parallel}$, which, together with the isotropic hyperfine splitting, a, can be inserted into equation 2.28 to obtain $\tilde{A}_{\perp}$. $\tilde{A}_{\parallel}$ and $\tilde{A}_{\perp}$ are used later to calculate $\bar{a}(\xi)$ and therefore the angle ξ between the director and the magnetic field when hyperfine lines appear at certain positions in the spectrum. The values of a, $\tilde{A}_{\parallel}$ and $\tilde{A}_{\perp}$ for all three samples just above the N-Sm transition are presented in table 6.2.

Table 6.2 The hyperfine splittings used in the interpretation of EPR spectra.

	sample 1	sample 2	sample 3
$\tilde{A}_{\parallel}$ / G	11.0	8.6	12.6
$\tilde{A}_{\perp}$ / G	17.0	18.2 §	16.2 §
a / G	15.0	–	–

§ a could not be measured for CBO6CT samples, therefore the indicated values were calculated assuming a=15.0G as for sample 1.

Upon cooling the nematic phase, the transition to the Sm phase was barely detectable without observing the angular dependence of the spectrum (described shortly). But gradually, just below the temperature identified as the N-Sm transition temperature, the form of the spectrum changes from a three-line spectrum, which indicates a breakdown in the uniform alignment of the sample director along the magnetic field. A shoulder develops on the outside of the high and low-field peaks which causes them to distort further from an antisymmetric shape, and indicates that a small portion of the director is no longer aligned along the magnetic field direction but lies at some small angle to it, although the bulk of the director still remains parallel to the magnetic field. Upon subsequent cooling, over a range of temperatures, the position of the two shoulders moves out and they become two distinct absorption peaks at either end of the spectrum, separated by a splitting which is recognised from table 6.2 to be $2\tilde{A}_{\perp}$. At the same time, the intensity of these outer peaks increases and the intensity of the inner peaks diminishes. As the temperature of the Sm phase is decreased, the proportion of the director at an angle to the magnetic field grows as the maximum angle between the magnetic field and a portion of the director in the sample grows toward 90°, although some of the director remains parallel to the magnetic field throughout. The change from the perfectly or nearly antisymmetric lineshape of the high and low-field peaks in the isotropic and nematic phases to the apparent absorption lineshapes in the Sm phase indicates that the director makes all angles between 0° and 90° with the magnetic field in the Sm phase. Upon further cooling, the position of the lines in the spectrum remains unchanged but the intensity of the outer pair of lines continues to increase at the expense of the inner lines indicating that more of the director makes a larger angle with the magnetic field and less remains parallel to the magnetic field at lower temperatures. The antisymmetric centre line remains essentially unchanged upon cooling as its position is dependent only upon the *g*-factor and is not as sensitive as that of the high and low-field hyperfine lines to the orientation and distribution of the director with respect to the magnetic field.

At certain points in the cooling cycle that has been described, the angle dependence of the spectrum was examined in order to give some more discriminating information on the director distribution within the sample. The angular dependence of the spectrum of sample 1 at several temperatures is shown in figure 4. In this figure and in the following description the angle referred to is the angle through which the sample has been rotated with respect to the 0° position (which is the position in which the sample was cooled from the nematic phase).

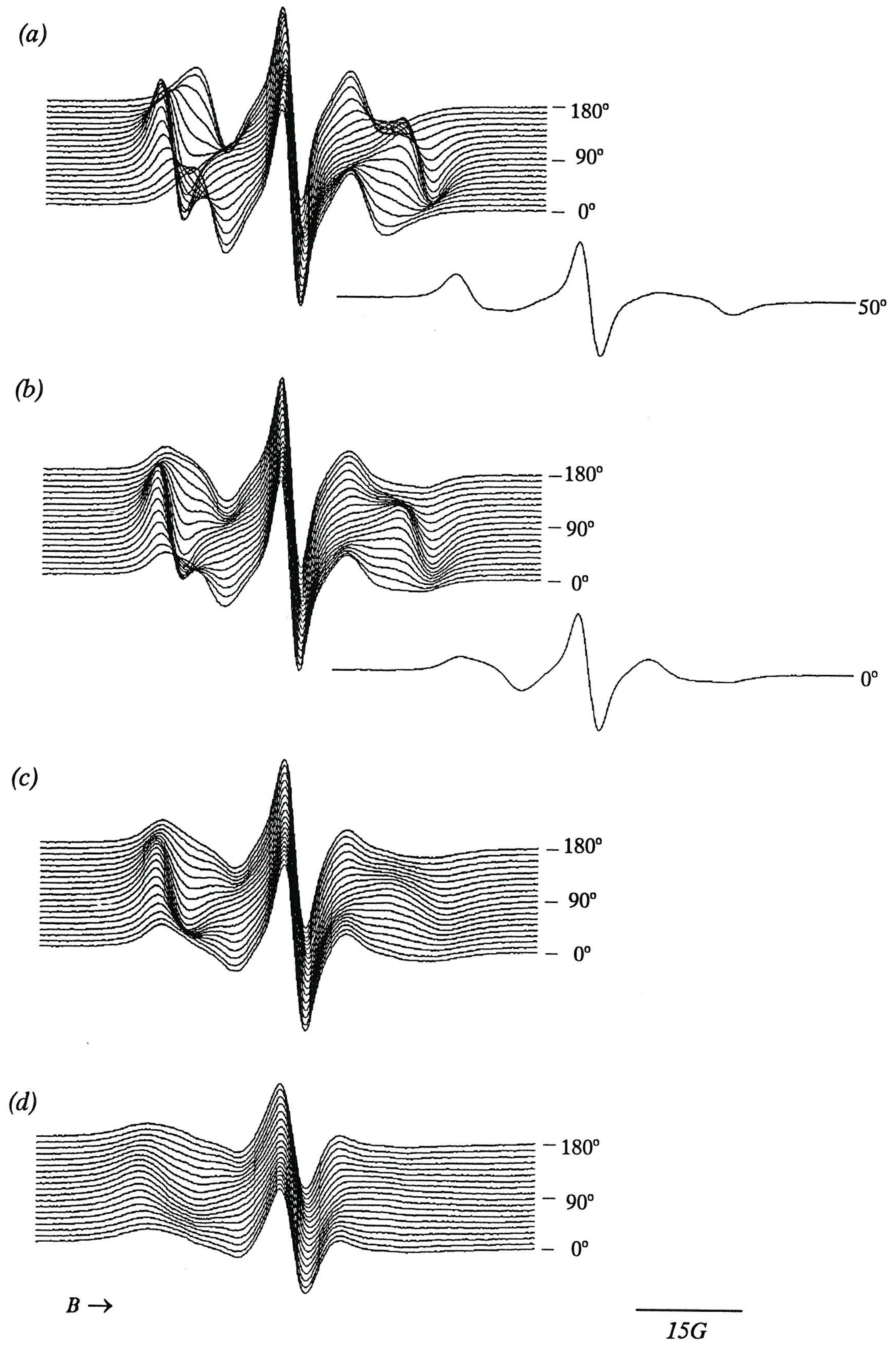

Figure 4 The angular dependence of the spectrum of cholestane in CB7CB as the sample is rotated through 180° at temperatures of (a) 98°C (b) 93°C (c) 78°C and (d) 58°C. Some of the spectra have been extracted from the stack plots to emphasize features referred to in the text.

The angle dependence of the spectrum at 98°C (figure 4a) obtained just before the transition to the Sm phase becomes noticeable in the spectrum, but obviously below the N-Sm transition, shows that the director was almost all, but not completely, aligned along the magnetic field direction in the Sm phase. This explains the difference between the angle dependence seen here and that of a monodomain smectic A phase (seen in figure 5d, Chapter 2); this is most noticeable in the spectra at intermediate angles between 0° and 90° where the lineshapes clearly indicate that the director makes a range of angles with the magnetic field. The spectrum at 50° extracted from the stack plot shows this very clearly. The same pattern of behaviour is also seen in the angle dependence of the spectrum at 93°C, although at this lower temperature the development of the Sm phase structure is more complete, and the presence in the sample of a range of director orientations is also more obvious in the lineshape of the 0° spectrum. As the sample is further cooled, the 0° spectrum at 78°C, with similar intensities in the inner and outer peaks and the absorption lineshape, is similar to that expected for a two-dimensional powder distribution of the director (recall the two-dimensional powder spectrum acquired in zero field gradient of the rapidly spinning nematic sample shown in figure 4, Chapter 5). This similarity is discussed later. The spectrum at 58°C is remarkable in showing very little angle dependence, although the large linewidths at this temperature tend to blur some of the structure in the spectrum in any case. In fact, the large linewidths for the cholestane spin probe in CB7CB, coupled with the rather small anisotropy in the hyperfine splitting ($\tilde{A}_{\perp}$-$\tilde{A}_{\parallel}$), tends to make a detailed interpretation of the spectrum difficult at all temperatures. For this reason, the spectrum of cholestane in CBO6CT, with its narrower lines on account of the higher transition temperatures and greater difference ($\tilde{A}_{\perp}$-$\tilde{A}_{\parallel}$), contains more accessible information and this is now discussed.

6.4.2 Sample 2: cholestane in CBO6CT

The temperature dependence of the spectrum of sample 2 during cooling from the nematic phase into the Sm phase is shown in figure 5.

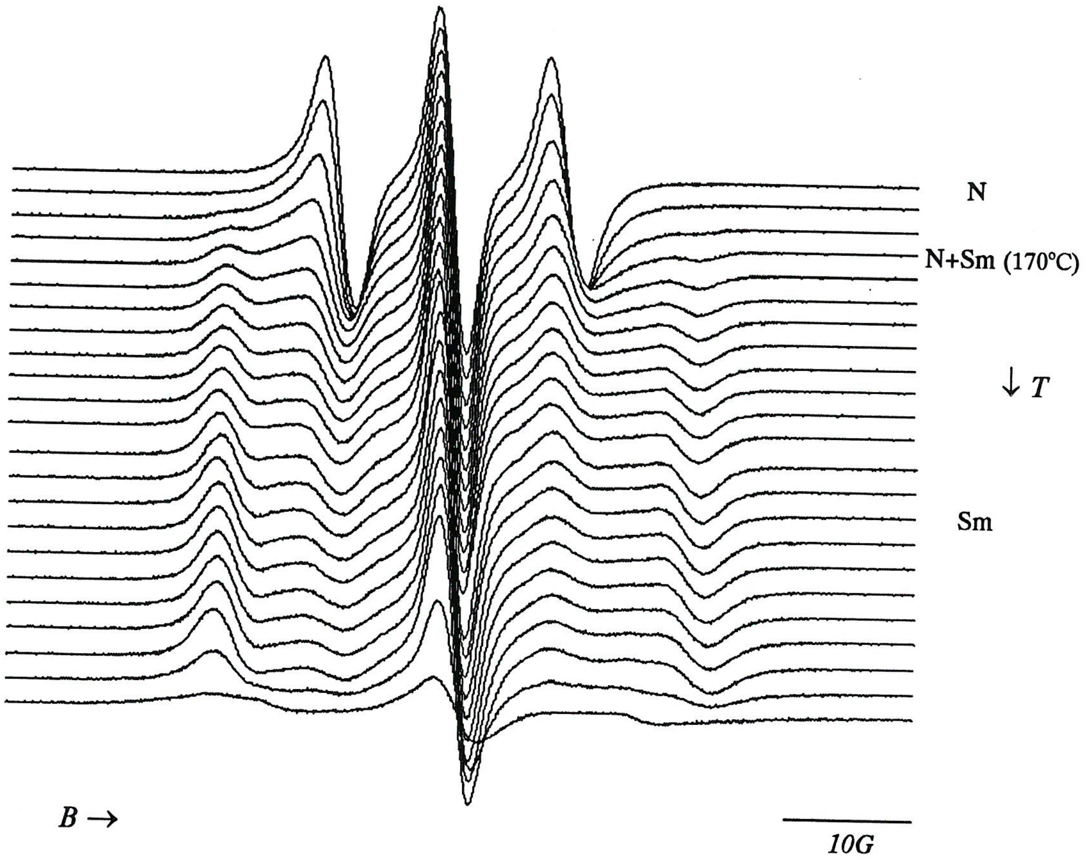

Figure 5 The spectrum of cholestane in CBO6CT as a function of temperature.

The temperature dependence of this spectrum shows the same qualitative form as that observed for sample 1. That is, the three-line spectrum of the sample in the nematic phase develops shoulders which separate and move out from the high and low-field lines of the spectrum to a separation of the estimated value of $2\tilde{A}_{\perp}$ as the Sm phase develops. The hyperfine splittings estimated for this sample were included in table 6.2. The only subsequent change as the temperature is further decreased is the increase in the intensity of the perpendicular features at the expense of the parallel features in the spectrum, as was also noted for sample 1. The principal differences between these spectra and those of sample 1 are the narrower linewidths, the antisymmetric lineshapes in the spectrum of the nematic phase, and the smaller hyperfine splitting in the nematic and Sm phases, $\tilde{A}_{\parallel}$ and therefore the larger value of $\tilde{A}_{\perp}$ and the difference $(\tilde{A}_{\perp}-\tilde{A}_{\parallel})$ for cholestane in CBO6CT. The first two features can be attributed to the faster rotational motion of the spin probe on the timescale of the EPR experiment in the nematic phase formed by this compound. The smaller value for $\tilde{A}_{\parallel}$ indicates that the orientational order of the cholestane spin probe with respect to the local director is larger in CBO6CT. These factors make for a more reliable parameterisation of the spectrum for the analysis that is applied later. This improves our ability to use the spectrum to distinguish between different possibilities for the director distribution in the sample by lessening the probability of different director distributions providing an equally good fit to the experimental spectra.

The angle dependence of the spectrum of sample 2 at 155°C and 135°C is shown in figure 6.

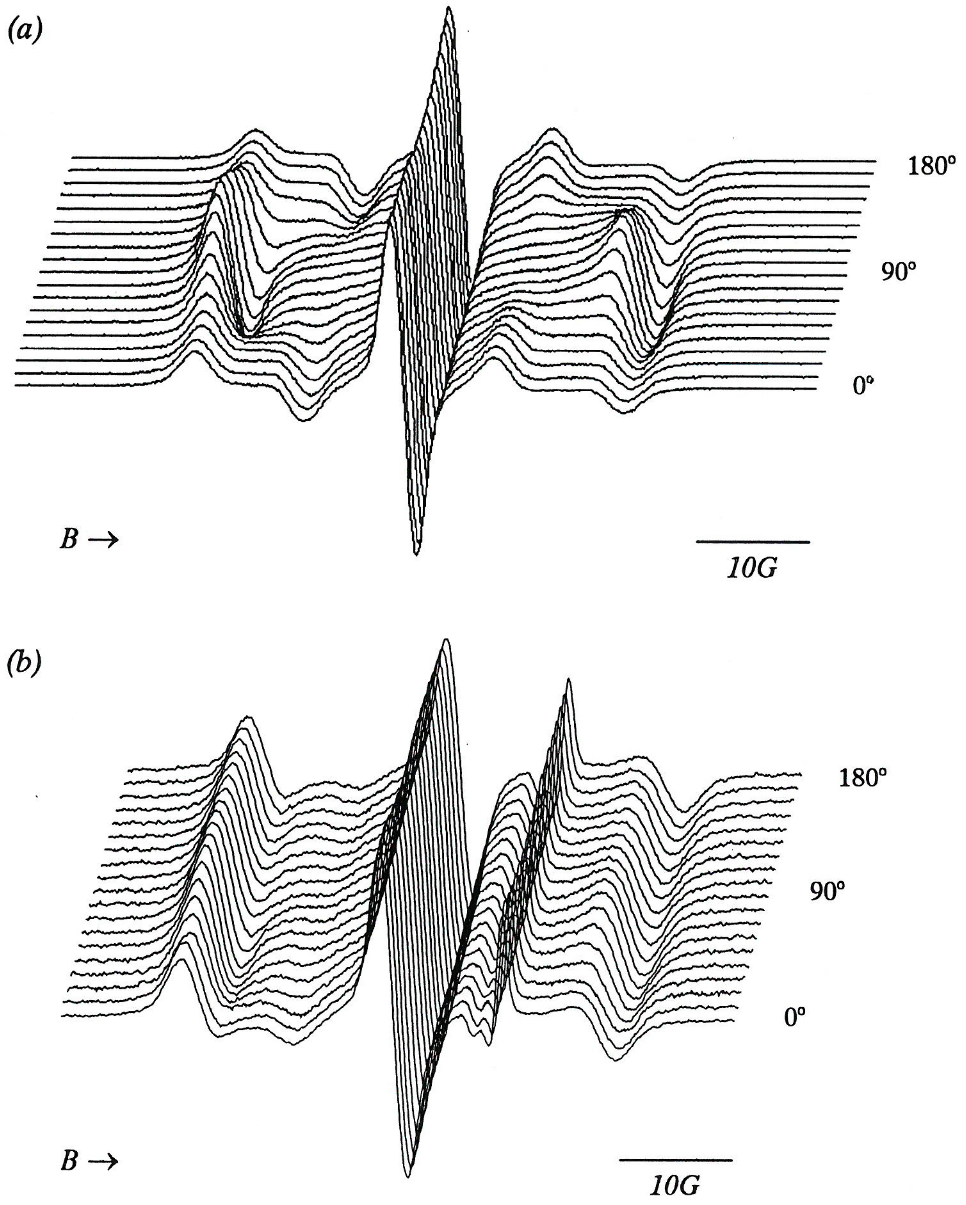

Figure 6 The angle dependence of the spectrum of cholestane in CBO6CT as the sample is rotated through 180° at (a) 155°C and (b) 135°C.

The angle dependence of the spectrum of sample 2 at 155°C shows the same qualitative behaviour as that seen for sample 1 at 78°C, subject to the cosmetic differences in the line shapes, widths and positions previously mentioned. In particular, the 0° spectrum, with the absorption and inverse absorption lineshape of the perpendicular and parallel features and their similar relative intensities is again that expected to arise from a two-dimensional powder distribution of the director. However, the development and the angle dependence of this spectrum would appear to preclude this possibility and this is discussed in the next section. The 0° spectrum of the sample at 135°C, with the high and low intensities of the perpendicular and parallel features respectively shows the same pattern as that seen in sample 1 at 58°C; the angle dependence of this spectrum is rather weak as was also noted for sample 1 at 58°C. The distribution of the director that this implies is considered in greater detail in the next section.

6.4.3 Sample 3: tempone in CBO6CT

A selection of spectra showing the temperature dependence of the EPR spectrum of sample 3 are shown in figure 7. The angle dependence of the spectra at temperatures of 155°C and 135°C is shown in figure 8.

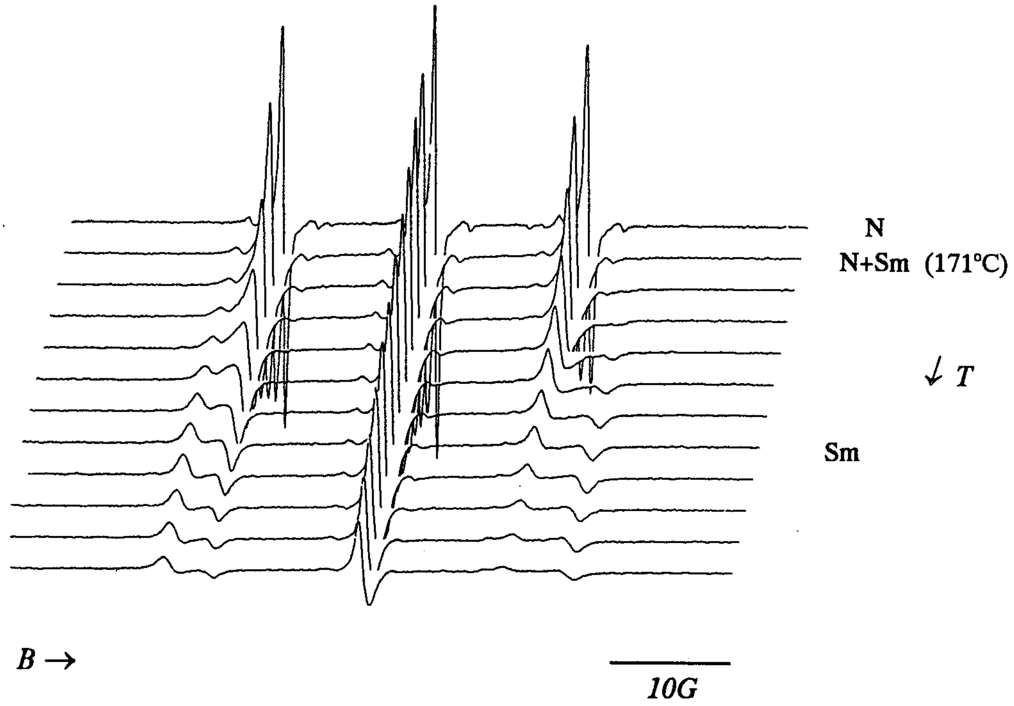

Figure 7 The spectrum of tempone in CBO6CT as a function of temperature.

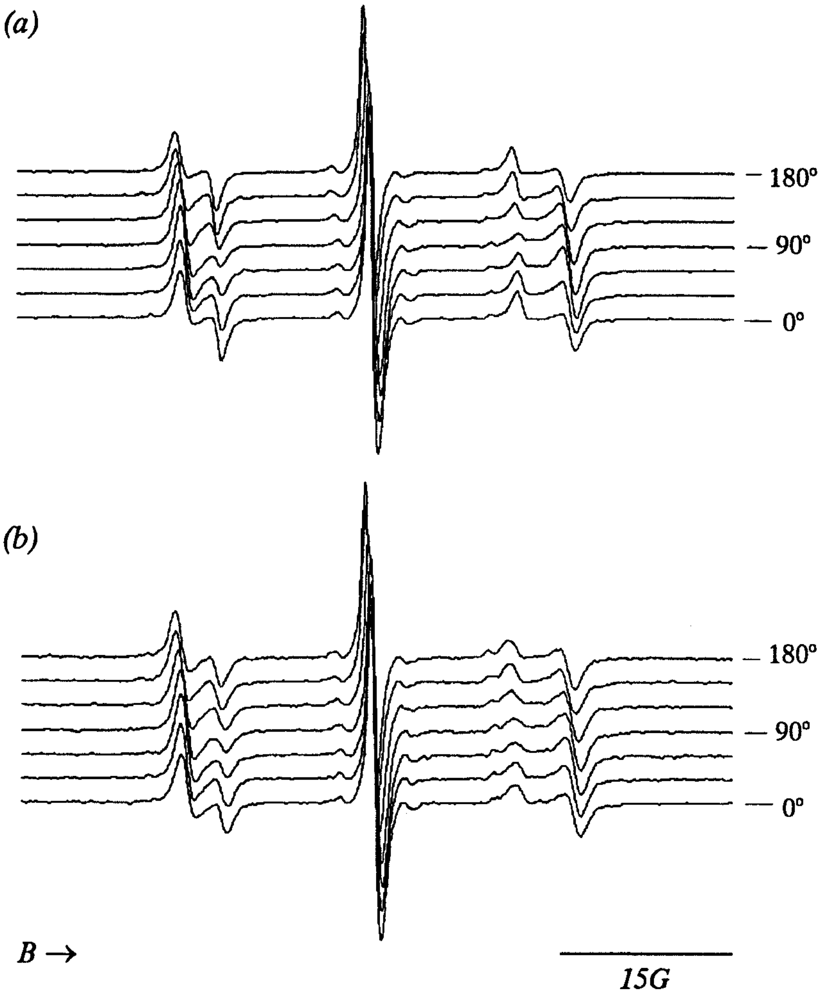

Figure 8 The angle dependence of the spectrum of tempone in CBO6CT as the sample is rotated through 180° in 30° intervals at (a) 155°C and (b) 135°C.

The spectra of sample 3 again indicate the same qualitative behaviour of the director distribution as a function of temperature and angle as that reported for samples 1 and 2 although the spectral form is a little different. Here we just make some brief comments on the temperature and angle dependence of the spectrum. The tempone spin probe is less anisotropic in shape and smaller than cholestane, therefore its orientational ordering is weaker and its rotational motions are faster when it is dissolved in CBO6CT at a given temperature. Consequently, the range of hyperfine splittings, $(\tilde{A}_{\perp}-\tilde{A}_{\parallel})$ indicated in table 6.2 is much smaller in the Sm phase. The spectrum in the nematic phase is made up of narrow, antisymmetric lines while the powder spectrum in the Sm phase is made up of a combination of narrow, antisymmetric hyperfine lines. However, the temperature dependence of the spectrum follows the pattern already established: the three-line spectrum of the nematic develops shoulders at the transition to the Sm phase which grow and separate as the phase develops. At the same temperature as sample 2, the spectrum goes through a stage when the parallel and perpendicular features have similar intensity and in which the angle dependence of the spectrum is strong (Again, this recalls the two-dimensional powder spectra acquired in zero field gradient seen in Chapter 5). By the time the temperature has been decreased to 135°C, the perpendicular features have increased in intensity at the expense of the parallel features and the angle dependence of the spectrum is weak (This recalls a three-dimensional powder spectrum).

Finally, two points concerning the stability of the various spectra and therefore the director distributions that produce them should be made. Firstly, the behaviour of the spectra of the three samples during cooling is entirely reversible upon heating. Secondly, as it is specifically our aim to study the director distribution, it is necessary to be certain that the director has adopted an equilibrium distribution that is truly representative of the Sm phase in the EPR experiment. Cooling through the nematic-smectic phase transition was therefore repeated for each sample at varying rates of temperature decrease and also using an annealing process at higher magnetic field strengths (6600G). On each occasion the same variation of the spectrum with temperature was observed for the Sm phase, suggesting that this is truly the director distribution characteristic of the Sm phase in the EPR experiment. The spectra of the sample as it is rotated from the 90° to the 180° positions reflect those seen as the sample is rotated from 0° to 90° and support the notion that the director structure is quite stable.

6.5 Discussion

It is the aim of this study to determine the form of the director distribution function from the experimental spectra with the eventual intention of proposing an arrangement of the layered structure in the Sm phase. However, it should be noted that the EPR experiments in this Chapter give no direct information about the spatial distribution of the director within the sample. Consequently, a completely successful outcome of these experiments relies on a unique model for the physical structure of the Sm phase being entirely consistent with the director distribution which is obtained from the analysis of the EPR experiments. With this aim and this limitation in mind it is first useful to consider two general points about the form of the spectra and the assumed symmetry of the director distribution in the sample in the EPR experiment and of the Sm phase itself before considering some of the features of the experimental spectra in greater detail. First, and most importantly, and without the need for a detailed spectral analysis, the director distributions inferred from this series of EPR experiments reveal the same peculiarities as seen in previous experiments on CBO6CB [10, 11]. That is, they do not conform to those expected of any previously characterised smectic phases although the apparent similarity of some of the experimental spectra to those anticipated for certain director distributions has been noted and is discussed later. Second, the series of EPR experiments that have been described employ a magnetic field as the only external constraint to orient the director during cooling from the uniaxial nematic phase and therefore cylindrical symmetry of the director distribution in the Sm phase about this direction is anticipated. This means that even if the Sm phase is actually biaxial, this will not be revealed directly in the angular dependence of the spectrum, as there is no second constraint to define the orientation of a second axis [19]. The other possibility is that the biaxial shape of the CB7CB and CBO6CT molecules causes preferential orientation of the short molecular axes about the director and that a biaxial distribution develops in the bulk sample without the need for a second external constraint. However, this is unlikely, and in any case, the results of repeated cooling experiments would be expected to show some differences according to how slowly or rapidly the Sm phase was formed. As reported earlier, no such differences were seen. We can therefore confidently expect cylindrical symmetry of the director distribution (about the direction of the magnetic field during phase formation) given the bulk sample size. In any event, the local symmetry of the Sm phase is at present academic. The first task is to determine the director distribution, as only then can we attempt to map proposed structures onto the known director distribution for the sample.

Having commented upon the symmetry of the director distribution in this series of EPR experiments and how this may or may not relate to the local symmetry of the Sm phase, we now discuss the similarities of some of the experimental spectra to those expected in certain familiar situations. In particular, the resemblance of the 0° spectra of the CB7CB sample at 78°C and the CBO6CT samples at 155°C to a two-dimensional powder spectrum was noted. At lower temperatures, the spectra of all three samples tend toward those expected to arise from a three-dimensional powder distribution of the director (that is, the perpendicular features become strong, the parallel features become very weak, and there is very little angle dependence of the spectrum). These different situations are now considered in more detail but first it is useful to describe a convenient way to refer to the director distribution.

In considering the appearance of the spectra and the director distribution from which they originate, it is useful to define a laboratory axis set and an axis set within the sample so that the behaviour of different features in the spectrum can be more easily traced back to the features of the director distribution. It should be noted that definition of a cartesian axis set within the sample serves only this purpose and is not intended to imply that there is a loss of the cylindrical symmetry of the director distribution. The laboratory axis set XYZ remains as defined in Chapter 3. Z is the magnetic field direction throughout the experiment, Y lies along the axis of the sample tube and is the axis about which the sample is rotated to acquire the angle dependence of the spectrum, the X-axis lies orthogonal to Y and Z. In the sample axis system, xyz, the z-axis is defined by the magnetic field direction Z as the sample is cooled through the N-Sm transition, this thereafter remains the symmetry axis for the director distribution. In using an angle to describe a particular spectrum from part of a sequence in which the angle dependence of the spectrum was recorded, the angle λ is the angle between the z and Z axes. The Y-axis lies along the axis of the sample tube and remains coincident with the Y-axis of the laboratory axis system throughout the experiment. The relationship between the different axis sets during the course of the experiment is pictured in figure 9.

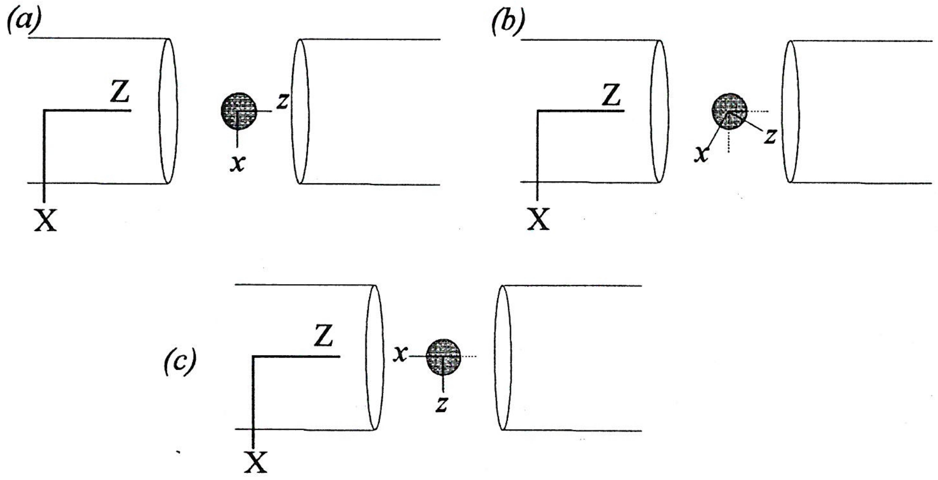

Figure 9 The relationship between the laboratory axis system (XYZ) and the sample axis system (xyz) during the EPR experiment shown in plan view, looking along the Y axis (a) at the 0° position during cooling from the nematic to the Sm phase, (b) at the 30° position during acquisition of the angle dependence of the EPR spectrum of the Sm phase.

First, using the axis systems just described, we consider the similarity of the 0° spectrum for sample 2 at 155°C to that of a two-dimensional powder spectrum and the implications this has for the director distribution in the sample. This similarity is considered in some detail for sample 2, because in this system, as compared with sample 1, the narrower linewidths make the correlation between the spectrum and the director distribution stronger than if large linewidths blur the different features in the spectrum. In addition, the relatively small angle dependence of the linewidths for cholestane, as compared with tempone, means that a preliminary qualitative interpretation of the spectra can be based with greater certainty on features of the director distribution, rather than being distorted by any linewidth effects. The two-dimensional director distribution is considered in some detail because of the resemblances in the spectrum and because it has previously been used to explain the structure of the Sm phase in terms of rippling of the layers [10, 12].

The 0° spectrum ($z \parallel Z$) shows features appearing at fields corresponding to parallel and perpendicular hyperfine splittings, it is immediately apparent that the very similar intensity of parallel and perpendicular features is just that expected in the spectrum of a two-dimensional powder pattern in which the magnetic field direction lies in the plane in which the director is confined [20]. As the sample is rotated the intensity of the perpendicular features increases steadily, whilst the intensity of the parallel features decreases. In the spectrum of the sample in the 90° position (x || Z), the perpendicular features are very strong indicating that the director largely lies in the yz plane. Although the parallel features are weak they have not disappeared completely, indicating that some of the director remains along the x direction. This fact, together with the observation that the perpendicular lines show an asymmetric shape implies that there remains a continuous distribution between the parallel and perpendicular extremes of the director orientation, that is, there is a continuous distribution in the director between the yz plane and the x direction.

Having noted the similarity between the experimental 0° spectrum and a two-dimensional powder spectrum, we should note that a true two-dimensional powder distribution of the director is not consistent with the requirement for cylindrical symmetry of the director distribution about the z-axis nor with the experimental spectra. Thus, a two-dimensional powder distribution contains a symmetry axis perpendicular to the plane in which the director is confined, but formation of a true two-dimensional powder director distribution consistent with the appearance of the 0° spectrum implies a loss of the cylindrical symmetry of the director distribution about the z-axis. Figures 10a and b shows the two extreme director distributions with respect to the magnetic field that result if a two-dimensional distribution is rotated through an angle of 90° with respect to the magnetic field and emphasizes the features that are likely to be prominent in the respective spectra. In this figure the plane in which the director is uniformly distributed is represented by a circle and a selection of director orientations are represented as spokes within the circle. The spectra that correspond to these two extremes are, first, a monodomain spectrum in which all of the spectral intensity is concentrated in the perpendicular features. This occurs if the magnetic field is rotated out of the plane in which the director is distributed and is represented in figure 10a. The experimental 90° spectrum indicated that most, but not all, of the spectral intensity was concentrated in the perpendicular features. At the other extreme, if the magnetic field remains in the plane in which the director is distributed, then rotation of the sample through any angle will not change the director distribution with respect to the magnetic field and the 90° spectrum, or indeed the spectrum when the sample is rotated through any angle, will be a two-dimensional powder pattern and the same as the 0° spectrum. This is shown in figure 10b. This is clearly *not* what happened to the experimental spectrum as the sample was rotated through 90°.

A distribution can be constructed that is more consistent with the experimental spectra and that preserves cylindrical symmetry about the z-axis; we coin the term 'extended two-dimensional distribution' to describe this distribution, because it has differences from, and similarity to, a true two-dimensional distribution. In this model, represented in figure 10c, the cylindrical symmetry of the director distribution about the z-axis is preserved by considering the overall distribution to be a superposition of a series of two-dimensional distributions lying in every plane containing the z axis. The spectra predicted for the extended two-dimensional distribution would appear to have qualitatively the same form as the experimental spectra for sample 2 at 155°C and it is worth stressing these points of similarity. The 0° spectrum for the extended two-dimensional distribution is the same as that of a true two-dimensional distribution. Now the 90° spectrum ($x \parallel Z$) broadly possesses the required form, that is, most of the spectral intensity is concentrated in the perpendicular features, as the director is concentrated close to the yz plane, but a small portion of the director is orientated along the x axis parallel to the magnetic field giving rise to a small parallel intensity. Additionally, in this model there is a continuous director distribution between perpendicular and parallel orientations projected onto the magnetic field direction when the sample is rotated to the 90° position, this was seen in the asymmetric perpendicular features of the experimental 90° spectrum. Having noted that extended two-dimensional distribution would appear to have qualitatively the correct form to produce some of the experimental spectra, this distribution is revisited in the analysis section in which simulations of the full angle dependence of the spectrum for this model distribution are described. These provide a more quantitative test for this distribution against the experimental observations.

The other observation from the earlier discussion that should be considered in more detail is that, upon decreasing the temperature, the spectra increasingly approach that predicted for an isotropic distribution of the director in three dimensions, that is, a three-dimensional powder pattern (the spectrum shown in figure 4b, Chapter 2).

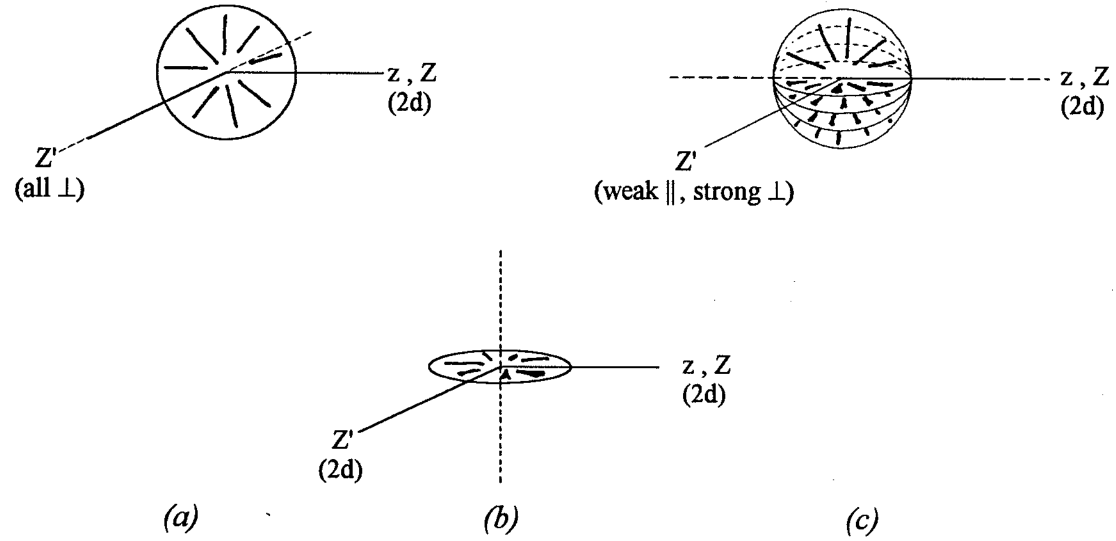

Figure 10 The different orientations (a) and (b) of a two-dimensional distribution and the different distribution in (c) the extended two-dimensional distribution are only obvious when the magnetic field (Z and Z') is rotated away from the z-axis. The symmetry axis of each of these distributions is indicated by a dotted line.

This is indicated by the increased intensity of the perpendicular features at the expense of the parallel features in the 0° spectra, but moreso by the observation that the angle dependence of the spectra is less at lower temperatures: in the limit of an isotropic director distribution over the sample, the spectrum will not show any angle dependence. In the CB7CB sample, a weak angle dependence could partly be attributed to slowed rotational motion of the spin probe at lower temperature increasing the linewidths and this has the effect of blurring the angle dependence of the spectrum. However, in the CBO6CT samples the linewidths remain narrow but the spectrum still approaches that of a three-dimensional powder pattern at lower temperatures. The simulations of the next section seek to ascertain the extent to which the experimental spectra of the CBO6CT sample resemble those of a three-dimensional powder pattern.

To conclude this section, it is noted that a qualitative interpretation of the spectra has produced two possible solutions for the director distribution which would appear to plausibly account for some of the experimental spectra although the distributions considered have not been exhaustive. These distribution functions are testable, and in the next section the simulations that are used to test these distributions against their experimental counterparts are described. Later in the next section more detailed simulations of the spectra of sample 2, the cholestane spin probe in CBO6CT, are used to determine the form of the distribution using a more objective model-independent approach. These distributions can then be tested impartially against various model distributions including the extended two-dimensional distribution and isotropic distributions which we have considered here and also against a statistical theory developed in Chapter 1 for a different purpose (see section 1.5).

6.6 Simulation

The aim of these simulations is to obtain the form of $f(\theta)d\theta$ for the director from the observed angle dependence of the EPR spectrum of the sample using a numerical approach (see Chapter 2). As the sample is rotated with respect to the magnetic field, the spectrum changes as a function of the distribution of the director with respect to the magnetic field $f(\xi)d\xi$ which can be related to the form of $f(\theta)d\theta$ and the angle through which the sample has been rotated. Cylindrical symmetry of the director distribution in the sample about the z-axis is assumed and therefore the form of $f(\theta)d\theta$ is the most detailed information we can expect to obtain about the distribution. Two strategies are adopted in the simulation of the EPR spectra. The first of these is a simple model-based approach in which an analytical expression is assumed for the director distribution and is used to calculate the angle dependence of the EPR spectrum. The second approach begins with the assumption of a random form for the director distribution for which a set of EPR spectra are calculated, this is then used as an input to a second stage in which elements of the distribution, $f(\theta)$, are varied and a least-squares fitting program based on a simplex algorithm is used to fit the set of calculated spectra to the experimental spectra. The advantage of this approach is that it uses a non-prejudicial method of calculating the coefficients that go into the distribution $f(\theta)$, which can then be objectively tested against various models for the form of the director distribution. As the whole set of angular-dependent spectra at a given temperature arise from a single director distribution the program calculates and simultaneously fits the spectra at several different angles corresponding to real spectra to obtain the best distribution consistent with all of the experimental data for a particular sample at a particular temperature.

The calculation of the spectrum for a given director distribution is common to both approaches. It is useful to consider in overview how the spectrum is dependent upon the director distribution within the sample. Formally, the spectrum of the sample is represented by the integration of equation 2.29 in which the spectral quantities have the angular dependences described in Chapter 2. For the purposes of simplifying the process of calculation (and later, fitting) of spectra, we do not evaluate this integral here. Instead, we calculate the spectrum of the sample, $S(B)$, as a function of the magnetic field strength B, as the sum of a number of subspectra $s(B)$ weighted with their respective probabilities of occurrence. The sample spectrum and the component subspectra depend upon the angle between the symmetry axis of the director distribution and the magnetic field, that is, the angle λ between the z and Z axes, thus the expression we evaluate is actually

$$S(B,\lambda) = \sum_{\mathrm{i}} s_{\mathrm{i}}(B,\lambda)\ p_{\mathrm{i}} \tag{6.1}$$

in which $s_{\mathrm{i}}(B,\lambda)$ represents a particular subspectrum and p_{i}, when suitably normalized ($\int p_{\mathrm{i}}\,\mathrm{d}\cos\theta = 1$), determines the magnitude of its contribution to the overall spectrum which reflects the distribution function f(θ).

Each subspectrum $s_{\mathrm{i}}(B,\lambda)$ is given by

$$s_{\mathrm{i}}(B,\lambda) = \sum_{\mathrm{r}} L(B, \widetilde{B}_{\mathrm{r}}(\mathrm{i}), T_2^{-1}(\mathrm{i})) \tag{6.2}$$

in which the spectral parameters, $\widetilde{B}_{\mathrm{r}}(\mathrm{i})$ and $T_2^{-1}(\mathrm{i})$ depend upon the angle ξ between the magnetic field and the local director orientation defined for each of the i points. This is an appropriate substitution here and in other cases where individual subspectra contribute independently of each other to the spectrum of the sample as a whole (this also reflects the fact that director motions are slow on the EPR timescale). The problem of specifying or determining the director distribution then becomes a problem of obtaining the set of values p_{i} which give the best agreement between the experimental and calculated spectra. The program EPRcalc was written in Fortran 77 both for varying the set of probabilities p_{i} and for direct calculation of spectra based on a specified distribution for the director. The operation of EPRcalc is described in the next section. A full listing of EPRcalc appears in Appendix C.

6.6.1 EPRcalc

A number of spectra of the sample rotated to different positions λ about the sample tube axis are calculated for comparison with the equivalent experimental spectra. Each of these spectra is obtained as follows. Points i on the surface of a sphere are generated in $(\cos\theta,\phi)$ space, θ represents the polar angle away from the z-axis of the sample, and ϕ is an azimuthal angle around the z-axis. Working in $(\cos\theta,\phi)$ space ensures that the same spectral weight applied to each vector i reflects a uniform density for the distribution of the vectors i over space, that is, represents an isotropic director distribution. Two angles are needed to specify the angle ξ made by each of the vectors i with the magnetic field in the general case when the field and the director are not coincident. A unit vector $(\cos\phi \sin\theta, \sin\phi \sin\theta, \cos\theta)$ points to each of these i points from the centre of the sphere. To calculate the 0° spectrum a set of angles $\xi_{i,0}$ between the vector i and the Z axis (z || Z in the 0° spectrum) are calculated. This is pictured for one of the i vectors in figure 11. This set of angles are used to calculate the value of the angle-dependent linewidth and of the resolved components of the $\tilde{\mathbf{A}}$ and $\tilde{\mathbf{g}}$ tensors for each point i using the system of equations developed in Chapter 2. The subspectrum for each point i, $s_i(B,0°)$ is then calculated by substitution of these values into the appropriate lineshape functions. The 0° spectrum is calculated as the sum of each of these subspectra multiplied by their respective weighting factors $p(\cos\theta_i)$ which are determined by the director distribution. In all calculations of the sample spectrum the cylindrical symmetry of the director distribution about the z direction is preserved by maintaining the same value of p_i for all points possessing the same value of $\cos\theta$ irrespective of ϕ : p_i therefore depends only upon $\cos\theta_i$. The process described for calculation of the 0° spectrum is then repeated for other values of the angle λ with the simulated magnetic field direction being moved to the appropriate positions to calculate the other sets of angles $\xi_{i,\lambda}$ and their dependent quantities. These are substituted into the lineshape function to calculate the component subspectra for each point i at each angle λ, $s_i(B,\lambda)$.

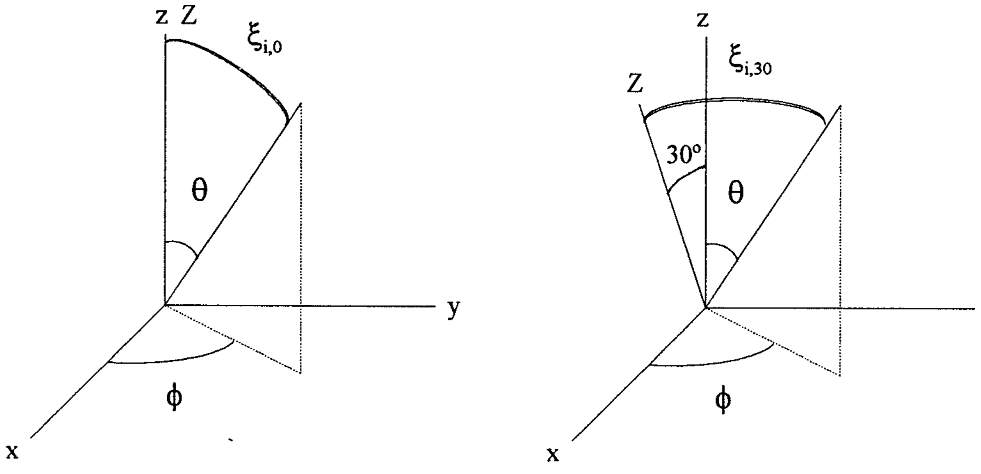

(a) *(b)*

Figure 11 The polar angles θ and ϕ that define the orientation of a vector i representing the director orientation with respect to the z axis, the angle ξ between the director and the magnetic field that is used to determine the values of the angle-dependent quantities for the point i, shown for the angles between the z and Z axes (a) $\lambda=0°$ and (b) $\lambda=30°$.

In the model-based approach, once the full set of subspectra that serve as components of the spectrum of the sample have been calculated, the sample spectrum $S(B,\lambda)$ is obtained simply by evaluation of the summation of equation 6.1 in which the $p(\cos\theta_i)$ take values based on the analytical model adopted for the director distribution within the sample.

In the least-squares fitting method, the fitting process is begun by evaluation of the same summation but from a starting configuration in which all $p(\cos\theta_i)$ take the value 1. This corresponds to a three-dimensional powder spectrum predicted for an isotropic director distribution. Four spectra for the sample rotated at different angles λ about the sample tube axis are calculated, these are to be compared with the experimental spectra measured with the sample in the 0° (z || Z), 30°, 60° and 90° (x || Z) positions. The error function E measures the deviation between the spectra calculated using these coefficients and the experimental spectra, E is calculated as the sum of the squares of the differences between the calculated spectra $S(B,\lambda)$ and the experimental spectra $h(B,\lambda)$ taken point-by-point,

$$E = \sum_{\text{fields } j}\ \sum_{\text{angles}\lambda} [\, h(B_j,\lambda) - S(B_j,\lambda)\,]^2 \qquad (6.3)$$

in which $h(B,\lambda)$ and $S(B,\lambda)$ are the experimental and calculated 0, 30, 60 and 90° spectra respectively. The aim of the fitting process is to minimise E by varying the values $p(\cos\theta_i)$ and in doing so, to determine the set of coefficients $p(\cos\theta_i)$ that best satisfy the experimental spectra.

In the least-squares fitting procedure used in this study, the set of coefficients $p(\cos\theta_i)$ are varied using the simplex algorithm which is summarised here and described in greater detail elsewhere [21]. In this method, n coefficients are treated as independent parameters in obtaining the best fit to the experimental spectra, that is, minimising E, and the fitting proceeds *via* the movement of a simplex (a geometrical figure) with $n+1$ interconnnected vertices over n-dimensions of space to locate the set of values for the n parameters that give the smallest value of E. The total number of points i for which subspectra are calculated is 500. These lie on a 20 by 25 grid in $(\cos\theta,\phi)$ space, $\cos\theta$ is varied from 0.025 to 0.975 in increments of 0.05, ϕ is varied from 3.6° to 176.4° in increments of 7.2°. The requirement for preservation of cylindrical symmetry about the z axis ensures that the number of independent parameters $p(\cos\theta_i)$ to be fitted is only 20, corresponding to the number of $\cos\theta$ values used, that is, n=20 in this case. So, although there are 500 different subspectra $s_i(B,\lambda)$ to be summed into each spectrum $S(B,\lambda)$, the weighting factor $p(\cos\theta_i)$ for each of these 500 subspectra takes one of only 20 values based on the value of $\cos\theta$. As already stated, the initial distribution simulated is the isotropic director distribution in which all of these $p(\cos\theta_i)$ take the same arbitrary intensity, 1. Twenty other director distributions are then constructed by addition of some incremental intensity to a different one of the 20 $p(\cos\theta_i)$ values. The angle dependence of the spectra for each of these 21 distributions is calculated, compared with the experimental spectra and a value of E calculated for each. The director distribution that gives the largest value of E (the worst agreement), is selected and then reflected through the simplex produced by the remaining 20 distributions to obtain a new set of values for the 21st distribution. The calculated spectra for the 21 distributions are used again to identify the worst fitting distribution, and this worst fitting distribution is recalculated by reflecting through the simplex formed by the other 20 distributions. This process is then simply repeated until a satisfactory level of agreement is obtained between the calculated spectra and their experimental counterparts. As the fitting proceeds, there is a convergence of the full set of distribution coefficients in the 21 distributions towards a limiting set which gives rise to the best agreement with the experimental spectra. The set of distribution coefficients so obtained can then be objectively tested against those that can be obtained from various analytical models for the director distribution in the sample.

6.6.2 Analysis Parameters

The spectra for sample 1 (cholestane in CB7CB) were not used in either analysis because of the large linewidths and the loss of the antisymmetric lineshape even before the transition to the Sm phase. This implied that molecular rotations are not in the fast motion regime in the EPR experiment on this sample. The analysis that is required for a correct parameterisation of the lineshape function in these cases is more complex [22] and is beyond the scope of this investigation. Simulations of the spectra for sample 2 (cholestane in CBO6CT) were undertaken using both the model-based approach and the least-squares fitting based on the simplex algorithm. The spectral parameters used in these simulations are listed in table 6.3. The $\tilde{A}$ values for sample 2 have been refined slightly from the estimates listed in table 6.2, as the value of $\tilde{A}_{\|}$ appeared to decrease slightly on cooling in the Sm phase. Simulation of the spectra for sample 3 were undertaken using the model-based approach only, the parameters used in these simulations are also shown in table 6.3. The model director distributions that were used to simulate spectra were the extended two-dimensional distribution and the isotropic distribution.

Table 6.3 The parameters used in the simulations of sample 2 and sample 3.

Spectral Parameters	sample 2	sample 3
$\tilde{A}_{\parallel}, \tilde{A}_{\perp}$ / G	8.4, 18.3	12.6, 16.2
$\tilde{g}_{\parallel}, \tilde{g}_{\perp}$ ‡	2.0032, 2.00285	2.00544, 2.00524
linewidth coefficients		
$m_I = +1$: A_0, A_2, A_4 / G §	1.4 , 0, 0	0.55 -0.1, 0.0
$m_I = 0$: A_0, A_2, A_4 / G §	1.3 , 0, 0	0.45, -0.1, 0.0
$m_I = -1$: A_0, A_2, A_4 / G §	1.5 , 0, 0	0.6, -0.1, 0.0
lineshape function †	L:G = 1:1	L

Program Parameters

number of subspectra used: 500, 20 values of cosθ, 25 values of ϕ

Least-squares fitting parameters

initial $p_i = 1$ (all i)

number of fitting steps = 20,000

---

§ - the linewidths are calculated separately for each hyperfine line using $T_2^{-1} = A_0 + A_2 P_2(\cos\xi) + A_4 P_4(\cos\xi)$

† - obtained by fitting in Microcal Origin, L = lorentzian, G=gaussian, L:G=1:1 = equal mixture of lorentzian and gaussian.

‡ - these are working g values based on the resonant fields $\tilde{B}_r(\parallel)$ and $\tilde{B}_r(\perp)$, not the true components of the $\tilde{\mathbf{g}}$ tensor

6.7 Simulation Results

The discussion of both the model-dependent spectral simulations and the model independent spectral fitting are collected together and follow the presentation of the following simulation results.

6.7.1 Spectral calculations

Simulated spectra corresponding to sample 2 calculated using the extended two-dimensional distribution are shown in figure 12, this should be compared with the experimental spectra acquired at 155°C from figure 6a. A simulation of the spectrum for the isotropic director distribution, shown in figure 13, should be compared with the experimental spectra from figure 6b acquired at 135°C. All spectra are normalized so that the integrated intensity of the spectra in the absorption mode equals one.

The distribution functions f(cosθ) that are implied by these director distributions are shown in figure 17. The equivalent set of spectra calculated using the parameters determined for sample 3 are shown in figures 14 and 15, these should be compared with the experimental spectra shown in figure 8a and 8b.

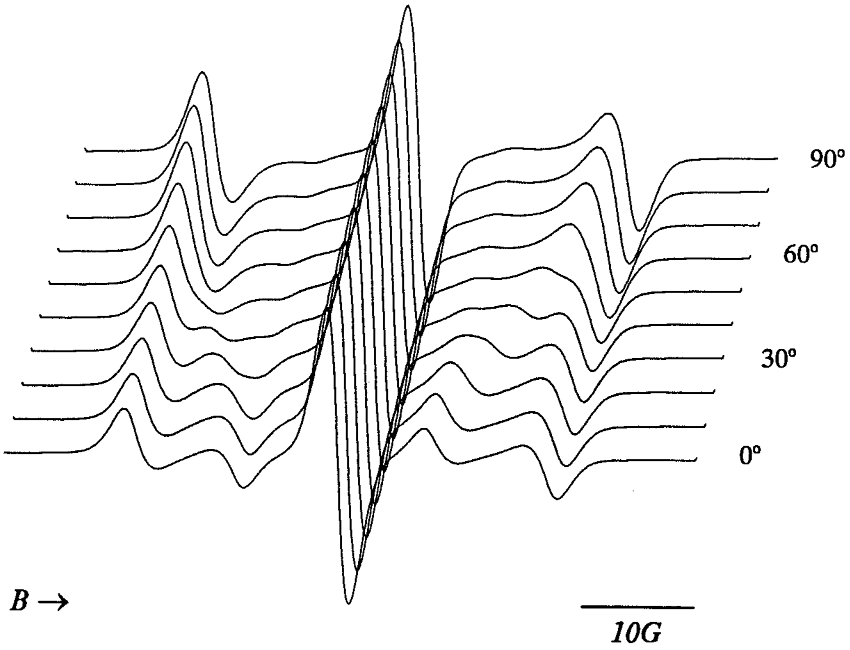

Figure 12 Calculated angle dependence of the spectrum using the extended two-dimensional director distribution for sample 2.

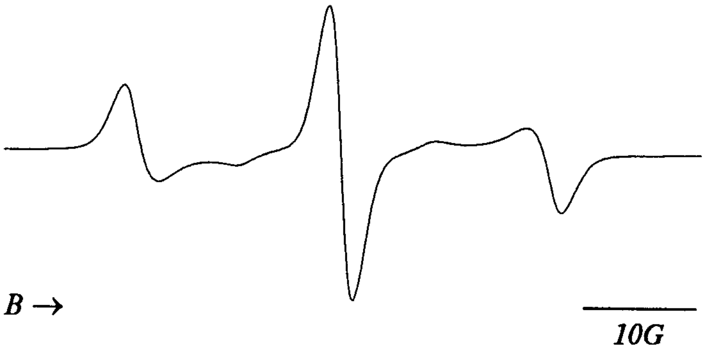

Figure 13 The spectrum for sample 2 simulated using an isotropic director distribution.

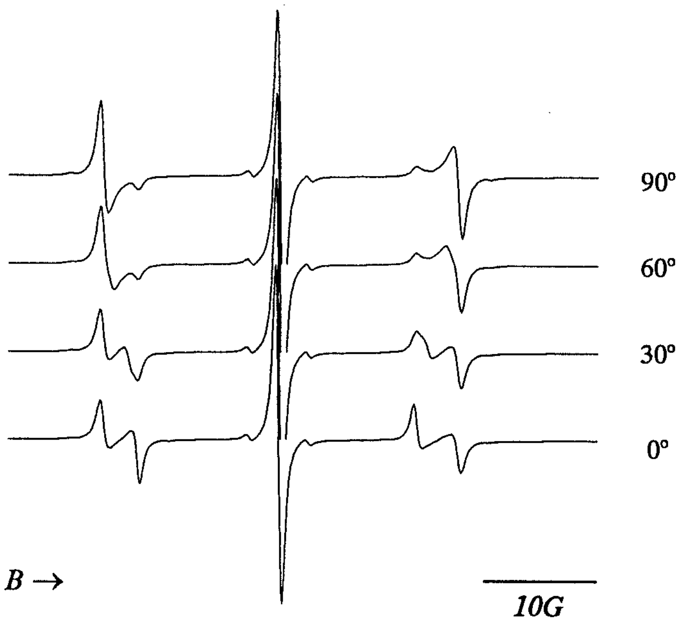

Figure 14 Calculated 0, 30, 60 and 90° spectra for sample 3 using the extended two-dimensional director distribution.

Figure 15 The spectrum for sample 3 simulated using an isotropic director distribution.

6.7.2 Fitting of sample 2 spectra at 155°C

In this analysis the error function E was reduced in 4500 recalculations of the simplex from 3×10^6 to ~65000 after which no further improvement in the quality of the fit was produced. The calculated spectra varied from the starting state of a three-dimensional powder spectrum (as shown in figure 13) to a set similar to the subset of the experimental set for sample 2 used in the analysis. This is shown in figure 16.

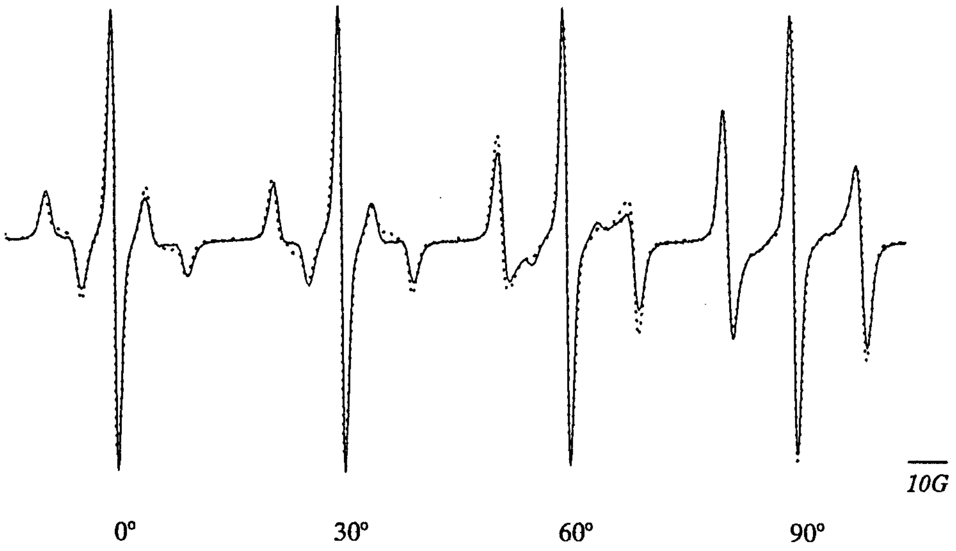

Figure 16 Spectral simulations using the simplex fitting in EPRcalc, showing the experimental (—) and the calculated spectra (---) corresponding to the 0, 30, 60 and 90° positions of the sample.

A plot of the calculated and normalized values of p_i used to obtain the best fit spectra of figure 16 against cosθ is shown in figure 17.

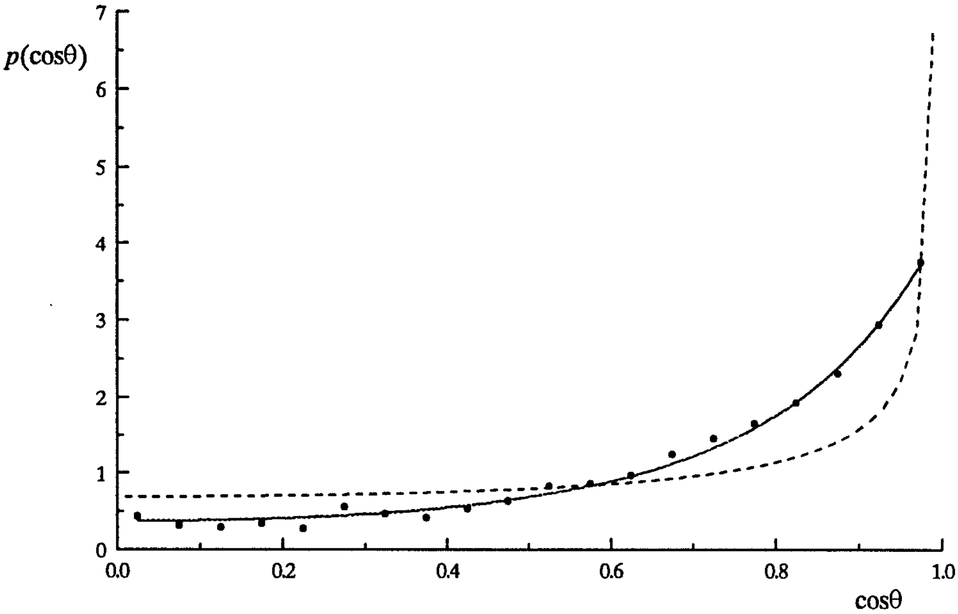

Figure 17 Fitted values (•) of $p(\cos\theta_i)$ *against* $\cos\theta_i$ *used to obtain the calculated spectra in figure 16. Also shown are the calculated distribution functions for the isotropic director distribution, (····), the extended two-dimensional distribution (----) and for the analytical function* $p(\cos\theta) = \exp(a_2P_2(\cos\theta))$ *with* $a_2=1.6$ *(—) discussed in the next section.*

6.7.3 Discussion of simulation results

None of the simulations calculated using either of the model distributions fit the experimental spectra perfectly. First, we consider the results of simulations using the extended two-dimensional director distribution and compare these against the experimental spectra acquired at 155°C shown in figures 6a and 8a in which a similarity to two-dimensional powder spectra had previously been identified. Examination of the spectral simulations for sample 2 shown in figure 12, show that although reasonable agreement is seen between the experimental and simulated 0° and 90° spectra, the agreement at intermediate angles is poor. Specifically, the movement of a feature which has its origin in the portion of the director oriented along the z-axis in the extended two-dimensional distribution can be traced in the angle dependence of the simulated spectrum, but no such feature can be identified in the experimental spectra shown in figure 6a. A comparison of the experimental spectra for sample 3 from figure 8a and their simulated counterparts in figure 14 also shows reasonable agreement of the 0° and 90° spectra but the agreement at 30° and 60° is not so good although, in this case, this could also be due to some subtle linewidth effects. For this reason and for other reasons outlined later we therefore note only that the extended two-dimensional distribution would not appear to be the best available approximation to the real director distribution in these samples at 155°C.

Second, we compare the results of simulations using an isotropic director distribution against the spectra recorded deep into the Sm phase that were observed to bear some similarity to a three-dimensional powder pattern (see the earlier Results section). A true isotropic distribution of the director will produce a spectrum that has no angle dependence, and the simulations correctly reproduce this behaviour. The three-dimensional powder spectra for samples 2 and 3, calculated using the parameters listed in table 6.3 and shown in figures 13 and 15, should be compared with the experimental spectra acquired at 135°C shown in figure 6b and 8b respectively, which do show a weak angle dependence. The fact that we observe an angle dependence in the experimental spectra indicate that the director distributions in the different samples are not truly isotropic, but the similarities between the calculated and the experimental spectra indicate that the director distributions are not far from being isotropic. We note therefore that the isotropic director distribution is not a bad approximation to the real distribution in these samples at temperatures deep into the Sm phase. This observation is now used in conjunction with the results from the model-independent fitting to propose an analytical form for the director distribution in these two samples.

The results of the model-independent fitting show that a set of coefficients $p(\cos\theta_i)$ do exist that give reasonable agreement with the experimental spectra for sample 2 at 155°C, as shown in figure 16, and we therefore seek an analytical expression for the director distribution that is consistent with this set of coefficients. Specifically, we seek an expression that is peaked along the symmetry axis z of the director distribution (that is, at $\theta=0$, $\cos\theta=1$), decreases steadily as the angle with respect to the symmetry axis increases, but reflects the fact there is evidence that all orientations of the director with respect to the symmetry axis are present in the sample. A simple functional form introduced in a different context in Chapter 1 (see section 1.5), can be parameterised to reflect these broad requirements. Thus, the analytical expression that we attempt to fit is

$$f(\cos\theta) = \exp(a_2 P_2(\cos\theta)) \qquad (6.4)$$

The set of coefficients $p(\cos\theta_i)$ calculated using the least-squares fitting routine in EPRcalc are fitted, in Microcal Origin, and used to obtain a value for the parameter a_2 in this expression. The best fit is given by $a_2=1.6$ and this is the solid line plotted in figure 17. The agreement between the calculated set of $p(\cos\theta_i)$ and the values calculated using this fitted value of a_2 is impressive. Some imperfections may arise from attempting to represent the continuous function $f(\cos\theta)$ with a finite number of weighting factors $p(\cos\theta_i)$ in the fitting routine or from imperfections in the parameterisation of the lineshape functions and the fact that no account has been taken of the angular dependence of the linewidths in the simulations for this sample. However, the quality of the fit is not noticeably improved by changing the number of points i or by variation of the lineshape or linewidth parameters. This implies that the fitting of the experimental spectra using this analytical model is robust. The set of spectra calculated using expression 6.4, with the fitted value of $a_2=1.6$ fed back into EPRcalc, are shown in figure 18a together with the relevant experimental spectra reproduced from figure 6a which are shown in figure 18b. Figure 18c shows the spectra calculated using a value of a_2=1.4, visually this also gives a good fit to the experimental spectra, this is particularly evident in the 0° spectrum.

Figure 18 The spectra calculated using values of (a) a_2=1.6 and (c) a_2=1.4 in the model expression $p(\cos\theta_i)=\exp(a_2 P_2(\cos\theta_i))$*. The corresponding experimental spectra are shown in (b).*

Following the apparent success of this model in this specific case we now seek to apply the same model to describe the evolution of the spectrum with temperature. Figure 19 shows the 0° spectrum calculated for sample 2 using equation 6.4 and a number of values of the parameter a_2. It is evident that adjustment of the single parameter a_2 in this model distribution is able to provide a reasonable representation of the director distribution in sample 2 and its evolution with temperature, as seen by a comparison of these calculated spectra with the experimental spectra of figure 5. In particular, as well as fitting the angle dependence of the spectrum at intermediate temperatures, the model also has the correct limiting forms, being close to a monodomain for high values of the parameter a_2 and giving an isotropic director distribution with the three-dimensional powder pattern shown in figure 19b for a_2=0. This is seen in the model distribution functions plotted in figure 20. In figure 21, the angle dependence of the spectrum calculated using a value of a_2= 0.6 is shown together with the corresponding experimental spectra for sample 2 acquired at 135°C (from figure 6b). Here, the agreement between the experimental spectra and those calculated using this model distribution is very good.

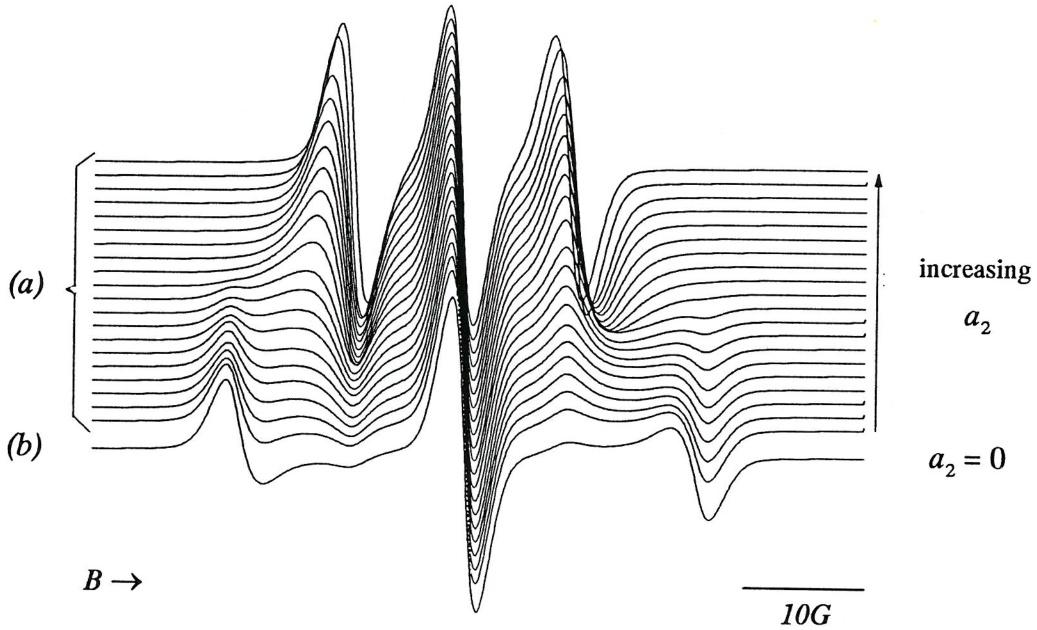

Figure 19 Calculated 0° spectra for sample 2 with (a) several values of a_2 in the range 20 to 0.2, from top to bottom, and (b) the three-dimensional powder spectrum calculated using a_2=0.0.

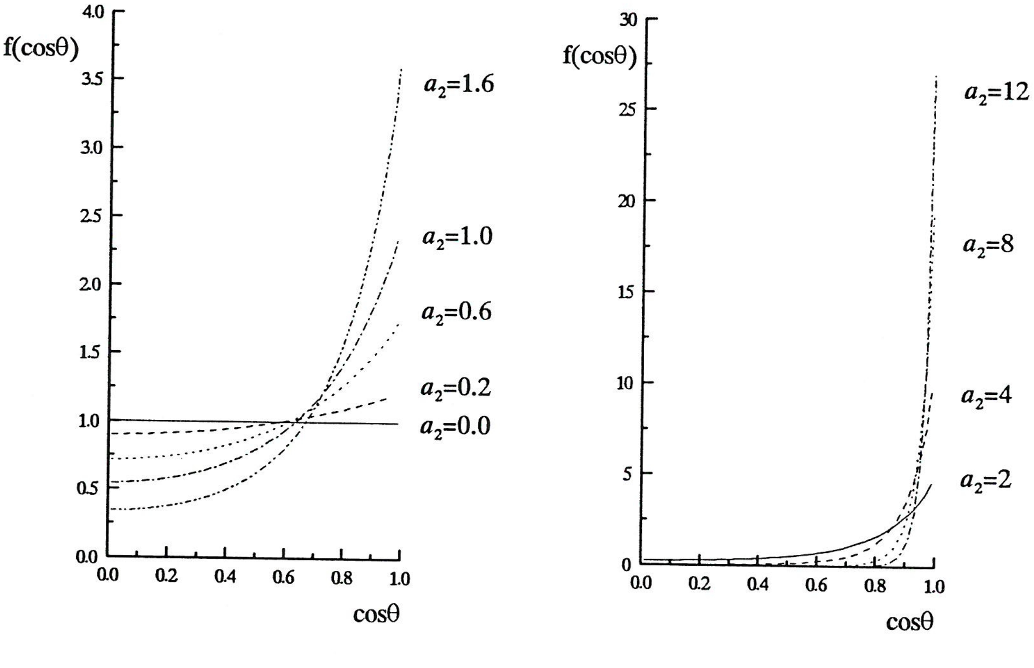

Figure 20 The distribution functions f(cosθ) *obtained from the model distribution* f(cosθ)=exp($a_2\,P_2$(cosθ)) *with some of the different values of a_2 used to calculate the spectra in figure 19. The plots are split to accommodate the change of scale.*

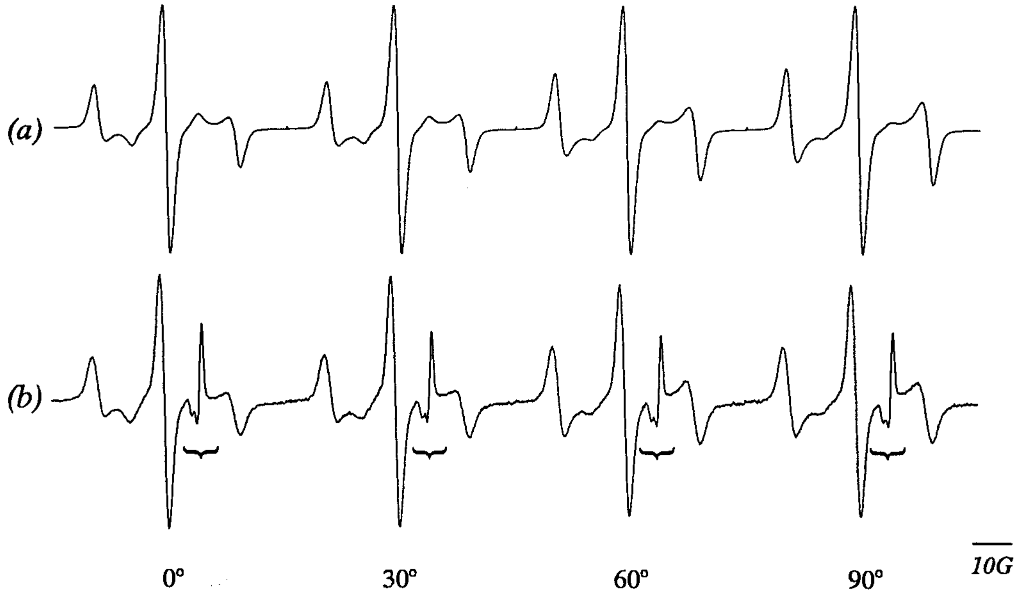

Figure 21 (a) The angle dependence of the spectrum calculated using a value of (a) a_2=0.6 in the model expression $p(\cos\theta_i)=\exp(a_2 P_2(\cos\theta_i))$. (b) shows the corresponding experimental spectra acquired at 135°C. The bracket indicates a background signal from the quartz heating jacket surrounding the sample.

Having used this model with some success to explain the appearance of the spectra for sample 2, we now seek to apply the same model to explain the appearance of the spectra for sample 3. The director distribution in a CBO6CT sample should be independent of the choice of spin probe and dependent only on temperature. The values of a_2 used to fit the spectra for sample 2 at 155°C and at 135°C should therefore also fit the spectra for sample 3 at these same temperatures. The angle dependence of the spectrum for sample 3 calculated using values of a_2=1.4 and a_2=0.6 are shown in figure 22 together with the corresponding experimental spectra taken from figure 8. Figure 23 shows the set of spectra calculated for sample 3 using a range of values for the parameter a_2, this set should be compared with the evolution with temperature of the experimental 0º spectrum of sample 3 shown in figure 7.

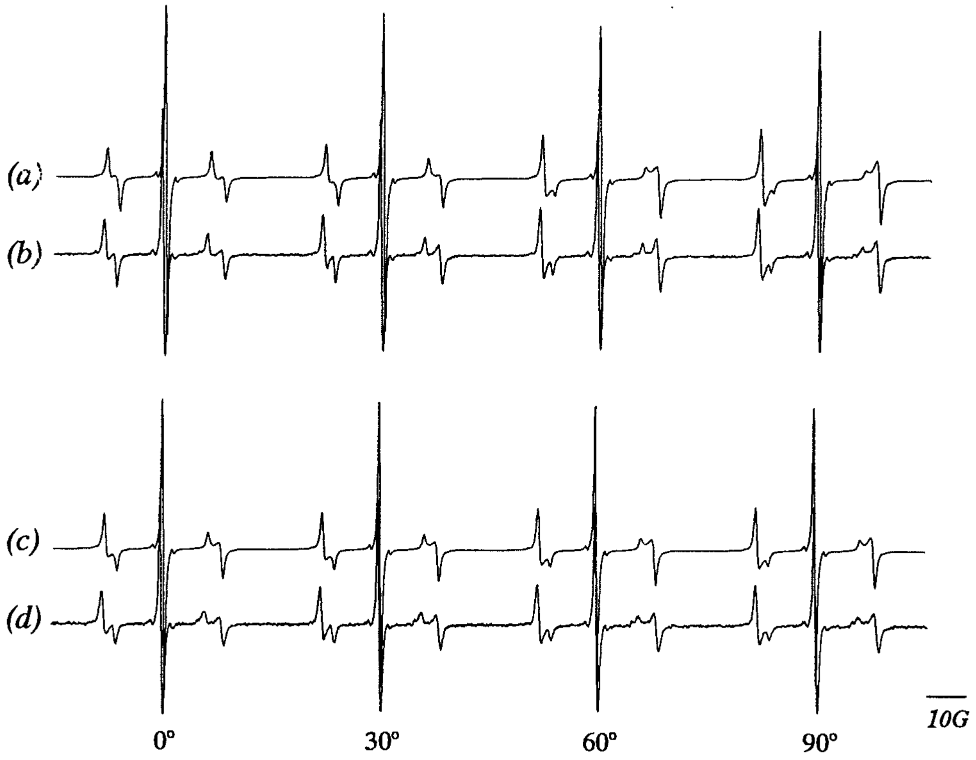

Figure 22 The simulated angle dependence of the spectra for sample 3 calculated with (a) a_2 = 1.4 and (b) a_2= 0.6 in the expression $p(\cos\theta_i)=\exp(a_2 P_2(\cos\theta_i))$. The corresponding experimental spectra from figure 8 are shown in (b) and (d) for comparison.

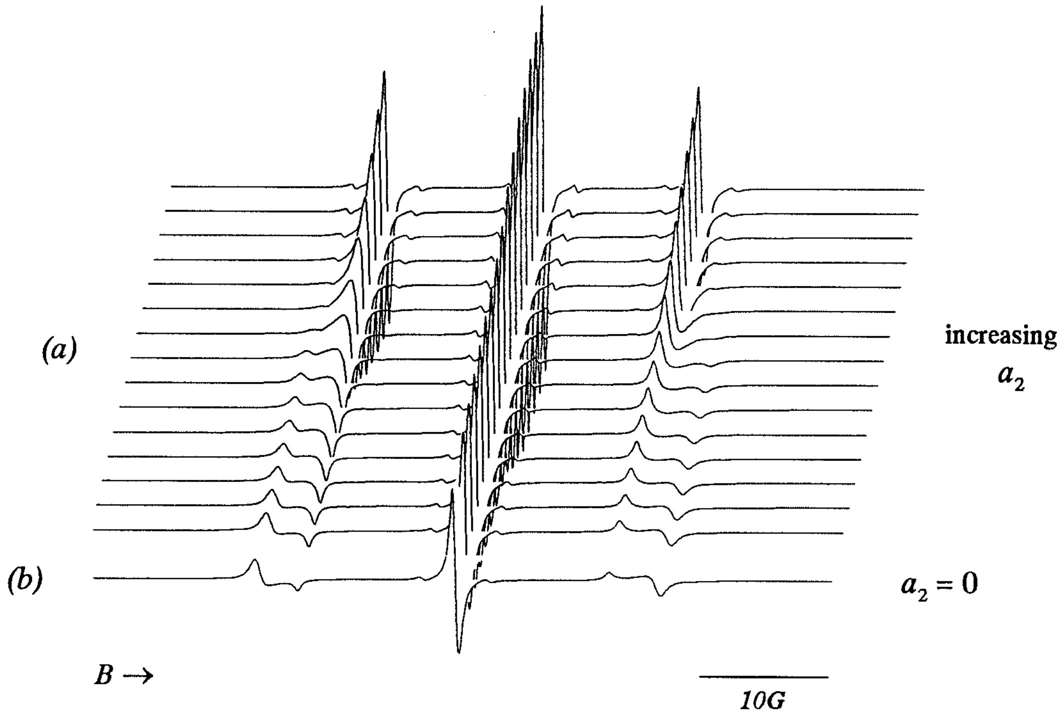

Figure 23 Calculated 0° spectra for sample 3 with (a) several values of a_2 in the range 20 to 0.2, from top to bottom, and (b) the three-dimensional powder spectrum calculated using a_2=0.0.

From the agreement between the calculated spectra and their experimental counterparts, shown in figures 18, 19, and 21 to 23, it is clear that the same model distribution can be applied with some success to the director distributions of both cholestane and tempone spin probes dissolved in CBO6CT (samples 2 and 3). It is unsurprising that the agreement is slightly less good in the case of the tempone spin probe in which the angle-dependent linewidths are more varied and difficult to ascertain for angles other than 0° between the director and the magnetic field. This problem is exacerbated by the rather narrow range ($\tilde{A}_{\perp}$-$\tilde{A}_{\parallel}$) which means that any incorrect parameterisation of the linewidths has a more dramatic effect upon the calculated spectrum.

6.7.4 Interpretation of simulation results

The combination of simulations of EPR spectra using model-dependent and model-independent distributions for the director in these systems enables us to propose at least an analytical form for the director distribution, if not a structure for the Sm phase in the compounds studied, and suggests that we should discount one previously considered form for the director distribution. The previous suggestion of a progressively rippled structure for the layers in the Sm phase is shown in figure 24 [10, 12]. This arrangement of the layers could plausibly account for the initial development of the director distribution in the Sm phase, although it is not clear how the director distribution could continue to evolve after the layers have rippled so that the director makes all angles with the magnetic field, the state shown in figure 24d. The corresponding 0° spectrum for this director distribution would be a two-dimensional powder pattern. However, experimentally, the similarity of the 0° spectrum to a two-dimensional powder pattern is only temporary and the spectrum continues to evolve as the temperature is lowered further. In the rippled layers model, the arrangement shown in figure 24d is a limiting case and no further modifications to this structure can be envisaged that are consistent with the experimental spectra. Further, in our analysis, simulations of the full angle dependence for this arrangement of the layers, equivalent to the extended two-dimensional director distribution when the cylindrical symmetry of the distribution is considered, predict a different angle dependence to that seen experimentally. The results of the model-independent fitting of the spectra simultaneously at several different angles suggest that a simple analytical expression for the director distribution can be parameterised to give a distribution that is consistent with the angle dependence of the spectra and broadly with their evolution with temperature. However, we are unable to propose an arrangement or evolution of the layers in the Sm phase that is consistent with this family of distribution functions.

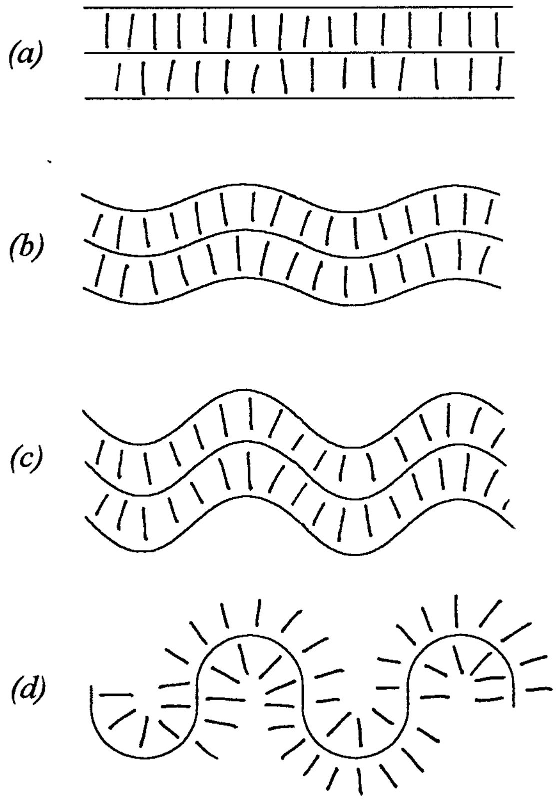

Figure 24 A schematic representation of the previously suggested layer structure in the Sm phase as a function of decreasing temperature in the order (a) to (d).

6.8 Conclusions

This study has examined the smectic phases formed by several odd dimers containing cyanobiphenyl and cyanoterphenyl mesogenic groups. The average molecular shapes of these systems are not obviously conducive to close packing in a layered structure which is sometimes known to drive smectic phase formation; it is also suggested that close packing in a regular layered arrangement would lead to repulsive forces between the strong dipoles of the mesogenic moieties in neighbouring molecules. However, we must be mindful of the fact that the optical texture confirms that this phase has a layered structure. The DSC data for these compounds show no particularly unusual behaviour. ^{2}H NMR experiments also fail to reveal anything particularly unusual, but do show that the orientational order in these systems is weak, which is consistent with the DSC data, although there is a strong possibility that the magnetic fields used in NMR experiments (4.7T) pin the director and modify the structure of the phase. X-ray diffraction experiments are normally a reliable way of obtaining detailed information about phase structure, but X-ray diffraction experiments have not been able to establish precise intermolecular distances in these systems, which implies that the Sm phase formed by these compounds is characterised by a disordered structure. The EPR spectra of spin probes dissolved in the Sm phase shows an unusual pattern that indicates that a director distribution exists in this mesophase that is unlike that seen in any other smectic phase. EPR is presently the only technique that is available to us for the study of the Sm phase that both shows the unusual properties of this phase and provides a means to study this unusual behaviour. The EPR spectrum is dependent upon the director distribution in the sample and therefore further progress in the understanding of the structure of the Sm phase using EPR spectroscopy is based on some model for the phase structure mapping on to the director distributions determined from the EPR spectra or *vice versa*. In this Chapter, we have obtained a numerical approximation to the director distribution that is consistent with the experimental spectra, and have fitted a simple functional form to this distribution, but are unable to propose an arrangement of the smectic layers that is consistent with this functional form. However, the results that we have presented can be tested against other functional forms that may be suggested in future that may give a similarly good fit to the experimental spectra, but have a more obvious connection with a proposed arrangement for the layers in the Sm phase. The method we have used of simultaneously fitting the experimental EPR spectra at a number of different angles offers a powerful route toward the solution of the director distribution for these Sm samples but it is also envisaged that this may be more widely applied toward the interpretation of other sets of EPR spectra and to the results of other, very different, experiments.

Since much of the experimental work in this Chapter was completed, an apparently tilted analogue of the Sm phase has also been examined in this laboratory by EPR spectroscopy [23]. A preliminary analysis again offers no obvious conclusion on the phase structure within this system. In those studies, some of which took place in a Q-band EPR spectrometer, the higher magnetic field of the spectrometer (15000G) appeared to produce a slight sharpening of the lines in the spectrum which suggests that the director distribution is more sharply defined. Further studies might also look at the effect of a stronger magnetic field strength on the Sm phases we have examined. Taken with the results of the experiments described here and previous work in this laboratory, it is suggested that these smectic phases form part of a wider class of rather disordered smectic phases that are at present poorly understood.

References 6.9

[1] GRAY, G.W. and GOODBY, J.W., *Smectic Liquid Crystals: Textures and Structures,* Leonard Hill, 1984, GOODBY, J.W., WAUGH, M.A., STEIN, S.M., CHIN, E., PINDAK, R. and PATEL, J.S., *J. Am. Chem. Soc.,* **111** 8119, 1989.

[2] IMRIE, C.T. and LUCKHURST, G.R., Chapter X, vol. 3, *Handbook of Liquid Crystals,* eds. D. Demus, J.W. Goodby, G.W. Gray, H.-W. Spiess and V. Vill, Wiley-VCH, 1998, ATTARD, G.S., DATE, R.W., IMRIE, C.T., LUCKHURST, G.R., ROSKILLY, S.J., SEDDON, J.M. and TAYLOR, L., *Liq. Crystals,* **16** 529, 1994, HARDOUIN, F., ACHARD, M.F., JIN, J.-I. and YUN, Y.,-K., *J. Phys. II France,* **5** 927, 1995.

[3] DEMUS, D., *Liq. Crystals,* **5** 75, 1989.

[4] TOYNE, K.J., Chapter 2, *Thermotropic Liquid Crystals,* ed. G.W.Gray, CRAC, John Wiley, 1987.

[5] IRVINE, P.A., WU, D.C. and FLORY, P.J., *J. chem. Soc. Faraday Trans. 1,* **80** 1795, 1984.

[6] DATE, R.W., IMRIE, C.T., LUCKHURST, G.R. and SEDDON, J.M., *Liq. Crystals,* **12** 203, 1992.

[7] see reference [1], Chapter 10.

[8] EMERSON, A.P.J. and LUCKHURST, G.R., *Liq. Crystals,* **10** 861, 1991.

[9] EMSLEY, J.W., LUCKHURST, G.R., SHILSTONE, G.N. and SAGE, I., *Mol. Cryst. Liq. Cryst. Lett.,* **102** 223, 1984.

[10] IMRIE, C.T., *PhD Thesis,* University of Southampton, 1988.

[11] CHIU, F.S.M., *Third Year Project Report,* University of Southampton, 1985.

[12] BARNES, P.J., *PhD Thesis,* University of Southampton, 1994.

[13] WILSON, M.J., *PhD Thesis,* University of Southampton, 1998.

[14] MCMILLAN, W.L., *Phys. Rev. A,* **4** 1238, 1971.

[15] GUILLON, D. and LUCKHURST, G.R., private communication.

[16] EMSLEY, J.W., LUCKHURST, G.R. and SHILSTONE, G.N., *Molec. Phys.,* **53** 1023, 1984.

[17] see, for example: Chapter 2, this Thesis, or LUCKHURST, G.R., Chapter 7, vol. 2, *Liquid Crystals and Plastic Crystals,* eds. G.W.Gray and P.A.Winsor, Ellis Horwood, 1974.

[18] Kimura, T., Toriumi, H. and Watanabe, H., *Preprints 14th Liquid Crystal Conference Japan*, **14** 238, 1988.

[19] This is similar to the observation that the director distribution in a bulk sample of a smectic C, which is a biaxial phase, possesses macroscopic cylindrical symmetry if no second constraint is applied to determine the tilt direction around the layer normal.

[20] Carr, S.G., Luckhurst, G.R., Poupko, R., and Smith, H.J., *Chem. Phys.*, 7 278, 1975.

[21] Leach, A.R., Chapter 4, *Molecular Modelling: Principles and Applications*, Longman, 1996.

[22] Freed, J.H., Nayeem, A. and Ranavare, S.B., Chapter 15, *The Molecular Dynamics of Liquid Crystals*, eds. G.R. Luckhurst and C.A. Veracini, Kluwer, 1994.

[23] Luckhurst, G.R. and Le Masurier, P.J., private communication.

Appendix A: Definition of Angles

β, angle between the molecular long axis/mesogenic group and the local director.

ξ, angle between the local director and the magnetic field.

Ω (= $\phi\theta\psi$), general Euler angles that relate two coordinate systems.

Ω (= $\alpha\beta\gamma$), Euler angles that specifically relate molecular-fixed axes to a sample reference frame containing the director.

123, molecular fixed axes, 1 lies along the molecular long axis/axis of the mesogenic group.

XYZ, laboratory fixed axes, Z defines the magnetic field direction.

xyz, sample fixed axes, z defines the *average* director orientation.

Appendix B: EPRIMAGE.for

This program takes the spectral parameters and magnetic field gradient, prescribed in *image.txt* and uses them to calculate a spectrum which is written to the file *image.prn.*

```
* EPRIMAGE.for
*******************************************************************************
*  THIS PROGRAM SIMULATES A 2d-powder FIELD GRADIENT EPR SPECTRUM   *
*******************************************************************************

      dimension  Bapp(1024), TOTSig(1024), Sig(1024)
      dimension AL024(3),AC024(3),AH024(3)
      dimension T2iAl(3)

      open (unit=10, file = 'image.txt', status = 'old')
      open (unit=22, file = 'image.prn', status = 'unknown')

      read (10,6) LTYPE
      read (10,*) Thresh,gPAR,gPER,Apar,Aper
      read (10,*) AL024(1),AL024(2),AL024(3)
      read (10,*) AC024(1),AC024(2),AC024(3)
      read (10,*) AH024(1),AH024(2),AH024(3)
      read (10,6) iPoint
      read (10,*) Bstart, Bwidth, fgrad, Elps
  6 format (I4)

      fghalf= .4*fgrad/2.
      C13hf=2.63
      gpar2  = gpar*gpar
      gper2  = gper*gper
      Apar2  = Apar*Apar
      Aper2  = Aper*Aper
      stepB  = Bwidth/(iPoint)
      gdiff2 = gpar2-gper2
      Adiff2 = Apar2-Aper2
*************************************************************
    do 60 i = 1,iPoint
      Bapp(i) = Bstart+(real(i)-1.)*(stepB)
  60 continue


*** LTYPE=1, Thresh=1 -> tangential distribution, thresh=0 -> radial **
      if (LTYPE.eq.1) then
   do 55 i = 1,iPoint
      TOTsig(i) = 0.0
      noGrid=0
    do 35 jX =-49,49,2
    do 25 kY =-49,49,2
      Xr  = real(jX)/50.0
      Yr  = real(kY)/50.0
      R2 = Xr*Xr + Yr*Yr
```

```
      if (R2.gt.1.0) then
         TOTSig(i) = TOTSig(i)
      else
         noGrid=noGrid+1
         Bexp = Bapp(i) + Xr*fghalf
**********
      if(R2.lt.Thresh) then
       cosAl2 = Y2/R2                **** (--> tangential distribution)
      else
       cosAl2 = X2/R2                **** (--> radial distribution)
      end if

         gAl = sqrt ((gdiff2)* cosAl2 + gPER2)
         Aal = sqrt ((Adiff2)*cosAl2 + Aper2)
         P2 = (               3.*cosAl2-1.)/2.
         P4 = (35.*cosAl2*cosAl2-30.*cosAl2+3.)/8.
         T2iAl(1) = AL024(1) + AL024(2)*P2 + AL024(3)*P4
         T2iAl(2) = AC024(1) + AC024(2)*P2 + AC024(3)*P4
         T2iAl(3) = AH024(1) + AH024(2)*P2 + AH024(3)*P4
***************************************************************
         Bres = 2.0023 * 3345.0 / gAl
         delB=Bexp-Bres
** non-normalised lorentzian
         SIGlow  = 1./T2iAl(1) *1./(1.+((delB+Aal)/T2iAl(1))**2)
         SIGo    = 1./T2iAl(2) *1./(1.+((delB     )/T2iAl(2))**2)
         SIGhi   = 1./T2iAl(3) *1./(1.+((delB-Aal)/T2iAl(3))**2)
         SIGal = (SIGlow + SIGo + SIGhi)
         TOTsig(i) = TOTsig(i) + SIGal
      end if

  25 continue
  35 continue
         PRINT*,Bapp(i),TOTsig(i)
         WRITE(22,15) TOTsig(i)
  15 format (f12.4)
  55 continue


*** elliptical distribution if LTYPE=2 ******************************
     else if (LTYPE.eq.2) then
         Eps2=Elps*Elps
         Eps4=Eps2*Eps2

     do 50 i = 1,iPoint
         TOTsig(i) = 0.0
     do 30 jX =-49,49,2
     do 20 kY =-49,49,2
         Xr  = real(jX)/50.0
         Yr  = real(kY)/50.0
         R2 = Xr*Xr + Yr*Yr

         if (R2.gt.1.0) then
         TOTSig(i) = TOTSig(i)
         else
         Bexp = Bapp(i) + Xr*fghalf
                Beta = atan(Yr/Xr)
```

```
      do 10 iEllip=1,89,2
        Phi=(real(iEllip)*3.1416/180.)
        cosPh2=cos(Phi)*cos(Phi)
        strong=(Eps2)/(1.+(Eps4-1.)*cosPh2)
        Alpha=Beta+Phi
        cosAl2=cos(Alpha)*cos(Alpha)
        gAl = sqrt ((gdiff2)* cosAl2 + gPER2)
        Aal = sqrt ((Adiff2)*cosAl2 + Aper2)
        P2 = (             3.*cosAl2-1.)/2.
        P4 = (35.*cosAl2*cosAl2-30.*cosAl2+3.)/8.
        T2iAl(1) = AL024(1) + AL024(2)*P2 + AL024(3)*P4
        T2iAl(2) = AC024(1) + AC024(2)*P2 + AC024(3)*P4
        T2iAl(3) = AH024(1) + AH024(2)*P2 + AH024(3)*P4
*****************************************************************
        Bres = 2.0023 * 3345.0 / gAl
        delB=Bexp-Bres
* non-normalised Lorentzian with 13C hyperfine interaction
        SIGlow = .9592/(T2iAl(1)*(1.+((delB+Aal      )/T2iAl(1))**2)) +
     +           .0204/(T2iAl(1)*(1.+((delB+Aal+C13hf)/T2iAl(1))**2)) +
     +           .0204/(T2iAl(1)*(1.+((delB+Aal-C13hf)/T2iAl(1))**2))
        SIGo   = .9592/(T2iAl(2)*(1.+((delB        )/T2iAl(2))**2)) +
     +           .0204/(T2iAl(2)*(1.+((delB   +C13hf)/T2iAl(2))**2)) +
     +           .0204/(T2iAl(2)*(1.+((delB   -C13hf)/T2iAl(2))**2))
        SIGhi  = .9592/(T2iAl(3)*(1.+((delB-Aal)/T2iAl(3))**2)) +
     +           .0204/(T2iAl(3)*(1.+((delB-Aal+C13hf)/T2iAl(3))**2)) +
     +           .0204/(T2iAl(3)*(1.+((delB-Aal-C13hf)/T2iAl(3))**2))
        SIGal = (SIGlow + SIGo + SIGhi)
        TOTsig(i) = TOTsig(i) + strong * SIGal
 10   continue
        end if

 20   continue
 30   continue
        WRITE(22,15) sig(i)
 50   continue

        end if
        close (10)
        close (22)
        stop
        end
```

The file *image.txt* used to calculate the simulated spectrum shown in figure 25(b).

2			Ltype, 1 gives either tangential or radial distribution depending on value of Thres, if set to 2 calculates using localized elliptical director distribution
1.0			Thresh, 1 gives a tangential distribution, 0 gives a radial distribution
2.0021	2.0023		gpar, gper values
12.3	15.75		Apar, Aper values
0.53	-0.19	0	Linewidth parameters for low-field line
0.49	-0.17	0	Linewidth parameters for centre line
0.65	-0.23	0	Linewidth parameters for high-field line
1024			Number of points in calculated spectrum,
3315	60		Starting field and range of field values over which spectrum calculated (G)
15			Simulated field gradient across sample (Gcm^{-1})
1.2			Eccentricity of the ellipse used when calculating a locally-defined elliptical distribution of the director

Appendix C: EPRcalc.for

EPRCalc.*for* calculates a number of angle dependent spectra for a sample as the sum of a series of subspectra using spectral parameters listed in *SpecPars.txt,* this set of spectra may then be compared with a target set of spectra, which may also be calculated or read in from a source file *ExSpec.prn.* The intensity coefficients of the subspectra may then be varied using a simplex algorithm to obtain the set of coefficients that give the best fit to the set of target spectra, which are output to the files *inteni.prn* and *out.prn* repectively.

```
************************************************************************
** EPRCalc.for                                                        **
************************************************************************
   dimension SPEC0(2732,-1:5000), SPECE(2732,0:5000)
   dimension B(2732),SPECfB(2732),exSPEC(2732),stSPEC(2732), Z(2732)
   dimension  inten(0:100,0:100),expint(1000),best(0:1000)
   dimension ctheta(5000),phi(5000),cosAlp(5000)
   dimension AL(3),AC(3),AH(3),ALE(3),ACE(3),AHE(3)
   dimension cosqA(5000,4),
   dimension Aal(5000,4),gAl(5000,4),Bres(5000,4), T2iL(5000,4), T2iM(5000,4), T2iH(5000,4)
   dimension AalE(5000,4),gAlE(5000,4),BresE(5000,4), T2iLE(5000,4),T2iME(5000,4)
   dimension T2iHE(5000,4), sumsq(30000), ERR(0:100),vector(0:100),centro(0:100)

   open(unit=10, file = 'SpecPars.txt',status = 'old')
   open(unit=14, file = 'inteni.prn', status = 'unknown')
   open(unit=16, file = 'out.prn'   , status = 'unknown')
   open(unit=18, file = 'exSPEC.prn', status = 'unknown')
   jacc=0
   k=0
   l=0
   test=1000000000.
   dev=0.0
   sqdev=0.0

   read (10,6) iCalc, noThet, noPhi
   read (10,*) sigma2,gPAR,gPER,Apar,Aper, AL(1),AL(2),AL(3)
   read (10,*) AC(1),AC(2),AC(3),AH(1),AH(2),AH(3)
   read (10,6) iPoint
   read (10,*) Bstart, Bwidth
   read (10,6) noits
   read (10,*) a, sumsq(1)
   read (10,*) gPARE,gPERE,AparE,AperE,ALE(1),ALE(2),ALE(3)
   read (10,*) ACE(1),ACE(2),ACE(3),AHE(1),AHE(2),AHE(3),Eps
   read (10,*) ratioL
   read (10,6) iTYPE
 6 format (15)

   f=0.9592*ratioL/3.1416
   f2=0.0204*ratioL/3.1416
   Gau=(1.-ratioL)*0.3989* 0.9592
   hf=2.63
```

```
   noSpec=4
   AparE2=AparE*AparE
   AperE2=AperE*AperE
   AdifE2=AparE2-AperE2
   gparE2=gparE*gparE
   gperE2=gperE*gperE
   gdifE2=gparE2-gperE2
   Apar2=Apar*Apar
   Aper2=Aper*Aper
   Adiff2=Apar2-Aper2
   gpar2=gpar*gpar
   gper2=gper*gper
   gdiff2=gpar2-gper2
   stepB  = Bwidth/(iPoint)

*** generate points in (cosΘ, ϕ) space for calculation of component subspectra
*** or in (Θ ,ϕ) space for calculation for extended 2-d distribution

   do 21 ispec=1,noSpec
    noI=0
   do 20 ithet= 1,noThet
    inten(0,iThet)=1.0
    top=(-1.999+(2.*real(iThet)))/(2.*real(noThet))
    bot=(-0.0+(2.*real(iThet)))/(2.*real(noThet))
    weight=acos(top) - acos(bot)
c  3d
    cosAlp(ithet)=(-1.+(2.*real(iThet)))/(2.*real(noThet))

   do 22 iphi = 1,nophi
      i=(ithet-1)*nophi + iPhi
      phi(i)   =(-1.+(2.*real(iPhi )))/(2.*real(nophi))*2.*3.1416
      ctheta(i)=cosAlp(ithet)
c  2d from 3d        expint(ithet)=weight
c calculation of exp(a2P2cosTheta) model distribution
     expint(ithet)=exp(a * (1./2.)*(3.*ctheta(i)*ctheta(i)-1.))

*** calculate angle between field and the local director, and angle dependent spectral parameters
      cosqA(i,1)=ctheta(i)*ctheta(i)
      cosqA(i,2)=(sqrt(0.75)*ctheta(i)  +    +                0.5*sin(acos(ctheta(i)))*(sin(phi(i))))**2
      cosqA(i,3)=(      0.5*ctheta(i)  +    +         sqrt(0.75)*sin(acos(ctheta(i)))*(sin(phi(i))))**2
      cosqA(i,4)=(sin(acos(ctheta(i)))*(sin(phi(i))))**2
******************************************************************************

   P2 =(                          3.*cosqA(i,ispec)-1.)/2.
   P4 =(35.*cosqA(i,ispec)*cosqA(i,ispec)-30.*cosqA(i,ispec)+3.)/8.
      Aal(i,ispec) = sqrt ((Adiff2)*cosqA(i,ispec) + Aper2)
      gAl(i,ispec) = sqrt ((gdiff2)*cosqA(i,ispec) + gper2)
      Bres(i,ispec) = 2.0023 * 3345.0 / gAl(i,ispec)
      T2iL(i,ispec) = AL(1) + AL(2)*P2 + AL(3)*P4
      T2iM(i,ispec) = AC(1) + AC(2)*P2 + AC(3)*P4
      T2iH(i,ispec) = AH(1) + AH(2)*P2 + AH(3)*P4
************************************************************ target **********
      AalE(i,ispec) = sqrt ((AdifE2)* cosqA(i,ispec) + AperE2)
      gAlE(i,ispec) = sqrt ((gdifE2)* cosqA(i,ispec) + gperE2)
      BresE(i,ispec) = 2.0023 * 3345.0 / gAlE(i,ispec)
      T2iLE(i,ispec) = ALE(1) + ALE(2)*P2 + ALE(3)*P4
      T2iME(i,ispec) = ACE(1) + ACE(2)*P2 + ACE(3)*P4
      T2iHE(i,ispec) = AHE(1) + AHE(2)*P2 + AHE(3)*P4
******************************************************************************
```

```
      noI=noI+1
  22 continue
  20 continue
  21 continue

** to calculate starting spectra as sum of subspectra

     do 31 iSp=1,noSpec
     do 30 intB= 1,iPoint
       B(intB) = Bstart+(real(intB)-1.)*(stepB)
       SpecfB(intB+(iSp-1)*iPoint)=0.0
       stSpec(intB+(iSp-1)*iPoint)=0.0

     if(iTYPE.eq.1)then
***** Lor lineshape with 13C splitting *****************************
     do 32 iThet=1,noThet
       SpThet=0.0
       SpTheE=0.0
       SpecE(intB+(iSp-1)*iPoint,iThet)=0.0
       Spec0(intB+(iSp-1)*iPoint,iThet)=0.0

     do 35 i=(ithet-1)*noPhi+1, iThet*noPhi
       delB=B(intB) - Bres(i,iSp)
      Siglo=f/(T2iL(i,iSp)*(1.+((delB+Aal(i,iSp)   )/T2iL(i,iSp))**2))+
     +     f2/(T2iL(i,iSp)*(1.+((delB+Aal(i,iSp)-hf)/T2iL(i,iSp))**2))+
     +     f2/(T2iL(i,iSp)*(1.+((delB+Aal(i,iSp)+hf)/T2iL(i,iSp))**2))
      Sigcp=f/(T2iM(i,iSp)*(1.+((delB           )/T2iM(i,iSp))**2))+
     +     f2/(T2iM(i,iSp)*(1.+((delB        -hf)/T2iM(i,iSp))**2))+
     +     f2/(T2iM(i,iSp)*(1.+((delB        +hf)/T2iM(i,iSp))**2))
      Sighi=f/(T2iH(i,iSp)*(1.+((delB-Aal(i,iSp)   )/T2iH(i,iSp))**2))+
     +     f2/(T2iH(i,iSp)*(1.+((delB-Aal(i,iSp)-hf)/T2iH(i,iSp))**2))+
     +     f2/(T2iH(i,iSp)*(1.+((delB-Aal(i,iSp)+hf)/T2iH(i,iSp))**2))
          SUB= (Siglo+Sigcp+Sighi)
          SpThet=SpThet+SUB

       delBE=B(intB) - BresE(i,iSp)
      SiglE=f/(T2iLE(i,iSp)*(1.+((delBE+AalE(i,iSp))/T2iLE(i,iSp))**2))+
     + f2/(T2iLE(i,iSp)*(1.+((delBE+AalE(i,iSp)-hf)/T2iLE(i,iSp))**2))+
     + f2/(T2iLE(i,iSp)*(1.+((delBE+AalE(i,iSp)+hf)/T2iLE(i,iSp))**2))
      SigcE=f/(T2iME(i,iSp)*(1.+((delBE          )/T2iME(i,iSp))**2))+
     + f2/(T2iME(i,iSp)*(1.+((delBE        -hf)/T2iME(i,iSp))**2))+
     + f2/(T2iME(i,iSp)*(1.+((delBE        +hf)/T2iME(i,iSp))**2))
      SighE=f/(T2iHE(i,iSp)*(1.+((delBE-AalE(i,iSp))/T2iHE(i,iSp))**2))+
     + f2/(T2iHE(i,iSp)*(1.+((delBE-AalE(i,iSp)-hf)/T2iHE(i,iSp))**2))+
     + f2/(T2iHE(i,iSp)*(1.+((delBE-AalE(i,iSp)+hf)/T2iHE(i,iSp))**2))
       subE= (SiglE+SigcE+SighE)
       SpTheE=SpTheE+subE

   35 continue

      SpecE(intB+(iSp-1)*iPoint,iThet)=SpTheE
      Spec0(intB+(iSp-1)*iPoint,iThet)=SpThet
      SpecfB(intB+(iSp-1)*iPoint)=SpecfB(intB+(iSp-1)*iPoint)+
     +             Spec0(intB+(iSp-1)*iPoint,ithet)*inten(0,ithet)


   32 continue
```

```
      elseif (iTYPE.eq.2) then
***** L-G mixture without 13C splitting *****************************

      do 33 iThet=1,noThet
       SpThet=0.0
       SpTheE=0.0
       SpecE(intB+(iSp-1)*iPoint,iThet)=0.0
       Spec0(intB+(iSp-1)*iPoint,iThet)=0.0

      do 36 i=(ithet-1)*noPhi+1, iThet*noPhi
       delB=B(intB) - Bres(i,iSp)
          Siglo=f/(T2iL(i,iSp)*(1.+((delB+Aal(i,iSp)  )/T2iL(i,iSp))**2))+
     +Gau/T2iL(i,iSp)*exp(-.5*(((delB+Aal(i,iSp)  )/T2iL(i,iSp))**2))
          Sigcp=f/(T2iM(i,iSp)*(1.+((delB           )/T2iM(i,iSp))**2))+
     +Gau/T2iM(i,iSp)*exp(-.5*(((delB           )/T2iM(i,iSp))**2))
          Sighi=f/(T2iH(i,iSp)*(1.+((delB-Aal(i,iSp)  )/T2iH(i,iSp))**2))+
     +Gau/T2iH(i,iSp)*exp(-.5*(((delB-Aal(i,iSp)  )/T2iH(i,iSp))**2))
       SUB= (Siglo+Sigcp+Sighi)
       SpThet=SpThet+SUB

       delBE=B(intB) - BresE(i,iSp)
          SiglE=f/(T2iLE(i,iSp)*(1.+((delBE+AalE(i,iSp))/T2iLE(i,iSp))**2))+
     + Gau/T2iLE(i,iSp)*exp(-.5*(((delBE+AalE(i,iSp))/T2iLE(i,iSp))**2))
          SigcE=f/(T2iME(i,iSp)*(1.+((delBE           )/T2iME(i,iSp))**2))+
     + Gau/T2iME(i,iSp)*exp(-.5*(((delBE           )/T2iME(i,iSp))**2))
          SighE=f/(T2iHE(i,iSp)*(1.+((delBE-AalE(i,iSp))/T2iHE(i,iSp))**2))+
     + Gau/T2iHE(i,iSp)*exp(-.5*(((delBE-AalE(i,iSp))/T2iHE(i,iSp))**2))
       subE= (SiglE+SigcE+SighE)
       SpTheE=SpTheE+subE

  36 continue

      SpecE(intB+(iSp-1)*iPoint,iThet)=SpTheE
      Spec0(intB+(iSp-1)*iPoint,iThet)=SpThet
      SpecfB(intB+(iSp-1)*iPoint)=SpecfB(intB+(iSp-1)*iPoint)+     +
Spec0(intB+(iSp-1)*iPoint,ithet)*inten(0,ithet)

  33 continue


      endif
**********************************************************************
      stSpec(intB+(iSp-1)*iPoint)=SpecfB(intB+(iSp-1)*iPoint)
  30 continue
  31 continue


* make slight change to each distribution to initiate points of simplex

      delta=-.1
      do 55 i=0,nothet
      do 57 j=1,noThet
        inten(i,j)=inten(0,j)
        inten(j,j)=inten(0,j)+delta
  57 continue
  55 continue
```

```
* to decide whether to calculate target spectrum or read in target spectra from file 'exSpec.prn'

    if (icalc.eq.1) then
     do 41 iSp=1,noSpec
     do 40 intB= 1,iPoint
        exSPEC(intB+(iSp-1)*iPoint)=0.0
     do 45 ithet=1,nothet
* expint puts director along z axis
     exSPEC(intB+(iSp-1)*iPoint)=exSPEC(intB+(iSp-1)*iPoint)+    +
SpecE(intB+(iSp-1)*iPoint,ithet)*expint(iThet)

  45 continue
  40 continue
  41 continue

    elseif (icalc.eq.0) then
      do 48 intB = 1,noSpec*iPoint
      read (18,*) exSPEC(intB)
  48   continue
    endif

* This part of the program calculates an error value E for the spectra calculated for each of the
director * distributions

    do 8 i=0,nothet
       ERR(i)=0.0
    do 60 iSp=1,noSpec
    do 62 intB=1,iPoint
       Z(intB+(iSp-1)*iPoint)=0.0

    do 64 j=1,noThet
       Z(intB+(iSp-1)*iPoint)=Z(intB+(iSp-1)*iPoint)+    +
Spec0(intB+(iSp-1)*iPoint,j)*inten(i,j)
  64 continue

    dev=Z(intB+(iSp-1)*iPoint)-exSpec(intB+(iSp-1)*iPoint)
    dev2=dev*dev
    ERR(i)=ERR(i) + dev2

  62 continue
  60 continue
   8 continue

      sumsq(1)=sqdev
      print*,sumsq(1)

*****************************************************************
** Iteration of SPECfB toward exSPEC from here, first, select worst distribution

    do 50 its=2,noits
    testHi=0.0
    testLo=100000000.

    do 70 i=0,noThet
    if (ERR(i).gt.testHi) then
     testHi=ERR(i)
     ichange=i
    endif
```

```
      if (ERR(i).lt.testLO) then
       testLO=ERR(i)
       iLow=i
      endif
      if (testLO.lt.test) then
       test=testLO
       Low=its
      endif
   70 continue

* now find the vector to the centroid of the remaining points and redefine changed point
      do 72 j=1,noThet
       cent=0.0
       centro(j)=0.0
      do 74 i=0,noThet
       cent=cent+inten(i,j)
   74 continue
       centro(j)=(cent-inten(ichange,j))/noThet
       vector(j)=centro(j)-inten(ichange,j)
       inten(ichange,j)=inten(ichange,j)+2.*vector(j)
   72 continue

* now calculate error of changed point
      ERR(ichange)=0.0
      do 80 iSp=1,noSpec
      do 82 intB=1,iPoint
         Z(intB+(iSp-1)*iPoint)=0.0
      do 84 j=1,noThet

Z(intB+(iSp-1)*iPoint)=Z(intB+(iSp-1)*iPoint)+(Spec0(intB+(iSp-1)*iPoint,j)*inten(ichange,j))
   84 continue
       dev=Z(intB+(iSp-1)*iPoint)-exSpec(intB+(iSp-1)*iPoint)
       dev2=dev*dev
       ERR(ichange)=ERR(ichange) + dev2
   82 continue
   80 continue
      print*,its,ichange,testHi,ERR(ichange),testLo
   50 continue

* output spectral parameters, starting spectra, target spectra and best fit spectra.
      write(16,*) iCalc,noThet,noPhi
      write(16,*) noI,sigma2,a
      write(16,*) noits,low,test
      write(16,*) iTYPE,sumsq(1),sumsq(noits)
      write(16,*) jacc,k,l
      write(16,*) ratioL,ratioL,ratioL
      do 90 intB=1,noSpec*iPoint
       write(16,*) stSPEC(intB),exSPEC(intB),Z(intB)
   90 continue

* output details of best and worst fits and converged distribution coefficients
      do 98 i=0,nothet
      do 99 ithet=1,nothet
      write(14,*) inten(i,ithet),best(ithet),expint(ithet)
   99 continue
   98 continue
      stop
      end
```